Developing Real-time MRI Using Simultaneous Multislice Acceleration and Compressed Sensing

Isaac Watson

Doctor of Philosophy

University of York
School of Physics, Engineering and Technology

July 2024

Abstract

Real-time MRI (rtMRI) is an imaging method which allows motion to be recorded at high temporal and spatial resolutions without the need for synchronization equipment or assumptions regarding periodicity of motion. To achieve a high temporal resolution, rtMRI methods employ fast imaging sequences and highly undersampled non-Cartesian k-space sampling. The need for fast data acquisition prevents the acquisition of multiple slices without loss of temporal resolution, limiting the anatomical coverage of rtMRI.

This thesis describes the development of an rtMRI sequence which uses radial sampling and simultaneous multislice (SMS) excitation to rapidly image multiple slices simultaneously. Thus, overcoming the single-slice limitation of standard rtMRI methods. This SMS rtMRI sequence can record movement at a temporal resolution of up to 37.5ms and spatial resolution of 2.2mm^2 in multiple (1-7) locations simultaneously. A compressed sensing image reconstruction pipeline is implemented and is shown to have improved performance, at the cost of increased reconstruction time, compared to standard reconstruction methods.

The thesis then explores potential applications of the rtMRI sequence. First applications in head/neck imaging are shown such as, recording speech and swallowing. Next, dynamic musculoskeletal imaging applications are shown such as, knee movement, foot/ankle movement and wrist movement.

Contents

List of Figures

Declaration

I declare that this thesis is a presentation of original work and I am the sole author. This work has not previously been presented for a degree or other qualification at this University or elsewhere. All sources are acknowledged as references.

Acknowledgments

This PhD has been a fantastic experience from start to finish, my deepest thanks go to all my supervisors: Aneurin Kennerley, Angelika Sebald and Martin Trefzer for their support and encouragement. You have been a brilliant, knowledgeable and supportive group of supervisors and I especially appreciate the corrections of my numerous typos.

In addition, I would like to thank Elisa Zamboni for her help, support and constant willingness to hop into the scanner. Thank you for bearing with mine (and Aneurin's) inability to properly organise anything!

Thanks also goes to the York Neuroimaging Center staff for providing support and training for the MR experiments. Additionally, I would like to thank everyone in Centre for Hyperpolarisation in Magnetic Resonance for their help and willingness to listen to my very unrelated work.

I also wish to thanks Mike Angus for his assistance in the design and construction of the dynamic phantom in Chapter 6. I thank David Mitchell for his invaluable clinical input which guided the head/neck imaging applications explored in this thesis.

I'm very grateful to the support from James McStravick for his assistance and guidance during scanning sessions at Manchester Metropolitan University, apologies for every time I crashed the scanner!

Finally, I would like to thank my family and friends for their support throughout the PhD. A special thanks goes to my partner Miglė for her

constant and unwavering support (and grammar corrections) over these four years, without which this thesis would not have been possible.

Chapter Contributions and Related Publications

Chapter Contributions

Chapters 1, 2 and 3 are background theory chapters. Unless stated otherwise, I acquired and reconstructed all the MR images shown in these chapters.

Chapter 4 describes the real-time MRI pulse sequence and reconstruction pipeline used in this thesis. I solely developed both the sequence and reconstruction code. All data shown in Chapters 5 and 7 was acquired and reconstructed using the developed sequence and reconstruction code.

Chapter 6 describes the development of a dynamic MRI phantom. I assisted in the design of this phantom and it was built by Mike Angus (technician in the School of Physics, Engineering and Technology). I acquired and reconstructed all the results shown in this chapter.

Related Publications

Section 7.2 is based on the following journal paper

> Aneurin Kennerley, David Mitchell, Angelika Sebald and Isaac Watson. Real-time magnetic resonance imaging: mechanics of oral and facial function. *British Journal of Oral and Maxillofacial Surgery*, 60(5):596-603, 2021.

Chapters 4 and 5 are based on the following conference abstract.

> Isaac Watson, Elisa Zamboni, James McStravick, David Mitchell, Martin Trefzer, Angelika Sebald and Aneurin Kennerley. Improving reconstruction of multiband real-time MRI. *Proceedings of the Internation Society for Magnetic Resonance in Medicine*, Singapore, 2024.

Section 7.3 is based on the following conference abstract.

> Isaac Watson, Elisa Zamboni, James McStravick, David Mitchell, Martin Trefzer, Angelika Sebald and Aneurin Kennerley. Improving reconstruction of multiband real-time MRI. *Proceedings of the Internation Society for Magnetic Resonance in Medicine*, Singapore, 2024.

Section 8.2.4 is based on the following conference abstract.

> Elisa Zamboni, Isaac Watson, Frida Torkelsen, James McStravick and Aneurin Kennerley. Neurovascular & experimental confounds when probing neuronal activity with fast fMRI: exploring evasive DIANA & DW-fMRI. *Proceedings of the Internation Society for Magnetic Resonance in Medicine*, Singapore, 2024.

Chapter 4 and Chapter 5 are based on the following paper in preparation.

> Isaac Watson, Mike Angus, Elisa Zamboni, James McStravick, David Mitchell, Angelika Sebald and Aneurin Kennerley. Simultaneous Multislice Real-time MRI with Compressed Sensing Reconstruction. *In preparation.*

1 Introduction

1.1 Introduction

Magnetic Resonance Imaging (MRI) is a non-invasive imaging modality which exploits the nuclear magnetic moment of atomic nuclei [1]. The most commonly imaged isotope in clinical MRI is hydrogen (^{1}H) as the body contains large amounts of this isotope in water and hydrocarbon based fat chains. The local chemical environment can alter the magnetic properties of the nuclei and hence, ^{1}H MRI can be used to generate a wide range of contrasts, which reflect different aspects of the anatomy. This can range from traditional structural images to contrasts unique to MRI such as susceptibility weighted imaging (which exploits subtle phase differences between populations of nuclei) [2].

MRI has the advantageous properties of being non-invasive and using non-ionizing radiation[1]. Unfortunately, compared to other medical imaging modalities (e.g. ultrasound and x-ray) MRI is slow to acquire data. This is due to the time needed to embed spatial information into the recorded signal [3]. In the past, this has limited MRI to the recording of static images or the monitoring of slow (on the timescale of seconds) or repetitive dynamic processes. However, a human body is defined not only by its structure but

also by its functions. Thus, a static representation of the body (in the form of an image), although useful, is limited. There is a need for MRI techniques that capture both structure and function [4].

From the 1970's, simultaneous developments in scanner hardware, computing hardware, data acquisition and reconstruction algorithms enabled numerous developments in MRI [4, 5]. This includes the development of cine MRI which uses the signal from an electrocardiogram (ECG) to synchronise data acquisition with the cardiac cycle, this synchronisation technique is referred to as gating. Gating substantially reduced artefacts caused by cardiac motion and has allowed MRI to become a key imaging modality in cardiac applications. However, this technique is not suitable for recording dynamic processes which are not repetitive (for example speech). This limitation motivated the development of MRI methods capable of recording motion at sufficient spatial and temporal resolutions without the need for additional synchronisation/timing equipment [4]. These methods are referred to as real-time MRI (rtMRI). This thesis is focused on a particular rtMRI method which was first introduced in 2010 by Uecker et al. [6, 4, 5] which combines highly undersampled acquisition strategies with iterative reconstruction algorithms. They used their method to achieve high temporal resolutions (20-250ms) with a spatial resolution of up to 1.4mm^2 [6]. This technique has provided unique insights into complex movement such as speech[7], cardiac motion [8] and joint movement [9].

The majority of current real-time MRI approaches (including the one presented by Uecker et al. (2010)) have the disadvantage that they can only record a single plane (known as a slice) during data acquisition (Fig.1.1 left)

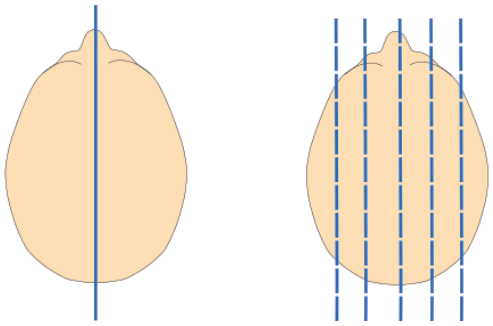

Figure 1.1: Illustration of single slice acquisition (left) and multi-slice acquisition (right) in the sagittal plane. For example, if the data sampling takes 100ms and data is acquired every 500ms the 400ms gap can be used to record an additional 4 slices.

[10]. This is due to there only being a small gap between acquiring data samples; in standard MRI it is common to use this gap to acquire data from a separate slice (Fig.1.1 right) [1]). Thus, recording multiple areas (while retaining temporal resolution) requires the acquisition to be repeated but at a different area. This introduces challenges when imaging the movement of structures which are not close together. The scans have to be repeated several times, requiring the subject to repeat the movement. It is impossible for the required movement to be repeated identically. This may be particularly problematic when observing processes where the structures operate synchronously. For example, the movement of both temporomandibular joints (TMJ) during speech and eating [10]. Additionally, the recording of multiple slices simultaneously is of interest when structural asymmetries, which may affect function in specific regions, are present.

This thesis develops novel rtMRI data acquisition methodologies capable of recording multiple slices simultaneously (this is referred to as simultaneous multi-slice (SMS) [11]). It further develops a reconstruction pipeline to pro-

cess SMS rtMRI data. To understand how these methods can be developed one must first appreciate the underlying physical principles of MRI.

1.2 Thesis Objectives

This thesis has three principle objectives:

- The development of real-time MRI imaging methodologies capable of recording movement at a temporal resolution of up to 37.5ms and spatial resolution of $2mm^2$ in multiple (1-7) locations simultaneously. These values have been selected as they have been shown to be suitable (in terms of spatial and temporal resolution) for the majority of speech imaging applications [7].
- The development of an image reconstruction pipeline capable of reconstructing both single slice and simultaneous multislice real-time MRI data, with improved image reconstruction quality compared to standard reconstruction approaches.
- The exploration of fast imaging sequences in a variety of clinical and sports science applications.

1.3 Background[1]

1.3.1 Introduction to MR Physics

The physical principle of MRI is based on the interaction of nuclei (usually ^1H, which is a single proton) with magnetic fields. These principles can be

[1] [12, 3, 13] are used as general references for this section.

approached from a semi-classical perspective, in which quantum mechanics is used to describe the behaviour of individual nuclei, whereas an ensemble average describes the behaviour of the macroscopic sample. In the following sections only protons (spin-1/2) will be discussed.

Protons have intrinsic angular momentum called spin. The value of the spin is denoted by the quantum number, m and for ^{1}H has the value $m = 1/2$. According to quantum mechanics, a spin-1/2 nuclei can only have two spin states, these are referred to as the spin-up ($m = +1/2$) and spin-down states ($m = -1/2$). The sign of m indicates the direction of the project of the angular momentum along the z-axis. When no magnetic field is present the two states are degenerate. The application of a magnetic field causes the two spin states to become separated by an energy gap, ΔE. This is known as Zeeman splitting (Fig.1.2). The energy gap is the energy required to transition between states, either by the absorption (to move from lower to higher energy state) or emission (to drop from the higher to lower energy state) of a photon with a specific frequency v (in Hz). The value of ΔE is determined by the Planck-Einstein relationship and is defined as the product of the photon frequency and the Planck constant, h, which has the value 6.626×10^{-34}J/Hz (eq.(1.1)).

$$\Delta E = vh \tag{1.1}$$

The photon energy can be related to the applied magnetic field strength (measured in units of Tesla), B_0, through eq.(1.2), where γ is a nuclei specific constant called the gyromagnetic ratio. For ^{1}H this has the value $42.58 \times 10^6 \mathrm{s}^{-1}\cdot\mathrm{T}^{-1}$. For nuclei with positive γ the lower energy level is the spin-up

state, and the higher energy level is the spin-down state.

$$\Delta E = \gamma h B_0 \tag{1.2}$$

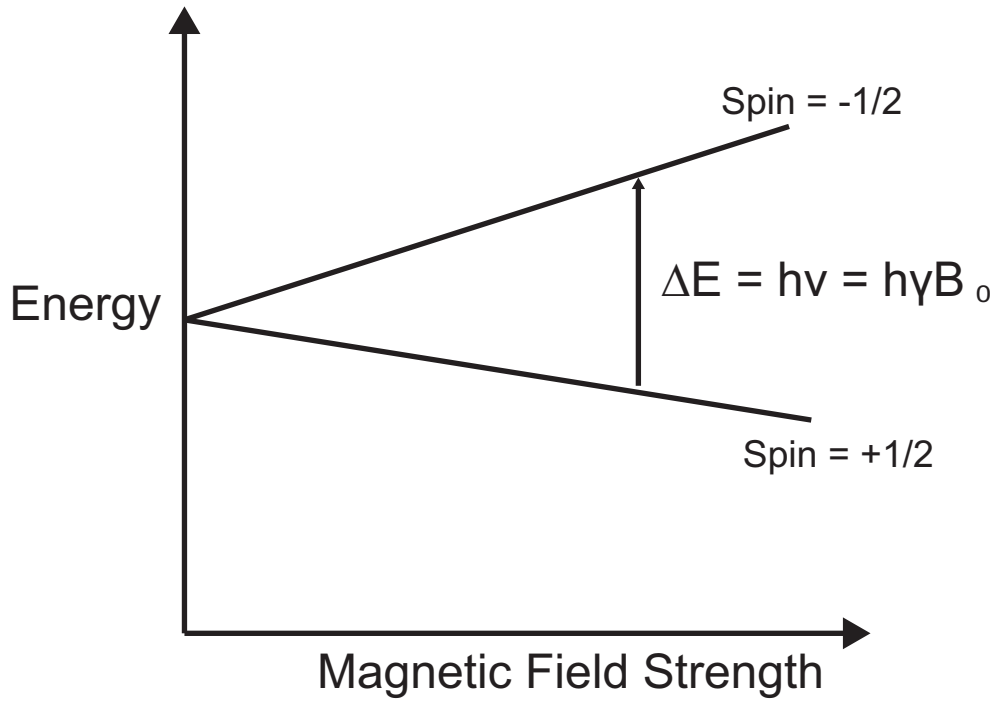

Figure 1.2: Diagram of Zeeman splitting. The increase in magnetic field strength results in an increased energy gap, ΔE, between the two spin states

The angular momentum of a nucleon is a vectorial property and its direction is referred to as the spin polarization axis (Fig.1.3). This vector can point in any direction in space. The angular momentum combined with the intrinsic electric charge of a proton results in a nuclear magnetic moment, μ. The value of μ is related to a quantum mechanical operator $\mathbf{S}$ through eq.(1.3). When no field is applied and $\gamma > 0$ the magnetic moment is parallel with the spin polarization axis. If we consider an ensemble of nuclei in a sample, without an external magnetic field applied, the distribution of

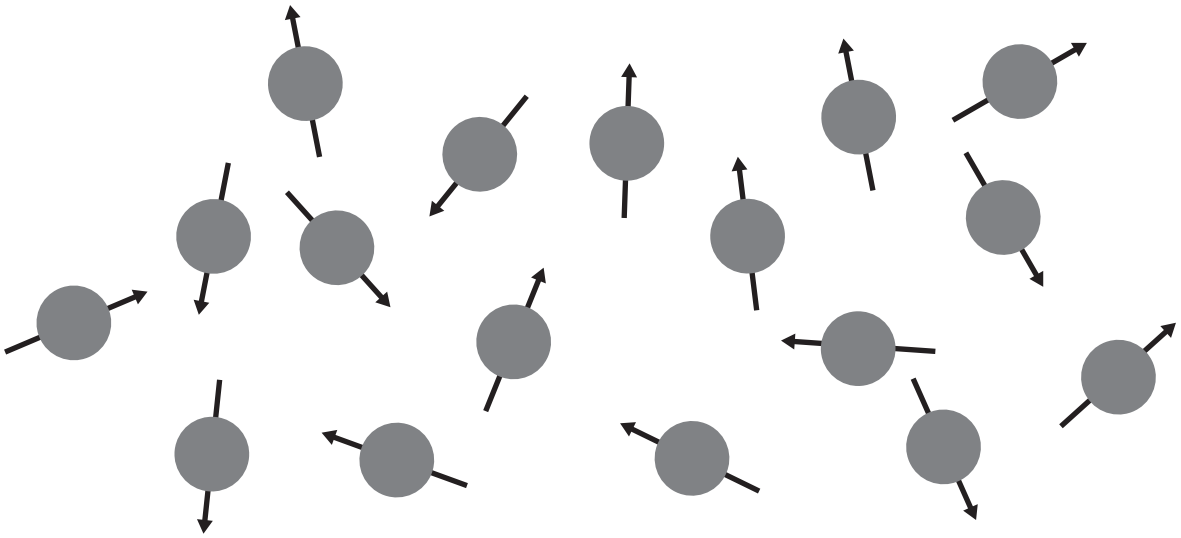

Figure 1.3: Diagram showing the spin polarization axis of a collection of nuclei. When no magnetic field is applied these axes point randomly in space.

magnetic moments will be near isotropic. Therefore, the net magnetization vector, $\mathbf{M}$, will be 0.

$$\mu = \gamma \cdot \mathbf{S} \tag{1.3}$$

The application of an external magnetic field will exert a torque on the nuclear magnetic moments. This torque results in the spin polarization axis rotating around the applied magnetic field at a constant angle between the nuclear magnetic moment and the applied field. This circular motion around the applied field is known as precession (Fig.1.4). In classical mechanics an analogy to this behaviour is a tilted gyroscope spinning on its own axis but also precessing around the gravitational axis. The frequency of the precession is given by eq.(1.4), where ω is the Larmor frequency and B_0 is the applied magnetic field. The negative sign indicates the direction of rotation around the axis. The magnitude value of the precession frequency is identical to the photon frequency energy gap (i.e. $|\omega| = v$) between the spin-up and

spin-down states.

$$\omega = -\gamma B_0 \tag{1.4}$$

The spin-up state has a magnetic moment which aligns with the spin polarization axis while the spin-down state has an anti-parallel alignment. The number of nuclei in the two energy levels is given by the Boltzmann distribution (eq.(1.5)), where N_0 is the number of spins in the lower energy level, N_1 is the number of spins in the higher energy level, k is the Boltzmann constant (1.38×10^{-23} J·k^{-1}) and T is the temperature in Kelvin. The excess of spins in the low energy spin-up state is small (approximately one in one million at a 1T field strength). This small excess of spins in the spin-up state results in a net magnetization vector which now aligns with the applied magnetic field (Fig.1.5), B_0. From this point forward we will take a classical physics perspective of how the magnetization vector can be manipulated.

$$\frac{N_1}{N_0} = e^{-\frac{\Delta E}{kT}} \tag{1.5}$$

The nuclei can be excited using a radio frequency (RF) pulse, applied using a current-carrying wire referred to as a coil. The current induces a magnetic field, this additional magnetic field is called the B_1 field. The RF pulse is applied perpendicular to the B_0 field with a frequency equal to the Larmor frequency. The application of the pulse results causes the spins in **M** to gain phase coherence and rotation of the **M** onto the transverse plane (relative to the direction of the main external magnetic field) by a given angle, θ. This angle is referred to as the flip angle of the pulse. The higher the desired flip angle, the longer the pulse must be left on for (or a high power

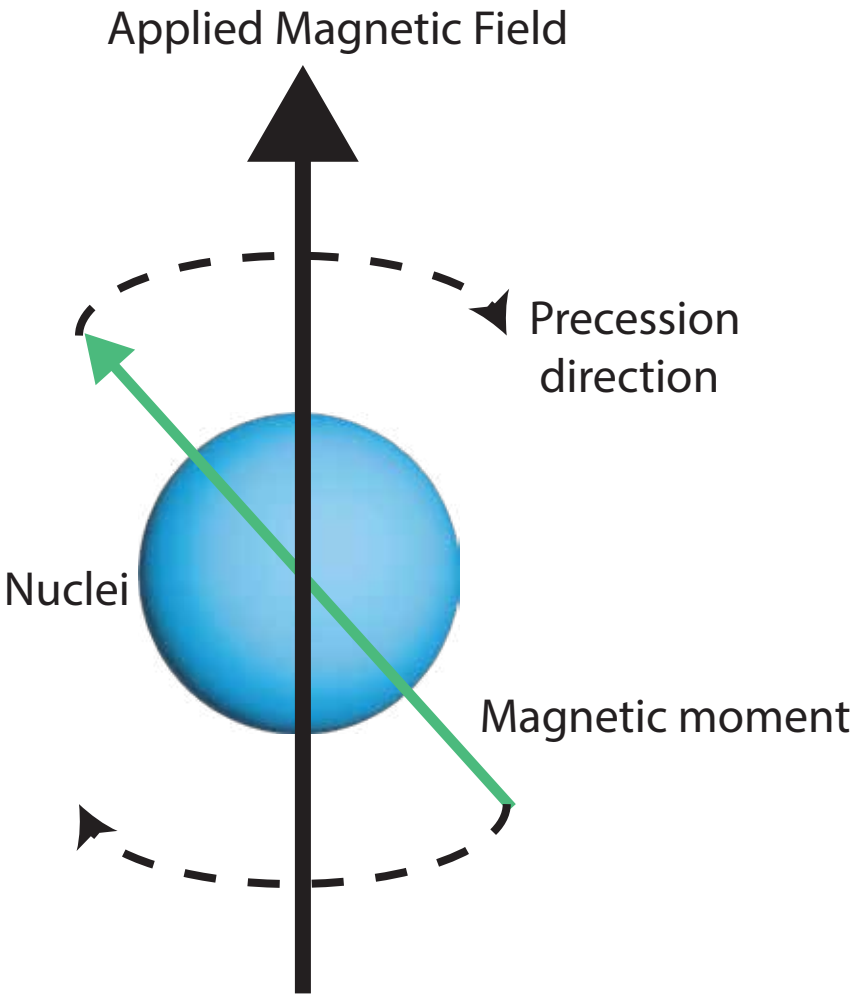

Figure 1.4: Diagram showing precession of the magnetic moment (green line) of a ^{1}H nuclei (blue) around an applied magnetic field (black line). The direction of precession is shown by the dashed lines.

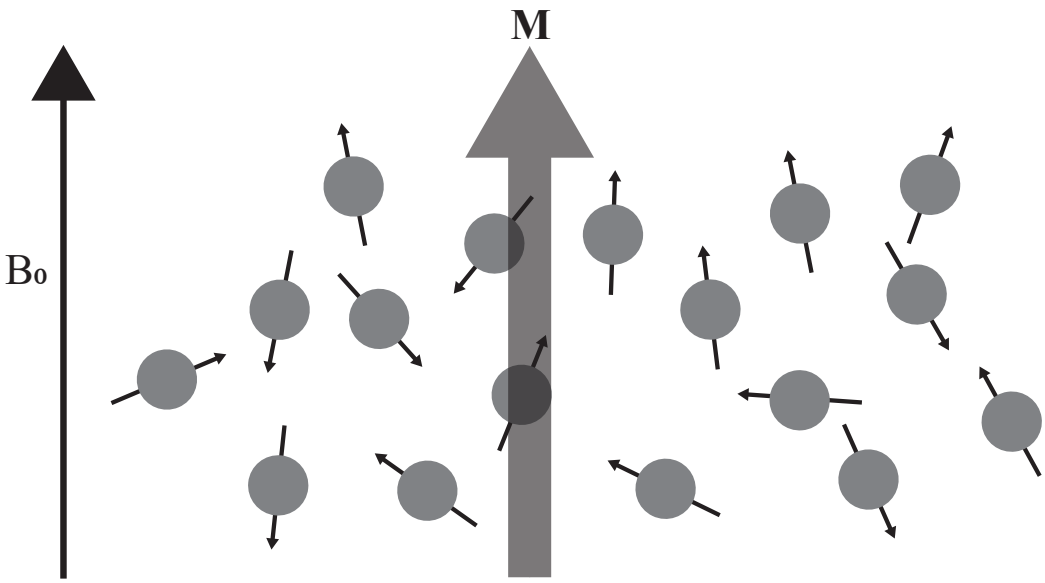

Figure 1.5: The application of an external magnetic field B_0 across a sample results in the net magnetization vector, $\mathbf{M}$, partially aligning in the direction of the field. This figure represents a snapshot of time, $\mathbf{M}$ will remain relatively constant but the individual nuclei may change there orientation due to interactions with their local environment.

must be used). After the application of the RF pulse, the magnetization vector will start to relax back to its initial alignment.

The relaxation process consists of two components which describe the evolution of the magnetization vectors in the longitudinal and transverse planes. Longitudinal relaxation (also known as spin-lattice relaxation) describes the recovery of longitudinal magnetization (i.e recovery of the magnetization in the direction of the B_0 field), this is described using eq.(1.6) which is an exponential recovery with the time constant T_1 and the equilibrium magnetization M_0. The longitudinal relaxation represents a loss of energy to the surrounding lattice as protons return from the high energy state to the low energy state. This results in the net magnetization returning to its thermal equilibrium. For biological tissues typical T_1 values (at a magnetic field

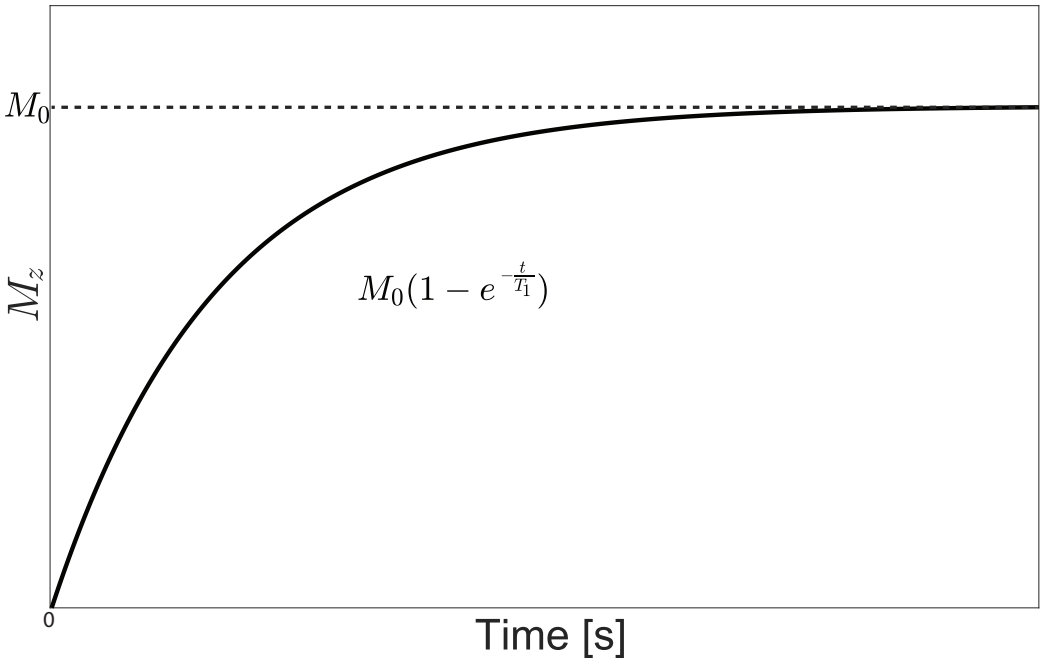

Figure 1.6: Plot of longitudinal relaxation. The longitudinal magnetization, M_z follows an exponential recovery to return to its initial value.

strength of 3T) range from $\approx$ 400ms (fat) to $\approx$ 4000ms (cerebrospinal fluid) [14].

$$M_z = M_0 \left(1 - e^{-\frac{t}{T_1}}\right) \tag{1.6}$$

The transverse relaxation (also known as spin-spin relaxation) describes the exponential decay of the magnetization, M_{xy}, on the transverse plane (perpendicular to the B_0 field). This is described mathematically as an exponential decay, from initial value M_{XY0}, with time constant T_2. This relaxation is due to the dephasing of excited nuclei as they interact (magnetically) with each other and the environment (inducing variable precession frequencies via eq.(1.4)). The loss of coherence results in the decay of the transverse component of the magnetization vector.

$$M_{xy} = M_{XY0} \cdot e^{-\frac{t}{T_2}} \tag{1.7}$$

In an ideal system the rate of the transverse magnetization decay is determined solely by the time constant T_2. In practice, the actual decay will be determined by the time constant T_2^*, this value is lower than T_2. The T_2^* value incorporates the spin-spin relaxation effects (T_2), but also includes system imperfections such as inhomogeneity in the B_0 field. The imperfections can be described using eq.(1.8) where $T_2^{'}$ is the additional contribution to the relaxation caused by magnetic field inhomogeneities. T_2 is on a shorter timescale than T_1. Examples of typical values in biological tissues (at 3T) are $\approx$ 40ms (muscle), $\approx$ 75ms (white matter) and $\approx$ 100ms (fat) [14].

$$\frac{1}{T_2^*} = \frac{1}{T_2} + \frac{1}{T_2^{'}} \tag{1.8}$$

The values of T_1 and T_2 differ between tissues due to the differences in molecular motion and interactions. The relaxation properties of tissues are used as a mechanism to generate image contrast in MRI. An MRI experiment can be designed to give images that emphasise either the differences in T_1 (T_1-weighted image) or T_2 (T_2-weighted image). Both T_1 and T_2 weighted images are also affected by the number of protons in the imaged volume; the number of protons is often referred to as the proton density.

1.3.2 Signal Detection

To record the decay of the transverse magnetization, M_{xy}, a coil is used. The signal reception coil can either be the same coil used for RF transmission or

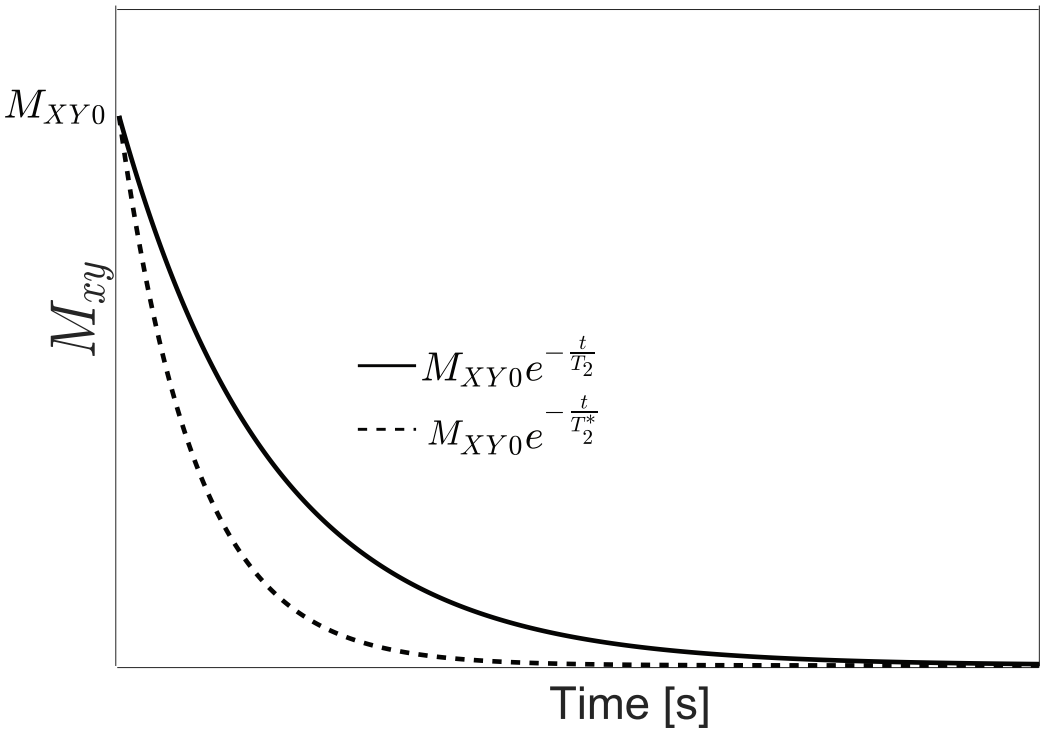

Figure 1.7: Plot of transverse relaxation. The transverse magnetization, M_{xy} follows an exponential decay. In an ideal system the time constant is T_2 (solid line) but in a real system the time constant will be T_2^* (dashed line).

can be an independent piece of hardware. The coil can be modelled as an LC circuit tuned at the Larmor frequency (Fig.1.8). The tuning capacitor, C_T, value is chosen such that the resonant frequency $\frac{1}{\sqrt{LC}}$ is equal to the Larmor frequency. The value of the matching capacitor, C_M, is set to adjust the impedance of the circuit to 50Ω to minimise signal reflection. In modern clinical systems the process of tuning the LC circuit is performed automatically using digitally controlled variable capacitors.

Due to Faraday's law of induction, the precessing magnetization will induce a time-oscillating current in the coil. This signal will be digitized using an Analogue-to-Digital converter (ADC) and will then be demodulated using a reference waveform supplied by the RF generation hardware. The demodu-

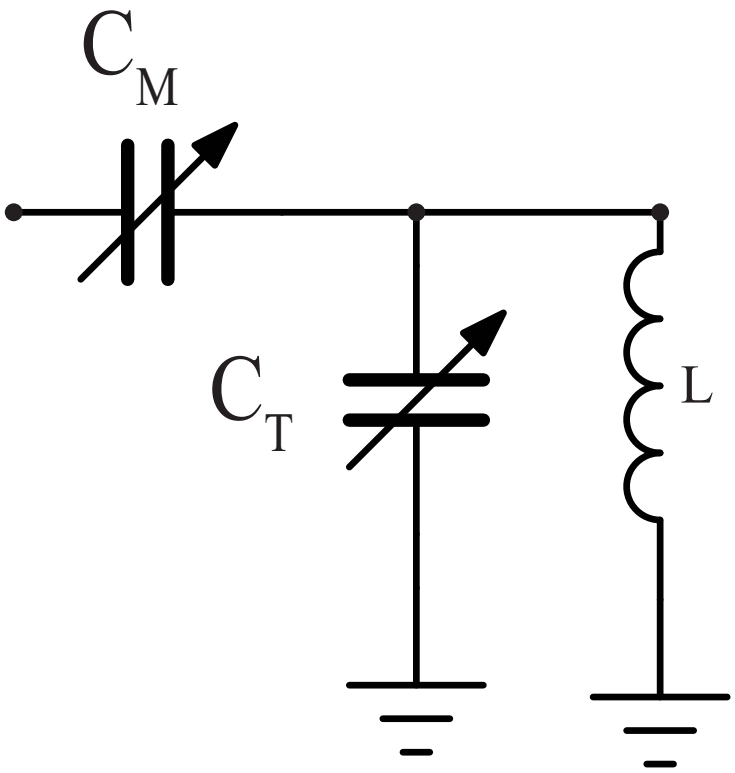

Figure 1.8: Circuit diagram of a simple reception coil consisting of a tuning capacitor C_T, matching capacitor C_M, and inductor L.

lation process results in two channels which represent the real and imaginary parts of the signal. The resulting time domain signal, $s(t)$, is known as a free induction decay (FID). It has the form of a dampened sinusoid (eq.(1.9)) oscillating at the Larmor frequency with a decay rate of T_2^* (Fig.1.9).

$$s(t) = \cos(\omega t) \cdot e^{-\frac{t}{T_2^*}} \tag{1.9}$$

1.3.3 Spatial Localisation and k-space

Recording the FID is not sufficient to generate an image, the resulting signal is a superposition of all ^{1}H nuclei excited by the RF pulse. To generate an

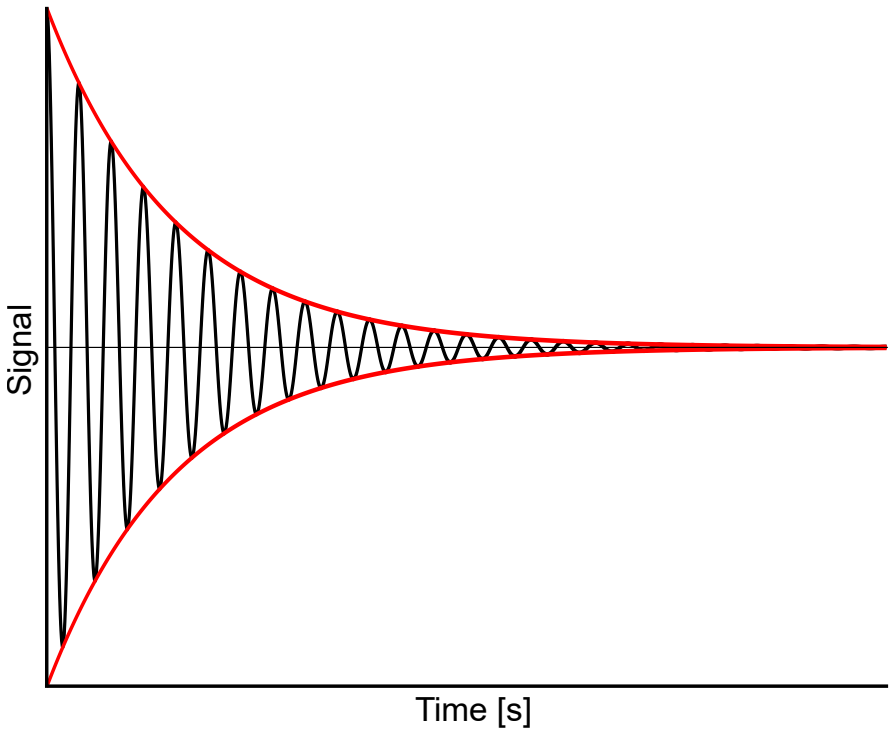

Figure 1.9: Plot showing the Free Induction Decay (FID) signal (black) over time. The red envelope represents the T_2^* decay over the same period.

image, additional spatial localisation is required. This is done using spatially varying magnetic field gradients (from now on just referred to as gradients). A gradient is defined as a spatial variation of the magnetic field (B_z). The amplitude of a gradient has the units mT/m. In MRI there are three magnetic field gradients, G_x,G_y and G_z, applied in the x, y and z directions respectively. Summing the three gradients yields the gradient vector G as shown in eq.(1.10), where $\hat{x}$, $\hat{y}$ and $\hat{z}$ are the Cartesian coordinate unit vectors. In this equation the magnetic fields in the x and y directions are assumed to be negligible and are therefore neglected.

$$G = \frac{\partial B_z}{\partial x}\hat{x} + \frac{\partial B_z}{\partial y}\hat{y} + \frac{\partial B_z}{\partial z}\hat{z} \equiv G_x\hat{x} + G_y\hat{y} + G_z\hat{z} \tag{1.10}$$

One of the gradients will be used for slice encoding (G_s), this is the slice selection gradient. The amplitude of the slice selection is varied linearly over space. This introduces a position dependent variation, $\Delta\omega$, around the Larmor frequency, ω. By applying an RF pulse at a specific carrier frequency, a specific region of the sample can be excited. The RF pulse, B_1, can be described as an amplitude modulated exponential function, eq.(1.11). The shape of the pulse is described by $A(t)$ and the exponential term, $e^{-j\Delta\omega t}$, provides the required frequency modulation to excite the desired location. The pulse shape is typically chosen to be a truncated sinc function. This is due to the Fourier transform of a sinc function being a square wave which provides uniform excitation across the slice [1].

$$B_1(t) = A(t) \cdot e^{-j\Delta\omega t} \tag{1.11}$$

The two other gradients are used following slice selection for in-plane localisation. These gradients are referred to as the phase encoding (G_p) and frequency/read encoding (G_f/G_r) gradients. The phase encoding gradient is used to generate a spatially dependent phase difference between magnetization vectors across the subject. This is done by briefly turning the gradient on (for a time T), which results in the spins precessing at different frequencies. The gradient is then turned off resulting in the spins returning to their original precession frequency, but there is now a spatially dependent phase difference between them. Mathematically, for the one-dimensional case of spins distributed over the y dimension, the phase at position y, $\phi(y)$, can be described using eq.(1.12).

$$\phi(y) = y \cdot \gamma \cdot \int_0^T G_p(t')dt' \tag{1.12}$$

The frequency encoding gradient, which is a linearly varying gradient, is applied during the readout of the signal. This results in the spins having different precession frequencies across the sample. Thus, by using these two gradients we can embed spatially dependent frequency and phase shifts into the signal we record. The resulting signal is referred to as k-space. In MRI, we typically vary the phase encoding gradient, in linearly increasing steps, to acquire parallel lines of k-space. This is referred to as Cartesian sampling as we obtain a set of equispaced k-space points. k-space can then be converted to the image domain using a Fourier transform (spatial frequency to distance). When Cartesian sampling is used, the Fourier transform can be computed extremely efficiently using a Fast Fourier transform algorithm [15].

Mathematically we can derive the Fourier relationship between k-space and image space by considering the spatial distribution of the transverse magnetization, $M(x, y)$, which is what we aim to recover. The signal, $s(t)$, (after demodulation and ignoring relaxation) will be the spatial integral of the transverse magnetization (eq.(1.13)). In this expression there is no way to recover the signal from each x and y position.

$$s = \int \int M(x, y)dxdy \tag{1.13}$$

The application of the two gradients (referred to as G_x and G_y) will cause a position dependent shift in the Larmor frequency. This can be incorporated into eq.(1.13) by introducing an additional exponential term where G_x and G_y are the spatially varying gradient values, this results in eq.(1.14).

$$s(t) = \int\int M(x,y) \cdot e^{-i \cdot \gamma [G_x x + G_y y] \cdot t} dxdy \tag{1.14}$$

We can now define the quantities k_x and k_y where, $\bar{\gamma} = \frac{\gamma}{2\pi}$.

$$k_x(t) = \bar{\gamma} \cdot G_x \cdot t$$
$$k_y(t) = \bar{\gamma} \cdot G_y \cdot t$$

This yields eq.(1.15). This equation shows that the signal is a spatial Fourier transform of the transverse magnetization.

$$s(t) = \int\int M(x,y) \cdot e^{-i \cdot 2\pi \cdot \gamma [k_x(t) x + k_y(t) y]} dxdy \tag{1.15}$$

In summary, when we record an MR signal, we are recording the spatial frequencies which make up the image. To convert to the image domain an inverse Fourier transform is used. For a more compact notation it is common to write eq.(1.15) as eq.(1.16) where $\mathbf{y}$ is the recorded k-space data, $\mathbf{y} \in \mathbb{C}^{N_s}$ is composed of N_s measurements, $\mathbf{x} \in \mathbb{C}^M$ is the image composed of $M = N_x \times N_y$ pixels and $\mathbf{F}$ is the 2D Fourier transform operator. This is known as the forward MRI model, which maps the image space to the recorded k-space. The MRI model can be extended to incorporate more complex effects such as multiple receiver coils (this is discussed in more detail in Chapter 3).

$$\mathbf{y} = \mathbf{F}\mathbf{x} \tag{1.16}$$

The left side of Fig.1.10 shows an example of a k-space and the resulting

image. The central area of k-space contains low frequency information, this provides information about the general shape and contrast of the image [16]. The center of Fig.1.10 shows the result of retaining only the central portion of k-space while discarding the high frequency information. The general shape and contrasts of the image can be seen but there is a lack of detail around the contours of the image. The outer portion of k-space encodes high frequency information, in the image domain this provides information about the edges and contours of the image (Fig.1.10 right).

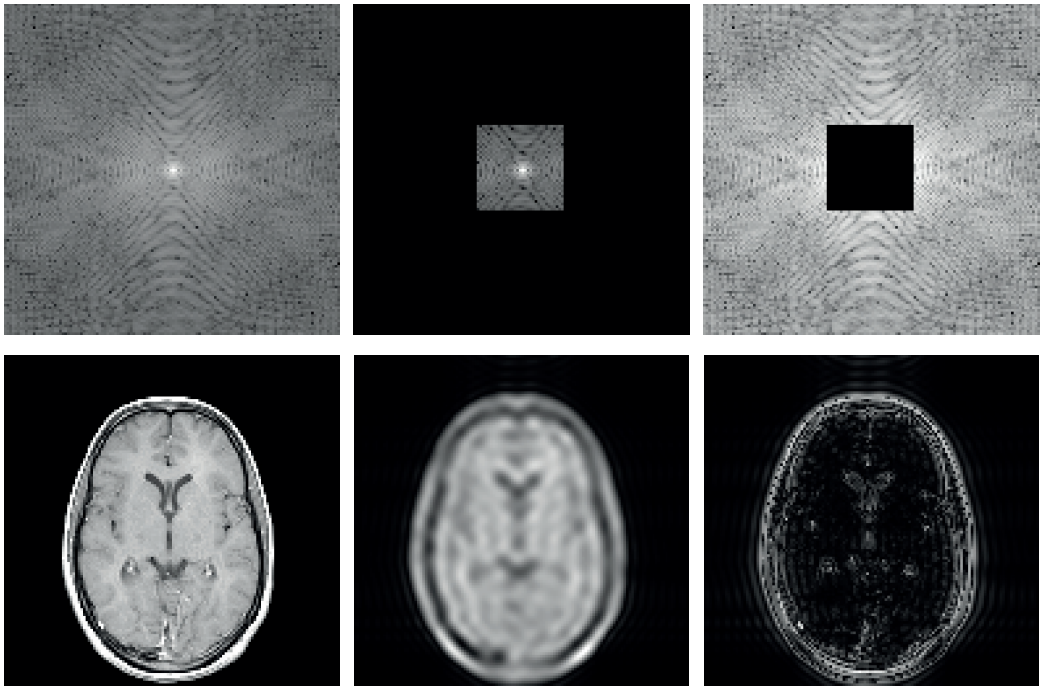

Figure 1.10: The effect of removing different regions of k-space. The full k-space and the resulting image are shown on the top and bottom left respectively. With only the inner section of k-space preserved (center top) the resulting image (center bottom) retains contrast but information about the edges is lost resulting in blurring. When only the outer portion of k-space is preserved (right top) the resulting image (bottom right) contains information about the edges of the image but all contrast has been lost.

The gap between k-space samples, Δk, determines the field-of-view (FOV)

of the image (i.e. the distance over which image is measured), this relationship is shown in eq.(1.17) [17]. In this equation, we assume that the FOV in the x and y direction is identical, this implies $\Delta k = \Delta k_x = \Delta k_y$. A rectangular FOV can be obtained by using separate Δk_x and Δk_y values. It can be shown the that the maximum k-space values, $k_{x,max}, k_{y,max}$, determine the image resolution, $\Delta x, \Delta y$, through eq.(1.18) and eq.(1.19).

$$\text{FOV} = \frac{1}{\Delta k} \tag{1.17}$$

$$\Delta x = \frac{1}{2k_{x,max}} \tag{1.18}$$

$$\Delta y = \frac{1}{2k_{y,max}} \tag{1.19}$$

In a standard MRI experiment the typical way of filling k-space is to acquire parallel lines of k-space. Thus, a large amount of the acquisition duration is spent acquiring high frequency k-space. More sophisticated acquisition schemes which exploit the structure of k-space to repeatedly acquire the low frequency information have been developed [4]. These allow for faster imaging and are described in more detail in Chapter 3.

1.3.4 MRI Methods

The combination of RF pulses and gradients (and the timings between them) is called a pulse sequence. A pulse sequence is commonly based on recording either a spin-echo (SE) or gradient recalled echo (GRE) [3]. In this thesis only GRE sequences are considered.

In a gradient echo sequence (Fig.1.11), an RF pulse (along with slice selection gradients) is applied, resulting in the rotation of the magnetization vector by flip angle θ. The resulting FID is then dephased (i.e. its decay accelerated) by turning on the read gradient, at the same time the phase encoding is applied. To form an echo, the read gradient (and the ADC is turned on) is reapplied with an inverted polarity. The rephasing of the spins creates an echo which is recorded by the ADC. This echo is referred to as a gradient recalled echo or more commonly a gradient echo. This process is repeated, with a linearly increasing phase encoding gradient, to acquire different lines of k-space.

In a GRE sequence, unlike a SE sequence, the flip angle of the pulse can be set to be a value less than 90°. The amount of magnetization that is tipped into the transverse plane is given by $M_0 \cdot \sin(\theta)$, where M_0 is the magnetization currently in the longitudinal plane. Using a high flip angle (such as a 90° pulse) results in more magnetization being transferred into the transverse plane, however, when the TR is short (relative to T_1), the magnetization will not have had sufficient time to move back to the longitudinal plane. Thus, there will be a smaller pool of longitudinal magnetization to rotate in subsequent excitations. Therefore, in short TR sequences it is beneficial to use a smaller flip angle in order to maintain a larger pool of magnetization which can be excited, and thus achieve a higher steady-state signal.

GRE sequences commonly employ spoiling, a technique which removes any undesired steady-state transverse magnetization [18, 2]. This ensures that the resulting image contrast will be T_1-weighted (unless TR and TE are made significantly longer to ensure T_2^*-weighting). The two most commonly

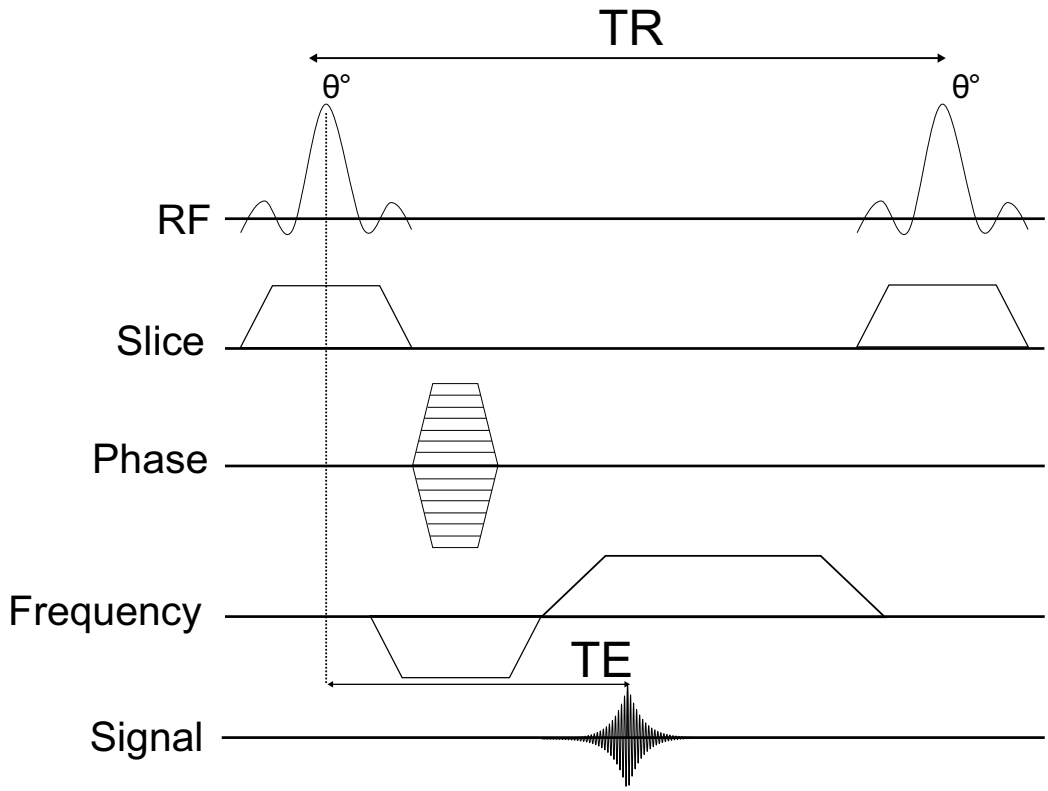

Figure 1.11: Pulse sequence diagram of a gradient-echo sequence.

used spoiling techniques (which can be used independently or combined) are RF-spoiling and gradient spoiling. In RF spoiling the phase of the RF pulse is altered every TR. It can be shown that this causes the transverse magnetization to be cancelled out. In gradient spoiling additional gradient pules (typically in the slice or read) direction are added after the frequency encoding gradient. This introduces additional dephasing of spins on the transverse plane. For a spoiled GRE sequence the recorded signal, s, can be related to TE, TR and θ through eq.(1.20) where [H] is the proton density. By lowering the TR (or increasing the flip angle) the recorded signal can be made more T_1-weighted. If the TR is kept high and the TE and flip angle kept low, the signal will mainly reflect the proton density of the tissues.

Thus, the contrast of a GRE sequence is dependent on three user controllable parameters: TE, TR and θ.

$$s = [\mathrm{H}] \cdot \frac{\sin(\theta) \cdot \left(1 - e^{-\frac{\mathrm{TR}}{T_1}}\right)}{1 - \cos(\theta) \cdot e^{-\frac{\mathrm{TR}}{T_1}}} \cdot e^{-\frac{TE}{T_2^*}} \tag{1.20}$$

The main advantage of using a GRE sequence is that the TR can be kept extremely short (in ms) compared to the hundreds of ms required for a SE sequence [19]. This allows for fast acquisition of k-space. This is important when imaging moving organs such as the heart or when the patient may not be able to tolerate extended periods of time in the MRI scanner. The main disadvantage of GRE sequences is that, unlike the SE sequence, the T_2^* effects are not eliminated.

1.4 Thesis Structure

Chapter 2: This chapter provides an overview of the MRI scanner system used in this thesis. This is followed by an overview of the software needed to implement pulse sequences and reconstruction algorithms.

Chapter 3: Provides an overview of techniques that are used to reduce the acquisition time in MRI. This begins with how spatial redundancy can be exploited, then more complex data sampling schemes are introduced. Finally, the concept of sparsity and compressed sensing is introduced.

Chapter 4: Based upon existing literature a real-time MRI sequence using radial sampling is developed. The sequence is extended to use SMS acceleration to acquire multiple slices with no loss of temporal resolution. A compressed sensing reconstruction pipeline is implemented for rtMRI data.

Chapter 5 Using the sequence developed in Chapter 4, in-vivo single-slice and multi-slice rtMRI data is acquired. The effect of undersampling, data compression and SMS acceleration on image quality and reconstruction time is evaluated.

Chapter 6: This chapter describes the design, construction and evaluation of a semi-realistic, dynamic phantom of the oral cavity for use in MRI scanners. Its application to dynamic imaging is discussed.

Chapter 7: Potential applications of the developed real-time MRI sequences are discussed. This includes applications in head/neck imaging and musculoskeletal imaging.

Chapter 8: This chapter summarises the main findings of the thesis. Future work extending the sequences and reconstruction algorithms is discussed.

2 Methods

2.1 Introduction

This chapter details the hardware and software used to acquire and reconstruct the MRI data used in this thesis. The MRI system is first introduced, followed by the software environment used to develop new pulse sequences. Finally, the reconstruction hardware and software is discussed.

2.2 Magnet and Gradient System

In this work all data was acquired on a clinical whole body 3T MAGNETOM Vida system (Siemens Healthineers, Germany) with a bore size of 70cm (Fig.2.1). A liquid helium cooled superconducting magnet provides the static B_0 field, at this field strength the Larmor frequency of ^{1}H is 127.74MHz. The gradient system equipped on this scanner is capable of gradient amplitudes of 45mT/m at a slew rate of 200T/m/s [20].

To improve magnetic field homogeneity, the system has additional sets of coils, known as shim coils [3]. The scanner system adjusts the current through these coils, thus adjusting the magnetic field generated by them. The summation of the shim fields with the B_0 results in a more homogeneous field.

The shim adjustment can either be done manually or through an automated process before the start of a scan. In this thesis the latter process is used.

Figure 2.1: Photograph of the 3T MAGNETOM Vida scanner.

2.3 RF Transmit and Receive System

The MRI system has a body coil around the magnet, this is used to transmit the RF pulse required to excite the spins. The resulting signal is recorded by an array of receiver coils located around the anatomy of interest.

The receiver array coils used in this thesis are: head/neck 64 coil receiver array, knee 18 coil receive/transmit array and a foot/ankle 10 coil array.

The knee coil has additional functionality to transmit RF in order to improve the homogeneity of spin excitation.

2.4 Data Acquisition and Processing

To acquire data, the scanner operator selects what sequence to run and the parameters of the sequence, which is referred to as the scan protocol. This is done at a computer located in the control room using a software application called syngo (Siemens Healthineers, Germany). This information is then passed to the measurement and reconstruction system (MARS). MARS is a Linux system that controls the application of the RF amplifiers, gradient amplifiers and turns on the ADCs to record data.

The signal recorded by the receive coils is digitised using an ADC and then sent through an optical link back to MARS. If an appropriate reconstruction algorithm is available the data is then reconstructed and images are sent back to the host computer. An overview of the system is shown in Fig.2.2.

Raw k-space data is referred to by Siemens as TWIX data and is stored separately to the image data. The raw data can be exported for reconstruction on a separate computer system.

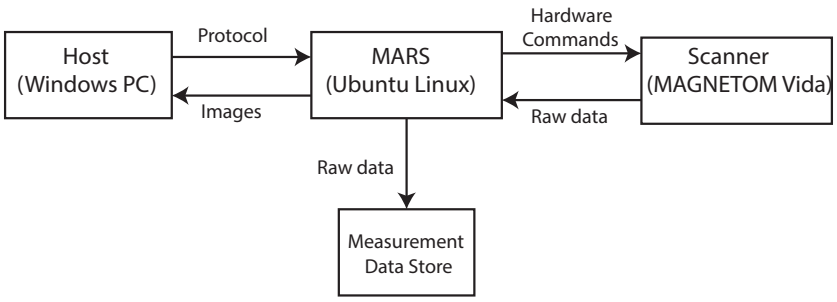

Figure 2.2: Block diagram showing the structure of the MRI system used in this thesis.

2.5 Sequence Development Software

Development of pulse sequences and reconstruction code is performed in the Integrated Development Environment for Applications (IDEA) (Version XA30; Siemens Healthineers, Germany). All pulse sequence and scanner reconstruction code is written using C++.

IDEA is divided into two sections:

- Sequence Development Environment (SDE): all pulse sequence development is done in the SDE section of IDEA. It is responsible for compiling the pulse sequence code to generate the dynamic linked libraries (DLL) and system object (SO) files needed to execute the sequence on the scanner. SDE also provides a basic simulation package to test sequences.

- Image Calculation Environment (ICE): image reconstruction code for the scanner is done in the ICE section of IDEA. ICE controls the compilation of the source code into DLL and SO files. Software to test reconstruction algorithms and open TWIX files is also provided.

The DLL and SO files generated by IDEA are then transferred onto the

scanner.

2.6 Computational Resources and Reconstruction Software

The k-space data is exported from the scanner and reconstructed on a separate computer. The computer used for reconstruction has the following specifications: AMD Ryzen 7700X, 64GB DDR5 RAM, NVidia 4070 GPU.

The majority of the reconstruction software used in this thesis is written in MATLAB (version 2023a, Mathwork) running on a CPU. The exception to this is the Non-Uniform Fast Fourier Transform algorithms. These are run on a Graphical Processing Unit (GPU) to reduce computation time. GPU code is implemented in the CUDA C programming language [21]. A MEX script is used to interface the CUDA C code to the main MATLAB scripts.

2.7 Standard Imaging Protocol

Due to the explorative nature of this project, a fixed imaging protocol is not used. However, a typical scanning session can be divided into two sections.

- The first section of the scan session consists of structural scans. This begins with a T_2-weighted localiser followed by a T_2-weighted high resolution (1mm^2) structural scan with the field of view and number of slices selected to cover the anatomy of interest.

- Real-time MRI scans (with parameters and slice position dependent on the application) are then performed. The static structural scans are

used to assist in determining optimum slice position/orientation.

2.8 Ethics

Ethical approval for all scanning was approved by Manchester Metropolitan University. All in-vivo scanning was conducted on healthy volunteers who signed a consent form and a general safety questionnaire.

All data was pseudo-anonymised and stored securely on an encrypted file store.

3 Background Theory of Accelerated MRI

3.1 Introduction

MRI provides a diverse array of clinical information through its ability to generate multiple types of contrasts [1]. A limitation of MRI is the long acquisition time required to fully sample k-space [22]. For standard Cartesian sampling the total acquisition time, TA, to acquire a single image (in milliseconds) is determined by the number of acquired k-space phase lines, N, and the repetition time, TR (in milliseconds).

$$\mathrm{TA} = N \cdot \mathrm{TR} \tag{3.1}$$

For example, a standard T_1-weighted GRE sequence with TR= 2.5ms and 128 lines of k-space would take 320ms to acquire. When imaging movement, such as cardiac motion or joint motion, the movement over the acquisition duration will result in motion artefacts [22]. It is also problematic when high-resolution data sets covering a large FOV are required as many k-space samples are needed. For example, to achieve a 1mm resolution (in the phase encoding direction) over a FOV of 300mm would require 300 lines of k-space. A long acquisition time is problematic as patients can struggle to remain still during the scan [23, 24].

Hardware improvements in MRI, such as fast-switching gradients, have allowed for faster data acquisition [25]. For example, early MRI systems had gradient slew rates of $\approx 10\text{T/m/s}$ compared to the 200T/m/s slew rate of the system used in this thesis [26]. Alongside these developments, over the past 30 years a wide variety of data sampling and reconstruction techniques have been developed to significantly (between 2-20 time reduction in scan time) accelerate MR imaging by acquiring fewer lines of k-space [27, 28, 23]. This chapter introduces the most significant developments in accelerated image acquisition and discusses how they can be combined to further reduce image acquisition time, preferably with minimal degradation in image quality.

3.2 Multi-coil Imaging

As discussed in Section 1.3.2, the MR signal is recorded using a coil placed near the subject. Modern clinical systems (including the system used in this work, Chapter 2) now use multiple small receiver coils located in different positions to record the MR signal (Fig.3.1) [29]. These small receiver coils record signal from a highly localised area. This provides an increase in signal-to-noise ratio (SNR) (in the area near the coil) compared to a single large coil. The N_c coils each record a k-space signal, $\mathbf{y}_l \in \mathbb{C}^{N_s}$ where $l = [1, \ldots, N_c]$, consisting of N_s samples. The k-space from each coil can be Fourier transformed yielding a set of images, $\mathbf{x}_l$. These images can then be combined to form a single image, $\mathbf{x}$. To combine the coil images, a root sum-of-squares approach is typically used (eq.(3.2)). Larsonn et al. (2003) proved that this combination method provides the optimal SNR when the only information available for reconstruction is the k-space data from each

coil [30].

$$\mathbf{x} = \sqrt{\sum_{l=1}^{N_c} \mathbf{x}_l^2} \tag{3.2}$$

3.3 Parallel Imaging

Initially, multiple reception coils were used solely to improve the SNR of images [31]. It can be shown that, theoretically, the SNR of the reconstructed image increases proportionally to the square-root of the number of coils [30]. In practice, when high numbers of small reception coils are used, the resulting SNR will vary spatially [32].

The signal recorded by each coil is not identical, it varies depending on the spatial position of the coil [33]. The signal recorded from tissues close to the coil is larger than tissues further away because each small coil acts as a surface coil. This embeds additional spatial information (along with spatial information embedded through gradient encoding) into the recorded signal [34]. This relationship between position and signal intensity is known as the coil sensitivity profile (Fig.3.1).

The effects of multiple coils and their respective sensitivity profiles can be incorporated into the MR signal model. The recorded signal can be linked to the image through eq.3.3. The additional term $\mathbf{S}_l$ has been introduced into the signal model. This term is a diagonal matrix with a size equal to the number of pixels in the image, which models the interaction between coil l's sensitivity profile and the image. This can be rewritten as eq.(3.4), where $\mathbf{A}_l = \mathbf{F}\mathbf{S}_l$ is referred to as the system matrix.

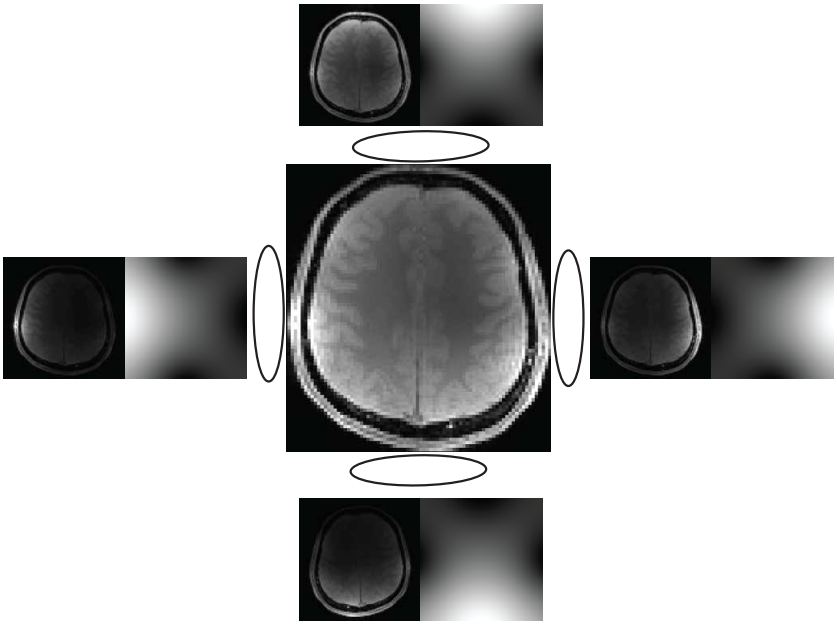

Figure 3.1: Illustration of multi-coil acquisition. Four coils located in different positions are used for signal reception. Each coil has a specific spatial sensitivity pattern. The data from each coil can be Fourier transformed to form an image. These can be combined using the root sum-of-squares (eq.3.2).

$$\mathbf{y}_l = \mathbf{F}\mathbf{S}_l\mathbf{x} \tag{3.3}$$

$$\mathbf{y}_l = \mathbf{A}_l\mathbf{x} \tag{3.4}$$

The set of measurements from each coil can be stacked to form a vector of size $N_s \cdot N_c$. The signal is now related to the image through eq.(3.5) where $\mathbf{A} = [\mathbf{A}_1, \ldots, \mathbf{A}_{Nc}]$ is a stacked matrix of forward operators for each coil.

$$\mathbf{y} = \mathbf{A}\mathbf{x} \tag{3.5}$$

The additional spatial information introduced by the coil sensitivity can be used to decrease the acquisition time. In effect, the SNR gain of using multiple receiver coils is sacrificed to reduce acquisition time. The methods to do this are collectively referred to as Parallel Imaging (PI) [35]. In PI, the scan time is reduced by lowering the number of k-space lines acquired during a scan. The process of reducing the scan time is commonly referred to as acceleration. The amount of acceleration is referred to as the acceleration factor, R, and is defined as the ratio of the number of k-space lines required to fully sample the image, N_{Full}, to the number of acquired k-space lines, N_{Acq} (eq.(3.6)) [36]. For example, skipping every other line in k-space would result in $R = 2$. If k-space lines are skipped, there are no longer enough spatial frequencies to reconstruct the image. In the image domain, this lack of information manifests itself as foldover/aliasing artefacts (Fig.3.2) [37]. The aim of all parallel imaging methods is to recover an undistorted image from the undersampled k-space measurements.

$$R = \frac{N_{Full}}{N_{Acq}} \tag{3.6}$$

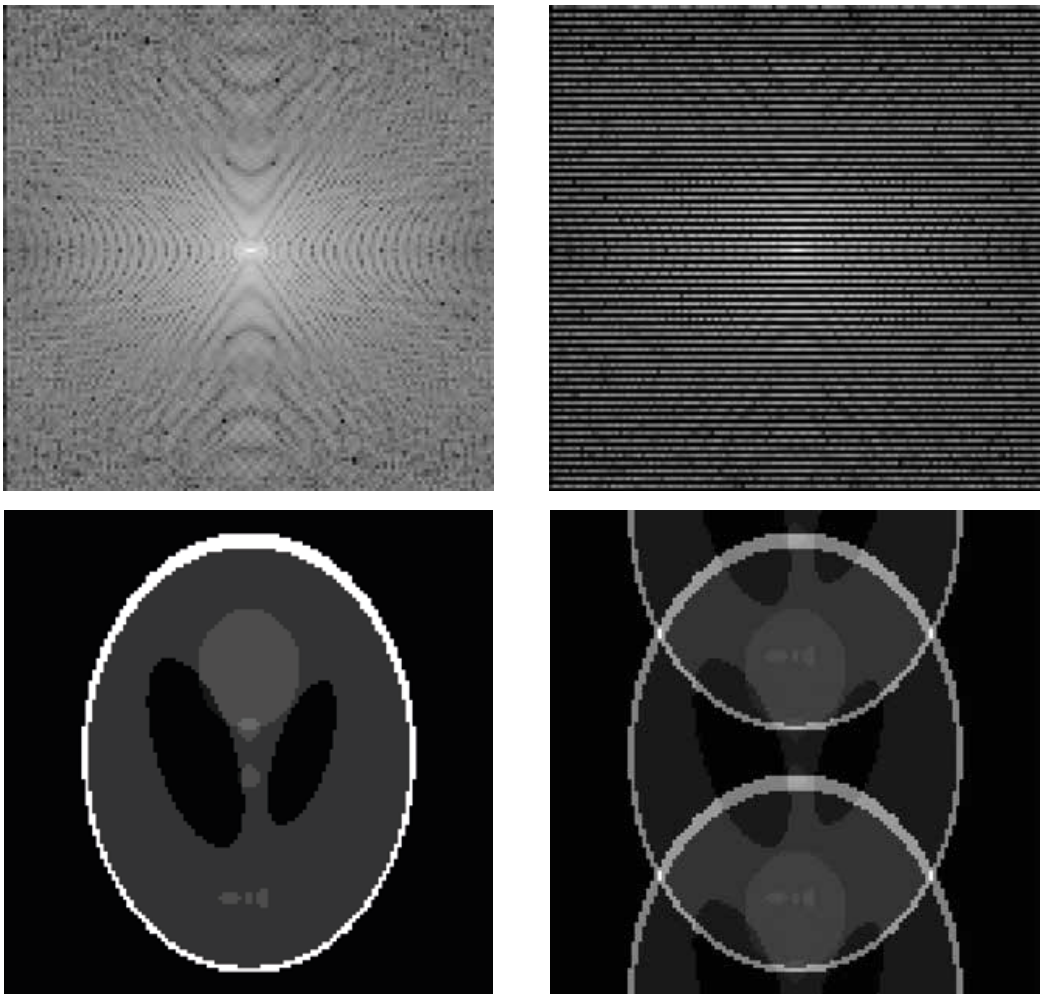

Figure 3.2: Left: fully sampled k-space (top) and the resulting image (bottom). Right: the same k-space with every other line removed (top) and the resulting reconstructed image which shows aliasing (bottom).

The earliest example of Parallel Imaging is Simultaneous Acquisition of Spatial Harmonics (SMASH) [38, 39]. The main principle of SMASH is that linear combinations of weighted coil sensitivities can be combined to synthesise the missing k-space lines. The required weights are found by

fitting the coil sensitivity profiles to spatial harmonics. SMASH requires extremely careful coil design in order to generate the spatial harmonics in the selected phase encoding direction with the high accuracy needed. This poses a limitation in clinical applicability as SMASH does not work effectively with all available coils [40].

One of the most commonly used parallel imaging methods is SENSE (SENSitvity Encoding) developed by Pruessmann et al. in 1997 [37, 41, 42]. Unlike SMASH, the SENSE method works with any coil array [40]. SENSE alters the system matrix to account for the data undersampling by introducing a diagonal matrix, $\mathbf{P} \in \mathcal{R}^{N_s \times N_s}$ (eq.(3.7)). The values along the diagonal can take the value of 1 or 0. The sampling operator, $\mathbf{P}$, can be viewed as a binary mask which selects if a k-space point has been sampled or skipped.

$$\mathbf{A}_l = \mathbf{P} \cdot \mathbf{F} \cdot \mathbf{S}_l \tag{3.7}$$

SENSE aims to find a solution to eq.(3.5). A common technique to do this is to pose the image reconstruction problem as a least-squares minimization problem (eq.(3.8)) [43, 41]. This optimization problem attempts to find an image, $\mathbf{x}$, which when transformed into k-space matches the data, $\mathbf{y}$, measured from each receiver coil. The final solution is given by $\hat{\mathbf{x}}$. Using the L_2 norm provides a measure of goodness of fit. The lower the norm, the more the generated image fits the measured data. This is referred to as the data fidelity term. It is common to add Tikhonov regularization ($\lambda \|\mathbf{x}\|_2^2$ term) [44]. Regularization assists in the finding of a unique solution and helps to prevent overfitting [45]. The level of regularization is controlled by λ and determining this parameter is critical to effectiveness of regularization.

The L_2 norm of an image is not expected to be small (as many pixels are a non-zero value) and forcing it be small (using an inappropriate λ value) can result in the reconstructed image being too smooth [46].

$$\hat{\mathbf{x}} = \arg\min_{x} \left[\frac{1}{2} \|\mathbf{A}\mathbf{x} - \mathbf{y}\|_2^2 + \lambda \|\mathbf{x}\|_2^2 \right] \tag{3.8}$$

This optimization problem has a closed form solution given in eq.(3.9), where $\mathbf{I}$ denotes the identity matrix. Directly implementing the matrix inversion would require an infeasible amount of memory for the computation [41]. Instead, the solution to this is found using an iterative algorithm, the most commonly used is the Conjugate Gradient (CG) algorithm [43, 41, 47].

$$\hat{\mathbf{x}} = (\mathbf{A}\mathbf{A}^{\mathbf{H}} + \lambda \mathbf{I})^{-1} \mathbf{A}^{\mathbf{H}} \mathbf{y} \tag{3.9}$$

A full derivation of the CG algorithm can be found in Shewchucks 1994 review [48]. The algorithm (Algo.1) requires the implementation of both $\mathbf{A}$ and its Hermitian, $\mathbf{A}^{\mathbf{H}}$. The Hermitian of the system matrix is given by eq.(3.10), and represents the transformation from the k-space domain to the image domain. The Hermitian of the Fourier transform term represents the inverse FT and $(.)^*$ denotes the complex conjugate.

The algorithm is run for N_{Iter} iterations or (optionally) until a convergence criterion is met. This criterion is typically based upon the ratio of the residual vector $\mathbf{r_i}$ at iteration i to the initial residual vector $\mathbf{r_0}$. If the ratio is below a certain threshold ε the algorithm is terminated. It is difficult to pick this termination threshold, thus most implementations of CG-SENSE are run for a set number of iterations [43].

$$\mathbf{A^H}_l = \mathbf{S}_l^* \cdot \mathbf{F^H} \cdot \mathbf{P} \tag{3.10}$$

Algorithm 1: Conjugate Gradient Algorithm

Input: System matrix $\mathbf{A}$, Convergence threshold ε, Number of iterations N_{Iter}

Output: Data at final iteration $\mathbf{x}$

Data: Recorded k-space data $\mathbf{y}$

$\mathbf{x_0} = 0$, $i = 0$, $\mathbf{b} = \mathbf{A^H y}$, $\mathbf{r_0} = \mathbf{p_0} = \mathbf{b} - \mathbf{A^H A v_0}$

while $i < N_{Iter}$ **do**

  $\sigma = \frac{\mathbf{r_i^H r_i}}{\mathbf{r_0^H r_0}}$

  if $\sigma \leq \varepsilon$ **then**

    Return $\mathbf{x_i}$

  $\alpha_i = \frac{\mathbf{r_i^H r_i}}{\mathbf{p_i^H A^H A p_i}}$

  $\mathbf{x_{i+1}} = \mathbf{x_i} + \alpha_i \mathbf{p_i}$

  $\mathbf{r_{i+1}} = \mathbf{r_i} - \alpha_i \mathbf{A^H A p_i}$

  $\beta_i = \frac{\mathbf{r_{i+1}^H r_{i+1}}}{\mathbf{r_i^H r_i}}$

  $\mathbf{p_{i+1}} = \mathbf{r_i} - \beta_i \mathbf{p_i}$

  $i = i + 1$

Accurate reconstruction using the SENSE method requires the coil sensitivity profiles [37]. This can be achieved using short scans before the main acquisition, these are known as prescans [49]. Prescans acquire low-resolution images from each coil by recording the central lines of k-space. Any movement between the prescan and the main acquisition will result in the misalignment between the coil sensitivity profiles and the actual image, significantly degrading the SENSE reconstruction [49]. To resolve this, it is now common to acquire a central region of k-space during the acquisition, which can then

be used to generate low-resolution images [34]. The disadvantage of this is that the overall acceleration is lower than the prescan approach as more lines of k-space are required. This method is referred to as autocalibrated reconstruction as the coil sensitivity is estimated for the data itself [34]. A variety of algorithms have been developed which use these low-resolution images to estimate the sensitivity of each coil [28, 34]. Coil geometry is another important aspect of parallel imaging [31]. There should be as little overlap as possible between the coil sensitivity profiles for each coil to record a unique signal. In practice, there will always be overlap in the coil sensitivity profiles.

Theoretically, the maximum achievable acceleration using PI is $R_{Max} = N_c$. This assumes that there is no noise present in the recorded data, the coil sensitivity profiles are known exactly for each coil and the coil sensitivity profiles are completely independent [50]. In reality, this is impossible to achieve, and the image quality of SENSE degrades significantly as the acceleration factor increases (Fig.3.3), resulting in severe artefacts and reduction in the signal-to-noise ratio [31, 40]. In clinical settings the maximum acceleration factor used (for 2D imaging) rarely exceeds $R = 3$ [51].

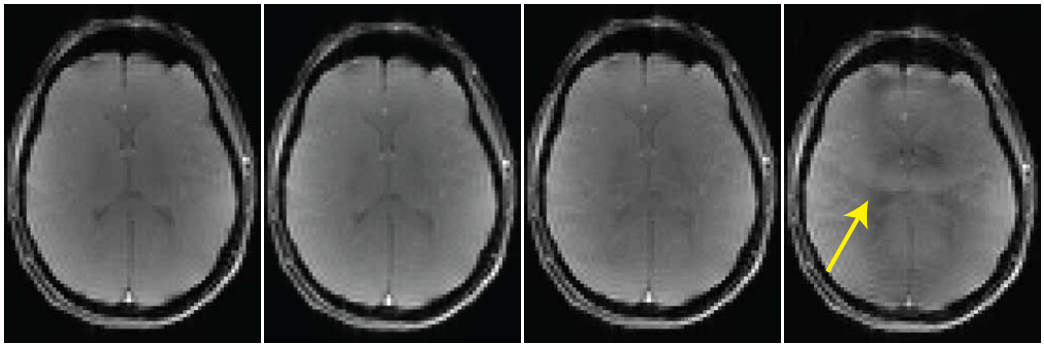

Figure 3.3: Four images of a brain acquired using a GRE sequence, the fully sampled k-space is composed of 128 lines. From left to right: no SENSE acceleration, $R = 2$ SENSE acceleration, $R = 3$ SENSE acceleration and $R = 4$ SENSE acceleration. At the higher levels of acceleration foldover artefacts can be seen, as indicated by the yellow arrow.

3.4 Non-Cartesian MRI

Another method to accelerate acquisition is to use non-Cartesian sampling schemes (also known as non-Cartesian trajectories). In non-Cartesian sampling, the low-frequency areas of k-space are typically acquired more frequently than in standard Cartesian sampling. The effect of this is to allow a large amount of data undersampling to be performed, while maintaining sufficient image quality. This is due to the structure of k-space (described in Section 1.3.3) in which the low-frequency area contains the majority of the important structural/contrast information and the high-frequency area contains the information about the edge in the images.

One of the most common non-Cartesian sampling schemes is Echo-planar Imaging (EPI) (Fig.3.4) introduced by Mansfield in 1977 [52]. EPI acquires multiple lines of k-space from a single excitation in contrast to Cartesian sampling which acquires a single line of k-space per TR [1]. This is done by repeatedly applying the frequency encoding gradient with alternating polar-

ity. The phase encoding gradient is applied at small amplitudes in between the application of the frequency encoding gradient. This results in the k-space being acquired in a snake or 'zig-zag' pattern (Fig.3.4 bottom). During the reconstruction, alternate lines of k-space are flipped such that all lines of k-space align, next, a standard FFT is used to transform the k-space to the image domain.

Compared to standard Cartesian sampling, EPI is susceptible to a variety of artefacts [2]. The most common artefact is ghosting in the phase encoding direction (Fig.3.5). The main cause of ghosting are eddy currents [2]. These result in shifts between the lines of k-space. Ghosting can be corrected using a variety of methods. The most common method involves a prescan which acquires the central line of k-space at alternating gradient polarities. This can then be used to generate a phase correction term which removes the ghosting.

Another limitation of EPI is sensitivity to B_0 inhomogeneity, this is typically referred to as off-resonance. This results in signal dropout and distortions around the area of off-resonance. This is particularly problematic at air-tissue boundaries such as those in the nasal sinuses [53], this is due to differences in magnetic susceptibility. Reconstruction techniques have been developed to overcome this issue [54, 55, 56]. However, no correction method is perfect and they introduce additional complexity into the reconstruction. Off-resonance effects can also be reduced using spin-echo sequences, at the cost of increased tissue heating [57, 58].

EPI is used extensively in functional MRI [59] and diffusion MRI [60] with typical temporal resolutions of $1 - 2$s. EPI has also been used for

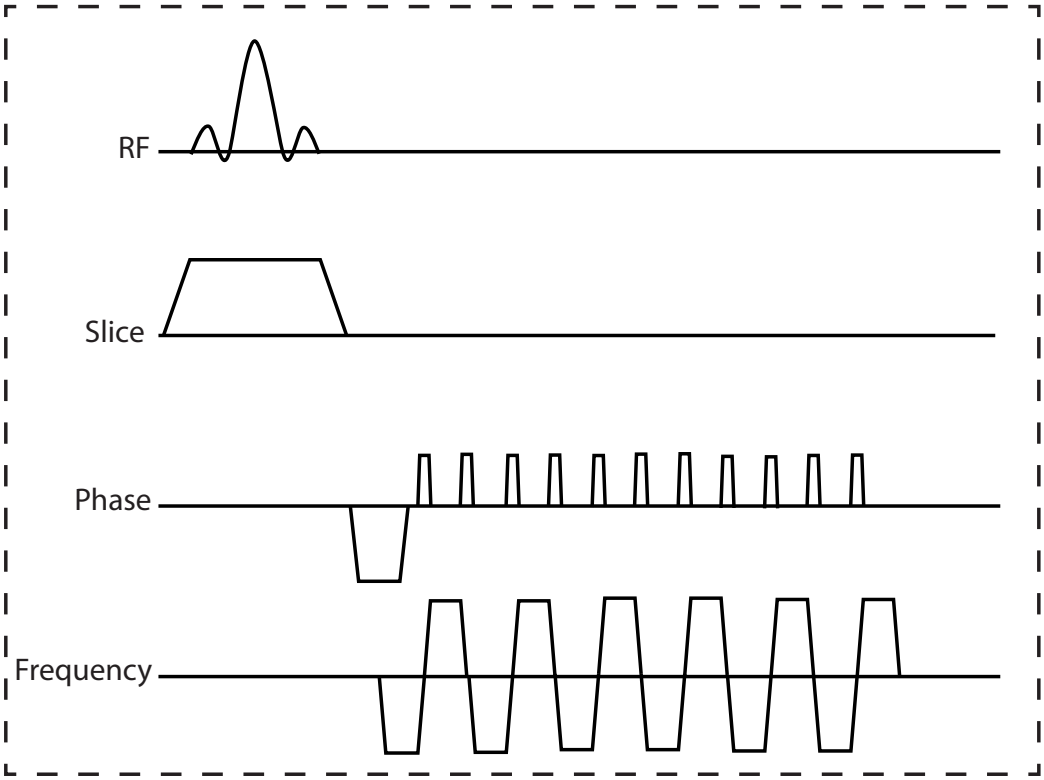

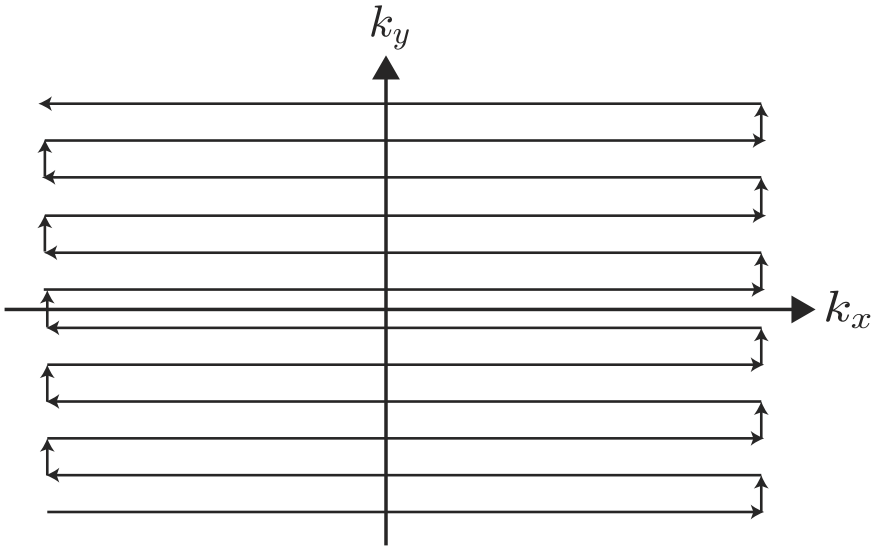

Figure 3.4: Top: GRE sequence with EPI sampling scheme. Bottom: The resulting EPI trajectory showing the snaking pattern through k-space.

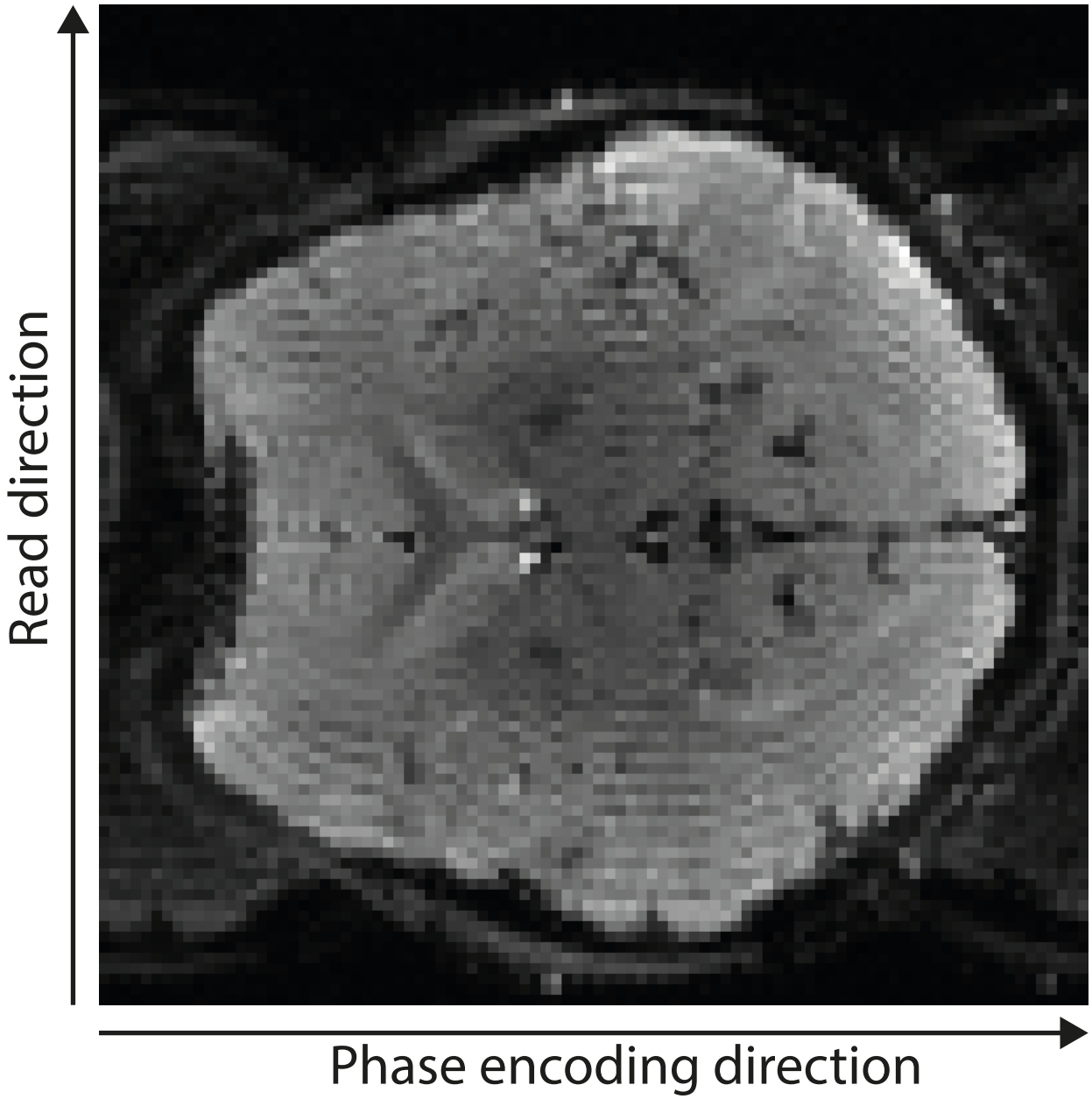

Figure 3.5: Example of ghosting in an EPI image. The ghosting can be seen at the front and back of the head.

dynamic imaging applications, such as joint and cardiac imaging. However, it is susceptible to motion artefacts which manifest in the image domain as geometric distortions and ghosting [4]. Many motion correction algorithms for EPI have been developed, however, these methods are not suitable for dynamic imaging applications in which we want to observe movement rather than correct for it [61, 62].

An alternative to EPI is spiral sampling [63]. This sampling scheme uses sinusoidally varying gradient waveforms (Fig.3.6 top) to acquire a k-space that starts at the center and spirals outwards (spiral-out)[63]. It is also possible to start at the outside of k-space and spiral inwards towards the center (spiral-in). A spiral-out sampling pattern is shown in Fig.3.6. The gradient waveform for spiral sampling must be carefully designed such that the rate of gradient change does not exceed the gradient systems slew rate and the maximum amplitude does not exceed the maximum gradient amplitude. A variety of analytical solutions have been developed to generate the spiral waveform [64].

An advantage of spiral sampling is that it allows for very short (near zero) echo times [65, 66]. This allows a spiral sequence to record signals from tissues with very short T_2 values, such as myelin [67].

Another advantage of spiral sampling is that, compared to Cartesian sampling and EPI, it is more robust to motion, due to oversampling of the central region of k-space. The robustness to motion allows spiral sampling to be used effectively for dynamic imaging. Spiral sampling has been used to acquire dynamic images of cardiac motion [68], joint kinematics [69] and speech [70].

As with EPI, spiral sampling is sensitive to blurring and signal drop out

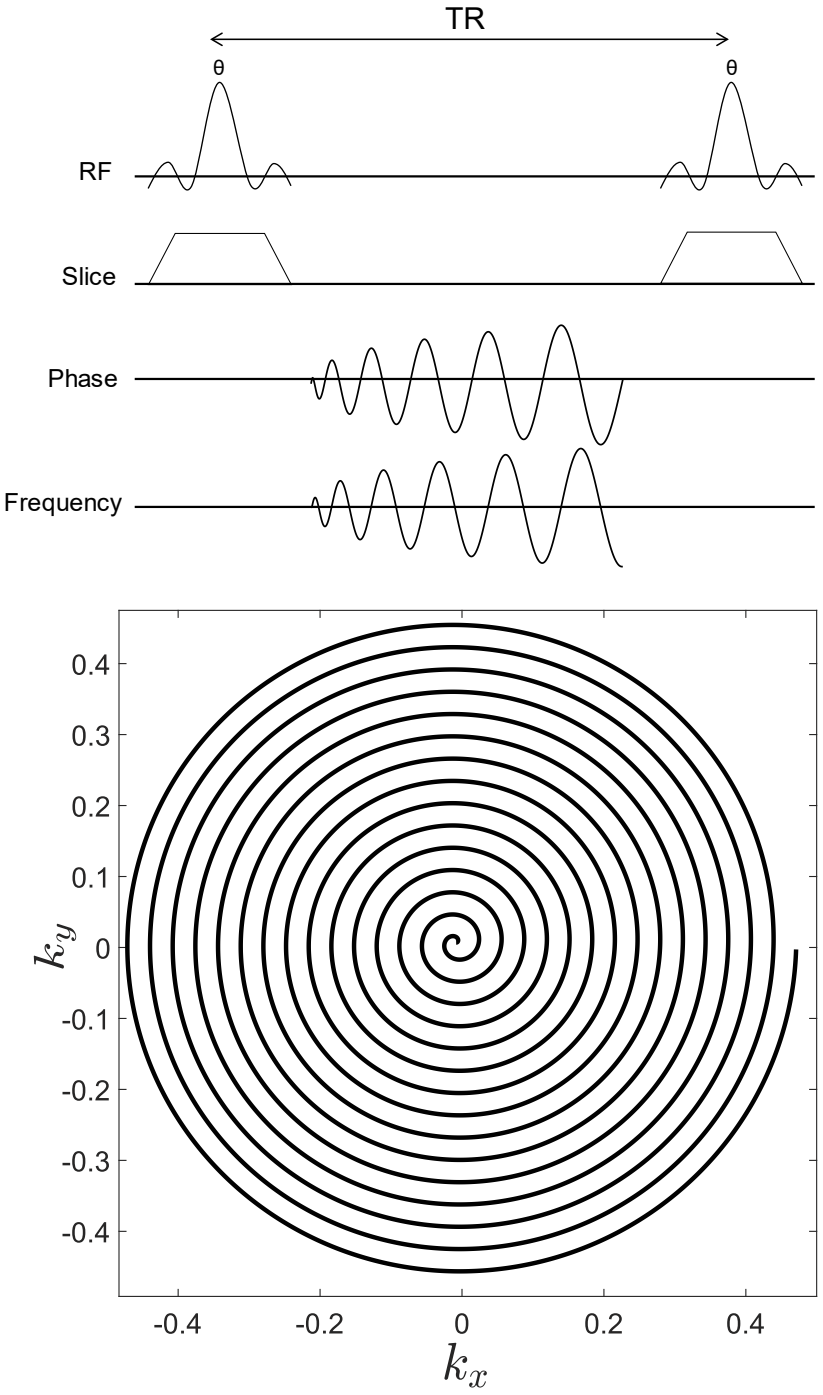

Figure 3.6: Top: GRE sequence using sinusidally varying gradients. Bottom: resulting k-space trajectory, starting from the center and spiralling out.

due to off-resonance artefacts [71]. For example, in spiral imaging of speech, it is common to see distortion around the tongue due to the air-tissue boundary [71]. A variety of correction methods have been developed. These involve estimating the inhomogeneity in the B_0 field either from a separate scan or from the data itself [71]. The inhomogeneity estimation can then be built into the reconstruction model.

Spiral sampling is also sensitive to imperfections in gradient hardware. If the gradients do not perform exactly as expected, the actual k-space trajectory will be different than expected, this introduces errors into the reconstruction. Additional hardware which monitors the fields applied by the gradient system in real-time can be used (for both spiral and EPI sampling) [72, 73]. These measurements can be used to calculate the exact trajectory used to acquire data. However, this hardware is expensive and not commonly available on clinical systems. Another calibration technique involves calculating the gradient impulse response function (GIRF) which measures the performance of the gradient system [74]. This involves a separate scan with a spherical phantom. The GIRF information is then used during reconstruction to account for gradient imperfections.

A final consideration of a sampling technique is known as radial acquisition. This was the first sampling scheme used in MRI, presented by Lauterbur in 1973 [75]. However, it was replaced with Cartesian sampling due to the latter sampling scheme being more robust to the high amount of gradient imperfections present in early MRI systems. In radial sampling, k-space is acquired using a series of lines, often referred to as spokes, which are rotated around k-space by an angle, θ [76]. Unlike spiral sampling, which

requires complex oscillating gradient waveforms, only simple modifications to the pulse sequence are required as trapezoidal gradients are still used. The read and phase encoding gradients (now denoted as G_x and G_y, however any combination of gradients can be used) are now applied simultaneously. Their amplitude is modulated by either a sine or a cosine term (eq.(3.11) and eq.(3.12)) where G_0 is the gradient amplitude required to sample the centre line of k-space.

$$G_x = G_0 \cdot \cos(\theta) \tag{3.11}$$

$$G_y = G_0 \cdot \sin(\theta) \tag{3.12}$$

The sampling efficiency (i.e. how many samples are required to fully sample the image) is lower than in Cartesian sampling [76]. It can be shown that a fully sampled radial image would require $\frac{\pi}{2}$ times the number of spokes compared to Cartesian sampling. However, the repeated acquisition of low-frequency k-space means that a significant amount of data undersampling can be performed while preserving image quality (in terms of noise, contrast and edge sharpness). This is due to the majority of information being contained in the low-frequency areas of k-space. An example of this is shown in Fig.3.8 where the number of acquired spokes is decreased. A degradation in image quality can be seen. However, there is no fold over artefact when compared to Cartesian undersampling, thus radial sampling can be used to achieve higher acceleration than Cartesian undersampling would allow.

Radial sampling, like spiral sampling, is robust to motion due to continued oversampling of the low frequency area of k-space. This has motivated

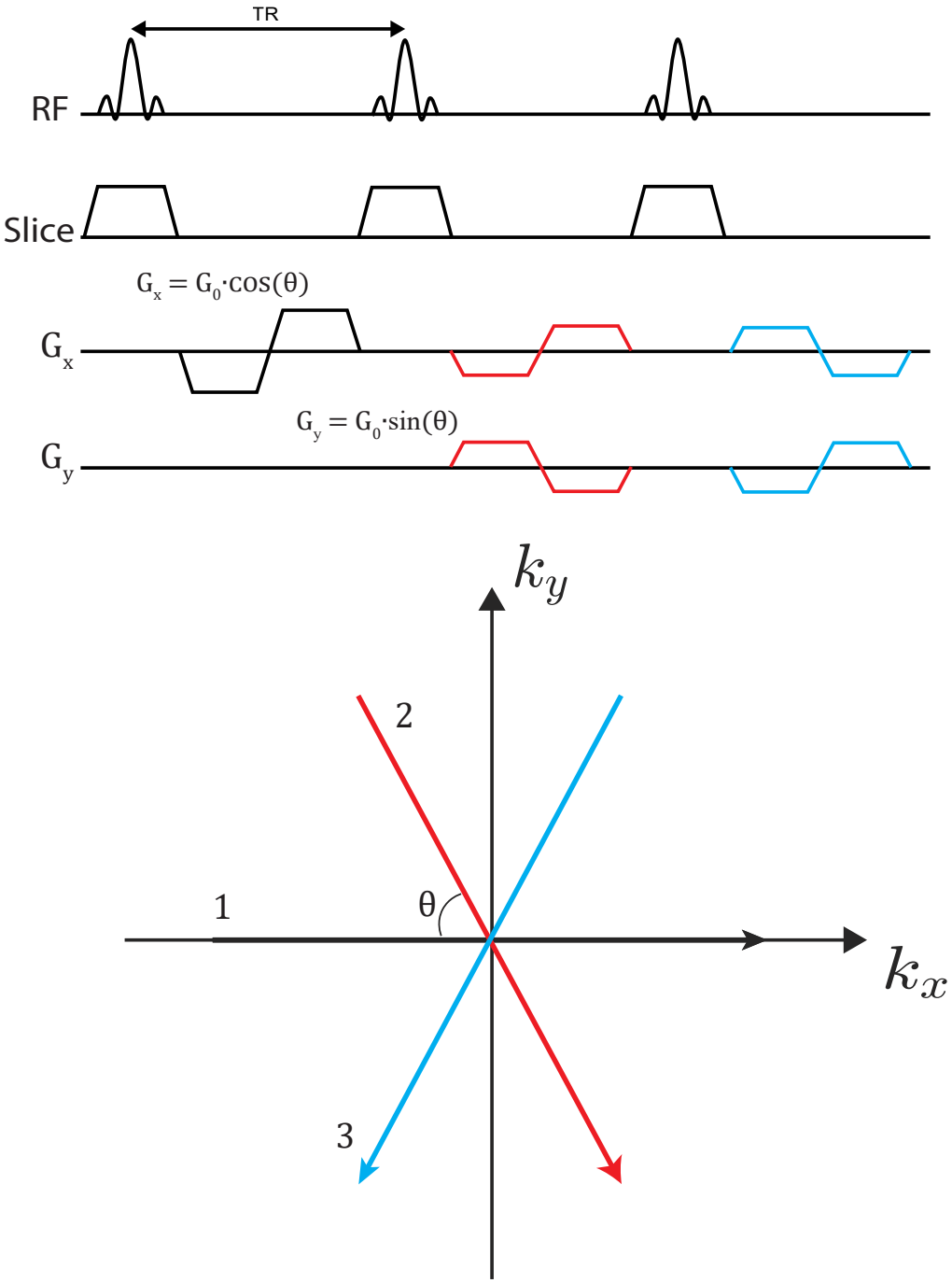

Figure 3.7: Top: a GRE sequence with radial sampling. The G_x and G_y gradients are applied simultaneously with there amplitude modulated by a cosine or sine term respectively. This results in k-space trajectory consisting of rotating spokes separated by an angle θ (bottom).

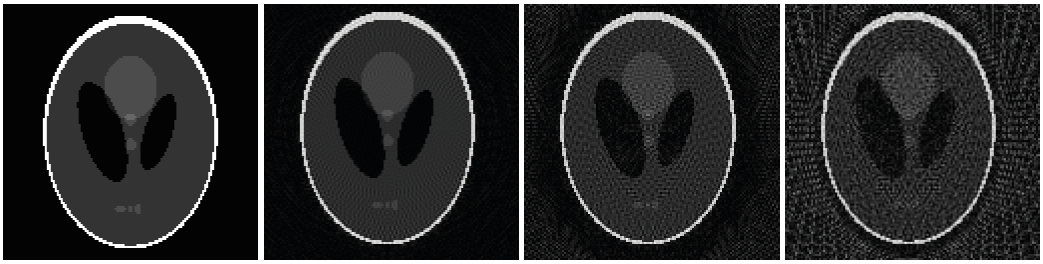

Figure 3.8: A numerical phantom (left) reconstructed using (from left to right) 128, 64 and 32 spokes. The increased level of undersampling results in an increase in aliasing throughout the image.

the use of radial sampling in dynamic imaging applications. For example, a large number of rtMRI methods employ highly undersampled radial sampling schemes to image movement; this will be discussed in detail in Chapter 4. In addition to rtMRI, other examples of the use of radial acquisition include imaging the change in image intensity after the injection of a contrast agent (Dynamic Contrast Enhanced MRI). Radial sampling is used in this application as the organ of interest (the liver) moves due to respiratory motion, resulting in artefacts if Cartesian sampling is used [77, 78].

Compared to EPI and spiral sampling, radial sampling is less susceptible to off-resonance artefacts, resulting in fewer artefacts around air-tissue boundaries. Radial sampling, like spiral sampling, is also sensitive to gradient imperfections. However, a wide variety of automated software-based trajectory correction methods exist, which can estimate the actual trajectory from either a set of prescans or from the data itself [79, 80, 81]. An additional advantage of radial sampling is that, due to the short readout times, the minimum TR when using radial sampling is typically lower than EPI or spiral sampling schemes.

3.5 Non-Cartesian Reconstruction

In standard Cartesian sampling, the Fourier transform, used to move between image and k-space, can be computed using a Fast Fourier transform (FFT) algorithm. The FFT assumes that sampled points lie on an equispaced Cartesian grid [82]. This assumption is no longer valid when using non-Cartesian sampling, thus making the image reconstruction problem challenging. Non-uniform Fast Fourier Transform (NUFFT) algorithms have been developed to overcome these challenges. Of specific interest to non-Cartesian MRI is the type-2 NUFFT which calculates the Fourier transform of frequency points at arbitrary sampling location [83].

The majority of type-2 NUFFT algorithms work by interpolating the acquired trajectory onto a Cartesian grid, which then allows for a standard FFT to be used. The NUFFT is a four or five-step algorithm:

- Density Compensation (optional)
- Convolution onto an oversampled Cartesian grid. This step is often referred to as gridding.
- FFT into the image domain
- Cropping to desired image size.
- Deapodisation

Density compensation is required to compensate for the increase in density of low frequency k-space values compared to higher frequency values [84, 85]. Without density compensation, there is an overweighting of the low-frequency values, which leads to blurring in the image domain (Fig.3.9).

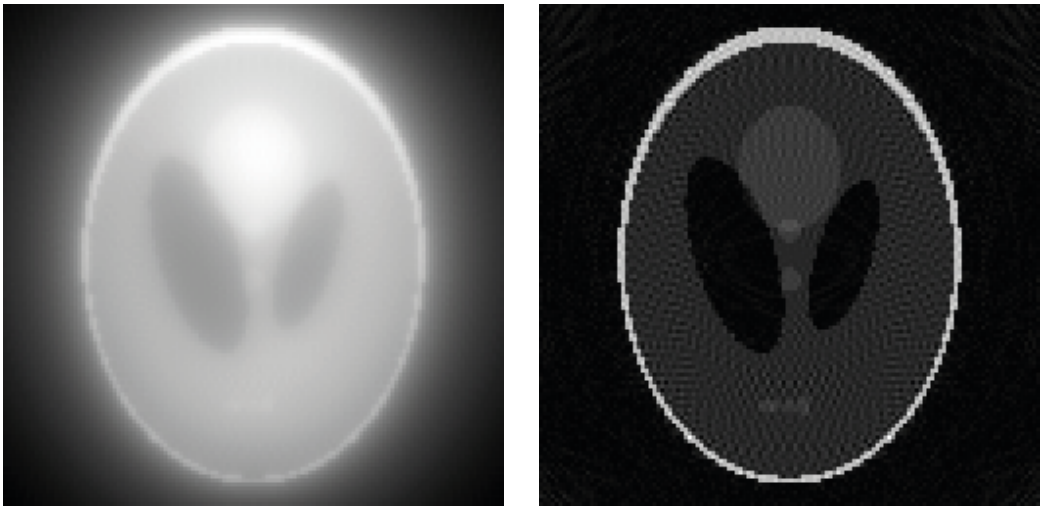

Figure 3.9: Image of a phantom reconstructed with 95 spokes without (left) density compensation and with density compensation (right). When density compensation is not used the image appears blurry due to the overweighting of the central region of k-space.

Density compensation is performed by multiplying the acquired data with a set of weights, d, referred to as density compensation coefficients. The calculation of d is dependent on the non-Cartesian trajectory used. For density compensation in radial sampling, a simple triangular filter can be used, eq.(3.13), where r is a point along the spoke and N_{Spk} is the number of spokes. This attenuates the lower k-space frequencies, thus removing the effect of them overweighting k-space. Iterative approaches can also be used to calculate the values of d. It has been shown that iterative design approaches can result in improved reconstruction quality compared to the triangular filter [85].

$$d(r) = |r| \cdot \frac{1}{N_{Spk}} \tag{3.13}$$

To move the non-Cartesian points, (k_x,k_y), onto a Cartesian grid, each point is convolved with a kernel function, $C(k_x, k_y)$. The result of this con-

volution is then sampled onto a Cartesian grid. The finite length of the convolution kernel results in artefacts around the sides of the image. To remove this, an oversampled grid can be used (i.e. the number of grid points is larger than the desired image size). The oversampling increases the field of view, thus pushing the artefacts away from the image. The amount of oversampling is typically denoted by α, with typical values ranging from 1.2 to 2 [86].

The ideal convolution kernel would be a sinc function of infinite duration, but this is not computationally possible. Instead, as was shown by Jackson et al. (1991), the Kaiser-Bessel window (KB-window) provides a good approximation [87]. The convolution kernel, using the KB-window, is defined in eq.(3.14) where I_0 is the zeroth order modified Bessel function. The Bessel function can be quickly and accurately approximated using a Chebyshev polynomial expansion [88]. The width of the kernel is determined by the parameter W, this value is chosen to balance numerical accuracy and computation time. A smaller kernel will decrease numerical accuracy but will also decrease computation time. Width values typically lie in the range of 3-7. The β value is a tuning parameter which modifies the shape of the KB-window, affecting the accuracy of the gridding. Beatty et al. (2005) showed the optimum β value for a given kernel width and oversampling factor is given by eq.(3.15). [86].

$$C(k_x, k_y) = \frac{1}{W^2} \cdot I_0 \left(\beta \sqrt{1 - \left(\frac{2k_x}{W} \right)^2} \right) \cdot I_0 \left(\beta \sqrt{1 - \left(\frac{2k_y}{W} \right)^2} \right) \quad (3.14)$$

Figure 3.10: Ground truth image of a phantom (left). When no deapodization is used (centre) variations in intensity can be seen in the centre of reconstructed image. This intensity variegation is suppressed when deapodization is applied (right).

$$\beta = \pi \cdot \sqrt{\frac{W^2}{\alpha^2}(\alpha - \frac{1}{2}) - 0.8} \tag{3.15}$$

A standard FFT can then be used to move from the Cartesian k-space to the image domain, and the image is then cropped to the desired size. The final step required is deapodization, which is the division of the image by the Fourier transform of the kernel. This step is required as the finite length of the kernel in the k-space domain results in intensity variations in the image domain (Fig.3.10).

Non-Cartesian trajectories are often used in conjunction with parallel imaging [47]. This allows for higher acceleration factors that neither non-Cartesian trajectories or PI could provide independently. Non-Cartesian PI reconstruction was first described in work by Prusseman et al. in 2001, they demonstrated that SENSE can be used with any non-Cartesian trajectories [41]. They showed that by combining SENSE with radial or spiral trajectories, it is possible to improve the temporal resolution of cardiac MRI from 112ms to 54ms. To use SENSE with non-Cartesian trajectories, the signal

equation previously shown was adapted to use a NUFFT rather than the simple FFT. After this alteration, the reconstruction can be carried out using the conjugate gradient algorithm. Non-Cartesian PI has now been applied to a variety of different non-Cartesian trajectories, including radial and spiral, in a variety of applications such as brain, cardiac and musculoskeletal imaging [47, 89, 90, 91]. One of the main drawbacks of this technique, in addition to the previously described problems with non-Cartesian trajectories, is the increase in reconstruction time required to repeatedly compute the NUFFT.

Density compensation is an optional step when using iterative reconstruction algorithms. It can be shown that density compensation improves the convergence speed of PI algorithms, allowing for fewer iterations and, therefore, a lower reconstruction time [41]. A disadvantage of using density compensation is that it can be shown to result in increased reconstruction error as measurements are attenuated [92].

As shown in Section 3.3 iterative PI methods require a transformation from the image domain to the k-space domain. For Cartesian trajectories, this is simple to accomplish using an inverse FFT. For non-Cartesian trajectories, this mean that as well as using the type-2 NUFFT discussed previously (Non-Cartesian k-space to Cartesian image space), a type-1 NUFFT which moves from Cartesian image space to non-Cartesian k-space is required [93]. The algorithm to do this is very similar to the type-2 NUFFT. Instead of cropping the image it is instead zero padded to the size of the oversampled grid, then an inverse FFT is used to create a Cartesian grid of k-space. The density correction step is not required as the Cartesian grid has a uniform density. The type-1 NUFFT can therefore be summarised as a four-step

algorithm:

- Application of deapodization function to the image.
- Zero-padding of the image to the size of the oversampled grid.
- Inverse FFT to transform from image domain to frequency domain.
- Convolution to move from Cartesian grid to the desired non-Cartesian trajectory.

3.6 Compressed Sensing

The parallel imaging techniques discussed so far exploit the redundancy in spatial information due to multiple receiver coils. In 2006, Candes et al. introduced a new mathematical optimization technique called compressed sensing (CS), which recovers a signal $\mathbf{x}$ of length M from a set of N_s measurements, $\mathbf{y}$, where $N_s < M$ [94, 95]. CS exploits the sparsity of the signal in the signal reconstruction algorithm [96]. The sparsity of a signal can be measured using the L_1 norm (eq.(3.16)) denoted by $\|\mathbf{x}\|_1$ - a lower value reflects a higher sparsity.

$$\|\mathbf{x}\|_1 = \sum_{i=1}^{M} |x_i| \tag{3.16}$$

The level of sparsity required to achieve perfect reconstruction can be analytically derived in extremely specific circumstances for matrices consisting of random values [94]. However, generally, it is not possible to compute the exact level of sparsity required for optimum reconstruction quality [96].

The methodology developed by Candes et al. (2006) remained mainly an abstract mathematical technique until it was applied to MRI image reconstruction by Lustig et al. in 2007 [97]. This work highlighted the three main components required for CS to work in the context of MRI image reconstruction:

- The image must be sparse in a transform domain.
- The image domain aliasing due to undersampling must be incoherent.
- A non-linear recovery algorithm must be used to recover the image from the set of undersampled k-space measurements.

Although an MR image is not sparse in the original image domain (with the exception of MR angiography images), they can be made sparse by using an appropriate transform. Lustig et al. (2007) showed the Total Variation (TV) transform and the Wavelet transform can provide a sparse representation of the image (Fig.3.11). The TV transform takes the difference between adjacent pixels, and if we assume that adjacent pixels have similar values, this results in a sparse representation. The Wavelet transform decomposes the image into a series of coefficients which represent band-passed filtered frequency values and hold both position and frequency information [98]. It can be shown that the wavelet coefficients decay rapidly, resulting in a sparse representation of the image in the wavelet domain. These two transforms are the most commonly used sparsity-promoting transforms due to their robustness in most situations - a wide variety of other transforms have been developed over the subsequent years [99].

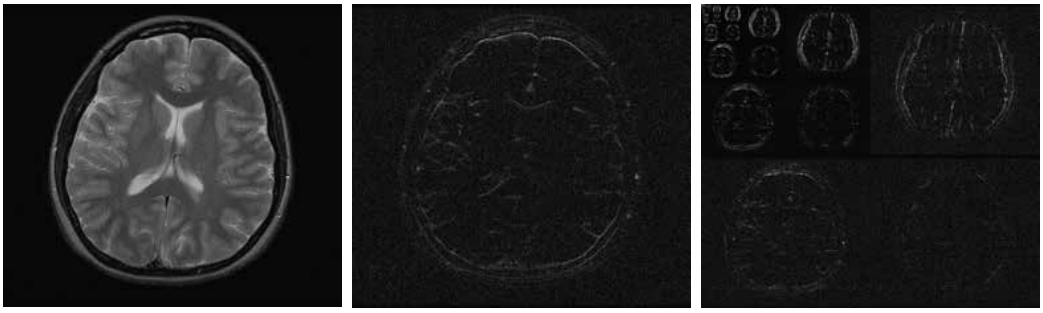

Figure 3.11: An MRI image of the brain (left), the same image after being transformed to the total variation (center) and wavelet (right) domains. In the two transform domains it can be seen that the image is now sparse, mainly consisting of pixels with low values.

The second requirement of incoherent aliasing can be achieved by randomly sampling the signal; this was the original technique used by Candes et al. (2006) in their theoretical work on CS [94, 100]. However, in the context of MRI, randomly sampling k-space is both not desirable and not practically possible [97]. It is not desirable as image information is mainly contained in the center of k-space, thus, it is beneficial to acquire more of these lower frequencies. It is also not possible to achieve truly random sampling as we acquire lines of k-space at a time rather than acquiring individual points. Achieving incoherent aliasing is not possible using the standard approach of skipping k-space lines used in SENSE, as this results in structured aliasing in the form of the folder over artefact shown previously in Fig.3.2. Instead, Lustig et al. (2007) proposed using a variable density Cartesian sampling scheme, which acquires a fully sampled centre region and then selects high-frequency lines to sample based on a Poisson distribution [97, 101]. They showed that this results in incoherent noise while still acquiring the useful low-frequency information. The requirement for incoherent aliasing is also fulfilled using radial and spiral trajectories, this was demonstrated in Fig.3.8,

which showed that the effect of radial undersampling was not structured foldover artefacts but instead an increase in noise throughout the image [47, 97].

Finally, to recover the images using sparsity constraints, Lustig et al. (2007) posed the MR image reconstruction problem as an optimization problem. The structure of the optimization problem is similar to that shown previously for parallel imaging, with the addition of the L_1 norm term (eq.(3.17)). Lustig et al. (2007) solve this optimization problem using a non-linear conjugate gradient algorithm (NLCG).

$$\hat{\mathbf{x}} = \arg\min_{x} \left[\frac{1}{2} \left\| \mathbf{F}\mathbf{x} - \mathbf{y} \right\|_2^2 + \lambda \left\| \mathbf{T}\mathbf{x} \right\|_1 \right] \tag{3.17}$$

This optimization problem balances the data consistency ($\frac{1}{2} \left\| \mathbf{F}\mathbf{x} - \mathbf{y} \right\|_2^2$) which measures how much our generated image $\mathbf{x}$ matches the data, $\mathbf{y}$, with the level of sparsity we desire. The $\left\| \mathbf{T}\mathbf{x} \right\|_1$ term measures the sparsity of the generated image in the transform domain, where $\mathbf{T}$ is an operator which converts from the image domain to the transform domain. The data fidelity term and sparsity term are balanced using λ.

There is currently no analytical way to select the optimum value of λ, instead this parameter is usually manually tuned to achieve "good" image quality [102]. The image quality can be measured using metrics such as the signal-to-noise ratio or contrast-to-noise ratio [103]. However, these metrics do not fully capture the artefacts present in the image (for example, blurring) [104]. Thus, it is routine to complement these metrics with visual inspection of the image quality and comparison against fully sampled reference images [103].

Compressed sensing can be combined with parallel imaging. For example, Liang et al. (2009) and Otazo et al. (2010) developed implementations of SENSE, which exploit both the spatial information introduced by coil sensitivity maps and the transform domain sparsity of images [105, 106]. To combine the two techniques, the SENSE reconstruction model is altered by adding a sparsity transform term to the SENSE optimization problem (eq.(3.7)) yielding eq.(3.18). This technique is often referred to as CS-SENSE. This combination of PI and CS allows for very high acceleration factors to be achieved. For example, Otazo et al. demonstrated that CS-SENSE can be used to perform cardiac imaging at a temporal resolution of 60ms with fewer artefacts than parallel imaging could achieve alone [106].

$$\hat{\mathbf{x}} = \arg\min_{\mathbf{x}} \left[\frac{1}{2} \left\| \mathbf{A}\mathbf{x} - \mathbf{y} \right\|_2^2 + \lambda \left\| \mathrm{T}\mathbf{x} \right\|_1 \right] \tag{3.18}$$

A disadvantage of CS is an increase in reconstruction time. For example, a fully sampled Cartesian k-space may take seconds to reconstruct using an FFT whereas CS reconstruction may take minutes or possibly hours [107]. This is problematic when images are required immediately, for example, to plan subsequent scans. The long computation time is a consequence of the reconstruction algorithm requiring multiple iterations to converge to a solution. Parallel computing is now used extensively to reduce the reconstruction time [108, 109]. The parallel computing approaches typically split the reconstruction problem into smaller sub-problems. For example, by performing reconstruction across each receiver coil in parallel [109, 110]. One main area of focus, in the context of non-Cartesian reconstruction, is reducing the computation time of the NUFFT operations. This is particularly important in

non-Cartesian parallel imaging applications due to the NUFFT needing to be applied repeatedly to the data recorded from each coil. It is typical for 90% of the overall computation time for CS reconstruction to be spent performing NUFFTs [111, 112]. A variety of GPU and multi-core CPU NUFFT algorithms have been developed, which significantly decrease the computation time [113, 114, 115]. The CS reconstruction time is also lowered through using more efficient optimization algorithms, which converge to a solution in fewer iterations compared to the NLCG algorithm. An overview of commonly used compressed sensing reconstruction algorithms can be found in a recent review paper by Fessler (2019) [116] and a specific discussion of the reconstruction algorithm used in this work can be found in Section 4.4.

3.7 Simultanteous-Multislice

3.7.1 Introduction to Simultanteous-Multislice

In standard MRI, an RF pulse excites a single region (a slice). If N_{Sli} slices are desired, then the acquisition will need to be repeated for each slice (assuming that the TR is not high enough to interleave slices). This results in a total acquisition time, which scales with the number of slices (eq.(3.19)).

$$\mathrm{TA} = N \cdot \mathrm{TR} \cdot N_{Sli} \tag{3.19}$$

The final acceleration technique, which will be discussed is Simultaneous Multislice (SMS) acceleration (also referred to as multiband acceleration). SMS enables data from multiple slices across a plane to be recorded simultaneously [117]. Thus, SMS is referred to as a through-plane acceleration

technique (rather than in-plane acceleration techniques such as SENSE).

3.7.2 RF Pulse Theory

The main component of SMS acceleration is a slice selective RF pulse, which can excite multiple regions via the application of multiple frequencies simultaneously [118]. A singleband pulse (i.e. a pulse that excites a single region), RF(t), can be described (in the time domain) as the product of two functions $A(t)$ and $P(t)$ (eq.(3.20)).

$$RF(t) = A(t) \cdot P(t) \tag{3.20}$$

The $A(t)$ component describes the shape of the pulse in the time domain; this is commonly a truncated sinc function. This determines the slice excitation profile (in the frequency domain), it is typically desirable that this profile be as close to rectangular as possible in order to have uniform excitation across the slice (Fig.3.12).

The second component is a phase modulation function (eq.(3.21)), which determines the slice position of the pulse and its phase (ψ). The position of the slice is determined by the frequency offset (relative to the Larmor frequency) $\Delta\omega$.

$$P(t) = \exp\left(i \cdot \Delta\omega \cdot t + \psi\right) \tag{3.21}$$

The simplest multiband pulse, $\mathrm{RF_{MB}}$, to excite N_{Sli} slices simultaneously can be described as the sum of single slice RF pulses at the desired slice locations (eq.(3.22)), where $\Delta\omega^j$ denotes the frequency offset required to

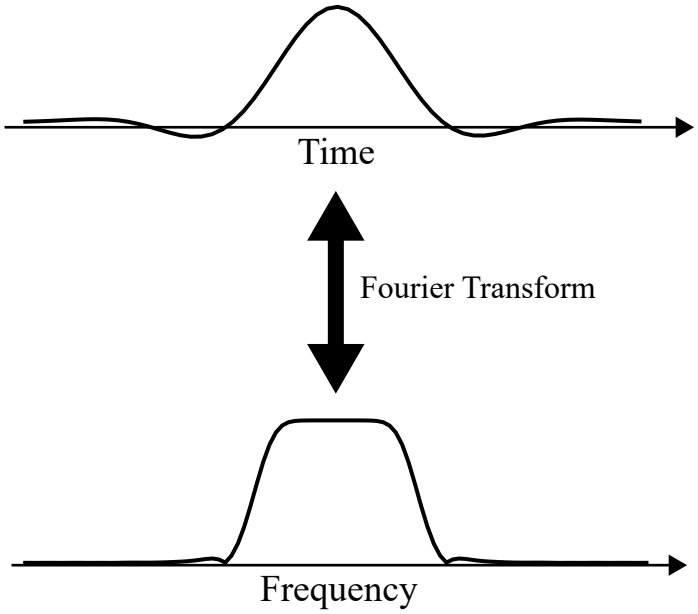

Figure 3.12: Illustration showing that the Fourier transform of a truncated sinc function (in the time domain) results in an approximately rectangular function in the frequency domain.

excite slice j [117].

$$\mathrm{RF_{MB}} = \sum_{j=1}^{N_{Sli}} \mathrm{RF^j} = A(t) \cdot \sum_{j=1}^{N_{Sli}} P^j(t) = A(t) \cdot \sum_{j=1}^{N_{Sli}} \exp\left(i \cdot \Delta\omega^j \cdot t\right) \qquad (3.22)$$

A consideration when using multiband RF pulses is the increase in energy deposited into the subject, resulting in increased tissue heating [117]. It can be shown that the power of the pulses is proportional to the square of the number of excited slices. This is particularly problematic when spin-echo sequences are used due to the inversion pulses, which often have large power requirements. This problem can be partially mitigated through the use of low flip angle GRE sequences (such as the one used in this thesis Chapter 4). More sophisticated RF pulse design methods can also be used to reduce the peak RF amplitude; however, these are not used in this thesis [119, 120,

121, 122].

3.7.3 Reconstruction

After excitation using a multiband pulse, the recorded signal, $\mathbf{y}^{MB}$, is a summation of the k-space data from each slice, this is shown in eq.(3.23) where $\mathbf{y}^{j}$ is the k-space data from slice j.

$$\mathbf{y}^{MB} = \sum_{j=1}^{N_{Sli}} \mathbf{y}^{j} \tag{3.23}$$

The inverse Fourier transform of this k-space results in a image, which is a superposition of the two excited slices (Fig.3.13). This is a consequence of the linearity properties of the Fourier transform (eq.(3.24)).

$$\mathbf{F^H}\mathbf{y}^{MB} = \sum_{j=1}^{N_{Sli}} \mathbf{F^H}\mathbf{y}^{j} = \mathbf{F^H} \sum_{j=1}^{N_{Sli}} \mathbf{y}^{j} \tag{3.24}$$

Without any additional information, it is impossible to separate the slices from the superimposed k-space data. However, as with parallel imaging, if multiple receiver coils are used there is spatial information embedded in the recorded signal through coil positions (Section 3.3). Consider two simultaneously excited slices A and B. The coils closer to slice A will weigh the data from that slice higher than the data for slice B, thus, embedding additional spatial information into the recorded signal. In contrast to PI methods discussed previously, we are now aiming to exploit the variations in coil sensitivity between slices rather than through a single slice. The SENSE model shown previously can be adapted for SMS image reconstruction. This is shown in eq.(3.25), where $\mathbf{A}^{j}$ is the forward model used to transform the

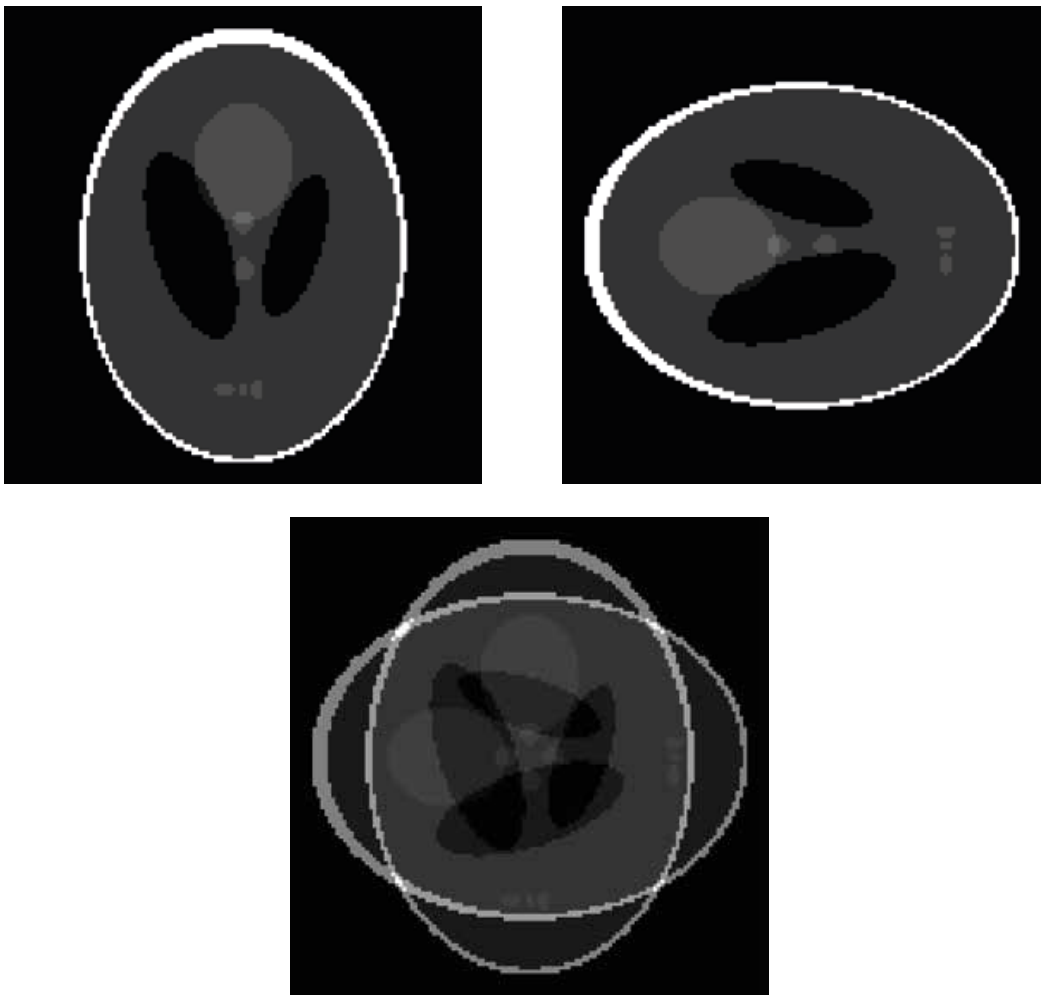

Figure 3.13: Illustration of slice superposition. The top two slices are added together, the result, shown in the bottom row, is a superposition of the two slices.

image for slice j, $\mathbf{x}^j$, into the k-space domain. As with the original SENSE problem this optimization problem can be solved using a variety of algorithms (such as the Conjugate gradient algorithm).

$$\hat{\mathbf{x}} = \arg\min_{\mathbf{x}} \left[\frac{1}{2} \left\| \sum_{j=1}^{N_{Sli}} \left(\mathbf{A}^j \mathbf{x}^j \right) - \mathbf{y} \right\|_2^2 \right] \tag{3.25}$$

3.7.4 CAIPIRINHA

The geometry of the coil array used to record the MRI signal has a substantial impact on the reconstruction algorithms' ability to separate slices [29]. If there is not enough variation between coil sensitivity profiles, then recovery of separate slices will not be possible. Breuer et al. (2006) introduced the Controlled Aliasing In Parallel Imaging Results in Higher Acceleration (CAIPIRINHA or CAIPI for short) method. The main principle of CAIPI is the introduction of additional aliasing between the excited slices; the result of this is that they are no longer superimposed. It can be shown that this additional aliasing improves slice separation. The aliasing is generated through the use of multiple RF pulses with slice dependent phase shifts between the bands of the multiband RF pulses.

The simplest example of CAIPI is the simultaneous excitation of two slices (Fig.3.14). Two multiband RF pulses, RF_1 and RF_2, are used to achieve a shift between slices A and B. A π phase shift is introduced between the bands in RF_1 and RF_2 that excites slice B. Applying these pulses sequentially will result in the desired shift of slice B in the image domain. Using a π phase difference results in a shift in the image domain that is equal to half the FOV.

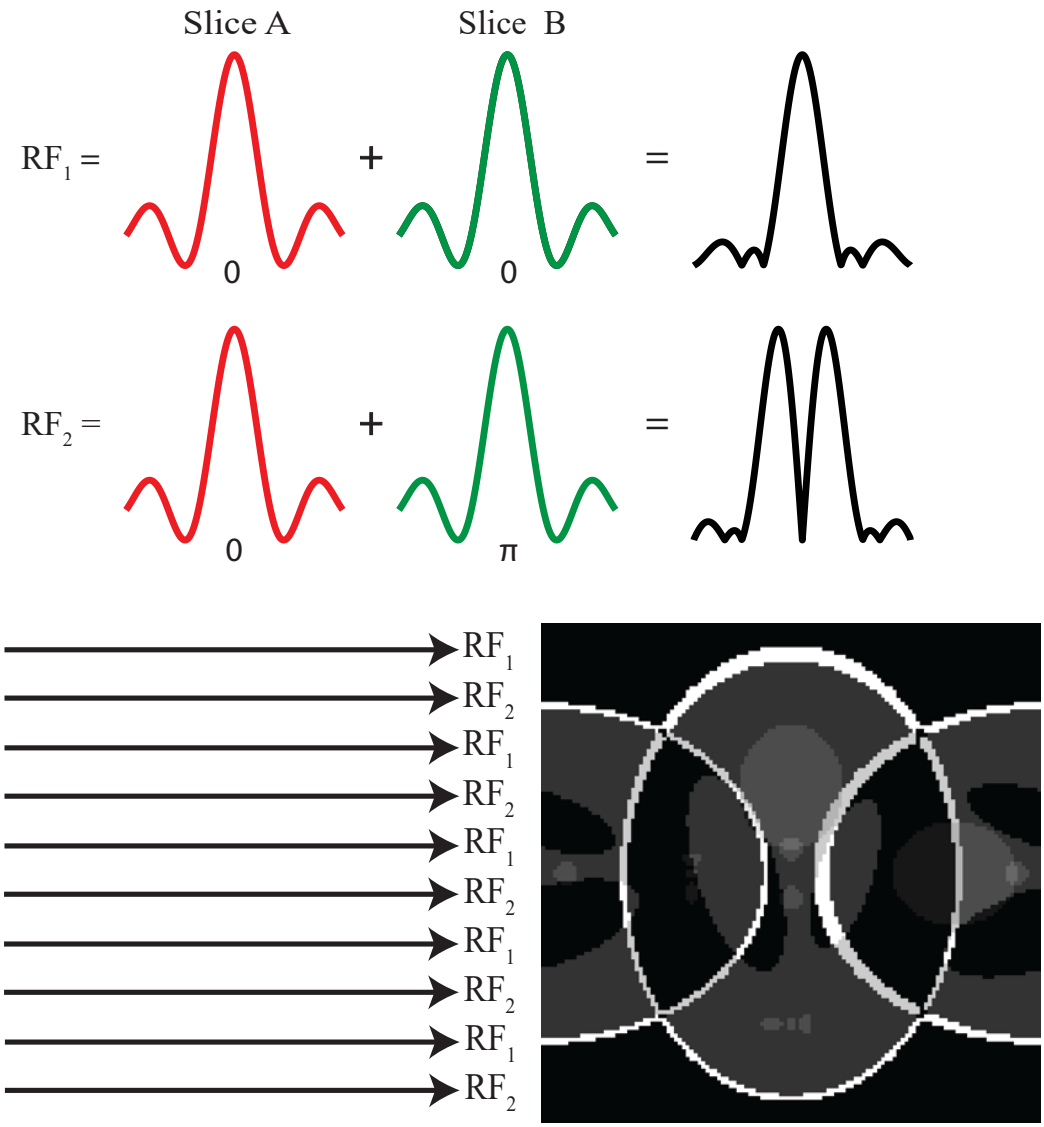

Figure 3.14: Diagram of the CAIPIRINHA technique. Two multiband RF pulses are generated with a π phase shift between the bands that excite slice 2 (green pulse). The application of these pulses in a sequential order (bottom left) results in slice 2 displaying aliasing.

When CAIPI phase cycling is used, the recorded k-space is modulated by the slice-dependent phase cycling profile $\mathbf{\Phi}^j \in \mathbb{C}^{N_s \times N_s}$ where j denotes the excited slice. The definition of $\mathbf{\Phi}^j$ is shown in eq.(3.27), it is a diagonal matrix where $\phi^j[a]$ denotes the phase modulation applied to the k-space point a in slice j.

$$\mathbf{y} = \sum_{j=1}^{N_{Sli}} \mathbf{\Phi}^j \mathbf{y}^j \tag{3.26}$$

$$\mathbf{\Phi}^j = \text{diag}(e^{i\phi^j[1,\ldots,N_s]}) = \begin{bmatrix} e^{i\phi^j[1]} & \ldots & 0 \\ \vdots & \ddots & \vdots \\ 0 & \ldots & e^{i\phi^j[N_s]} \end{bmatrix} \tag{3.27}$$

The previous SMS reconstruction model shown in eq.(3.25) must be modified to take into account the phase modulation. This is done through the addition of $\mathbf{\Phi}$ into the forward model term yielding eq.(3.28).

$$\hat{\mathbf{x}} = \arg\min_{\mathbf{x}} \left[\frac{1}{2} \left\| \sum_{j=1}^{N_{Sli}} \left(\mathbf{A}^j \mathbf{x}^j \right) - \mathbf{y} \right\|_2^2 \right] = \arg\min_{\mathbf{x}} \left[\frac{1}{2} \left\| \sum_{i=j}^{N_{Sli}} \left(\mathbf{\Phi}^j \mathbf{F} \mathbf{S}^j \mathbf{x}^j \right) - \mathbf{y} \right\|_2^2 \right] \tag{3.28}$$

The initial CAIPI paper used standard Cartesian sampling. Yutzy et al. (2011) showed that SMS with CAIPI phase cycling can be combined with radial sampling [123]. The effect of phase cycling when radial sampling is used is very different to Cartesian sampling. Rather than a FOV shift between slices, the phase cycling results in destructive interference between spokes. Returning to the two-slice example, the CAIPI phase cycling pattern described previously is used with radial sampling, slice A is preserved while slice B, which has the $0 - \pi$ modulation between adjacent spokes, becomes

noise due to destructive interference (Fig.3.15 shows a simulation of this for a Shepp-Logan phantom). Maximum destructive interference is achieved when radial spokes with differing phase modulations are located close together in k-space.

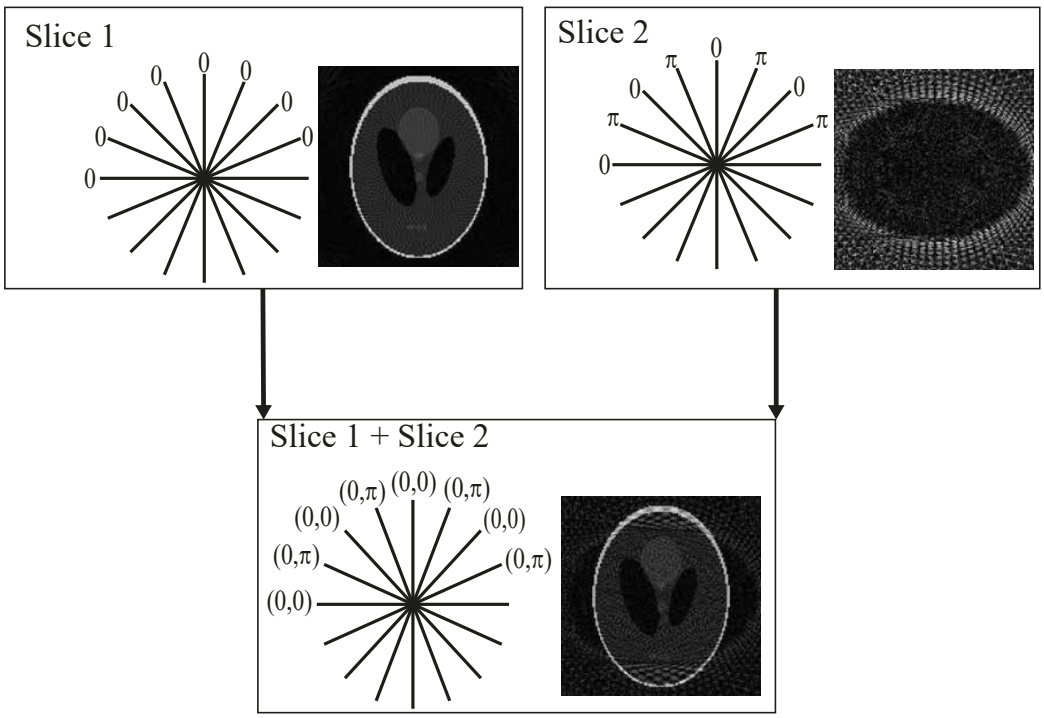

Figure 3.15: Simulation of CAIPIRINHA with radial sampling. Slice 1 has no phase modulation between spokes and slice 2 has π modulation between spokes. The result of this modulation is destructive interference that effectively results in slice 2 becoming noise. The summation of the two slices therefore appears as a noisy version of slice 1. The slices can be recovered using SENSE reconstruction.

3.7.5 SMS Acceleration in Dynamic Imaging

The first example of simultaneous multislice acquisition was demonstrated by Larkman et al., in this work 4 slices across the knee were acquired [11].

SMS acceleration in conjunction with EPI and PI is now routinely used to accelerate functional MRI and diffusion MRI sequences [117, 124, 125, 126, 118].

SMS is emerging as a useful acceleration technique in dynamic imaging sequences [4]. The motivation for using SMS accleration in dynamic imaging applications is based upon the necessity of using short TRs in order to attain high temporal resolutions. This small time between excitation limits the sequence from acquiring multiple slices in between the excitation gaps. Thus, dynamic sequences typically have reduced anatomical coverage. Achieving anatomical coverage, therefore, requires repeating the scan multiple times at different slice positions, increasing the overall time spent in the scanner or by increasing the TR which would lower the temporal resolution. Through using SMS acceleration - multiple slices can be acquired with no loss of temporal resolution.

The majority of dynamic SMS sequences are focused on cardiac applications [127, 128, 129]. This is likely due to two main factors. The first is clinical need: cardiovascular disease is the most common cause of death in the world [130]. It is important that imaging methodologies are developed, which can be used for evaluation of cardiac health. The second reason is that gating techniques can be used to synchronise acquisition and cardiac movement. Nazir et al. (2018) demonstrated gated cardiac imaging using SMS acceleration. This work doubled the in-plane spatial coverage of a standard cardiac perfusion sequence using SMS acceleration while preserving temporal resolution, through-plane spatial resolution and image quality [131]. Sun et al. (2020) demonstrated a gated cardiac imaging sequence combining spiral

sampling and SMS (with CAIPI phase modulation) [132]. Using this sequence, they acquired three slices simultaneously and showed that the image quality, using metrics such as ventricular volume and mean-squared error, is comparable to the equivalent single-band acquisition.

There is a limited number of examples of non-gated SMS dynamic sequences. One example is a work by Wang et al. (2016), this work demonstrated the combination of a radial trajectory with CAIPI SMS acceleration, reconstructed using a compressed sensing pipeline [133]. In-vivo examples of perfusion imaging were shown in dogs and humans at temporal resolutions (with 3 excited slices) of 144ms. If cardiac applications are excluded, the number of relevant examples is extremely limited. Wu et al. (2016) presented a radial SMS sequence with compressed sensing reconstruction pipeline and used this to excite four slices simultaneously [134]. They used this technique to study the shape of the upper airway in healthy volunteers and sleep apnea patients [134, 135]. This technique required the use of a custom array coil designed specifically for upper airway imaging; in addition to this, the temporal resolution achieved was relatively low (96ms - 128ms). Although sufficient for the desired application, this temporal resolution is not fast enough for some speech related tasks, which can require temporal resolutions of 70ms [7].

3.8 Summary

In this chapter, a variety of methods to accelerate MRI acquisition have been presented. Although the level of acceleration is determined by the sequence (i.e acquiring less k-space), the reconstruction plays a critical role

in recovering the final image. This interlinked connection between acquisition and reconstruction is critical to the success of all acceleration methods.

4

Development of Compressed Sensing Real-time MRI

4.1 Introduction

As discussed in Section 1.1, the human body is defined through both its structures and the functions these structures enable [136]. This has motivated the development of dynamic imaging methods capable of recording the body in motion. Of particular interest is real-time MRI as it makes no assumptions regarding the periodicity of motion and does not require gating equipment. An early example of an rtMRI method, called MR fluroscopy was presented in 1986 by Riederer et al. [137, 138]. This work used a Cartesian GRE sequence and was capable of acquiring an image every 500ms. At this slow temporal resolution, MRI is unable to capture the fast motion that occurs in many situations, such as speech and swallowing [136, 4, 7]. Developments in hardware, computational speed and parallel imaging have substantially increased the temporal resolutions that rtMRI methods are capable of achieving [4]. A key work presented by Uecker et al. (2010) demonstrated, through using a highly undersampled radial GRE sequence and parallel imaging reconstruction, that temporal resolutions of up to 30ms can be achieved in cardiac imaging (with no gating) with a spatial resolution of $2mm^2$ [6]. In the same work, examples

of speech imaging using rtMRI at a temporal resolution of 55ms and spatial resolution of 2.2mm^2 were demonstrated. To further increase temporal resolution, while maintaining image quality, compressed sensing reconstruction can be used. For example, Steeden et al. demonstrated the use of a spiral rtMRI sequence to asses ventricular volumes at a temporal resolution of 29.5ms at a spatial resolution of 1.68mm^2; they also showed that the image quality was comparable to standard gated acquisitions [139].

The majority of rtMRI sequences (including the examples above) are single slice due to the short TRs required. In this chapter, a radial GRE sequence is developed for rtMRI acquisition with the aim of improving anatomical coverage using SMS acceleration. The sequence is designed such that it is able to record both standard single slice rtMRI data and multiple slices using SMS acceleration. In terms of reconstruction, a compressed sensing pipeline is developed to reconstruct the highly undersampled radial k-space data. The results from using this sequence will be shown in Chapter 5.

4.2 Data Acquisition

For data acquisition, a GRE sequence is used to enable short TRs and, thus, attain a higher temporal resolution. Alternative short TR sequences exist such as balanced steady state free precession sequences (bSSFP), which have are used for rtMRI [140, 141, 142]. bSSFP has the advantage (compared to GRE) of having a higher SNR and improved contrast. However, bSSFP is extremely susceptible to off-resonance artefacts at 3T (and above) field strengths. These artefacts appear as dark bands across the image [2]. This problem is exacerbated when non-Cartesian sampling is used due to the fast

switching of gradients which cause eddy currents [143].

If the sequence is set to acquire multiband data, then the multiband RF pulses are generated at sequence runtime following the summation of singleband pulses shown previously in eq.(3.22). A Hanning-windowed sinc-shaped pulse with a pulse duration of 0.6ms is used for excitation.

A radial trajectory is used to sample k-space and was mainly chosen for three reasons:

- High levels of undersampling can be used while preserving image quality. This allows for high temporal resolutions to be achieved.
- As discussed in Section 3.4, compared to EPI and spiral sequences, radial sampling is more robust to off-resonance effects. This is particularly important for head/neck imaging applications where many tissue/tissue and tissue/air boundaries are present.
- Radial undersampling results in incoherent aliasing, this allows radial data to be reconstructed using compressed sensing algorithms to improve image quality.

At the start of this thesis there was no pulse sequence code for radial imaging available. Therefore, I developed a radial pulse sequence for this thesis. Radial rtMRI data consists of F frames, each acquired frame consists of K radial spokes, which are then transformed into the image domain. The order that radial spokes are acquired in is important to the resulting image quality. It is desirable that k-space coverage (per frame) is maximised, thus acquiring the greatest amount of information [5]. Two methods of ordering spokes are used in this thesis. The first ordering method is golden-angle

(GA) sampling [144]. In this sampling scheme $N = F \cdot K$ radial spokes are acquired. The number of spokes is chosen to reach the total acquisition time. For example, using a TR = 2.5ms and a total acquisition time of 15s, the number of spokes required is $N = 15/0.0025 = 6000$ spokes. The angle of spoke i in degrees, θ_i, is given by eq.(4.1) where $GR = \frac{1+\sqrt{5}}{2} \approx 1.618$ is a constant referred to as the golden ratio. This results in each spoke being rotated by 111.25° relative to the previous spoke (Fig.4.1). It can be shown that using this angular increment maximises k-space coverage when K is a Fibonacci number and provides near uniform k-space coverage when an arbitrary number of spokes are used per frame [76].

$$\theta_i = \text{mod}\left[(i-1)\cdot\frac{180}{GR}, 360\right] \tag{4.1}$$

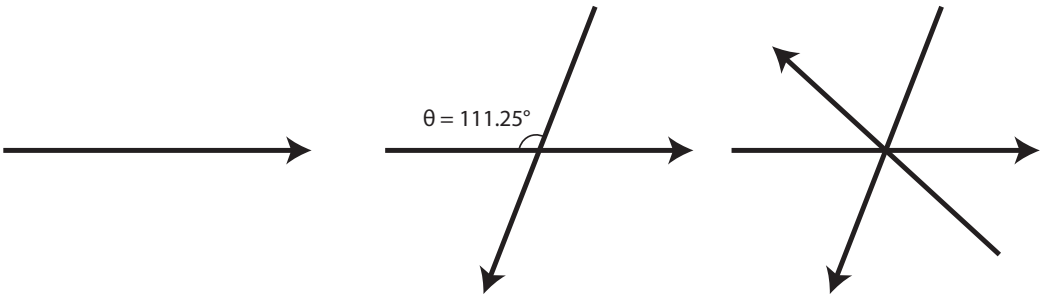

Figure 4.1: Demonstration of golden-angle sampling with three spokes. The angular increment between subsequent spokes is given by $\theta = 111.25°$

Another advantage of GA sampling is that the same location in k-space will not be repeated. Thus, when a large number of spokes is used, such as in rtMRI, the resulting k-space will be fully sampled. This fully sampled k-space can then be used for coil sensitivity profile estimation.

The CAIPRINHA phase modulation scheme proposed by Wu et al. was used in this thesis [134]. In this scheme a number of pulses equal to the num-

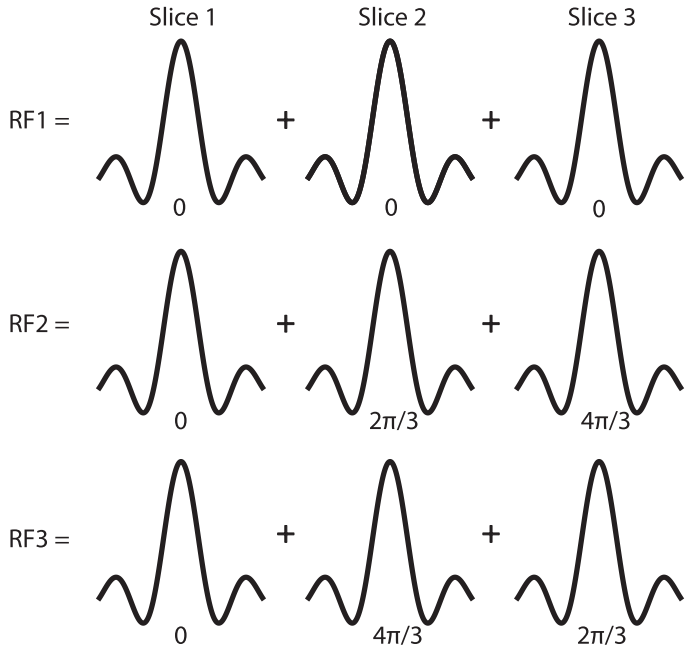

Figure 4.2: A demonstration (for 3 slices) of the phase cycling scheme used to generate the RF pulses required for the sequence.

ber of slices, N_{sli}, are generated (Fig.4.2). For multiband pulse n the phase difference, ψ_n, between the summed single-band pulses is cycled following eq.(4.2).

$$\psi_n = \mathrm{mod}\left[\frac{2\pi}{N_{sli}} \cdot n, 2\pi\right] \tag{4.2}$$

As discussed in Section 3.7.4, it is desirable when using radial sampling with CAIPIRINHA that the spokes with different phase modulations are close together in order to maximise destructive interference. When GA sampling is used, this does not occur, reducing the amount of interference. The second ordering method is referred to as SMS adapted Golden-Angle (SMS GA), proposed by Wu et al. (2016). It is designed to improve the destructive interference [134]. To achieve this. a modified form of GA sampling,

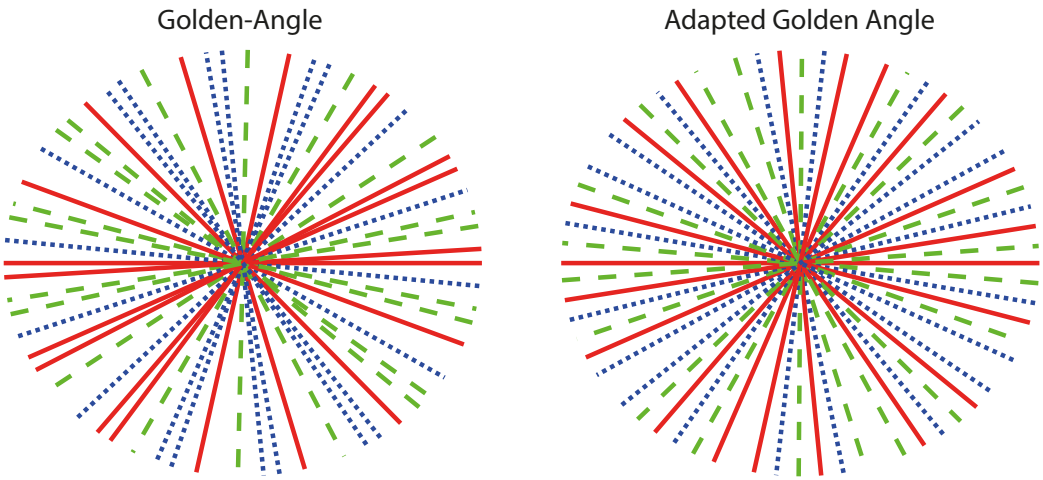

Figure 4.3: Comparison of Golden angle (left) and SMS adapted Golden angle (right) sampling schemes, showing the SMS GA trajectory creates a more even distribution of the RF pulses. This improves the destructive interference between slices. The sampling patterns shown are for a frame consisting of 25 spokes and three slices acquired simultaneously. The red solid lines correspond to the first RF pulse, green dashed lines correspond to the second RF pulse and the blue dotted lines correspond to the third RF pulse.

shown in eq.(4.3), is used. The angle between spokes is now related to the number of slices acquired simultaneously. This adjustment results in spokes with different phase modulations being closer together. Fig.5.35 provides a comparison of the two trajectories when 25 spokes are used and three slices are simultaneously excited. It can be seen that the SMS GA method results in a more uniform distribution of the phase modulated spokes. However, the publication by Wu et al. (2016) did not compare the sampling scheme they proposed to the standard GA sampling.

$$\theta_i = \mathrm{mod}\left[(i-1)\cdot\frac{180}{GR\cdot N_{Sli}}, 360\right] \tag{4.3}$$

The scheme proposed by Wu et al. is similar to the Tiny Golden angle (TGA) scheme proposed by Wundrak et al. [145]. In TGA the angle between

spokes is given by eq.(4.4), where the additional parameter T has been introduced. The effect of T is to reduce the angular increase between spokes. The reduction in angular increase also reduces the changes in gradient amplitude, which reduces the amount of eddy currents. The value of T can be decided arbitrarily while in Wu et al. it is determined by the number of slices excited simultaneously.

$$\theta_i = \mathrm{mod}\left[(i-1)\cdot\frac{180}{GR+T-1}, 360\right] \tag{4.4}$$

4.3 Choice of Sequence Parameters

The temporal resolution of a radial rtMRI sequence is defined by the number of spokes per frame multiplied by the TR. Thus, to achieve a high temporal resolution (for a given number of spokes), the sequence parameters must be chosen to minimise the TR.

A low TR requires a low TE. To reduce the TE, a high receiver bandwidth is used, as this allows for a shorter gradient duration. A receiver bandwidth of 1447 Hz/Pixel is used. Slightly higher bandwidths are possible. However, it was observed that past the chosen value, the reduction of TE/TR is minimal, indicating that receiver bandwidth is no longer the limiting parameter. The limiting parameter at this point is likely the RF pulse duration, reducing this further would increase the RF heating particularly when SMS acceleration is used.

The TE is also affected by the number of points acquired per spoke. Lower numbers of points allow for a shorter TE at the cost of reduced image resolution. This value was set to 128, over a field of view of 280mm, resulting

in an in-plane spatial resolution of 2.2mm^2. A slice thickness of 8mm is used. Using a lower number of points and a higher slice thickness would further reduce the TE; however, this would reduce the image resolution, resulting in a blocky appearance lacking anatomical detail.

The flip-angle of the sequence does not affect the acquisition time but has a significant effect on the contrast of the image. The optimum flip-angle to attain maximum signal for a spoiled GRE sequence is given by the Ernst angle, θ_e, which is determined by the T_1 value of the tissue being imaged and the TR (eq.(4.5)) [146].

$$\theta_e = \cos^{-1}\left(e^{-\frac{\text{TR}}{T_1}}\right) \tag{4.5}$$

Using a TR=2.5ms and assuming a $T_1 = 800\text{ms}$ (an average value for muscle tissue in the head [14]) results in an Ernst angle of $\theta_e = 4.55^\circ \approx 5^\circ$. This is verified by performing a set of in-vivo scans using the developed radial sequence in which the flip angle is varied between $3 - 15^\circ$. The images are reconstructed by gridding the data from each coil and combining them using the root sum-of-squares, 95 spokes/frame are used.

Results from this experiment are shown in Fig.4.4 and Fig.4.5. At a flip angle of 3° (smaller than the Ernst angle), there is little contrast between different tissues. The contrast improves as the flip angle increases, this improvement is particularly visible in the brain. However, past the Ernst angle, the overall signal level begins to decrease, resulting in the images appearing nosier and containing increased levels of streaking artfacts. The increase in streaking artefacts could be caused by out-of-slice aliasing from the shoulders.

The mean signal in the frontal area of the brain is plotted in Fig.4.6.

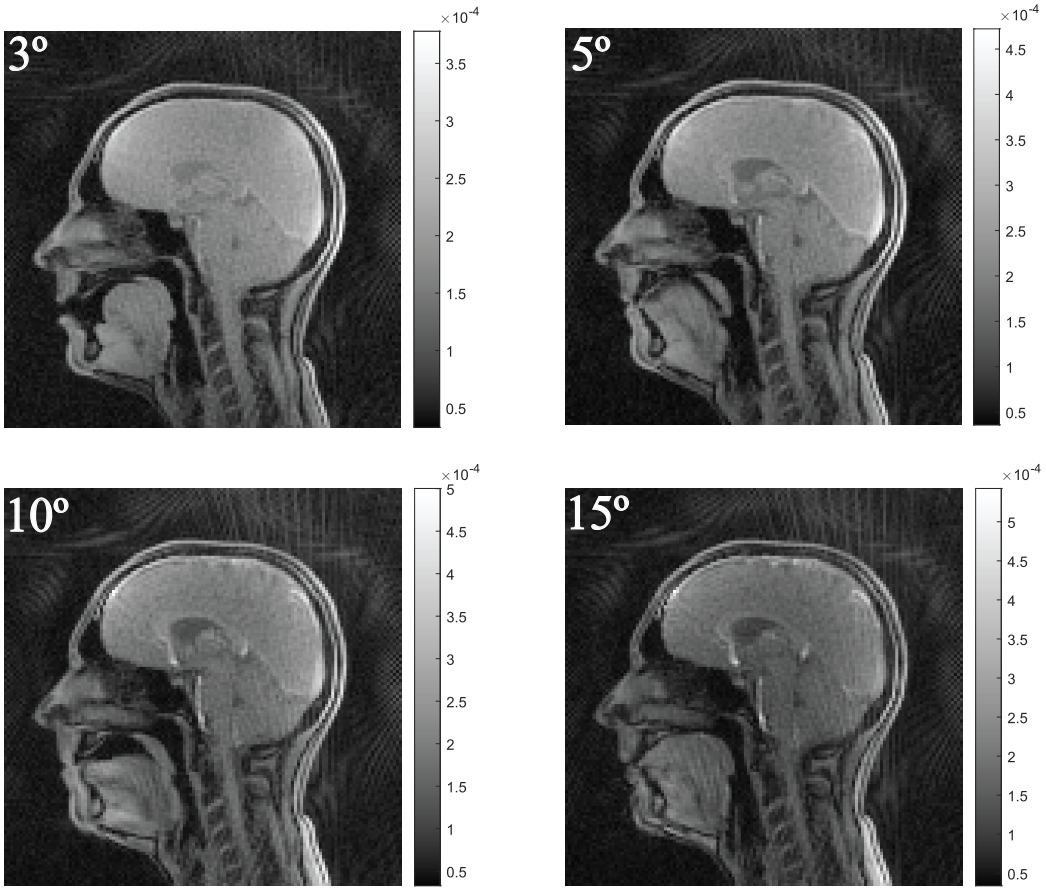

Figure 4.4: A frame from rtMRI videos acquired using a variety of flip angles (indicated in the top left corner), each image is scaled independently. As the flip angle increases past the Ernst angle (5°), an increase in contrast can be seen, at the cost of an overall reduced signal level.

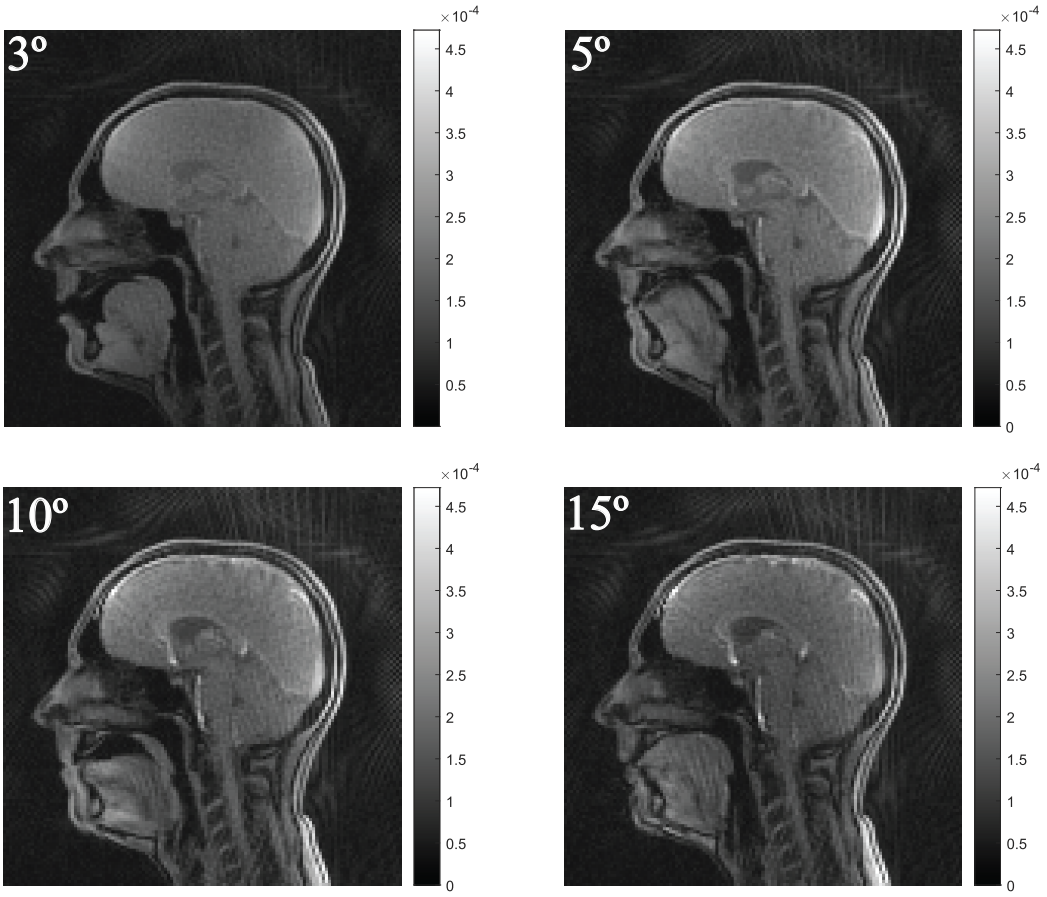

Figure 4.5: The same frames shown in Fig.4.4, normalized to the same intensity scale. This aids in highlighting the differences in signal levels/contrast between the images.

This plot confirms that the signal is maximised at the estimated Ernst angle. The noise levels in the images are quantified using the SNR. The SNR is calculated using eq.(4.6) where S is the mean signal in a selected region of interest (ROI), σ is the standard deviation of the noise.

$$\text{SNR} = \frac{S}{\sigma} \tag{4.6}$$

The value of σ is found by selecting a ROI in the background of the image (i.e where signal should be zero if no noise was present). In practice, multiple noise ROIs are chosen and the mean value used to calculate σ. In the following results four noise ROIs, placed in the corners of the image, were used. These areas were selected to attempt to minimize the amount of contribution from streaking artefacts (which would result in a underestimated SNR) in the SNR calculation. However, it was not possible to fully avoid contamination from streaking artefacts. Although SNR is not an ideal metric for image quality quantification (as will be discussed in detail in Section 5.5), it can be seen (Fig.4.7) that the SNR decreases as the flip angle increases. Based upon visual inspection and the quantitative results, a flip angle of 5° is selected.

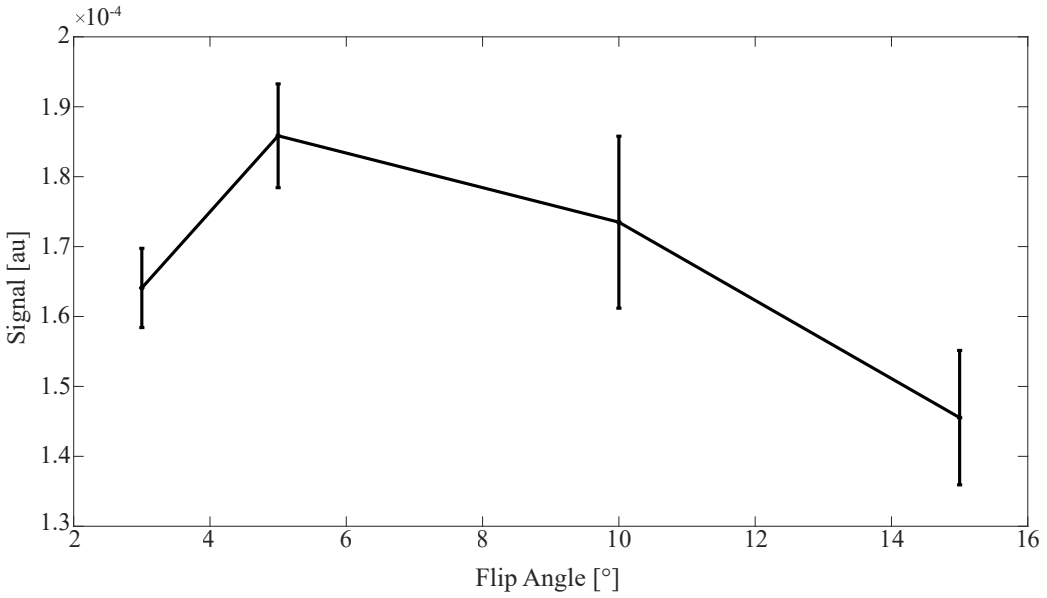

Figure 4.6: Plot of the mean signal acquired from the frontal region of the brain at varying flip angles, error bars reflect the standard deviation in signal intensity in the selected region. A peak at the Ernst angle ($5°$) can be seen.

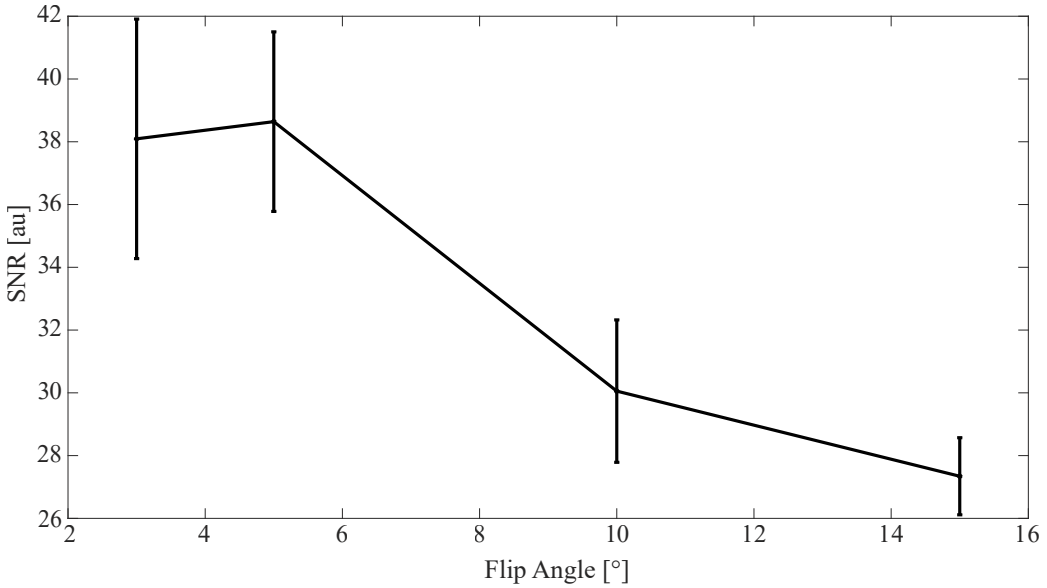

Figure 4.7: Plot of the SNR measured at varying flip angles, error bars reflect the standard deviation in SNR from four different noise regions. As the flip angle increases, a clear decrease in SNR can be observed.

4.4 Reconstruction Models

4.4.1 Singleband Reconstruction Model

In rtMRI the k-space data is binned to create set of k-spaces for each frame; this is often referred to as k-t space. The multi-coil k-space data from time frame t can be related to its image domain representation, $\mathbf{x}_t$, through eq.(4.7) where $\mathbf{A}_t$ is the forward operator. The forward operator changes between frames due to different k-space sampling patterns for each frame. In this work, the coil sensitivity profiles are assumed to be invariant over time.

$$\mathbf{y}_t = \mathbf{A}_t\mathbf{x}_t = \mathbf{F}_t\mathbf{S}\mathbf{x}_t \tag{4.7}$$

The data from each time point is stacked to yield a single variable $\mathbf{y} = [\mathbf{y_1}, \mathbf{y_2}, \ldots, \mathbf{y_{Nt}}]$. This is repeated for the image series and the forward operator yielding $\mathbf{x} = [\mathbf{x}_1, \mathbf{x}_2, \ldots, \mathbf{x}_{Nt}]$ and $\mathbf{A} = [A_1, A_2, \ldots, A_{Nt}]$. Using these two variables a linear forward model is established where $\mathbf{Ax}$ maps the image frames to the k-t space.

This forward model is combined with the compressed sensing reconstruction model shown previously in Section 3.6, yielding the reconstruction model shown in eq.(4.8). The regularization term, $\mathbf{T}$, is an operator which takes the difference between adjacent image frames. This form of regularization exploits sparsity present in the temporal dimension.

$$\hat{\mathbf{x}} = \arg\min_{\mathbf{x}} \|\mathbf{Ax} - \mathbf{y}\|_2^2 + \lambda \|\mathbf{Tx}\|_1 \tag{4.8}$$

Theoretically, regularization in the spatial dimensions can be incorporated into the proposed reconstruction model. Using spatial regularization

was attempted, however, it caused a oversmoothing of images resulting in a loss of fine detail, such as blurring of the tip of the tongue. Thus, in this work, only temporal regularization is used.

4.4.2 Multiband Reconstruction Model

When multiband excitation is combined with radial k-t sampling, the forward model for a time frame is given by eq.(4.9) where $\mathbf{x}_t^j$ denotes the image from slice j at time frame t and $\mathbf{A}_t^j$ is the forward operator for that time point and slice.

$$\mathbf{y_{MB}} = \sum_{j=1}^{N_{Sli}} \mathbf{A}_t^j \mathbf{x}_t^j \tag{4.9}$$

Combining this forward model with the compressed sensing model yields the optimization problem shown in eq.(4.10), where $\hat{\mathbf{x}} = [\mathbf{x}^1, \ldots, \mathbf{x}^{NSli}]$ is the multislice data for every time frame. The temporal regularization is applied to each slice.

$$\hat{\mathbf{x}} = \underset{\mathbf{x^1},\mathbf{x^2},\ldots,\mathbf{x^{N_{Sli}}}}{\arg\min} \left\| \sum_{j=1}^{N_{Sli}} \mathbf{A}^j \mathbf{x}^j - \mathbf{y} \right\|_2^2 + \lambda \sum_{j=1}^{N_{Sli}} \left\| \mathbf{T}\mathbf{x}^j \right\|_1 \tag{4.10}$$

4.4.3 Reconstruction Algorithms

The optimization problems shown in Section 4.4.1 and Section 4.4.2 are solved using the Alternating Direction Method of Multipliers (ADMM) algorithm [147]. ADMM was chosen for two main reasons:

- ADMM is known to have good convergence properties so will tend towards a solution quickly [148].
- The algorithm is relatively simple to implement, requiring only three

steps per iteration [147].

ADMM is used to solve optimization problems of the form shown in eq.(4.11) where $f(x)$ and $g(x)$ are convex functions and x is the variable we are minimizing and $\hat{x}$ is the optimum solution.

$$\hat{\mathbf{x}} = \arg\min_{\mathbf{x}} \left(f(\mathbf{x}) + g(\mathbf{x}) \right) \tag{4.11}$$

In the context of this thesis, the $f(\mathbf{x})$ term represents the data fidelity (eq.(4.12)) and the $g(x)$ term represents the sparsity promoting regularization (eq.(4.13)).

$$f(\mathbf{x}) = \frac{1}{2} \left\| \mathbf{A}\mathbf{x} - \mathbf{y} \right\|_2^2 \tag{4.12}$$

$$g(\mathbf{x}) = \lambda \left\| \mathbf{T}\mathbf{x} \right\|_1 \tag{4.13}$$

ADMM solves the optimization problem by first making the variable substitution $\mathbf{z} = \mathbf{T}\mathbf{x}$, resulting in the constrained optimization problem shown in eq.(4.14).

$$\hat{\mathbf{x}} = \arg\min_{\mathbf{x}} \left(\frac{1}{2} \left\| \mathbf{A}\mathbf{x} - \mathbf{y} \right\|_2^2 + \lambda \left\| \mathbf{z} \right\|_1 \right) \quad s.t.\, \mathbf{z} = \mathbf{T}\mathbf{x} \tag{4.14}$$

It can be shown that problems in this form can be reformed into an unconstrained form referred to as the Augmented Lagrangian (eq.(4.15)). This requires the introduction of two new variables. The first is $\mathbf{u}$, which is referred to as the scaled dual variable. The second parameter, ρ, is referred to as the Augmented Lagrangian penalty parameter.

$$\mathcal{L}(\mathbf{x}, \mathbf{z}, \mathbf{u}, \rho) = \frac{1}{2} \|\mathbf{A}\mathbf{x} - \mathbf{y}\|_2^2 + \lambda \|\mathbf{z}\|_1 + \frac{\rho}{2} \left(\|\mathbf{T}\mathbf{x} - \mathbf{z} + \mathbf{u}\|_2^2 - \|\mathbf{u}\|_2^2 \right) \quad (4.15)$$

ADMM then solves the Augmented Lagrangian using an approach called dual descent - this approach alternates between descent updates of the variables $\mathbf{x}$ and $\mathbf{z}$ and an ascent update of $\mathbf{u}$. This results in an iterative three step algorithm to find the optimum solution for $\mathbf{x}$. The algorithm is run for N_{Iter} iterations. The first step solves eq.(4.16) to find an updated estimate of $\mathbf{x}_i$, where i denotes the current iteration. A few iterations (typically between 1-5) of the conjugate gradient algorithm are used to find an approximate solution to this problem.

$$\mathbf{x}_{i+1} = \left(\mathbf{A}^\mathbf{H}\mathbf{A} + \rho \mathbf{T}^\mathbf{H}\mathbf{T} \right)^{-1} \left(\mathbf{A}^\mathbf{H}\mathbf{y} + \rho \mathbf{T}^\mathbf{H} \left(\mathbf{z}_i + \mathbf{u}_i \right) \right) \quad (4.16)$$

Next, the $\mathbf{z}$ value is updated using eq.(4.17) where soft() is the soft-thresholding function defined in eq.(4.18) .

$$\mathbf{z}_{i+1} = \text{soft} \left(\mathbf{T}\mathbf{x}_{i+1} + \mathbf{u}_i, \frac{\lambda}{\rho} \right) \quad (4.17)$$

$$\text{soft}(\mathbf{x}, \alpha) = \begin{cases} 0 & \text{if } |\mathbf{x}| \leq \alpha \\ \frac{(|\mathbf{x}| - \alpha)\mathbf{x}}{|\mathbf{x}|} & \text{if } |\mathbf{x}| > \alpha \end{cases} \quad (4.18)$$

The final step updates the dual variable, $\mathbf{u}_i$, through a simple summation (eq.(4.19)).

$$\mathbf{u}_{i+1} = \mathbf{u}_i + (\mathbf{T}\mathbf{x}_{i+1} - \mathbf{z}_{i+1}) \quad (4.19)$$

In the standard ADMM implementation the value of ρ is fixed. This parameter requires careful selection as it affects the convergence rate of the algorithm. In this thesis, ρ is adapted dynamically using the residual balancing method described by Wohlberg (2017) [149].

For single-slice rtMRI the proposed ADMM reconstruction is compared against two reference methods:

- Coil-by-coil gridding: this is a non-iterative approach and requires no knowledge of the coil sensitivity maps. The k-space data from each channel is gridded and Fourier transformed independently (using a NUFFT) to form an image. The images from each coil were then combined using the root sum-of-squares to form the final image. This process is repeated for every frame of the rtMRI data.

- CG-SENSE: this reconstruction algorithm was shown previously in Section 3.3. In brief, the sparsity term shown in eq.(4.8) is removed, leaving the data fidelity term. The resulting optimisation problem is then solved using the conjugate-gradient method. This algorithm was selected as it is a widely used iterative reconstruction algorithm and is commonly used as a benchmark to analyse the performance of new reconstruction approaches [150, 43]. The CG-SENSE algorithm was run for 8 iterations. This value was determined empirically based upon visual inspection of images at different iterations.

When SMS acquisition is used, the coil-by-coil gridding approach can no longer be used as coil sensitivity profiles are required to separate the simultaneously excited slices. Thus, only the CG-SENSE algorithm, with 15 iterations, is used as a comparison.

The algorithms are compared in terms of reconstruction quality and reconstruction speed in Chapter 5.

4.5 Preprocessing

4.5.1 Coil Compression

The use of multiple receiver coils is critical to parallel imaging-based reconstruction techniques. The data from each coil requires separate Fourier transforms, which increases the overall reconstruction time. This is particularly problematic when iterative reconstruction is used with non-Cartesian sampling, as it requires multiple NUFFT operations, which are computationally expensive. To reduce the computational burden, compression algorithms have been developed to reduce the set of N_C coils to a smaller set of N_{VC} "virtual" coils. This compression is purely software based and requires no adaptation to the physical receiver coils used to record the signal.

In this thesis, a compression method based upon Sigular Value Decompositon (SVD) is used [151]. The compression algorithm requires a set of calibration data; in this work, the full set of recorded spokes is used (i.e. the data before it is binned into frames). The calibration data from each of the N_c coils contain N_s samples. This is arranged into a $N_s \times N_c$ matrix $\mathbf{\Phi_{comp}}$, this can either be done in the image or k-space domains. This work keeps the data in the k-space to avoid applying additional NUFFT operations. SVD is then used to decompose Φ into a set of three matrices (eq.(4.20)) [88]. These three matrices are: the left singular values $\mathbf{U} \in \mathbb{C}^{N_s \times N_s}$, singular values $\mathbf{\Sigma} \in \mathbb{C}^{N_s \times N_c}$ and the right singular values $\mathbf{V} \in \mathbb{C}^{N_c \times N_c}$.

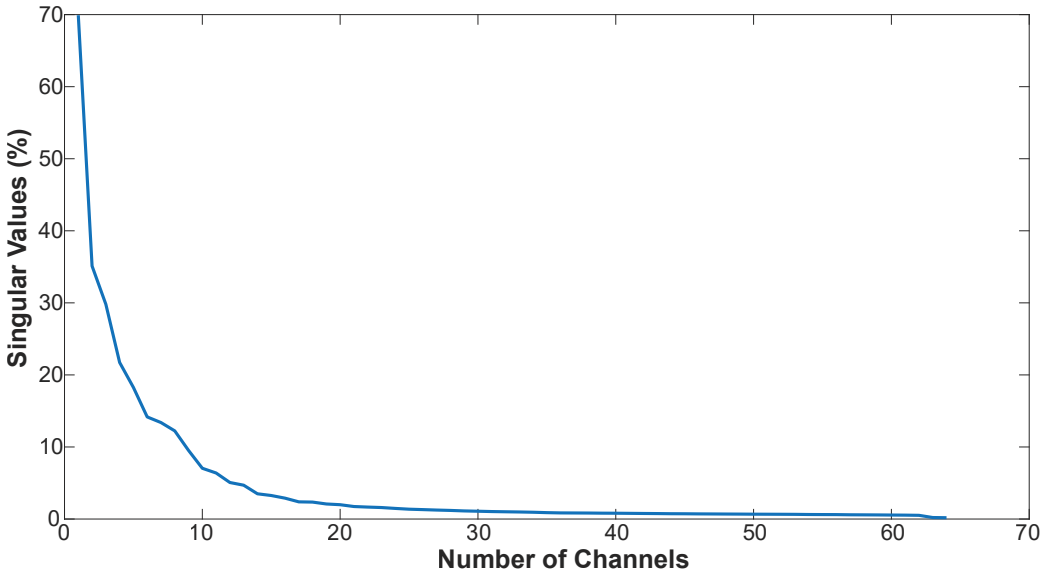

Figure 4.8: Plot showing the rapid drop of the magnitude of singular values using data obtained from a 64 channel head coil.

$$\mathbf{\Phi_{comp}} = \mathbf{U\Sigma V^H} \tag{4.20}$$

Fig.4.8 shows that the magnitude of the singular values decreases rapidly. For example, using the data shown in Fig.4.8, to retain 90% of the total singular value magnitude, only approximately 10 singular values need to be retained. Using this information, a calibration matrix id designed such that the resulting compressed signal retains a fixed percentage of the total magnitude of singular values.

To construct the calibration matrix, the right singular values $\mathbf{V^H}$ are used. These represent the eigenvectors of the covariance matrix, $\mathbf{\Phi_{comp}^H \Phi_{comp}}$. The compression matrix, $\mathbf{\Gamma}$, is formed by retaining the first N_{VC} right singular values, resulting in a matrix of dimensions $N_{VC} \times N_C$. This matrix can then be applied to the recorded multi-channel data $\mathbf{y} \in \mathbb{C}^{N_C \times N_s}$ through

multiplication (eq.(4.21)), yielding the compressed data $\mathbf{y_{comp}} \in \mathbb{C}^{N_{VC} \times N_s}$.

$$\mathbf{y_{comp}} = \mathbf{\Gamma y} \tag{4.21}$$

A discussion of the effect of coil compression on image quality and reconstruction time is shown in Section 5.2.4.

4.5.2 Coil Sensitivity Estimation

Both the reconstruction models shown in Section 4.4 and the CG-SENSE algorithm requires the coil sensitivity profiles of each receiver coil (or virtual coil). To estimate the coil sensitivity profiles, all of the recorded k-space data is used (rather than a single individual frame). A widely used approach, proposed by Uecker et al. (2014), called ESPIRIT is used to estimate the profiles [152]. In brief, ESPIRIT forms a calibration matrix from a central region of the multichannel k-space. It can be shown that the eigenvectors corresponding to the eigenvalues = 1 are the coil sensitivity profiles. ESPIRIT cannot be directly applied to non-Cartesian data. To resolve this, the central data (1/3 of the data) from the radial k-space is transformed to the image domain (using a NUFFT). This yields a low resolution image for each coil. These low resolution images are then transformed back to the Cartesian k-space domain using a standard FFT. The central region (of size 24×24) of this k-space is then extracted and used for the ESPIRIT coil sensitivity estimation.

When multiband acquisition is used, the coil sensitivity estimation step is slightly adapted. First, the k-space data from each slice must be separated from the simultaneously acquired k-space. This is achieved through multi-

plying the measured k-space by the complex conjugate of the CAIPIRINHA phase cycling profiles. Once the k-space for each slice is obtained, the coil sensitivity estimation method described previously is used.

4.6 Post-processing

Radial undersampling results in increased levels of noise. This problem is exacerbated when CAIPI based SMS is used due to the introduction of destructive interference. To reduce residual noise post reconstruction, following the approach demonstrated by Uecker et al., a temporal median filter is applied to every frame [6]. The filter calculates the mean value of a pixel over a series of frames, the width of the filter determines how many frames are used. The effect of median filter window size is discussed in Section 5.4.

In theory a median filter could be replaced by increasing the level of regularization. However, in practice the median filter is more effective. This could be due to the non-Gaussian nature of the streaking/aliasing being more amenable to removal through median filtered than through temporal finite difference regularization (which typically assumes Gaussian noise). Work by Ahmad et al. has shown that median filtering can be used as a regularizer in ADMM, this approach could be explored in the future to remove the need for this post-processing step [153].

4.7 Reconstruction Pipelines

The post-processing, reconstruction and post-processing steps are joined to form the reconstruction pipeline used in this thesis. The pipeline for single-

slice reconstruction is shown in Fig.4.9 and the pipeline for SMS rtMRI reconstruction (for the case of three simultaneously excited slices) is shown in Fig.4.10.

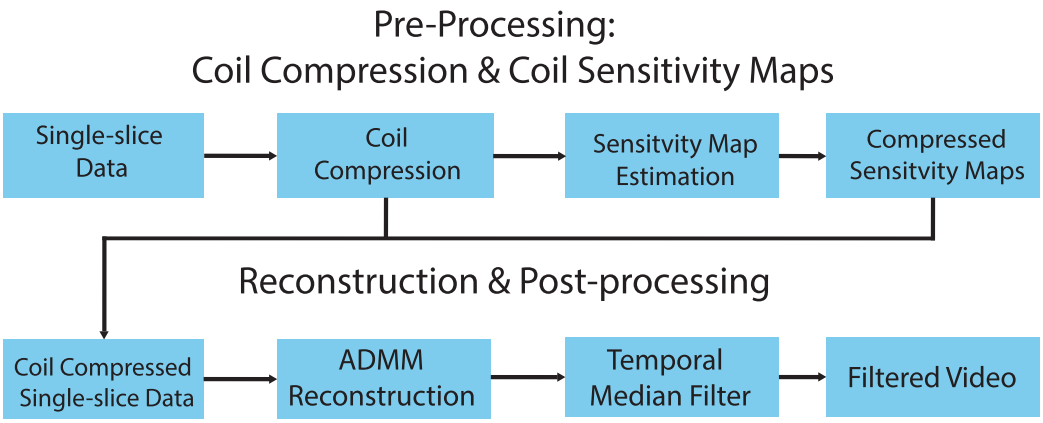

Figure 4.9: Reconstruction pipeline for single-slice rtMRI data. The pre-processing stage compresses the data and estimates the coil sensitvity profiles. This compressed data is then reconstructed using the ADMM reconstruction algorithm. After which it is filtered using a temporal median filter.

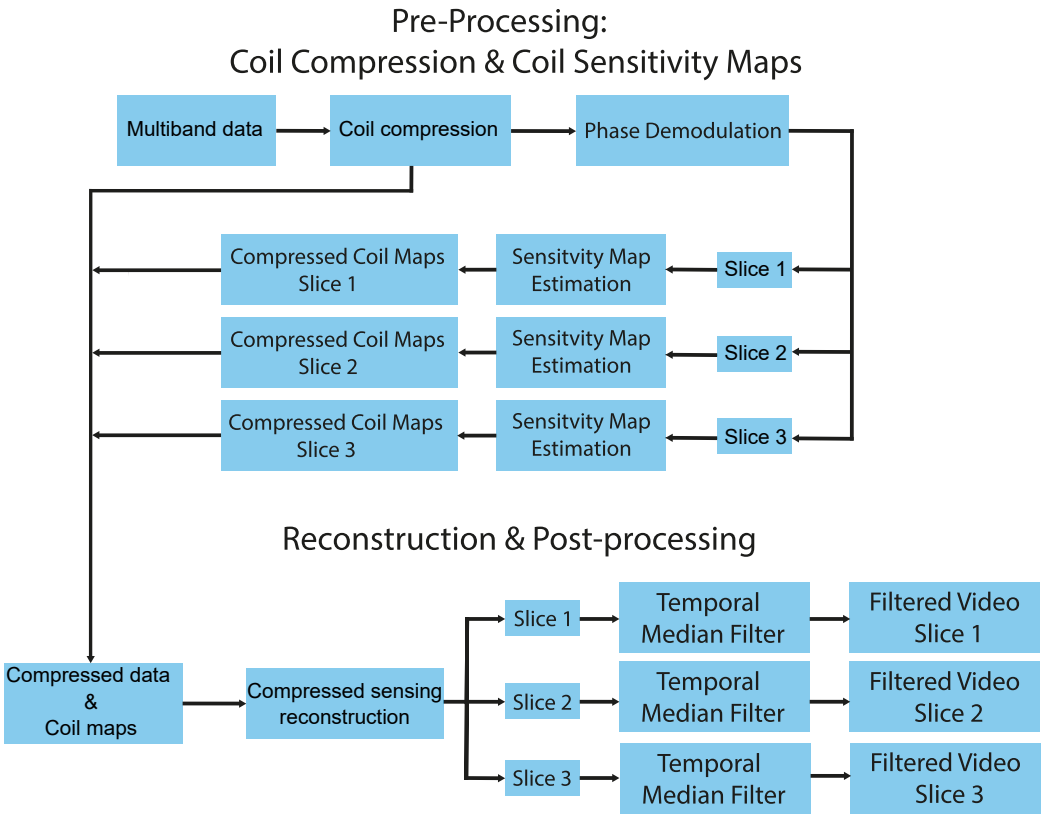

Figure 4.10: Reconstruction pipeline of SMS rtMRI data. The pre-processing stage compresses the data and estimates the coil sensitivity profiles for each slice. This compressed data is then reconstructed using the ADMM reconstruction algorithm, this produces an rtMRI video for each slice. These videos are then filtered using a temporal median filter.

4.8 Sliding Window Viewsharing

Viewsharing is a technique to improve apparent temporal resolution in dynamic MRI. In this technique, rather than binning the k-space into completely separate groups, a sliding window is used to combine the k-space spokes into frames (Fig.4.11). This allows for the sharing of spokes between frames. The stride of the window denotes how many spokes the sliding window moves between frames. The maximum value of the stride is equal to the number of spokes per frame. This prevents spokes from not being used in

the reconstruction.

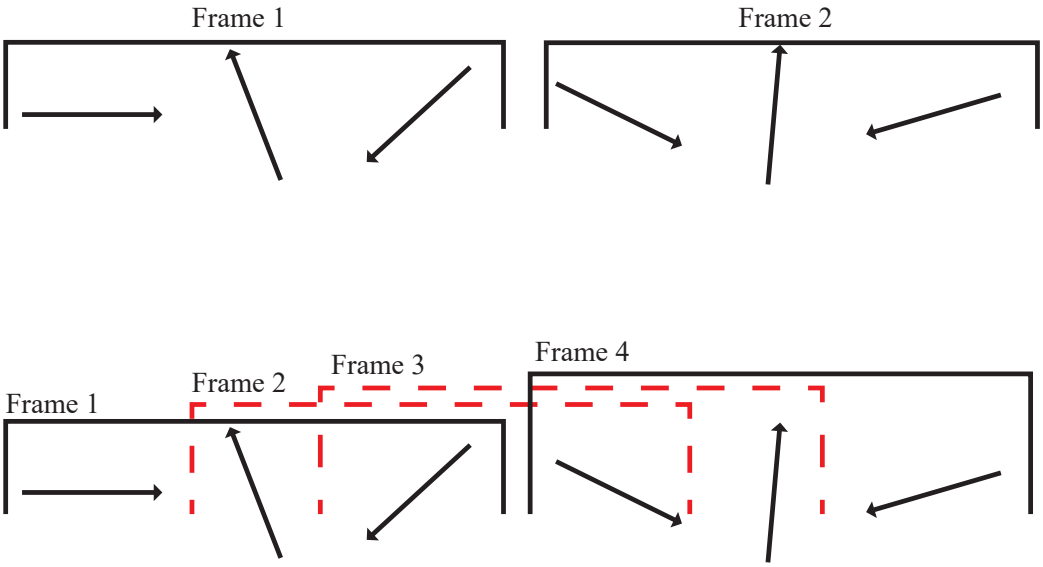

Figure 4.11: Example of sliding window viewsharing using 6 spokes and 3 spokes per frame. When no viewsharing is used (i.e. a stride of 3) this results in 2 frames with no spokes shared between frames. If a stride of 1 is used, then 4 frames will be reconstructed. The red dotted lines indicate the extra frames generated through the use of the sliding window.

The sliding window does not create any additional information or remove motion artefacts; it can be viewed as a form of temporal interpolation, which results in videos with smoother movements. A disadvantage of viewsharing is the substantial increase in overall reconstruction time. This is due to the large number of frames that need to be reconstructed.

4.9 Summary

In this chapter, a radial real-time MRI GRE sequence capable of both single-slice and SMS acquisition has been developed. This sequence was developed as there was no openly available radial pulse sequence code to use. The data

recorded using this sequence is then inputted into the appropriate (single-slice or SMS) CS reconstruction pipeline. The results for using this sequence are presented in the next chapter.

5 Evaluation of Compressed Sensing Real-time MRI

5.1 Introduction

This chapter evaluates the rtMRI sequence and reconstruction pipeline developed in Chapter 4. First, results for single-slice rtMRI are shown. Videos are reconstructed at a variety of temporal resolutions, levels of regularization and levels of coil compression. The results are evaluated in terms of image quality, temporal resolution and computation time. This process is repeated for SMS accelerated rtMRI using both sampling schemes discussed in the previous chapter. Next, the performance of the post-processing temporal median filter is evaluated. This chapter concludes with a discussion on why the quantification of image quality in rtMRI (and in dynamic MRI more generally) is a challenging problem.

5.2 Singleband Real-time MRI

5.2.1 Methods

The experimental data used in this section was obtained (using the head coil discussed in Chapter 2) from a volunteer performing a simple tongue

mobility test in which they extend and retract their tongue. This task is chosen for two reasons. The first is that it involves both large scale motion within the confines of a standard MR head coil, such as the mouth opening, and small scale motion such as the tip of the tongue moving. Secondly, this task demonstrates a useful future clinical application of rtMRI for assessing tongue mobility and movements.

Real-time MRI data is recorded for 15s using the sequence parameters described in Section 4.3, this results in a total of 6000 spokes. These were then binned to the desired temporal resolution. To reduce the computation time, the data from the 64 coils is compressed to 15 virtual coils using the coil compression method described in Section 4.5.1 (the effect of the coil compression on image quality and reconstruction time will be discussed in Section 5.2.4).

5.2.2 Parameter Selection

The ADMM reconstruction algorithm requires the selection of the regularization value, λ. This parameter was found using a search approach. The data used for this search is the previously described rtMRI dataset of tongue movement binned to an undesampling level of 25 spokes/frame. This level of undersampling was chosen as it results in a temporal resolution 62.5ms which is adequate for most applications in head/neck imaging [7, 154].

Initially, a coarse search (Fig.5.1) was performed on a scale ranging from 1×10^{-4} to 1×10^{-1} with values increasing in logarithmic steps. At λ values between 1×10^{-4} and 1×10^{-3} there is relatively little difference between the images. For values between 1×10^{-3} and 1×10^{-2} an improvement in image

quality, in terms of noise reduction, can be seen. However, when λ reaches 1×10^{-1}, the resulting images are over-smoothed, eliminating most of the contrast, indicating that the regularization value is too high.

Fig.5.2 shows the effect of regularization on an intensity profile. Between $\lambda = 1 \times 10^{-4}$ and $\lambda = 1 \times 10^{-3}$ there is little difference between the profiles. The transition between tissue edges is sharp, this is seen in the transition into the ventricles (denoted by the red lines). However, inside the ventricular space, variations in signal intensity, which may be a result of random noise, are visible. At $\lambda = 1 \times 10^{-2}$ the edge transition remains sharp and the intensity profile through the ventricle shows less variations. Further increasing the regularization to 1×10^{-1} results in an extremely smooth signal inside the ventricle, however, as can be seen in both the image and the profile, the transitions are no longer sharp, showing that contrast between tissues has been reduced and the edges of the image are blurred.

Based upon visual inspection of these results, it appears that the optimum parameter, in terms of producing the best image contrast and edge sharpness, for this application is between 1×10^{-3} and 1×10^{-2}. The λ search is then performed on a more refined scale between 1×10^{-3} and 1×10^{-2} in steps of 0.001. Fig.5.3 shows the results from this fine search. It can be seen that past $\lambda = 5 \times 10^{-3}$ there is little visible difference in image quality. Based upon this search, a $\lambda = 5 \times 10^{-3}$ is selected as it provides noise reduction while preserving contrast between different tissues. Unless stated otherwise, this λ value is used throughout this section.

The λ search approach described above is inefficient due to the large number of images required to be reconstructed, a more efficient approach

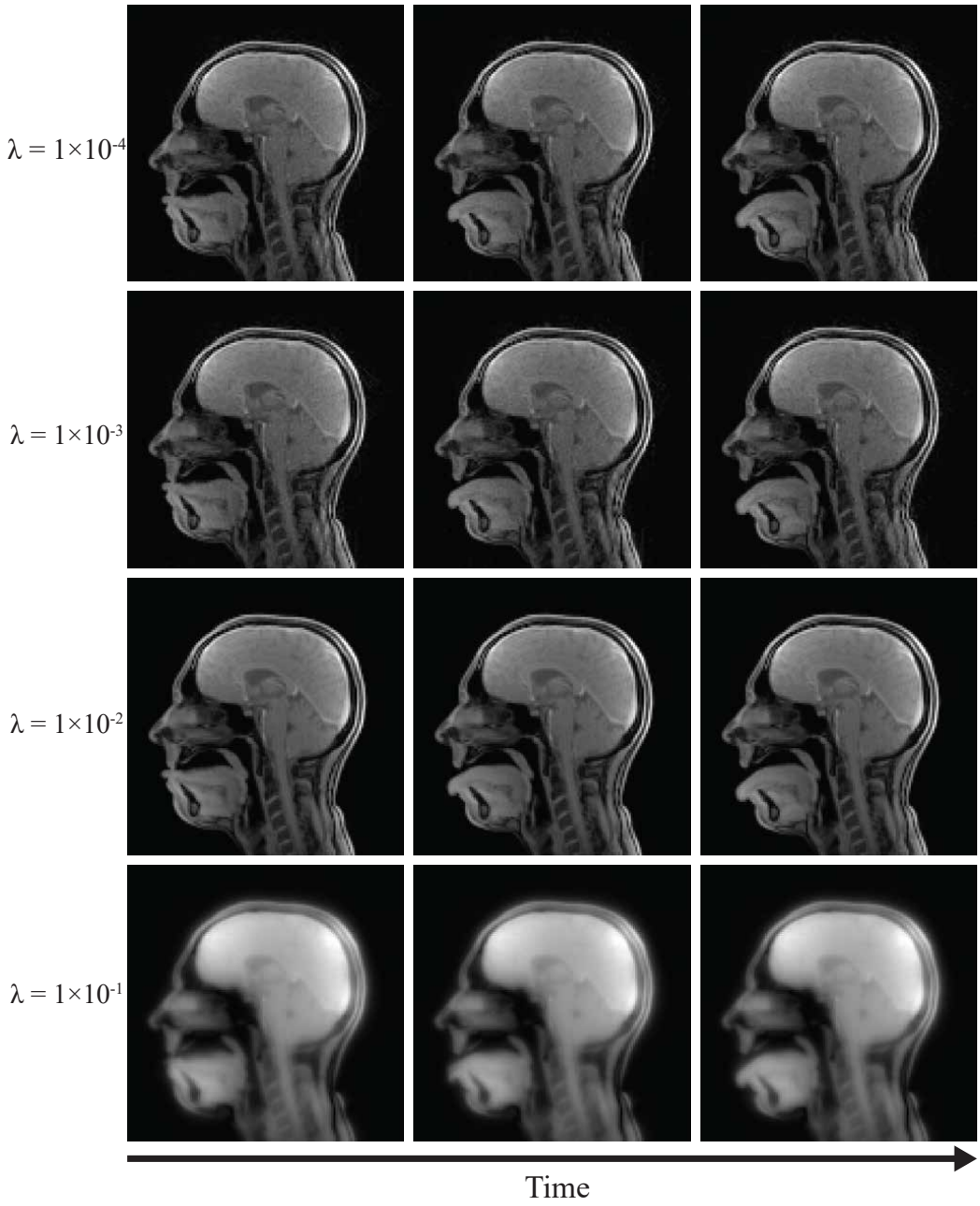

Figure 5.1: Results (three frames 1s apart) from the coarse λ search. From this coarse search it can be seen that the optimum λ value lies between the range of $\lambda = 1 \times 10^{-3}$ and $\lambda = 1 \times 10^{-2}$.

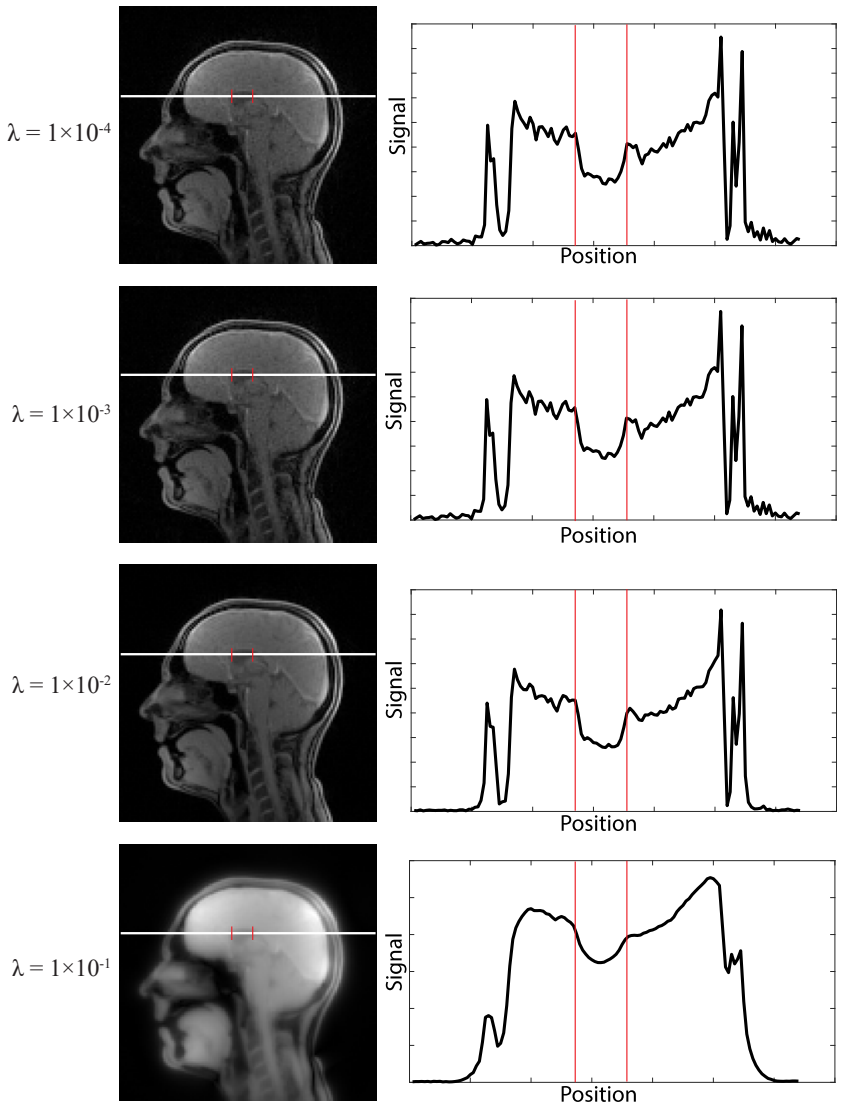

Figure 5.2: A rtMRI frame (left) and a profile through the frame (right) at increasing levels of regularization. The white line indicates the position of the profile and the red lines indicate the approximate position of the ventricles.

would be a binary search based method, but the brute force approach used in this thesis effectively demonstrates the substantial effect of varying λ.

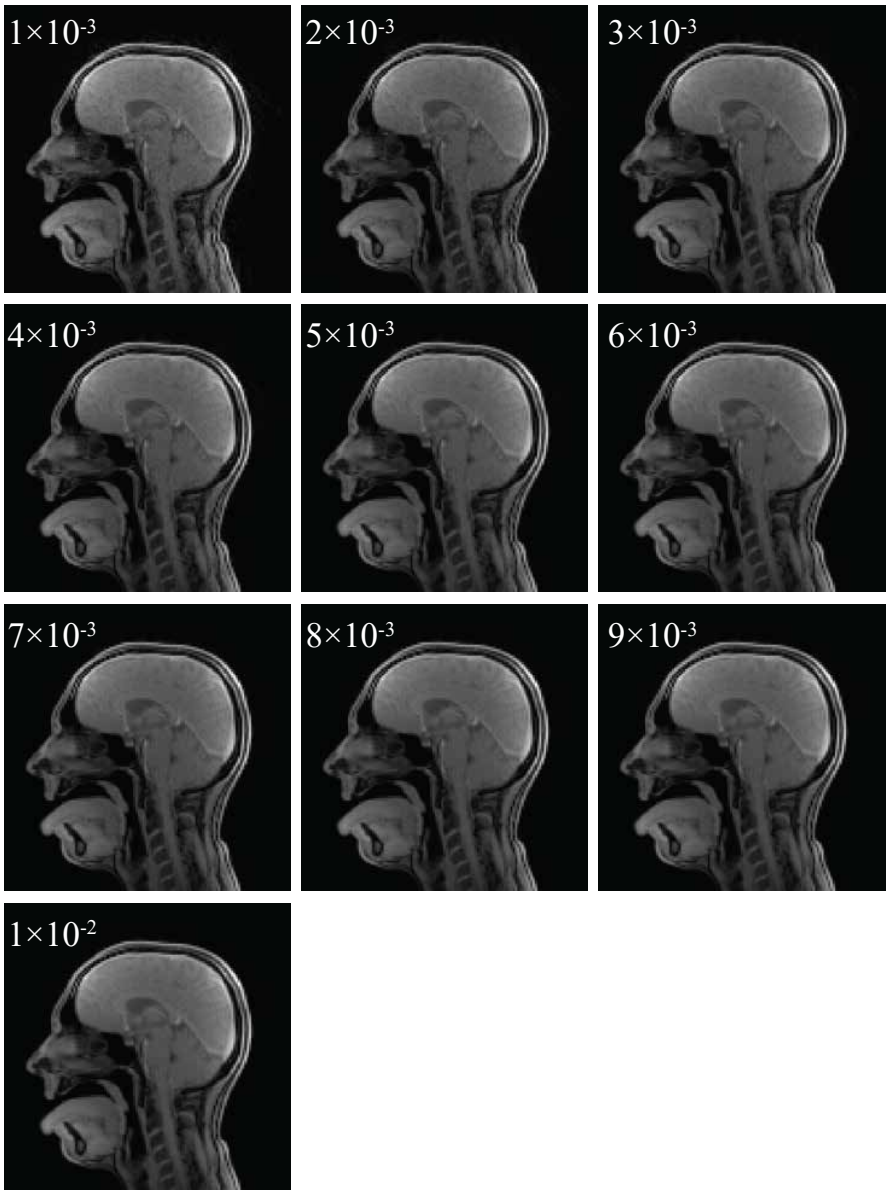

Figure 5.3: Results taken from the fine λ search showing the same frame reconstructed with λ values ranging from 1×10^{-3} to 1×10^{-2} in steps of 1×10^{-3}. From these results a value of $\lambda = 5 \times 10^{-3}$ is chosen.

The required number of iterations for the ADMM algorithm is determined

by performing reconstruction using a high number of iterations (100) and saving the result after each iteration. This is done for three levels of undersampling (45, 25 and 10 spokes/frame). The convergence of the ADMM algorithm is quantified using the approach described by Le et al (2017) [155]. This approach calculates the normalized root-mean-squared distance (NRMSD, eq.(5.1)) between the final solution, $\mathbf{x}^{100}$, and the solution at the current iteration, $\mathbf{x}^{it}$.

$$\text{NRMSD} = \frac{\|\mathbf{x}^{it} - \mathbf{x}^{100}\|_2^2}{\|\mathbf{x}^{100}\|_2^2} \tag{5.1}$$

Fig.5.5 shows a convergence plot for a variety of undersampling levels. The NRMSD rapidly drops for the first 10 iterations before leveling off. From a visual perspective (Fig.5.5) a clear improvement in image quality can be seen between iterations 1 and 10 with more fine detail becoming clearer. Changes in image quality between 10 iterations and 25 iterations are more subtle. After this there is little visible change as the number of iterations is increased. Fig.5.6 shows the difference images between iterations, it can be seen that the areas with the largest changes are the edges in the image and the background of the images. Based upon the visual results and the quantitative results, the number of iterations used is set to 25. The number of iterations is important as it affects not just the reconstruction quality but also the reconstruction time. Using 100 iterations (for 25 spokes/frame) takes approximately 2.5 hours to reconstruct (the entire rtMRI video) while 25 iterations require 40 minutes. If a faster reconstruction time is required and some image quality can be sacrificed, fewer iterations could be used.

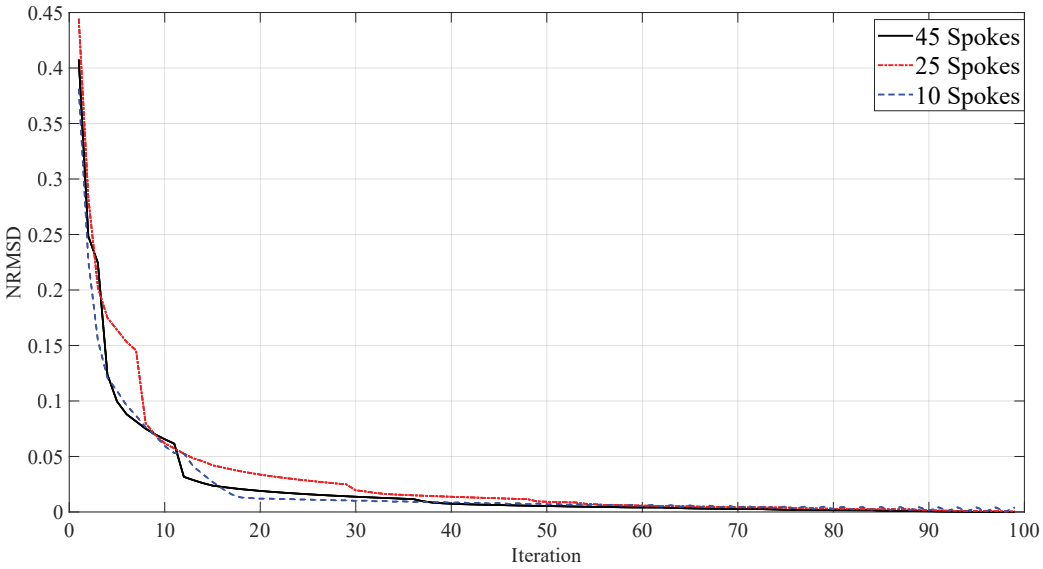

Figure 5.4: Plot of convergence, measured using NRMSD, at a range of undersampling factors. For all undersampling factors a steep initial drop in NRMSD is seen before the slope levels off.

5.2.3 Undersampling Experiment

The temporal resolution of an rtMRI scan is defined as the product of the number of spokes per frame and TR. Therefore, for a fixed TR the only way to increase temporal resolution is to reconstruct a frame from fewer spokes. However, higher levels of undersampling may result in reduced image quality in the form of blurring, increased noise and structural artefacts.

To ascertain the effect of undersampling on image quality, the rtMRI data is binned to increasingly lower numbers of spokes/frame. The number of spokes is lowered from 95 to 10 in steps of 5. The images are reconstructed using the proposed ADMM algorithm and the two reference methods discussed in Section 4.4. Fig.5.7 shows three frames acquired at the increasing levels of undersampling (Video 5.1 shows the full rtMRI videos). At low levels of undersampling all three methods produce similar image quality. When

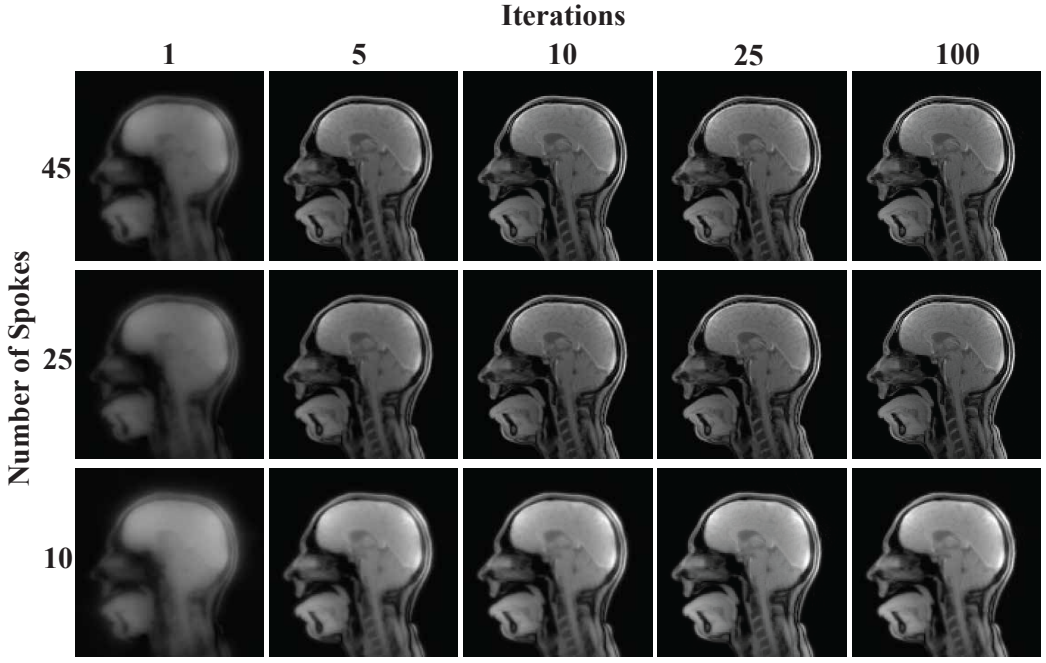

Figure 5.5: Visual comparison of reconstructed images (at a range of undersampling levels), at different iterations of the proposed reconstruction algorithm. A clear improvement in image quality can be seen between iterations $1-10$. The improvements in image quality are subtle between iterations 10 and 25. Very little difference can be seen between iteration 25 and iteration 100. Differences in image contrast are due to the images being normalized to the same intensity scale.

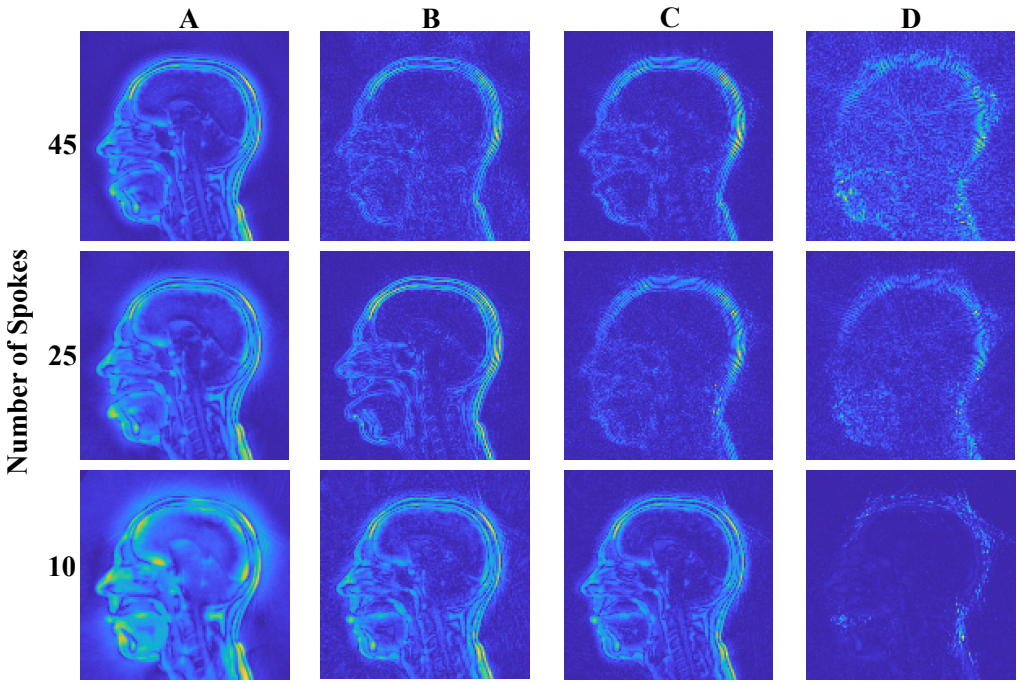

Figure 5.6: Difference images, at different levels of undersampling, between A: 1 and 5 iterations, B: 10 and 5 iterations, C: 25 and 10 iterarations and D: 100 and 25 iterations.

a moderate level of undersampling (45 spokes/frame) is used, the images reconstructed using CS and CG-SENSE are visually similar. In contrast, the images reconstructed using gridding appear to have increased levels of noise. For 20 and 15 spokes/frame, the proposed reconstruction method yields significantly improved image quality compared to the reference methods. When 10 spokes/frame is used the proposed method does show blurring and the contrast between tissues is reduced. However, the image quality is still higher than the reference methods.

A high level of undersampling is required to reach high temporal resolutions. To visualise the effect of undersampling on temporal fidelity, a line of pixels across the lower lip is extracted for each time frame and plotted (this is referred to as an x-t plot). This is performed for 75 spokes/frame (temporal resolution 187ms) and for 15 spokes/frame (temporal resolution 37.5ms). At the higher temporal resolution (Fig.**??**) the x-t plot has a smoother appearance compared to the lower temporal resolution (Fig.5.8). This allows for rapid motion to be viewed, for example, the tip of the tongue moving, which may be blurred if lower temporal resolutions are used. This is demonstrated in Fig.5.9, which compares a frame from an rtMRI video reconstructed with 75 spokes/frame against the equivalent timepoint reconstructed with 15 spokes/frame. The lower temporal resolution image shows blurring in the lower lip, tongue and chin. A profile through both images shows that when 15 spokes/frame are used, the transition between the air/tongue boundary is clearer. In this example, the temporal median filter has not been applied; this was done to emphasise that the motion artefact is due to the lower temporal resolution rather than being caused by the post-processing

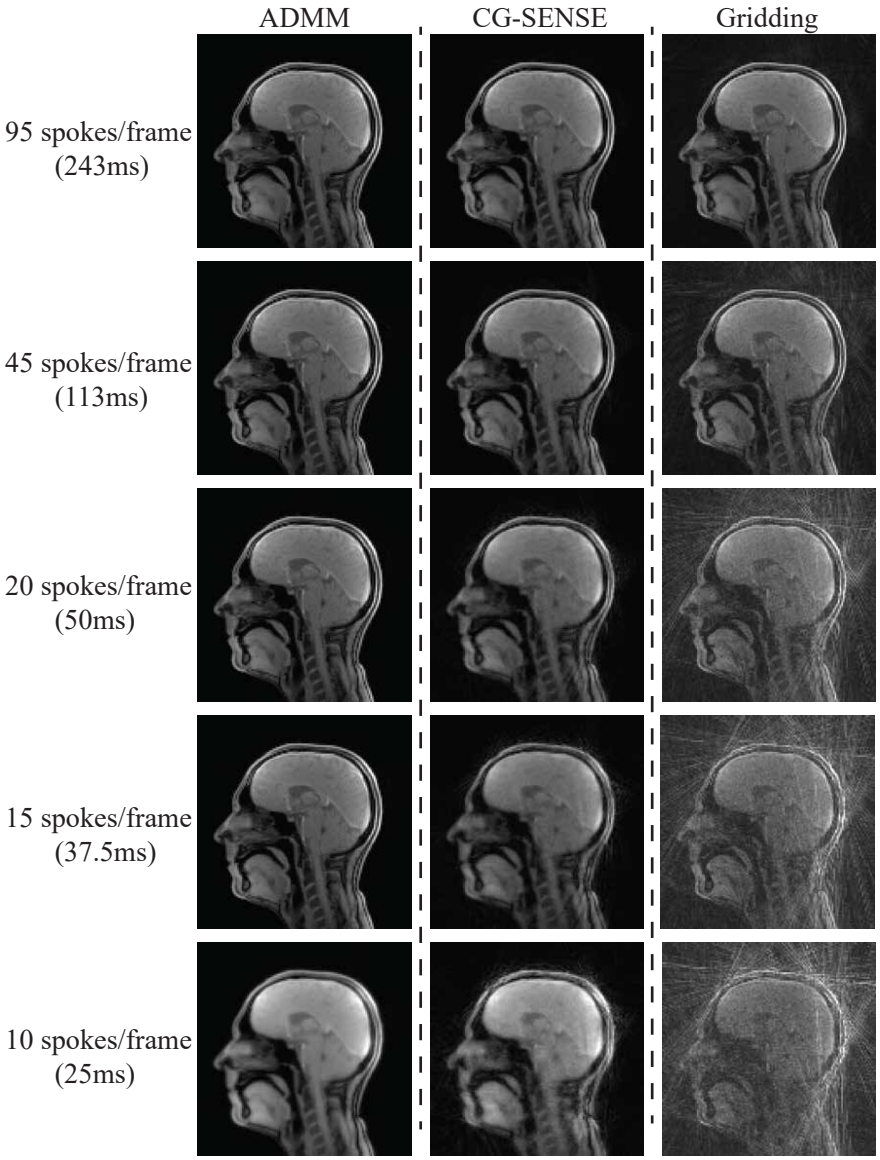

Figure 5.7: A comparison of three reconstruction algorithms (ADMM, CG-SENSE and coil-by-coil gridding) at a range of undersampling levels (from top to bottom 95 45, 20 15 and 10 spokes/frame). The ADMM algorithm results in higher image quality at all levels of undersampling. However, at the highest level of undersampling the resulting image appears blurry and lacking contrast.

step.

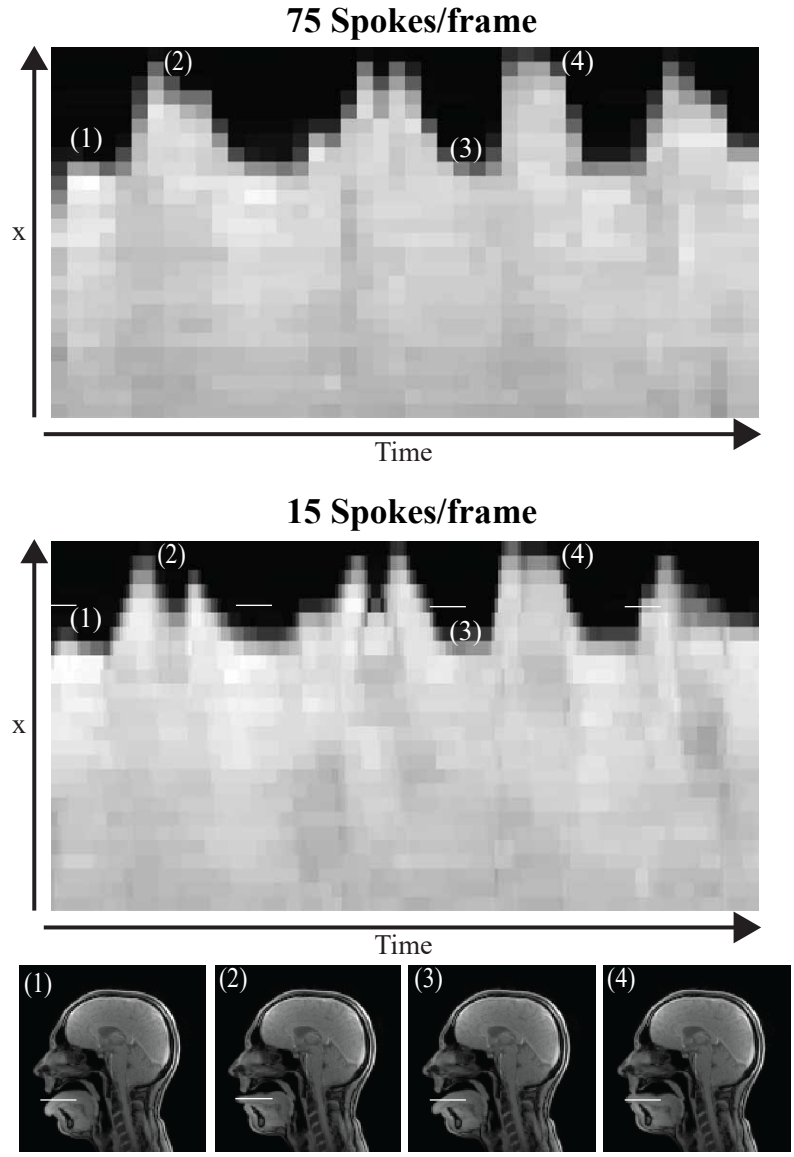

Figure 5.8: Top: x-t plot of rtMRI data binned to 75 spokes/frame (temporal resolution of 187ms. Middle: the x-t plot of the same rtMRI data now binned to 15 spokes per frame. The numbers on the plot correspond to the images shown at the bottom of the figure. The white marker on the images shows the line of pixels used to form the x-t plot.

The maximum temporal resolution (without sliding window viewsharing) achieved, without significant degradation in image quality, is 37.5ms (15

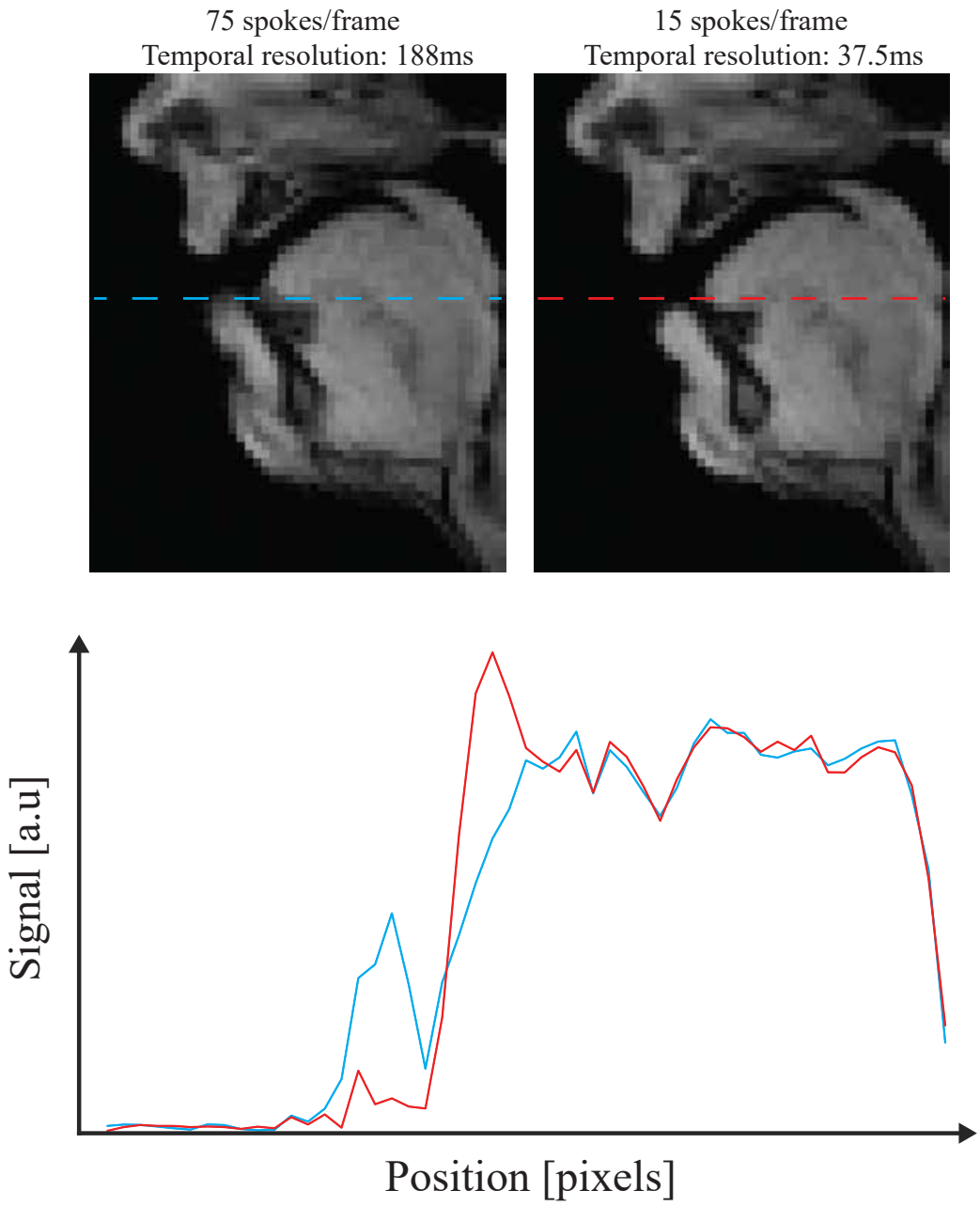

Figure 5.9: Comparison of two frames (at the equivalent time point) acquired using 75 spokes/frame (top left) and 15 spokes/frame (top right). When a higher number of spokes is used (i.e lower temporal resolution) blurring around the chin, lower lip and tongue is seen. The coloured lines through the frames form a line plot (bottom). It can be seen that the 15 spokes/frame line plot (red) shows a steeper rise in intensity compared to 75 spokes/frame plot (blue), this is due to the reduced blurring around the tongue.

spokes/frame) at an in-plane spatial resolution of 2.2mm^2. This temporal resolution is sufficient, following guidelines of rtMRI speech imaging proposed by Lingala et al. (2016), to image the fastest articulating movements which occur during speech [7]. The performance of this approach (in terms of temporal resolution) is slightly inferior to the 33ms temporal resolution reported by Niebergall et al. (2013), which used a radial GRE sequence to study speech [156]. However, in this thesis a standard clinical head/neck coil is used rather than a custom upper-airway coil which would provide more signal in the desired area of interest.

5.2.4 Coil Compression Results

As discussed in Section 4.5.1, coil compression is used to accelerate reconstruction time by compressing the data acquired from all coils into a reduced set of virtual coils. To measure the effect of coil compression on image quality, the number of virtual coils is varied from 63 to 2. Real-time MRI videos (25 spokes/frame) are then reconstructed using the ADMM algorithm. These are then compared to a reconstruction using the uncompressed data from all 64 coils.

Fig.5.10 shows examples of the effect of coil compression on image quality (Video 5.2). From this figure, it can be seen that only high levels of compression result in substantial changes to image quality. The reduction in image quality appears in the form of signal dropout.

The image quality, compared to using all 64 coils, is measured using two metrics. The first is the root mean-square error (RMSE), defined in eq.(5.2), where x_j is the value of the image at pixel j when coil compression is used

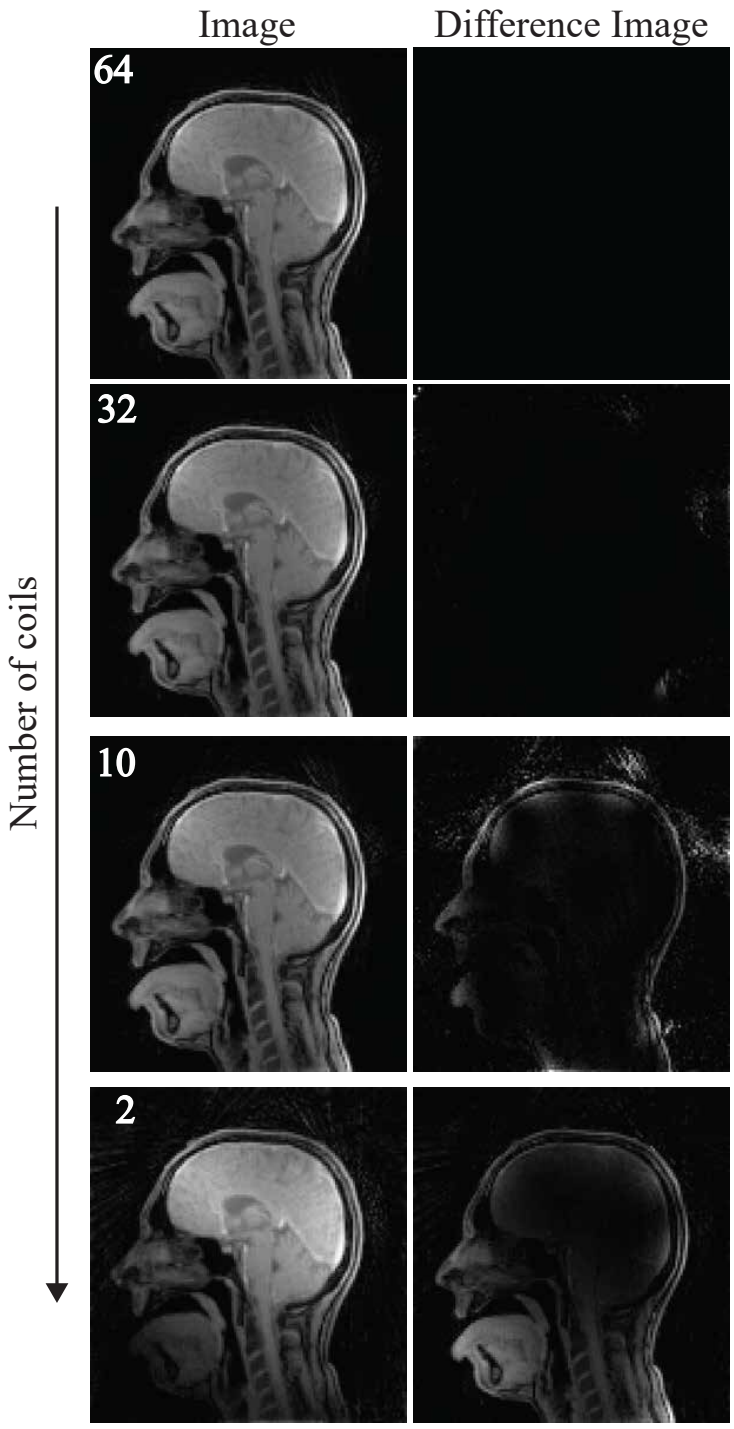

Figure 5.10: The effect of varying levels of coil compression on image quality. The top image is reconstructed using the data from all 64 coils. The compression level is then increased, with the number in the top left corner indicating the number of virtual coils used. The left images are a frame reconstructed from the compressed data and the right images are the absolute difference between the frame reconstructed using the compressed data and the reference image.

and $\hat{x_j}$ is the value at the same pixel location when no coil compression is used. A lower RMSE indicates that there is only a small difference between the two images (i.e. the coil compression has had minimal effect on the image quality). The second metric used is peak signal-to-noise ratio (PSNR), defined in eq.(5.3), where $\max(\hat{\mathbf{x}})$ is the maximum pixel intensity of the image when no coil compression is used. A higher PSNR value indicates that the compressed data closely matches the uncompressed data.

$$\text{RMSE} = \sqrt{MSE} = \sqrt{\sum_{j=1}^{N} x_j - \hat{x_j}} \tag{5.2}$$

$$\text{PSNR} = \frac{\max(\hat{\mathbf{x}})^2}{\text{MSE}} \tag{5.3}$$

Fig.5.11 and Fig.5.12 show plots of the RMSE and PSNR. Both plots show the degradation in image quality at very high levels of compression. However, in both plots the image quality rapidly improves as the level of compression is lowered. This matches the visual results shown in Fig.5.10.

The effect on image reconstruction time is shown in Fig.5.13. This plot highlights a disadvantage of the proposed reconstruction method, its long reconstruction time. For example, at the proposed level of 15 virtual coils the ADMM reconstruction time is 1031s substantially longer than the CG-SENSE reconstruction time of 61s and the gridding reconstruction time of 2s. The per coil reconstruction time for all three reconstruction methods is estimated through performing a linear fit to the measured data and calculating the gradient. This value for the proposed CS reconstruction algorithm is 42.5s; this is 15 times higher than CG-SENSE (2.8s) and 436 times higher

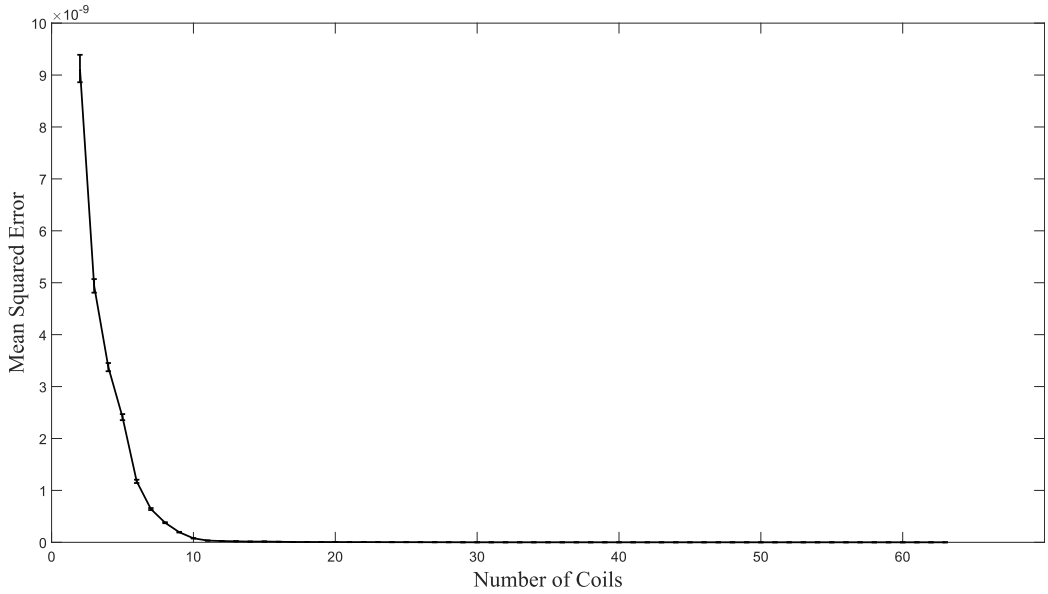

Figure 5.11: Plot of RMSE at varying levels of coil compression (2-63 coils).The error bars represent the standard deviation of RMSE across the entire time series of frames. From the plot it can be seen that RMSE drops rapidly, this indicates that a high level of compression can be used with minimal difference between compressed and uncompressed images.

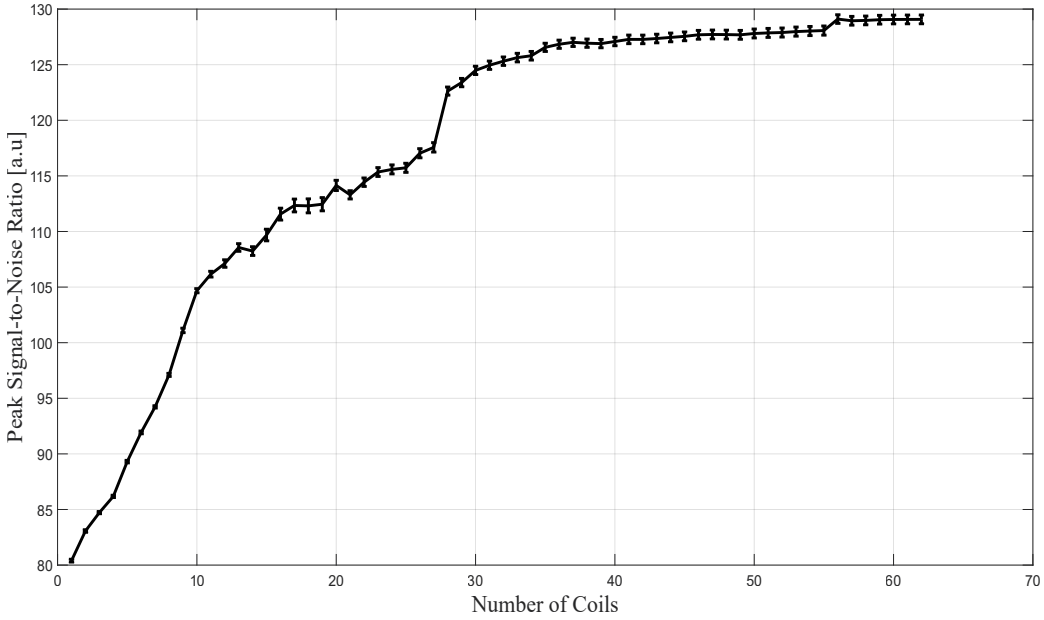

Figure 5.12: Plot of PSNR at different levels of coil compression ($2 - 63$ coils). The error bars represent the standard deviation of PSNR across the entire time series of frames. Using a higher number of coils results in a higher PSNR. However, even at very high levels of compression (10 coils) the PSNR is only 20% lower despite the 85% reduction in the number of coils.

than gridding (0.09s).

These results support the use of the current level of coil compression (15 coils) and suggest that even higher levels of coil compression would be an appropriate way to further reduce the reconstruction time for some applications.

The current reconstruction pipeline uses GPU acceleration for the NUFFT operations solely. To further reduce computation time multiple GPUs in parallel could be used, with data from each coil processed in parallel [110]. This parallelisation scales extremely well as the application of the NUFFT, which is the main computational burden in the reconstruction, can be applied to the data from each coil separately. Additionally, to speed up reconstruction, other parts of the reconstruction could be moved onto the GPU (such as the finite different transforms and coil sensitvity multiplications).

The loss of information being focused around the front of the head is likely related to hardware used for signal reception. Although the used array coil is technically designed to image the head and neck, the majority of receiver elements are located around the top of the head. Thus, the coil compression algorithm may be preserving information from these areas. The current coil compression algorithm does not take into account the desired anatomy of interest (in this case the oral cavity) as prior information. A more sophisticated coil compression algorithm called region-optimized virtual coils (RoVir), presented by Kim et al. in 2021, may provide the solution for this problem as it allows a region of interest to be specified and the signal from that region to be preserved [157].

An alternative to coil compression is manually turning off coil elements

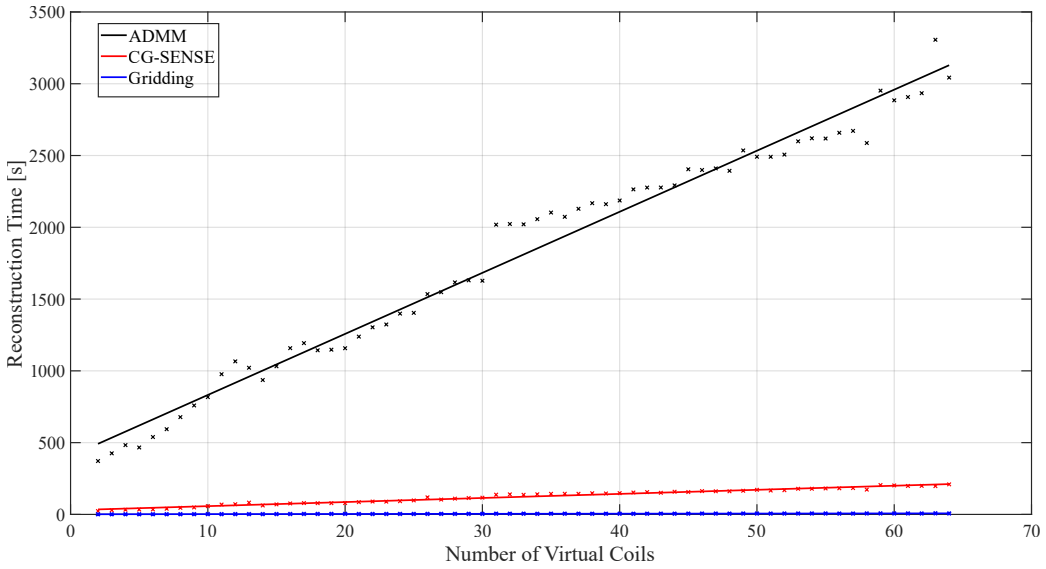

Figure 5.13: Plot of reconstruction time (in seconds) for an entire 15s rtMRI video (25 spokes/frame) at varying number of virtual coils for the three different reconstruction techniques. The ADMM reconstruction (black) is substantially higher than both the CG-SENSE reconstruction (blue) and the gridding reconstruction (red). An undersampling level of 25 spokes/frame is used for data shown in this plot.

before running the scan. This has the equivalent effect of reducing the data size and, therefore, lowering the reconstruction time. However, on Siemens systems, only blocks of coils (typically 8 at a time) can be turned off. This is a reduced level of control compared to coil compression (where any number of coils can be selected). Additionally, manually turning off coils requires knowledge of the coil geometry, this has not been provided by Siemens.

5.2.5 Evaluation

This section of the chapter has shown that the proposed reconstruction pipeline improves image quality of rtMRI images, particularly at very high levels of undersampling, compared to CG-SENSE and gridding. This is important for applications, such as speech, which require high temporal resolutions in order to image the fast movement of articulators. Further improvements in image quality may be obtained through the use of different regularization approaches. For example, by combining the temporal regularization with spatial regularization or by using low-rank regularization (discussed in Section 8.2.2).

The main drawback of the proposed approach, as discussed in Section 5.2.4, is the substantial (15 times higher than CG-SENSE and 436 times higher than gridding) increase in the per coil reconstruction time (compared to the reference methods). This prevents the proposed algorithm from providing near real-time reconstruction on the scanner (which can be achieved when gridding reconstruction is used). An additional limitation of the CS reconstruction is the regularizer is non-causal as it relies on having the time series available, for real-time reconstruction the regularizer would need to be

adapted to only use images that are currently available. Thus, the developed method is currently only relevant in applications where it is acceptable to not have the images available immediately after the acquisition.

5.3 Simultaneous Multislice Real-time MRI

5.3.1 Methods

The experimental data used in this section was obtained from a healthy volunteer performing the tongue mobility test described in the previous section. Using the sequence parameters described in Section 4.3 15s of SMS rtMRI data is recorded resulting in 6000 spokes. An SMS acceleration factor of 3 is used (i.e. 3 slices are acquired simultaneously). Data is acquired using the GA and SMS GA sampling schemes to allow for a comparison to be performed. A slice thickness of 8mm was used and the slice distance varied (an illustration of slice thickness and slice distance is shown in Fig.5.14).

Based upon the results from single-slice rtMRI reconstruction, the SMS k-space data is compressed to a set of 15 virtual coils to accelerate reconstruction.

5.3.2 Parameter Selection

The search approach to select an appropriate λ parameter was repeated. The data used in this search is sampled using the SMS GA sampling scheme and is binned to 25 spokes/frame. The results (for all three slices. 12mm slice distance) from the coarse search (using the same coarse λ range shown previously) are shown in Fig.5.15. A line profile through the central slice was

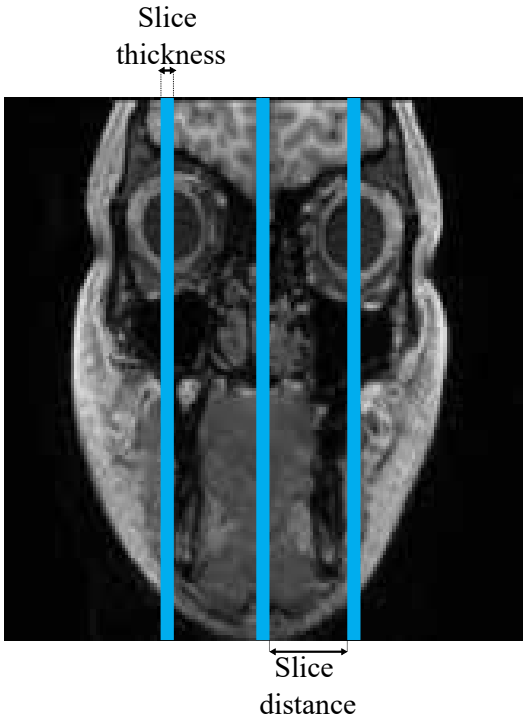

Figure 5.14: An illustration of slice thickness and slice distance.

then used to assist in the evaluation of edge sharpness and noise (Fig.5.16). From these profiles it was decided that $\lambda = 1 \times 10^{-2}$ provides the best balance of edge sharpness and noise reduction.

A fine search was then performed between the range of $\lambda = 1 \times 10^{-2}$ and $\lambda = 1 \times 10^{-1}$ in steps of 1×10^{-2} (Fig.5.17). From these results $\lambda = 4 \times 10^{-2}$ was selected as, from a visual perspective, it best balances noise reduction and blurring. This λ value is higher than the λ used for single-slice rtMRI. This could be due to needing more regularization to remove the additional noise introduced by the CAIPI phase modulation. An additional reason the regularization values may have changed between the single-slice and SMS results is the change in problem scaling due to the increase in the number of slices, and, therefore, an increase in the overall number of voxels in the

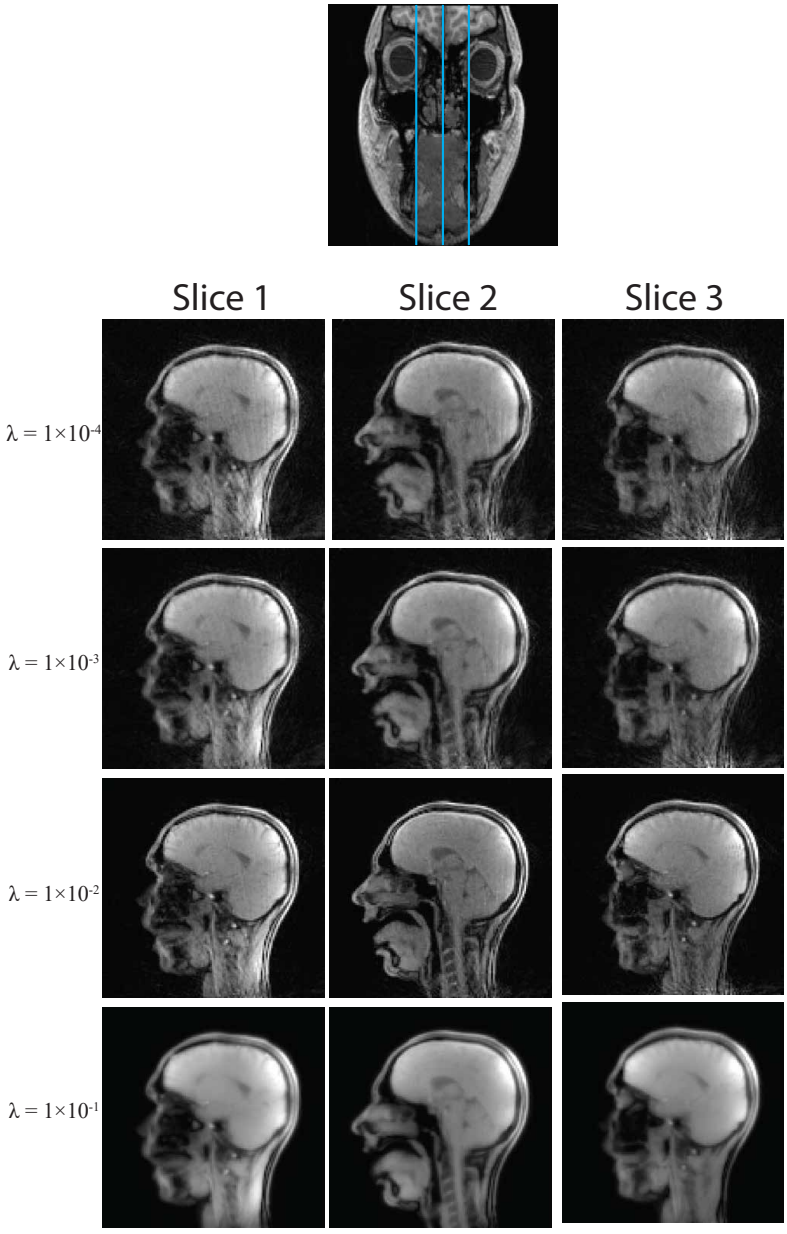

Figure 5.15: Results (showing all 3 slices, 12mm apart, the blue lines through coronal slice at the top of image show the approximate slice locations) from the coarse λ search. From this coarse search it can be seen that the optimum λ value lies between the range of $\lambda = 1 \times 10^{-2}$ and $\lambda = 1 \times 10^{-1}$.

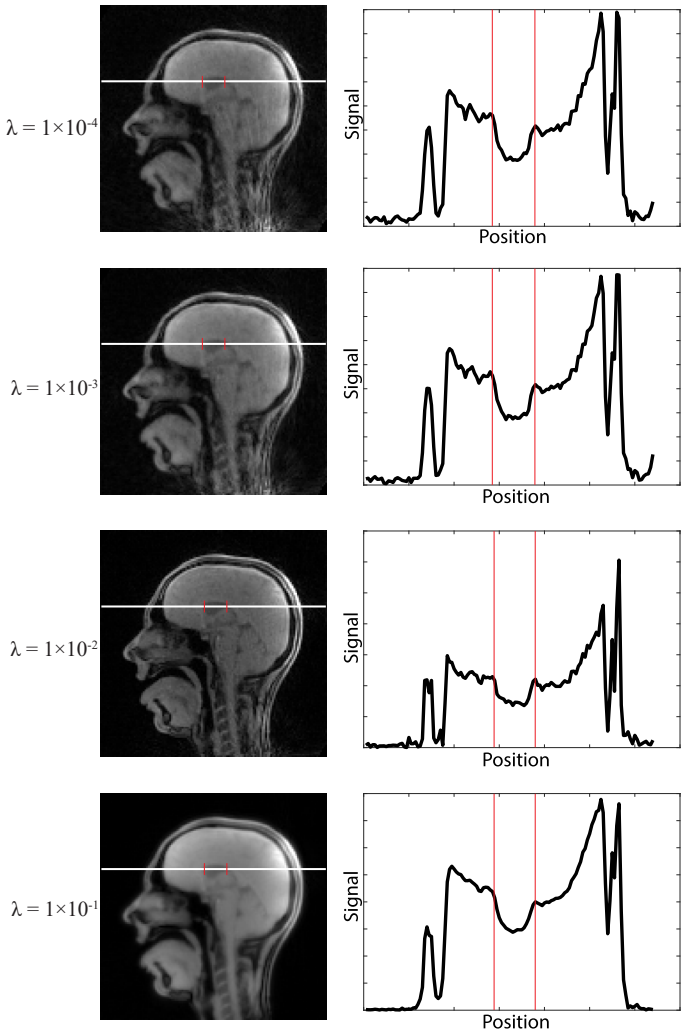

Figure 5.16: A central slice of an SMS rtMRI frame (left) and a profile through the frame (right) at increasing levels of regularization. The white line indicates the position of the profile and the red lines indicate the approximate position of the ventricles.

image. Although not investigated in this thesis, it could be useful to explore normalizing the λ values (for example, by dividing by the number of total voxels) in order to make the regularization parameter more consistent across single-slice and SMS rtMRI.

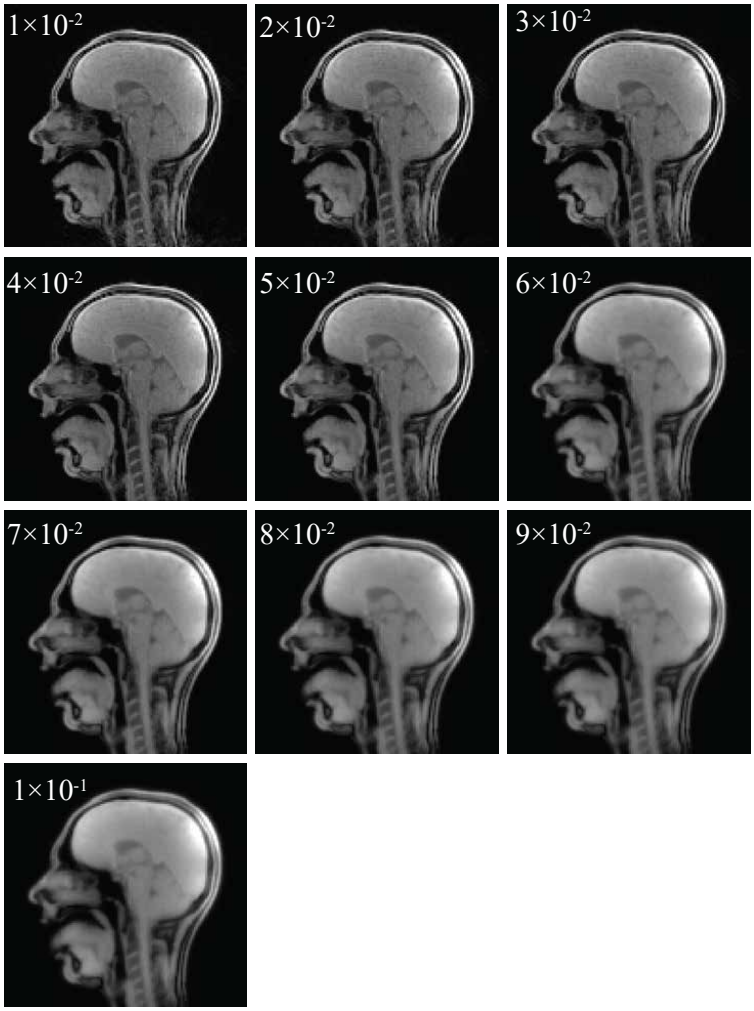

Figure 5.17: Results from a fine λ search (only central slice shown) with λ values increasing from $\lambda = 1 \times 10^{-2}$ to $\lambda = 1 \times 10^{-1}$ in steps of 1×10^{-2}. Past $\lambda = 5 \times 10^{-2}$ blurring is visible.

To determine the number of ADMM iterations that should be used, the convergence experiment shown in Section 5.2.2 is repeated for SMS rtMRI.

Fig.5.18 shows convergence plots at a range of undersampling factors when SMS GA sampling is used. There is a steep initial decline, which then levels off. Examples of image quality (from the central slice) are shown in Fig.5.19 for three different undersampling levels. In all three levels of undersampling, the initial ten iterations result in the most substantial changes in the images. There is little visible difference between iterations 25 and 100.

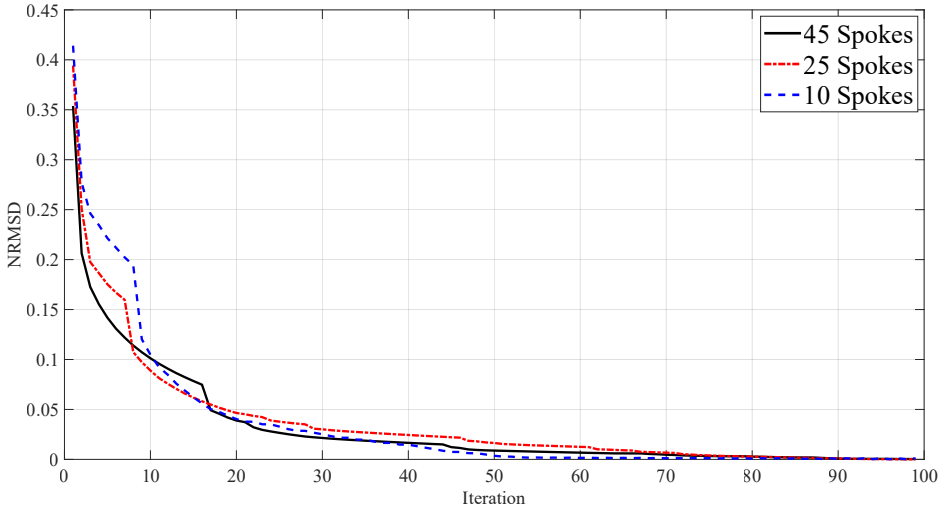

Figure 5.18: Plot of convergence when SMS GA sampling is used (3 slices, 12mm slice distance), measured using NRMSD, at a range of undersampling factors. A steep initial drop in NRMSD is seen before the slope levels off for all undersampling factors.

This convergence experiment is repeated for the GA sampling scheme (Fig.5.21). The convergence rate for the 25 and 15 spokes/frame level of undersampling is reduced compared to the SMS GA sampling (Fig.5.20). The plot also shows that the convergence at 45 spokes/frame is faster than the higher levels of undersampling. This is not seen in the convergence plots when SMS GA sampling is used (where all three levels of undersampling converge at approximately the same rate). This indicates that the convergence of GA

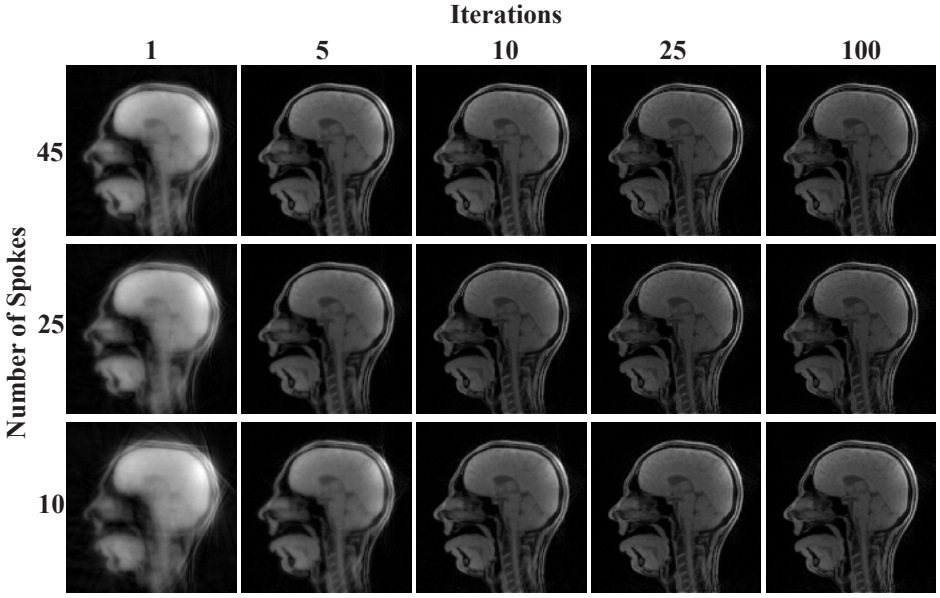

Figure 5.19: Visual comparison of reconstructed images (acquired using SMS GA sampling, 3 slices, 12mm slice distance) at different iterations of the proposed reconstruction algorithm. Results (from the central slice) are shown at 3 different levels of undersampling. A clear improvement in image quality can be seen between iterations $1-25$, however, little difference can be seen between iteration 25 and iteration 100.

sampling is more strongly coupled to the level of undersampling compared to SMS GA sampling. It is reflected in Fig.5.21, which shows that at the highest level of undersampling (10 spokes/frame), the image quality (in terms of blurring and contrast) at five iterations appears worse than at the equivalent point in the SMS GA sampling scheme.

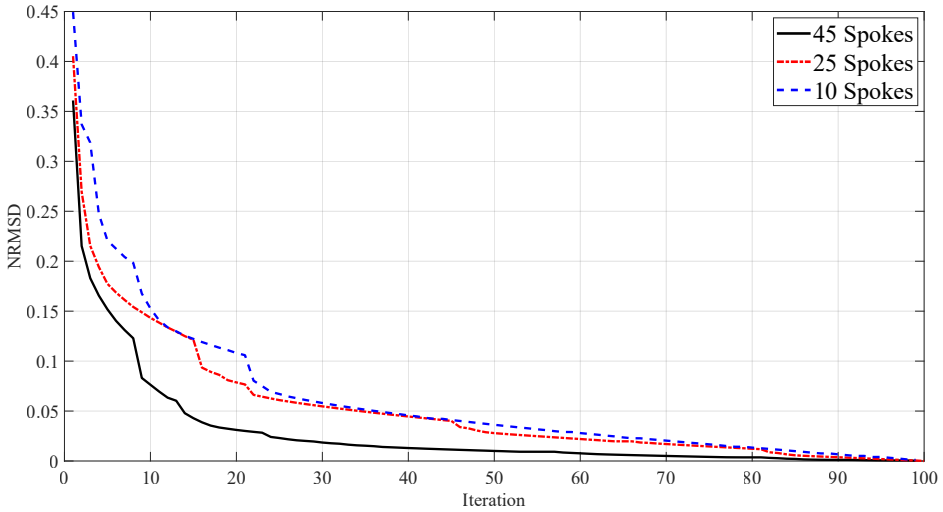

Figure 5.20: Plot of convergence when GA sampling is used (3 slices, 12mm slice distance), measured using NRMSD, at 3 different undersampling factors. The rate of convergence of the 45 spokes/frame level of undersampling is higher than the other two levels of undersampling.

Based upon these convergence experiments, the number of iterations was set to 25. This value is chosen for both sampling schemes due to the result at 25 iterations having near identical image quality to the results at 100 iterations.

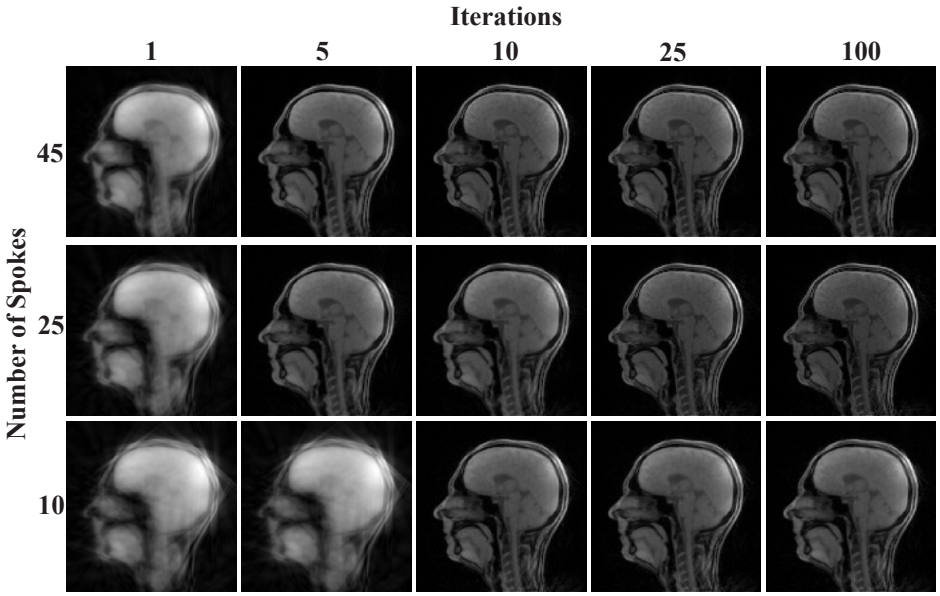

Figure 5.21: Visual comparison of reconstructed images (acquired using GA sampling, three slices, 12mm slice distance) at different iterations of the proposed reconstruction algorithm. Results (from the central slice) are shown at three different levels of undersampling. A clear improvement in image quality can be seen between iterations $1 - 25$, however, little difference can be seen between iteration 25 and iteration 100.

5.3.3 Undersampling Experiment

The undersampling experiment conducted for single-slice rtMRI is repeated for the multiband datasets acquired using the SMS GA and GA sampling schemes.

Fig.5.22 shows the effect of undersampling on SMS rtMRI data acquired using the SMS GA trajectory (at a slice distance of 4.8mm). When 95 spokes/frame are used, the proposed reconstruction method and CG-SENSE have similar image quality. At the four higher levels of undersampling (45, 20, 15, 10 spokes/frame), the CG-SENSE reconstruction shows increasing levels of blurring, artefacts and noise. When the proposed reconstruction pipeline is used, these artefacts are removed. This figure shows a single frame from rtMRI videos - the main effect of undersampling is most apparent in Video 5.3 (which compares the image quality at different undersampling levels). From this video, it is seen that the main artefact is temporal variations in signal intensity, these are particularly visible around the top of the head.

This experiment is also repeated for data acquired using standard GA sampling (Fig.5.23, Video 5.4). If two frames from both sampling schemes are directly compared (Fig.5.24), there is little visual difference. However, it can be seen in Video 5.5 that, when GA sampling is compared to SMS GA sampling, increased variations in intensity are visible, particularly around the top of the head. This is likely due to the destructive interference (introduced by the CAIPI phase modulation) not being fully removed during the reconstruction process.

The difference between GA and SMS GA sampling is visualised using temporal SNR (tSNR) images. The definition of tSNR (for pixel i) is shown

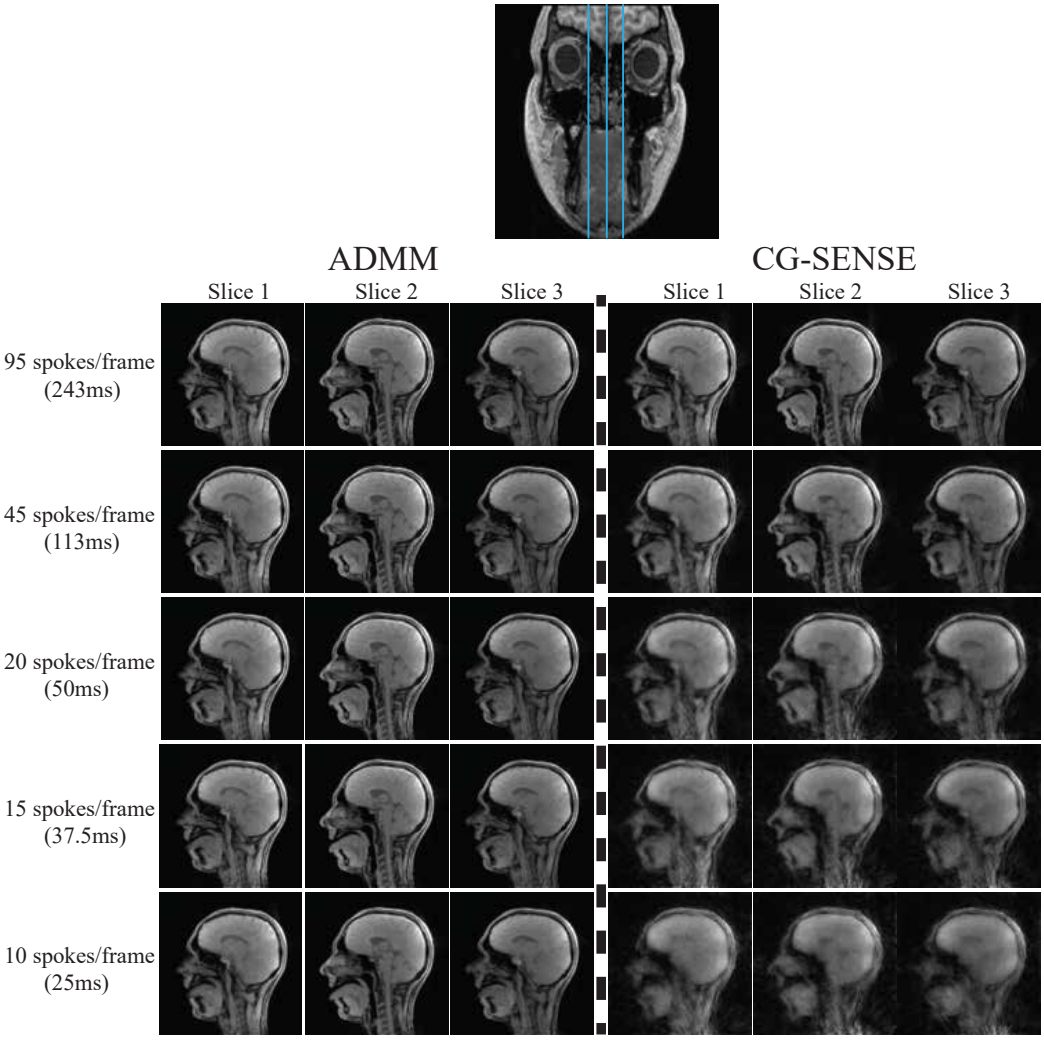

Figure 5.22: A comparison of two reconstruction algorithms (ADMM and CG-SENSE) at a variety of undersampling levels (from top to bottom 95 45, 20 15 and 10 spokes/frame). The data used in this experiment is acquired using SMS GA sampling with a slice distance of 4.8mm, the blue lines through the coronal slice at the top of the figure indicate the approximate positions of the three slices. The ADMM algorithm results in higher image quality at the highest levels of undersampling.

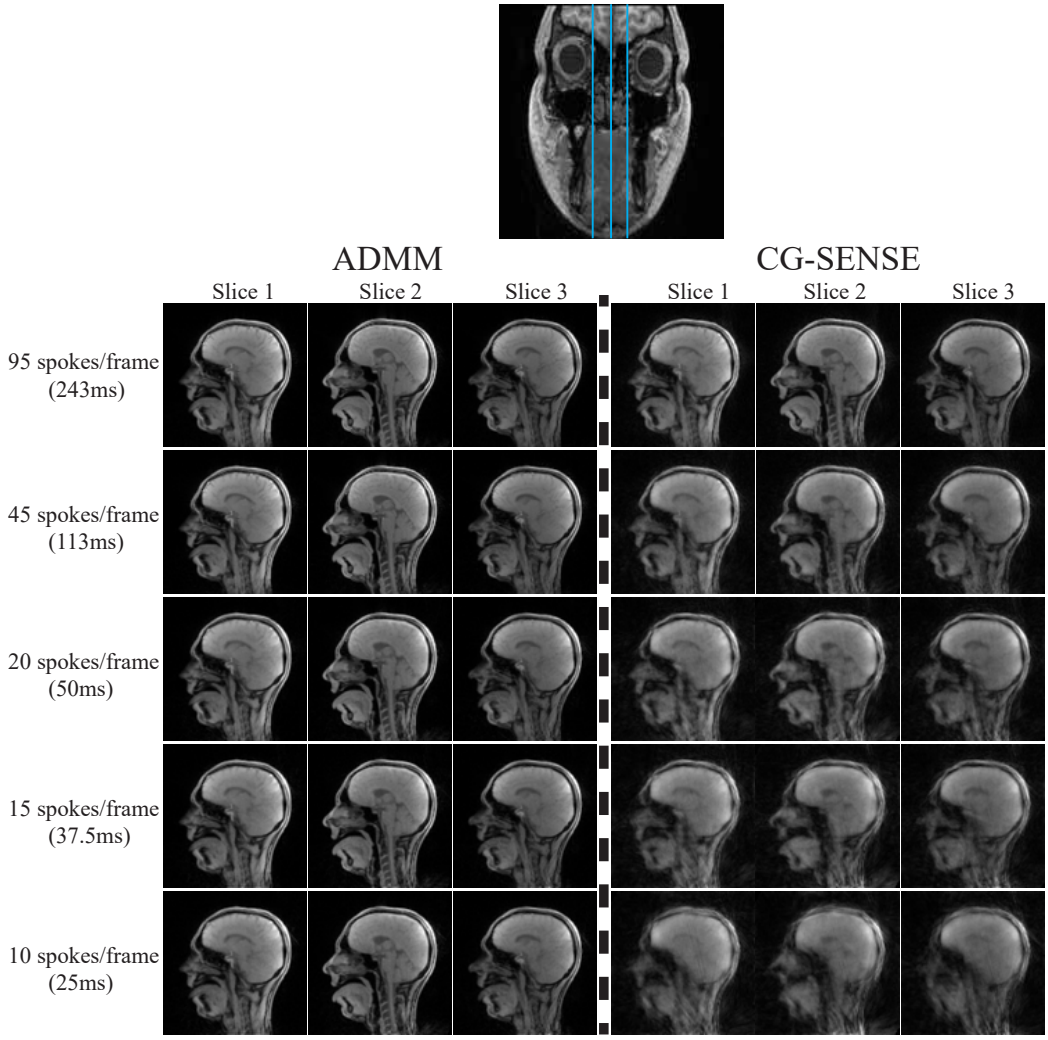

Figure 5.23: A comparison of two reconstruction algorithms (ADMM and CG-SENSE) at a variety of undersampling levels (from top to bottom 95 45, 20 15 and 10 spokes/frame). The data used in this experiment is acquired using GA sampling with a slice distance of 4.8mm, the blue lines through the coronal slice at the top of the figure indicate the approximate positions of the three slices. The ADMM algorithm results in higher image quality at the highest levels of undersampling.

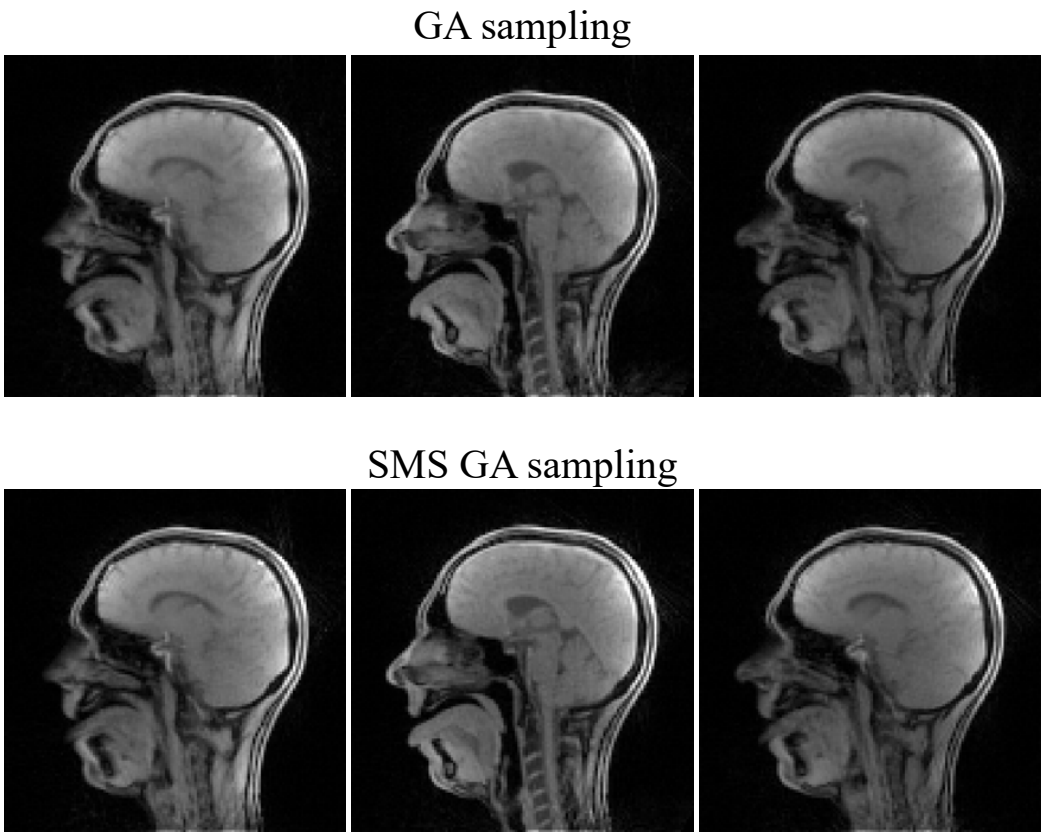

Figure 5.24: Comparison of a frame (15 spokes/frame) reconstructed from data acquired using GA sampling (top) and SMS GA sampling (bottom). Both frames appear visually very similar with the bottom frame having slightly more fine detail visible in the brain.

in eq.(5.4) where $\text{mean}_{\text{time}}(i)$ and $\sigma_{\text{time}}(i)$ are respectively the mean and standard deviation of pixel i over the entire time series; the tSNR is calculated for every pixel to generate the tSNR images.

$$\text{tSNR}(i) = \frac{\text{mean}_{\text{time}}(i)}{\sigma_{\text{time}}(i)} \tag{5.4}$$

As expected, in both sampling schemes, the region with the lowest tSNR is the mouth as this is where bulk movement occurs (thus, the standard deviation is high). However, the GA sampling scheme shows an overall lower tSNR than the equivalent data acquired using SMS GA sampling. The areas of low tSNR (in the brain) correspond to areas where intensity variations can be seen. This visualisation is repeated for an undersampling factor of 45 spokes/frame (Fig.5.26). The tSNR in the brain appears higher and more homogeneous compared to Fig.5.25.

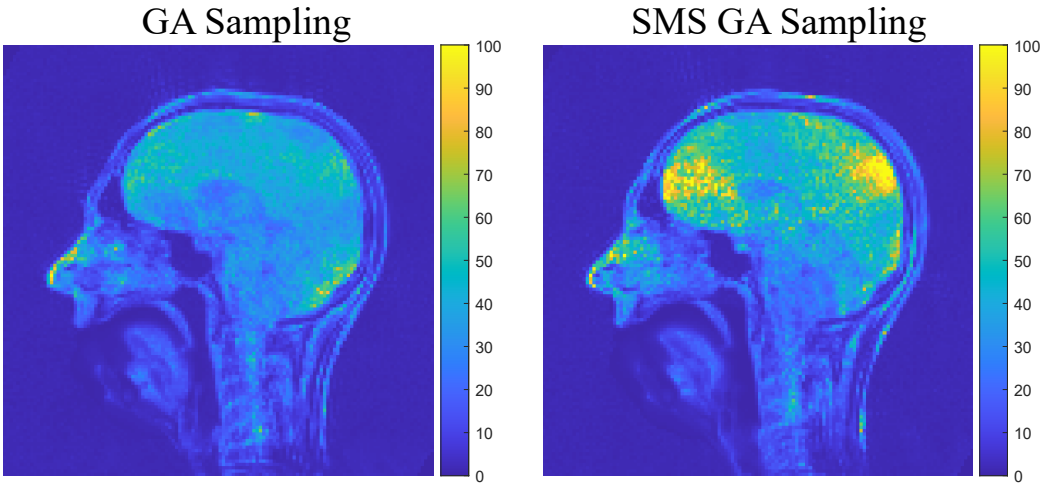

Figure 5.25: The tSNR of the central slice of 3 slice SMS rtMRI data reconstructed with 15 spokes per frame acquired using the GA (left) and SMS GA (right). The images have the same intensity scaling (maximum intensity limited to 100) to emphasise the overall higher tSNR in the data acquired using SMS GA sampling.

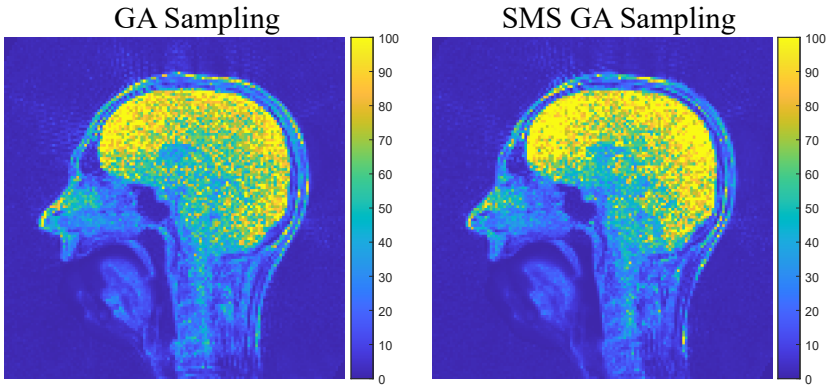

Figure 5.26: The tSNR of the central slice of 3 slice SMS rtMRI data reconstructed with 45 spokes per frame acquired using the GA (left) and SMS GA (right). The images have the same intensity scaling (maximum intensity limited to 100) to emphasise the overall higher tSNR in the data acquired using SMS GA sampling.

The differences in tSNR, at the different undersampling levels, are caused by changes in either the signal level or noise level (or both). To determine which variable is causing the change, the mean and standard deviation of a ROI in the center of the brain (which is not affected by movement) was calculated for the 15 and 45 spokes per frame datasets (this was repeated for both sampling schemes). The mean values, when using SMS GA sampling, were 4.108×10^{-4} and 4.104×10^{-4} for the 15 and 45 spokes per frame datasets respectively. The standard deviation values were 1.158×10^{-5} and 5.907×10^{-6} for the 15 and 45 spokes per frame datasets respectively. The large decrease in standard deviation, as the number of spokes increases, indicates that the main contribution to the change in tSNR is an increase in noise (or increase in radial undersampling aliasing). The same trend was seen when GA sampling is used, the mean values were 4.109×10^{-4} and 4.096×10^{-4} for the 15 and 45 spokes per frame datasets respectively. While the standard deviation results were 2.222×10^{-5} and 7.978×10^{-6}.

5.3.4 Effect of Slice Distance

The previous results showed data reconstructed from three slice data with a slice distance of 4.8mm and slice thickness of 8mm. SMS rtMRI data at a range of slice distances is acquired to see if the proposed sequence and reconstruction pipeline is robust at smaller slice distances. The following slice distances are used: 16mm, 12mm, 8mm, 4.8mm and 2mm. Fig.5.27 and Fig.5.28 shows images reconstructed at these slice distances using 25 spokes/frame acquired respectively with the GA and SMS GA trajectories (Video 5.6 shows the rtMRI videos at these slice distances). In both cases no artefacts in the images can be seen. These results indicate that the proposed technique is robust even at small slice distances. This is important for applications in which it may be desirable to image multiple slices close together. When viewing the central slice acquired at a 2mm slice distance, finer details can be seen, particularly in the brain, compared to the same slice acquired at a 16mm slice distance. The difference image between the 16mm and 2mm slice distance is shown in Fig., the extra details visible seen in the 2mm slice distance are emphasized in the difference image. A potential reason for the differing levels of fine details is that at the high slice distances the non-central slices contain large regions of no signal, particularly in the sinuses. This results in a lower proton density which reduces the overall signal level. This reduction in signal may be preventing the reconstruction algorithm from recovering fine details.

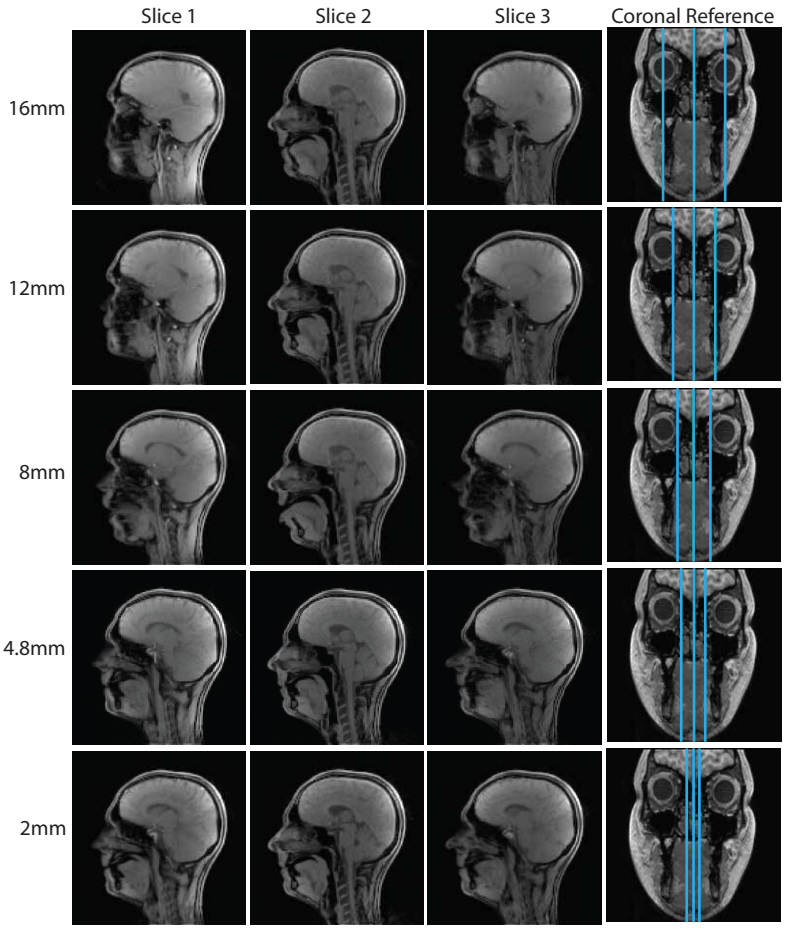

Figure 5.27: Images (3 slices, 25 spokes/frame) reconstructed using data obtained with GA sampling at a range of slice distances. From top to bottom: 16mm, 12mm, 8mm, 4.8mm and 2mm slice distances. No artefacts due to slice leakage are visible.

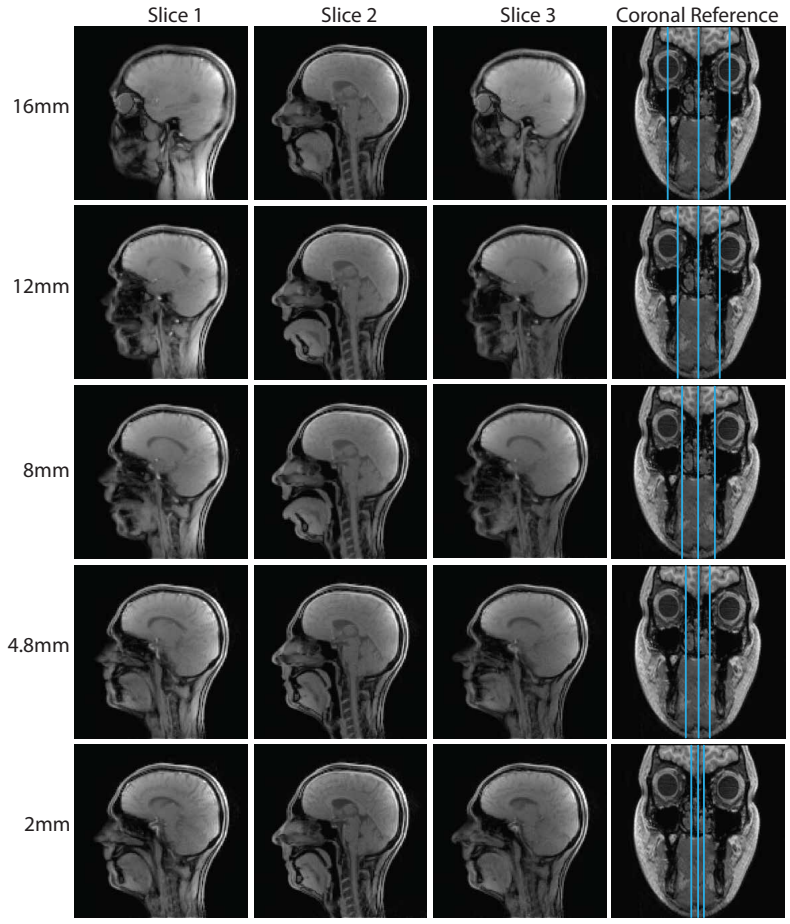

Figure 5.28: Images (3 slices, 25 spokes/frame) reconstructed using data obtained with SMS GA sampling at a range of slice distances. From top to bottom 16mm, 12mm, 8mm, 4.8mm and 2mm slice distances. No artefacts due to slice leakage are visible.

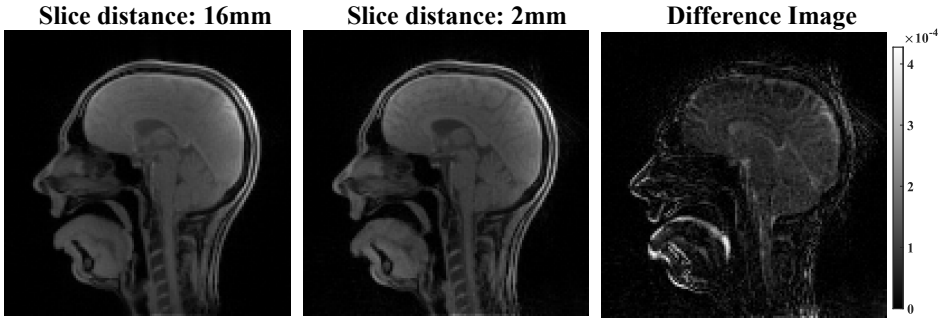

Figure 5.29: A frame from three slice SMS rtMRI videos acquired with slice distances of 16mm (left) and 2mm (middle). The difference image between these two images is shown on the right. This difference image shows the fine details in the brain, which is seen in the middle image but not the left image.

5.3.5 Effect of Increased SMS Acceleration

The previously shown SMS rtMRI results demonstrate the use of SMS excitation to image three slices simultaneously. In some applications it may be desirable to further increase the number of excited slices in order to further increase anatomical coverage. For example, Fig.5.30 shows the results of a five slice reconstruction (16mm slice distance, 25 spokes/frame) using the SMS GA and GA sampling schemes respectively. The extra slices may be useful when imaging motion enabled by anatomy across a wide region. For example, when imaging swallowing it is useful to see the central slices (to observe the main process of swallowing), but also see the temporomandibular joints at the sides of the head, as dysfunction in these joints can cause issues when swallowing.

To see the effect of data undersampling at this higher level of SMS acceleration, the undersampling experiment shown in the previous section is repeated for the five slice rtMRI data. rtMRI videos at undersampling levels of 45, 25 and 15 spokes/frame are reconstructed (Video 5.7). Fig.5.31 com-

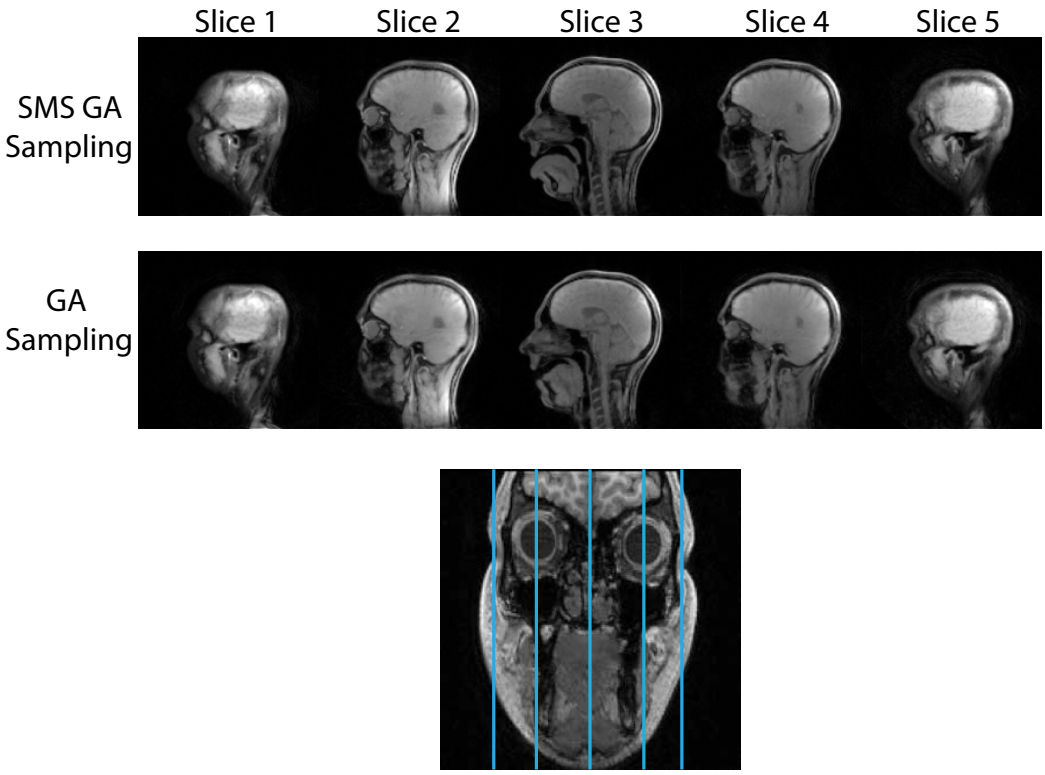

Figure 5.30: Frames from five slice rtMRI data (25 spokes/frame) acquired using SMS GA sampling (top) and GA sampling (bottom). The blue lines through the coronal slice (bottom) indicate approximate positions of these slices.

pares three frames, reconstructed using 15 spokes/frame, acquired using GA sampling and SMS GA sampling and, in both cases, significant blurring and artefacts are visible. The tSNR images (Fig.5.32) show that the artefacts in the GA sampling appear to have more structure compared to the SMS GA sampling scheme.

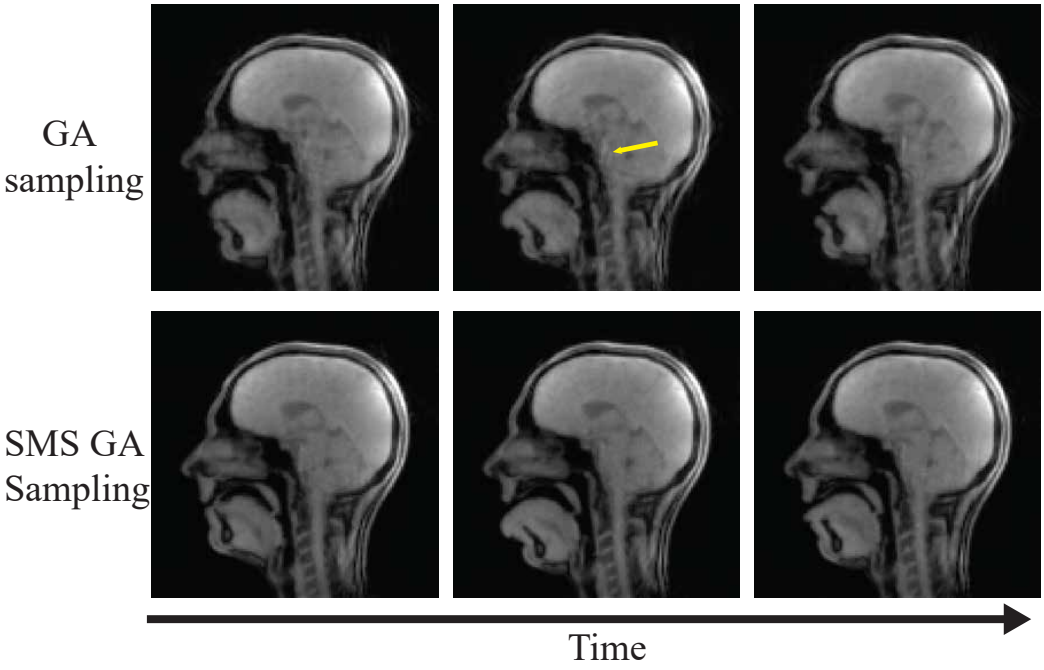

Figure 5.31: Comparison of three frames (15 spokes/frame) acquired using the GA sampling scheme (top) and SMS GA sampling scheme (bottom). The central slice from a 5 slice acquisition is shown. Blurring and artefacts are present in both sampling schemes. An example of one of these artefacts is indicated by the yellow arrow.

Increasing the number of spokes/frame to 25 suppresses the most severe artefacts at the cost of reducing temporal resolution from 37.5ms to 62.5ms (Fig.5.33). This reduction in artefacts is reflected in the tSNR images (Fig.5.34). Compared to the previous tSNR image (Fig.5.32), the overall tSNR (in areas without movement) is increased, and the large artefacts

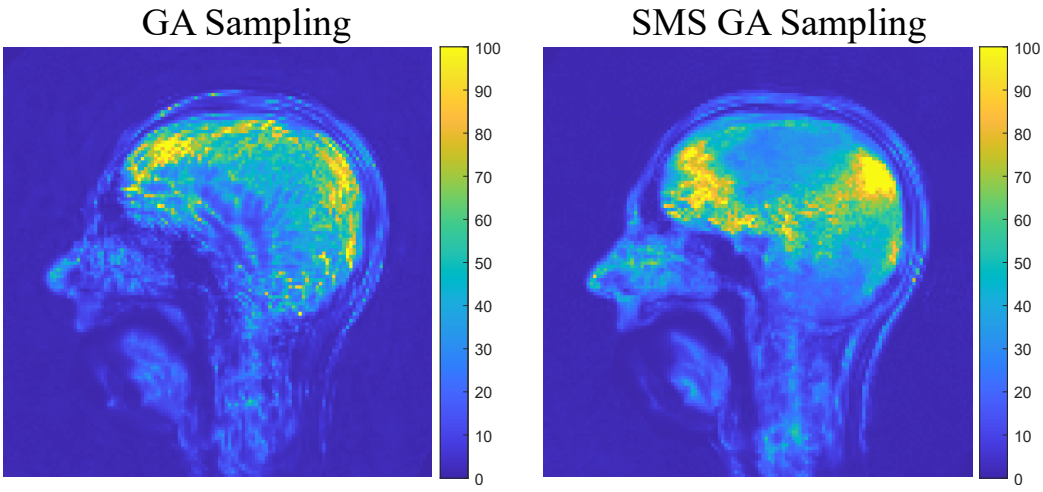

Figure 5.32: The tSNR of the central slice of 5 slice SMS rtMRI data reconstructed with 15 spokes/frame acquired using the GA (left) and SMS GA (right) sampling schemes. Both images have the same intensity scale with a maximum of 100.

present in the GA sampling scheme appear reduced. In Video 5.7, the SMS GA sampling scheme appears to have an increased level of intensity variation compared to GA sampling, this is also reflected in the tSNR images. This could indicate that the reduction in k-space coverage (shown in Fig.5.35) using SMS GA sampling is outweighing the benefit of improved destructive interference.

At 45 spokes/frame (Fig.5.36) the intensity variations in both sampling schemes are further reduced. The tSNR images (Fig.5.36) reflect this with the tSNR in the brain appearing larger and more homogeneous than the previously shown tSNR images. However, this improvement in image quality requires a reduction in temporal resolution from 37.5ms to 112ms. This temporal resolution is now below the recommended temporal resolution of 70ms, required to image the fastest movements which occur during speech [7].

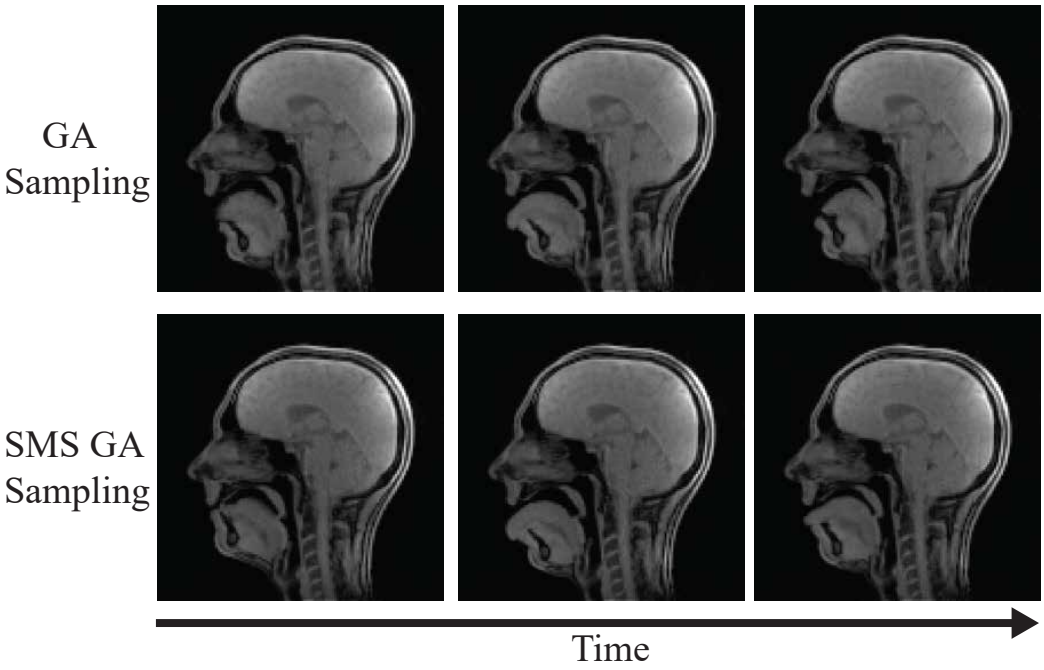

Figure 5.33: Comparison of three frames (25 spokes/frame) acquired using the GA sampling scheme (top) and SMS GA sampling scheme (bottom). The central slice from a 5 slice acquisition is shown.

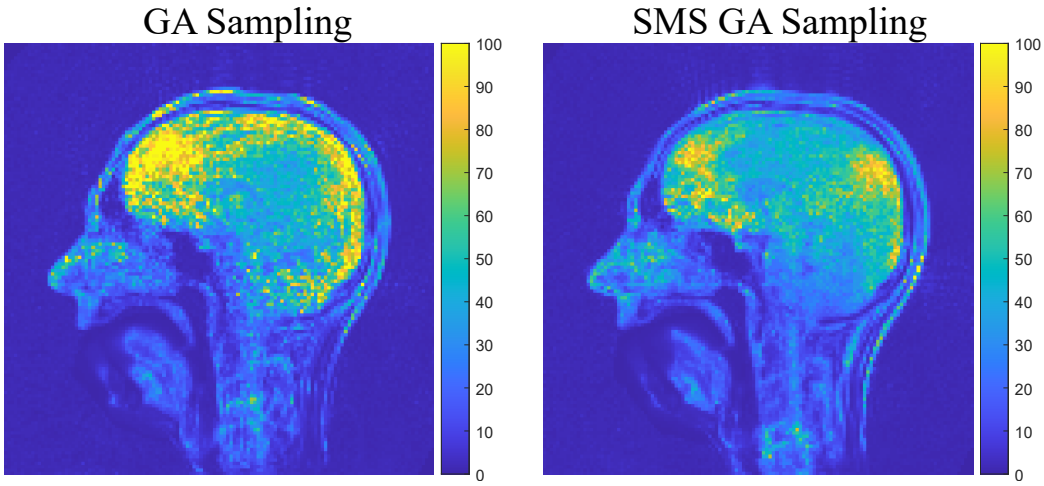

Figure 5.34: The tSNR of the central slice of 5 slice SMS rtMRI data reconstructed with 25 spokes/frame acquired using the GA (left) and SMS GA (right) sampling schemes. Both images have the same intensity scale with a maximum of 100.

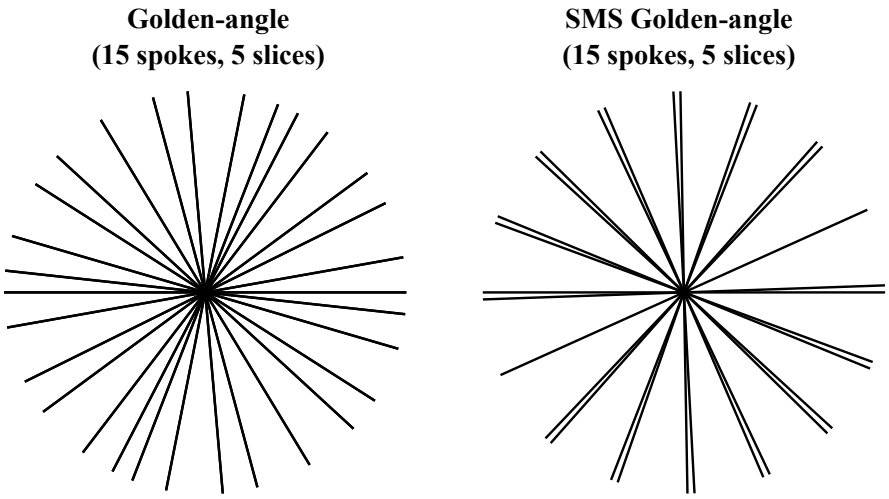

Figure 5.35: Illustration of the golden-angle trajectory (left, 15 spokes and 5 slices) and the SMS golden-angle trajectory (right, 15 spokes and 5 slices). The SMS GA trajectory has a reduced k-space coverage compared to the GA trajectory.

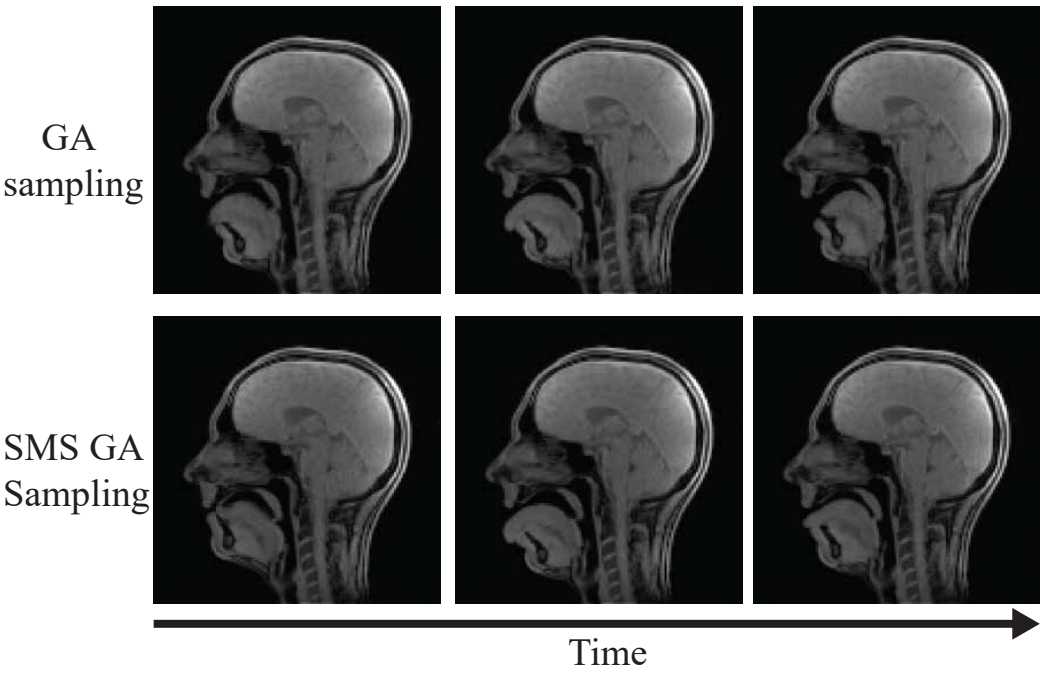

Figure 5.36: Comparison of three frames (45 spokes/frame) acquired using the GA sampling scheme (top) and SMS GA sampling scheme (bottom). The central slice from a 5 slice acquisition is shown.

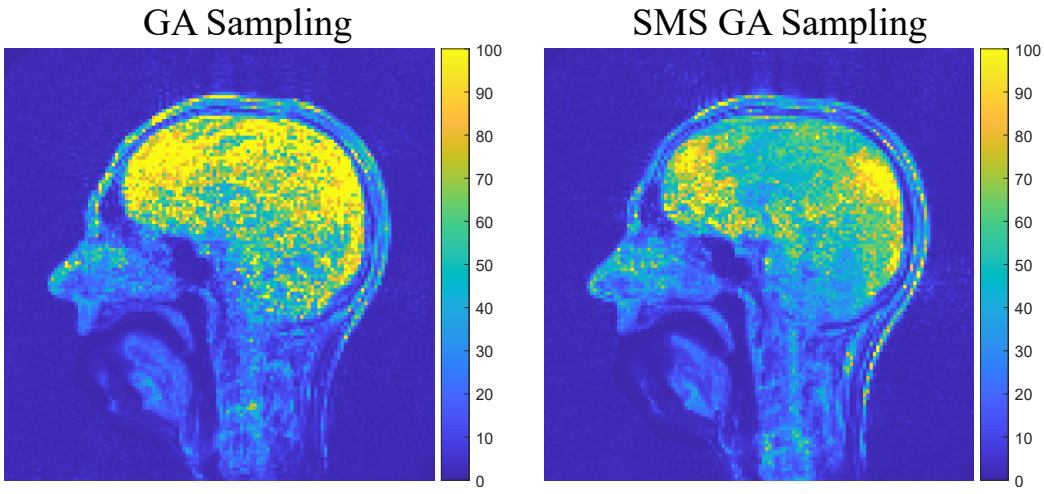

Figure 5.37: The tSNR of the central slice of 5 slice SMS rtMRI data reconstructed with 45 spokes/frame acquired using the GA (left) and SMS GA (right) sampling schemes. Both images have the same intensity scale with a maximum of 100.

These five slice results are obtained using the previously determined $\lambda = 4 \times 10^{-2}$. However, this parameter is based upon a λ search performed for three-slice rtMRI data, thus, it is not optimized for higher levels of SMS acceleration. Repeating the reconstruction with the value of λ increased to 5.5×10^{-2} reduces the intensity variations (Video 5.8). However, care is needed as further increasing λ to 6 results in blurring. These results show that careful parameter tuning is necessary in order to maximise the performance of the proposed reconstruction approach.

Further in-plane acceleration using an SMS acceleration factor of 7 will now be briefly explored (using $\lambda = 5.5 \times 10^{-2}$) at a slice distance of 12mm. Fig.5.38 shows the anatomical coverage achieved at this level of SMS acceleration (and slice distance).

Frames reconstructed at undersampling levels of 15 spokes/frame and 25 spokes/frame are shown in Fig.5.39 and Fig.5.40 respectively (these results

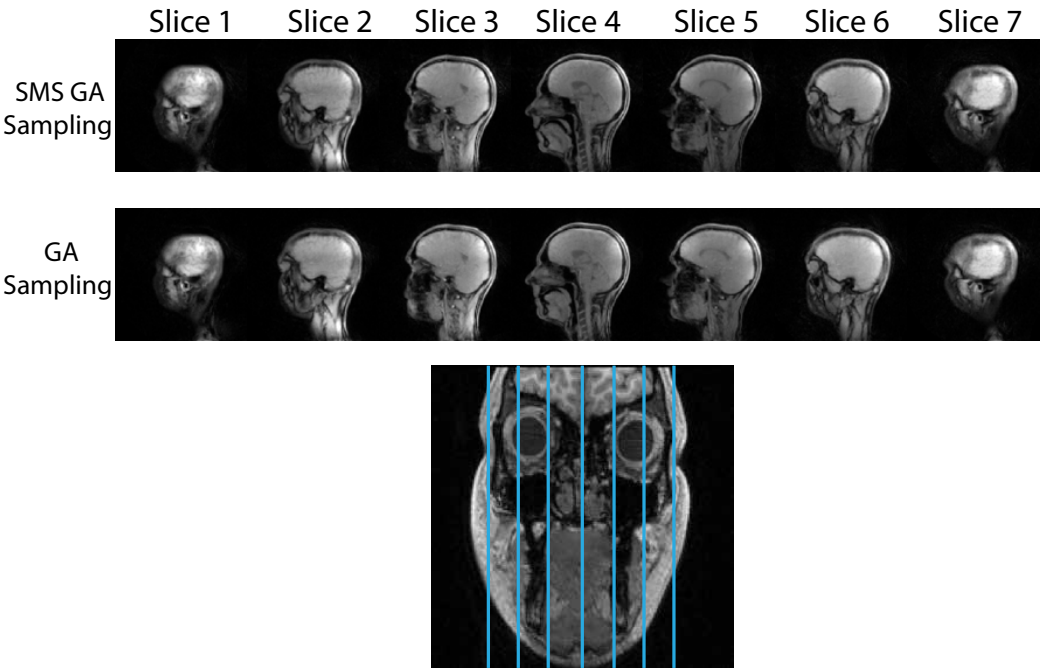

Figure 5.38: A frame reconstructed from seven slice (25 spokes/frame, 12mm slice distance) rtMRI data acquired using GA sampling (top) and SMS GA sampling (middle). The blue lines through the coronal slice (bottom) show the approximate positions of all seven slices.

are also shown in Video 5.9). A large amount of blurring is visible at the highest level of undersampling. Yet, the large artefacts seen previously for the five-slice results are not present - this may be due to the larger λ value suppressing some of these effects. Increasing the number of spokes/frame to 25 reduces the blurring, however, the variations in intensity can still be seen. Finally, at 45 spokes/frame (Fig.5.41) these artefacts are removed, however, this improvement in image quality requires a reduction in temporal resolution (from 37.5ms to 112ms) which may not be acceptable in some applications.

These results show the trade off between through-plane and in-plane acceleration. If high (above three slices) SMS acceleration is desired, then temporal resolution must be reduced (i.e. more spokes acquired per frame)

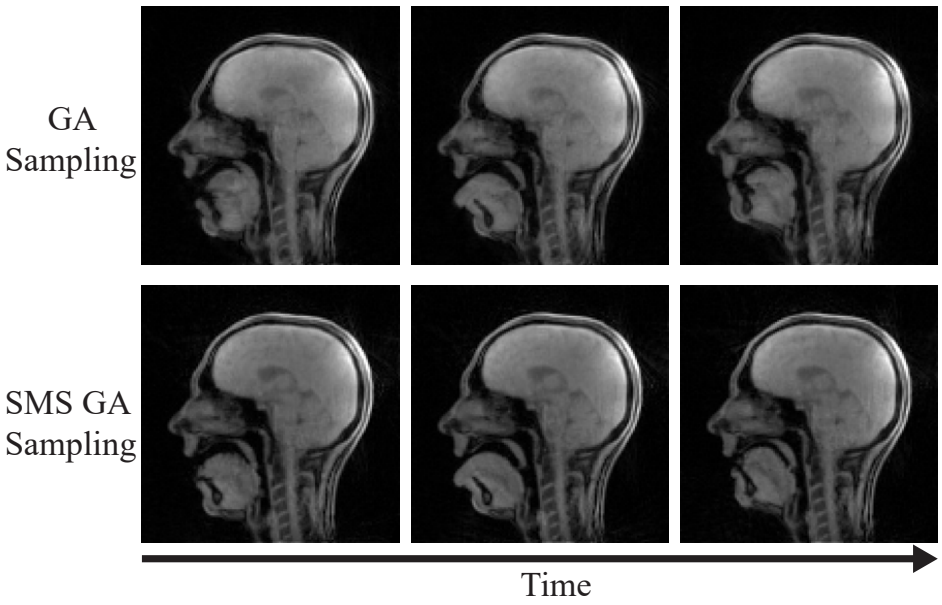

Figure 5.39: Comparison of three frames (15 spokes/frame) acquired using the GA sampling scheme (top) and SMS GA sampling scheme (bottom). The central slice from a seven slice acquisition is shown. Due to the high level of undersampling and high SMS acceleration artefacts are visible, particularly in the brain.

to maintain an equivalent image quality. Further exploration of regularization parameter tuning is needed to maximise the image quality at a particular level of SMS acceleration and data undersampling. In addition to this, the data for all SMS acceleration factors is compressed to 15 virtual coils, the next section will show that this is suitable for three slices. However, more testing is needed to verify that this compression level can be used at higher levels of SMS acceleration.

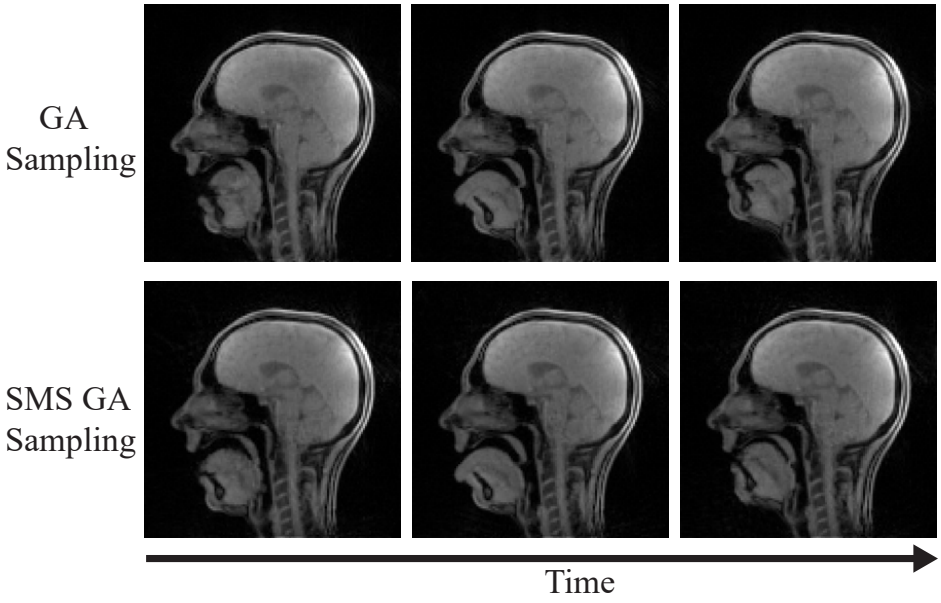

Figure 5.40: Comparison of three frames (25 spokes/frame) acquired using the GA sampling scheme (top) and SMS GA sampling scheme (bottom). The central slice from a 7 slice acquisition is shown.

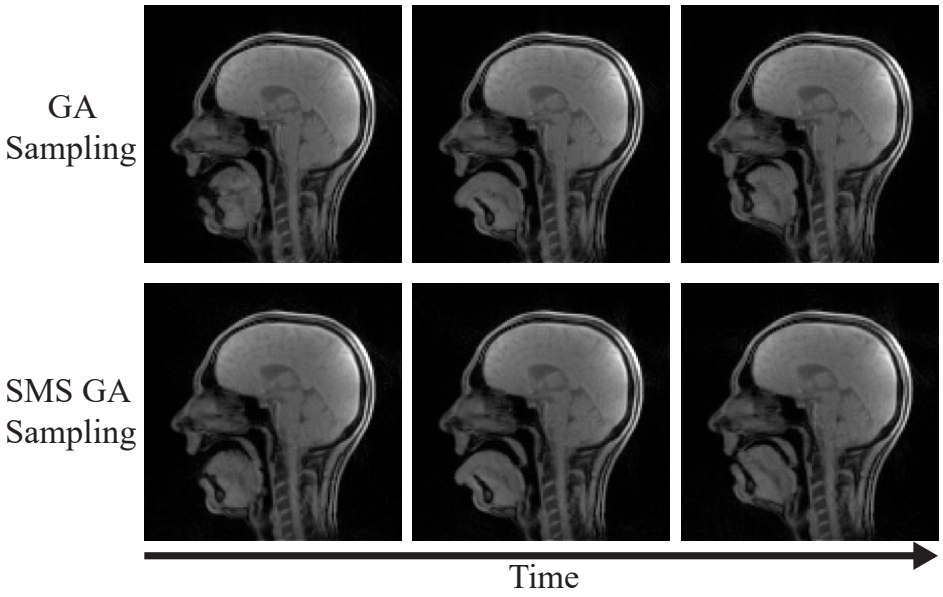

Figure 5.41: Comparison of three frames (45 spokes/frame) acquired using the GA sampling scheme (top) and SMS GA sampling scheme (bottom). The central slice from a seven slice acquisition is shown.

5.3.6 Coil Compression

The coil compression experiment shown in Section 5.2.4 is repeated for SMS rtMRI (Video 5.10). A dataset with a slice distance of 2mm is used for this experiment. This slice distance is chosen as it is the smallest distance used. Therefore, this presents the biggest challenge (in terms of slice separation): if the compression is robust for this distance, it is expected to be robust for the larger distances. As with the single-slice experiment, the data is binned to 25 spokes/frame.

Examples of image quality (for the central slice) at increasing levels of coil compression are shown in Fig.5.42. As with the single-slice rtMRI results, it can be seen that a significant degradation in image quality (compared to the reconstruction using all coils) is only seen at very high levels of compression. The MSE and PSNR are calculated (for the central slice) at each level of coil compression, these are shown in Fig.5.43 and Fig.5.44 respectively. These plots, as is seen in the single-slice results, show that the degradation in the image quality decreases rapidly as the level of compression is reduced (i.e. the number of virtual coils is increased). In the PSNR plot, a sharp decrease in the PSNR can be be seen between 42 and 41 virtual coils. The reason for this is not known, however, it does not appear to have a noticeable effect on image quality. These quantitative and visual results indicate that the level of coil compression used (15 virtual coils) does not substantially degrade the image quality and higher levels of compression could be used to reduce the computation time.

As discussed in the single-slice results, the use of RoVir to focus on specific areas may improve performance. The combination of RoVir and SMS is

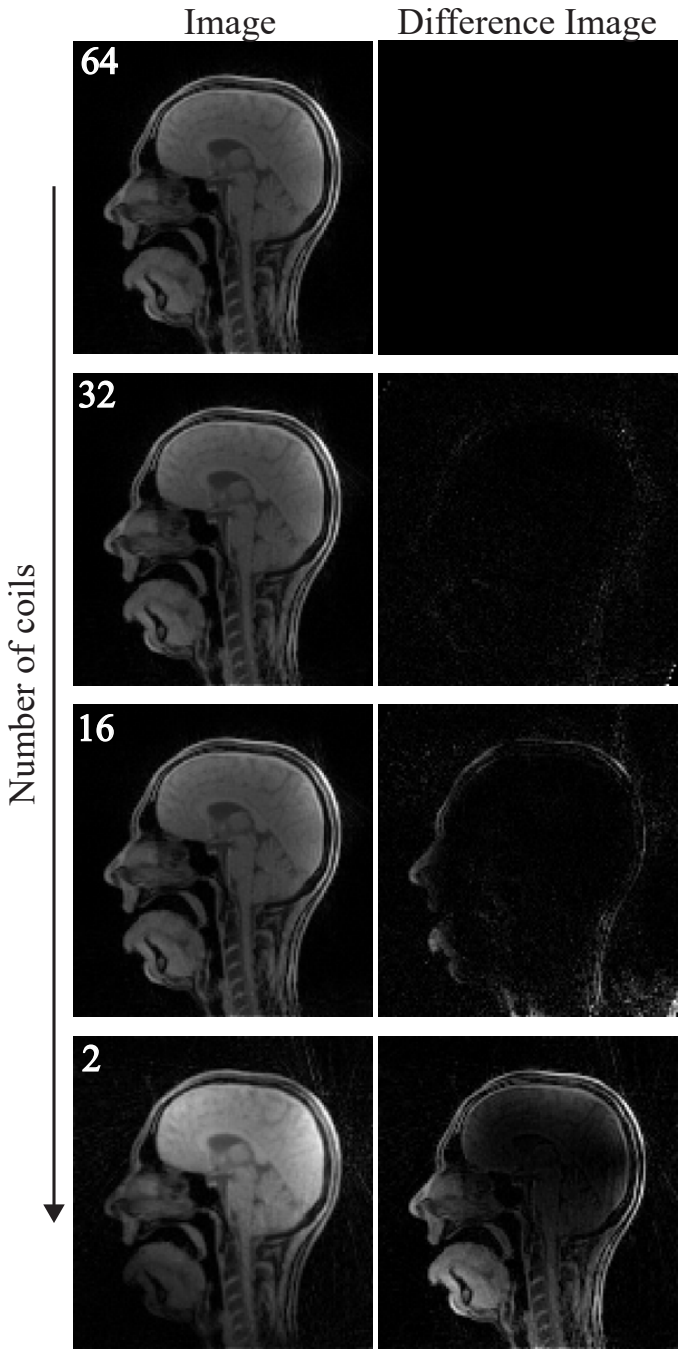

Figure 5.42: The effect of coil compression on SMS rtMRI data (3 slices, 2mm slice distance) at varying levels of coil compression. The top left image (the central slice of the 3 slices) is reconstructed using all 64 coils. The compression level is then increased, with the number in the top left corner indicating the number of virtual coils used. The left images are a frame reconstructed from the compressed data and the right image is the absolute difference between the frame reconstructed using the compressed data and the reference image (using all coils). The intensity scaling of each image is independent, this is done to emphasize the areas of anatomy affected by the coil compression.

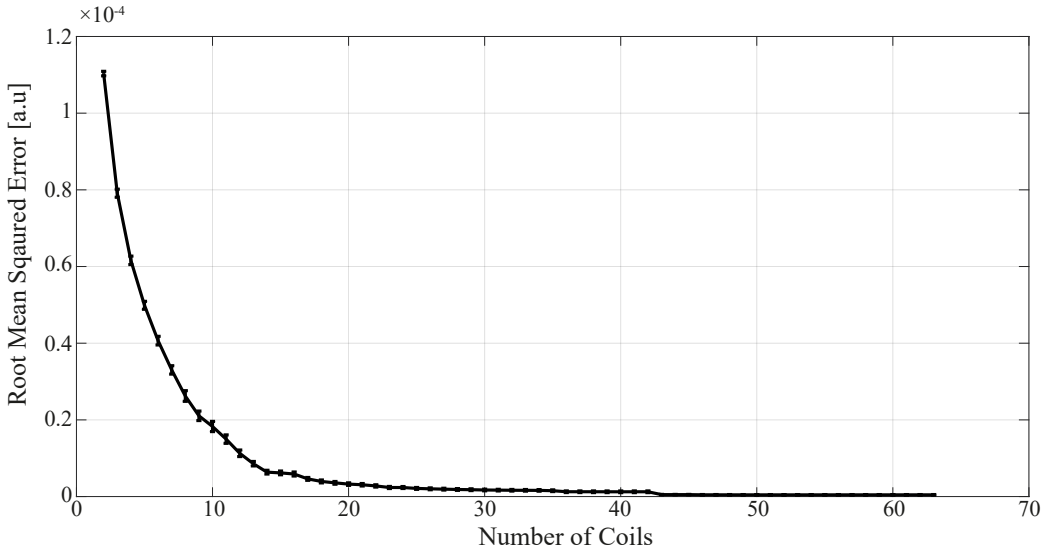

Figure 5.43: Plot of RMSE (for the central slice) at varying levels of coil compression (2-63 coils).The error bars represent the standard deviation of RMSE across the entire time series of frames. From the plot it can be seen that RMSE drops rapidly. This indicates that a high level of compression can be used with minimal difference between compressed and uncompressed images.

demonstrated in a recent work by Kim et al. (2023), which applied the combination of these two techniques for use in gated cardiac imaging [158]. They show that whole heart coverage can be achieved in a single breath-hold compared to the nine breath-holds required without the acceleration.

As was shown in the single-slice rtMRI results, the proposed algorithm requires a substantially longer reconstruction time than CG-SENSE. The per coil reconstruction time for both methods is estimated using the linear fit method described in Section 5.2.4. The ADMM algorithm has a per coil reconstruction time of 126.3s, this is 10.5 times higher than the per coil reconstruction time of CG-SENSE (12.03s). Compared to single-slice rtMRI, using SMS rtMRI further increases reconstruction time as multiple slices are reconstructed. For example, at 20 virtual coils, the single-slice

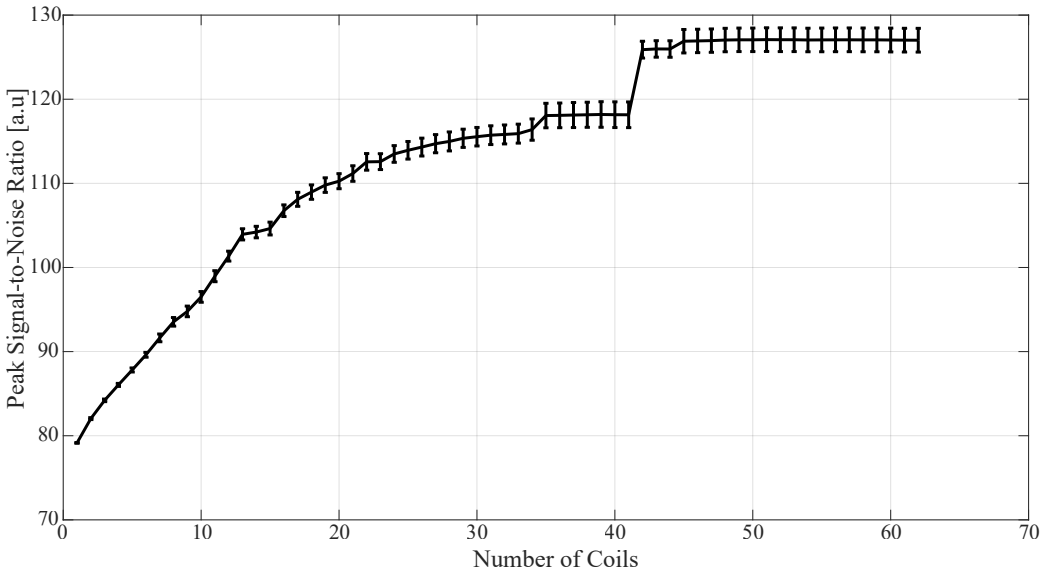

Figure 5.44: Plot of PSNR (for the central slice) at different levels of coil compression ($2-63$ coils). The error bars represent the standard deviation of PSNR across the entire time series of frames. Using a higher number of coils results in a higher PSNR. However, even at very high levels of compresssion (10 coils) the PSNR is only 18% lower despite the 85% reduction in the number of coils.

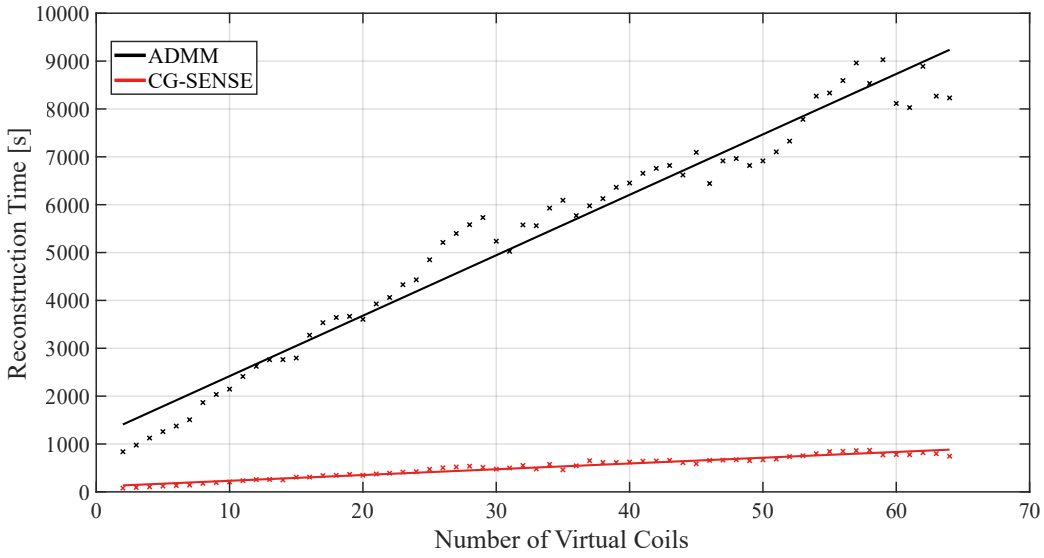

Figure 5.45: Plot of reconstruction time (in seconds) at a range of coil compression levels for the both reconstruction techniques. The ADMM reconstruction (black) is substantially higher than both the CG-SENS recon (blue). An undersampling level of 25 spokes/frame is used for data shown in this plot.

rtMRI CS reconstruction takes 1200s, while the three-slice SMS rtMRI has a 3700s reconstruction time. This is approximately a threefold increase in reconstruction time, which is expected as there are three slices to reconstruct, thus, triple the number of computational operations is required.

5.3.7 Evaluation

This section has shown that the developed SMS rtMRI sequence combined with CS reconstruction enables motion across three slices to be recorded at temporal resolutions equivalent to single-slice rtMRI shown in the previous section.

The SMS GA sampling scheme has also been directly compared to the standard GA sampling. In the case of three slice acceleration, the use of

SMS GA sampling scheme results in reduced intensity variations compared to GA sampling. This is shown in both videos and tSNR images. However, at higher levels of SMS acceleration, the results indicate that for both sampling schemes, the temporal resolution must be reduced to reduce artefacts. In addition to this, it appears that the standard GA sampling scheme, at these higher levels of SMS acceleration, has reduced intensity variation compared to SMS GA sampling. However, tuning the λ parameter for specific SMS acceleration levels has a large impact on the resulting image quality.

There are two main limitations of the current SMS sequence and reconstruction pipeline. The first, as with single-slice rtMRI, is the lengthy reconstruction time compared to CG-SENSE (10.5 times higher). The second limitation is the degradation of image quality at higher SMS acceleration factors. As shown in Section 5.3.5, at 5 and 7 slice acceleration the temporal resolution must be sacrificed. From a reconstruction perspective, the use of more advanced regularization techniques may improve the image quality. SMS rtMRI may also benefit from array coils designed specifically to image the oral cavity. An example of this a 12 coil array designed by Voskuilen et al. (2020) to image the tongue [159]. They show improved SMS performance (in diffusion imaging) in terms of SNR over a conventional head coil similar to the one used in this thesis.

5.4 Effect of post-processing

In Sections 5.2 and 5.3, unless stated otherwise, a temporal median filter of width 3 has been applied to the reconstructed images. The aim of this filter is to suppress residual noise present after reconstruction.

To determine the effect of the filter, images are compared at filter widths of: 0 (i.e. no filter applied), 3, 5 and 7. This experiment is performed for single-slice rtMRI and three-slice SMS rtMRI. In both cases, a temporal resolution of 37.5ms is used (i.e. 15 spokes/frame).

Results for single-slice rtMRI are shown in Video 5.11, it can be seen that even when no filter is applied, there is little noise present after the reconstruction, indicating that the post-processing step, only has minimal effect on the final images. The tSNR images reflect this (Fig.5.46): there is little visible difference between the different filter widths. These results also demonstrate the effectiveness of the proposed reconstruction approach as the unfiltered video does not display a visibly noticeable amount of noise compared to its filtered equivalents.

When SMS rtMRI is used, the effect of the median filter is more substantial. Video 5.12 compares the results from a three-slice SMS rtMRI video, reconstructed using 15 spokes/frame, at a variety of filter lengths. From this video, it can be seen that the median filter suppresses some of the variations in image intensity. This can also be observed in the tSNR images (Fig.5.47): when no filter is applied there are areas (indicated with a black arrow) which show reduced tSNR compared to the rest of the head. As the filter width is increased the tSNR becomes more uniform. This indicates that, in the case of SMS rtMRI, the median filter is a necessary post-processing step. Improvements/fine tuning of regularization may suppress these artefacts making the median filter post-processing step less important.

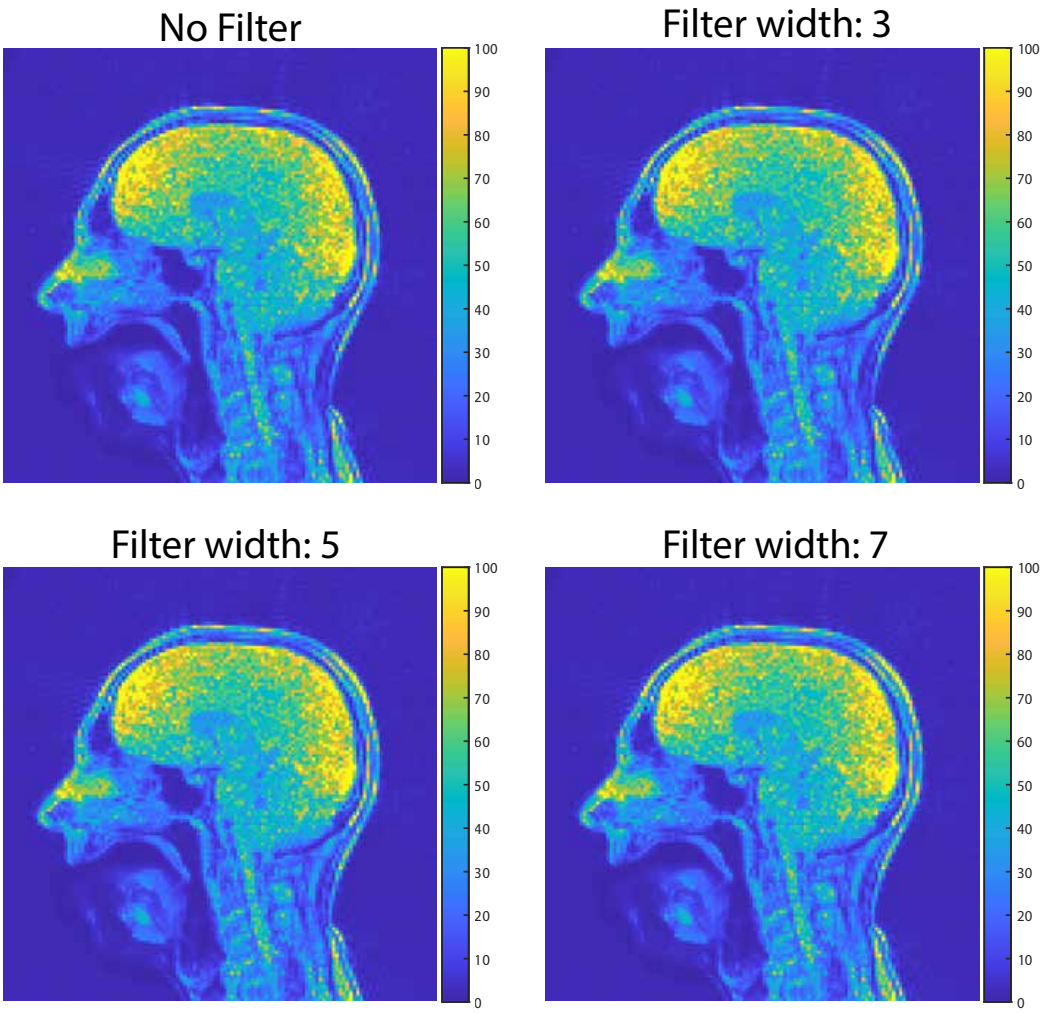

Figure 5.46: A comparison of tSNR from rtMRI videos (15 spokes/frame) with different filter widths applied after reconstruction. It can be seen that there is little difference between the tSNR images.

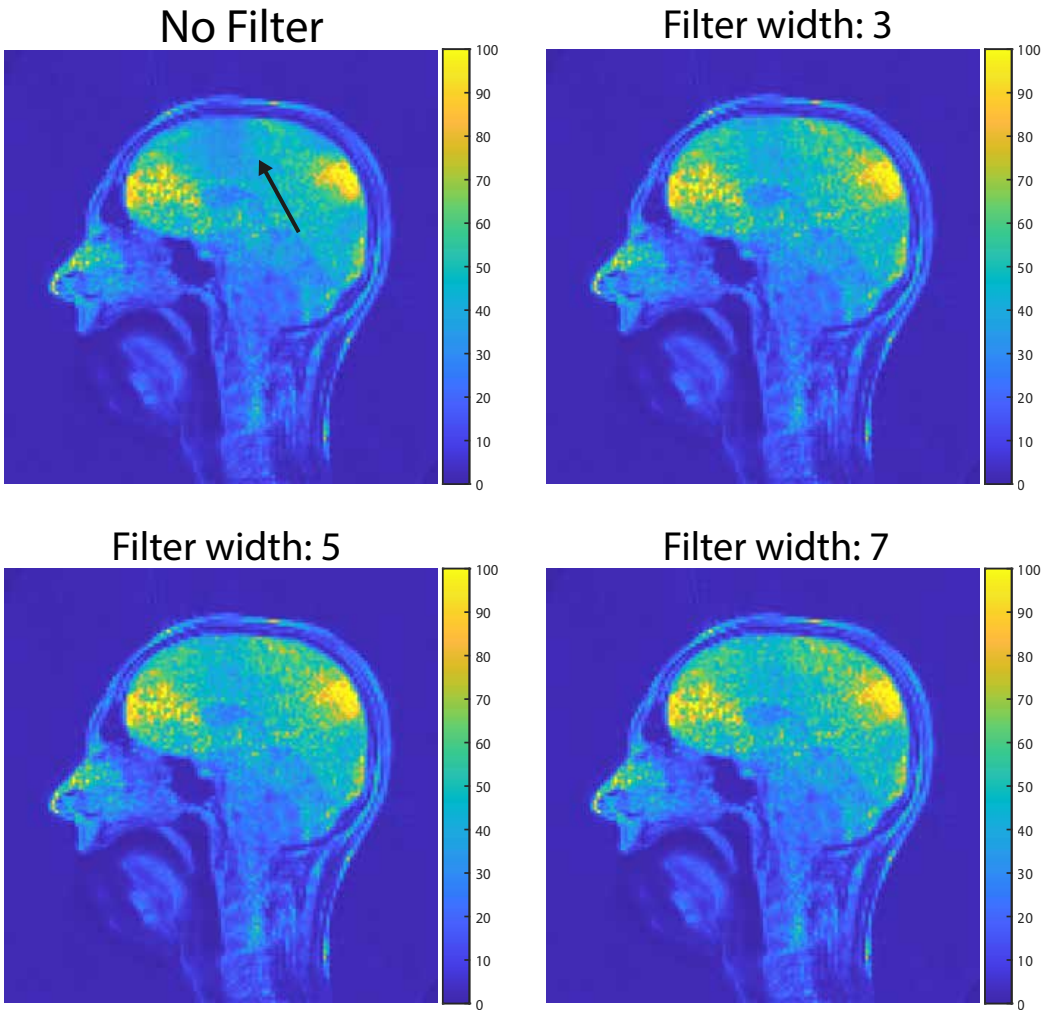

Figure 5.47: A comparison of tSNR from SMS rtMRI videos (three slices, 15 spokes/frame, SMS GA sampling scheme) with different filter widths applied after reconstruction. The black arrow indicates a region of low tSNR present when no filter is applied.

5.5 Quantitative Evaluation

In general, the previous sections describe image quality in terms of visual appearance (for example, if blurring is present in the image). It is desirable to have quantitative image quality metrics to complement this visual assessment. Unfortunately, the quantification of image quality in dynamic MRI reconstruction is an extremely challenging problem. For example, a standard metric to judge image quality in image reconstruction/processing is SNR, this was defined previously (eq.(4.6)) . This metric assumes that the profile of the noise is Gaussian (or Rician when magnitude images are used) [32]. This is not a valid assumption when coil sensitivity profiles are incorporated into the reconstruction as they introduce spatial variations into the noise profile. This assumption is also not true when radial sampling is used as the streaking artefacts, caused by undersampling, do not obey a Gaussian distribution. The use of CS reconstruction introduces further challenges in the use of SNR as the artefacts introduced by CS may not be captured. For example, consider Fig.5.48, the image on the left is reconstructed using a $\lambda = 1 \times 10^{-3}$ while the image on the right is reconstructed with $\lambda = 1 \times 10^{-1}$. Although the left image has better contrast and edge sharpness, the tSNR is an order of magnitude lower than the right image. If image quality was solely judged on this metric, the over-regularized image would be considered the best image despite the severe loss of image detail.

For static imaging, to overcome this limitation, it is typical to first acquire a fully sampled k-space and the retrospectively undersample it. The undersampled k-space is then reconstructed using the proposed and reference approaches. The images are then compared to the fully sampled reference

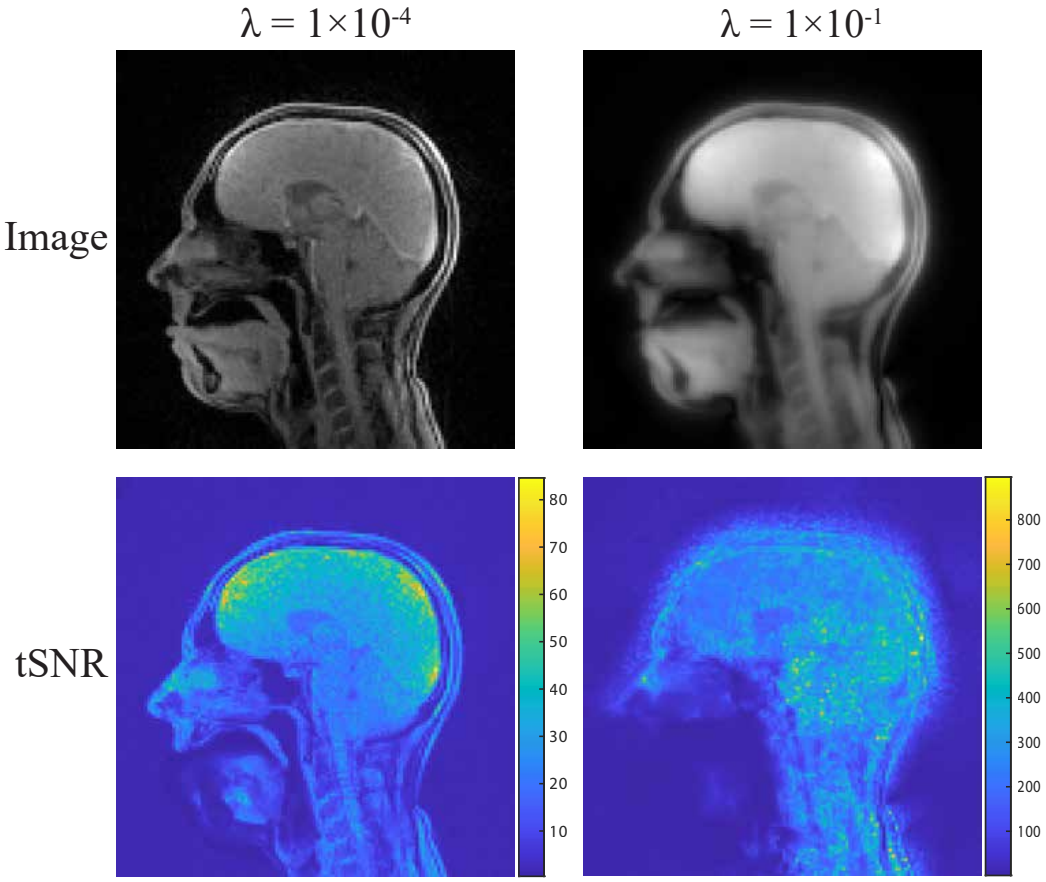

Figure 5.48: Top: comparison of an rtMRI (25 spokes/frame) reconstructed using $\lambda = 1 \times 10^{-3}$ (left) and $\lambda = 1 \times 10^{-1}$ (right). This shows that although large regularization suppresses noise, it also results in elimination of structural details (for example, the tip of the tongue), and contrast. Bottom: comparison of the tSNR using these regularization values, the higher regularization results in an order of magnitude increase in tSNR.

image using a variety metrics, such as the Structural Similarity Index Metric [160], Mean-Squared Error and Peak Signal-to-Noise. Unfortunately, in ungated dynamic imaging this is not possible, as no fully sampled reference image exist, as undersampling is required to obtain images at high temporal resolutions. Referenceless metrics have been proposed which do not require a ground truth. A recent review by Kastryulin et al. (2023) describes a variety

of these methods and highlights that the results from these metrics do not always align with the clinicians perceived image quality [161].

A limitation of all rtMRI techniques (and for other MRI methods) is the lack of such rigorous quantitative evaluation of image quality due to the problems described above. A potential solution to obtain semi-quantitative results would be by conducting an expert reader trial. This involves showing a group of expert readers (typically a selection of experienced radiologists) a selection of images, in a random order, reconstructed using the proposed approach or the reference approaches. The images are then scored (typically on a 5-point scale) for a variety of criteria. Relevant criteria for this work could include: perceived SNR, perceived temporal fidelity and ability to distinguish relevant anatomy such as the tip of tongue. The scoring results can then be analysed to determine if the proposed approach outperforms the reference methods. This is not a perfect method due to issues such as reader bias and fatigue [161]. However, it does provide a measure of how a group of clinicians judge a newly developed method against existing methods.

Finally, application specific metrics may provide a useful way to quantify image quality. For example, in speech imaging, a metric which has been proposed is the tongue boundary sharpness score, which attempts to quantify blurring at the air-tissue boundary of the tongue [71]. However, by their definition, these metrics are only useful for a specific application so cannot provide general measurements of image quality.

5.6 Summary

In this chapter, the rtMRI sequence and reconstruction pipeline introduced in Chapter 4 has been evaluated in the context of single-slice and SMS rtMRI. For single-slice rtMRI, it has been shown that a temporal resolution of up to 37.5ms is achievable. When SMS rtMRI acceleration is used it has been shown that this temporal resolution of 37.5ms is still achievable, however, at higher levels of SMS acceleration the temporal resolution must be reduced to preserve the image quality. The performance, in terms of image quality, between SMS GA and GA sampling is hard to determine. In the case of three slice SMS acceleration, the SMS GA sampling scheme results in a higher and more homogeneous tSNR. However, at higher levels of SMS acceleration, the GA sampling scheme shows improved performance. It is likely that fine tuning λ (at different levels of SMS and in-plane acceleration) for both sampling schemes is needed to fully determine which of the two schemes should be used. The effect of slice distance has also been evaluated for SMS rtMRI, it has been shown that, in the case of three slices, a slice gap of 2mm is achievable with no artefacts. However, further exploration is needed to understand the effect of higher SMS acceleration on slice distance. In addition to these results, this chapter has described the challenges, due to the lack of a ground truth and the reconstruction techniques used, in quantitatively evaluating image quality.

6 Dynamic MRI phantom of the oral cavity

6.1 Introduction

Using phantom objects in the design and evaluation of novel MRI sequences is standard practice [162]. Typically, and depending on the purpose of the new MRI experiment, phantoms are made of plastic sample tubes containing water or aqueous solutions, various hydrocolloids, small plastic objects with known dimensions (for example, LEGO bricks or plastic beads and rods) with or without added relaxation agents. Such phantoms are cheap, versatile, and easily accessible tools for laboratory-based work.

Where MRI methodology development is aimed at clinical applications, often the next step in the process will be scanning sessions with animals such as rats, or with healthy human volunteers. However, the step from water-filled plastic tubes to humans in the MRI scanner is large. Simple phantoms cannot reproduce the rich and dense structural details and functions of certain parts of the human anatomy. Furthermore, static phantoms are of limited use in the testing of dynamic imaging techniques such as real-time MRI [6, 4]. These shortcomings can be addressed by using a more anatomically realistic phantom with biomimetic structure and movements. This can provide an intermediate stage in the development of an MRI methodology,

allowing it to be evaluated to a more advanced level before animal or human subjects are required. It also allows for the exploration of experimental conditions that would otherwise not be feasible with human volunteers.

Real-time MRI of the oral cavity is an example of circumstances in which a dynamic phantom with semi-realistic anatomical features and MRI properties offers a useful intermediate step toward clinical applications. This chapter describes the design, construction and testing of a dynamic oral cavity phantom suitable for the evaluation of a range of rtMRI studies of the oral cavity.

The phantom described in this chapter was developed before the SMS rtMRI sequence was completed. Thus, only single-slice rtMRI results are shown in this chapter. Due to the limitations of the phantom (discussed in this chapter) SMS rtMRI data of the phantom was not acquired.

6.2 Phantom Design

As a complement to the standard T1/T2 weighted structural imaging toolkit, the emphasis of rtMRI investigations of the oral cavity is on functional/movement aspects. This defines the design criteria for the phantom. Considering the oral cavity and its mobile components, a modular oral-cavity phantom needs to include a mandible, a tongue, cheeks, and a floor of the mouth. Each of these components needs to have semi-realistic dimensions, range of motion, and range of movement speeds. Some of the natural movements of the mouth are compound and require concerted motion of some components, whereas other natural dynamic behaviours are more isolated (such as sticking the tongue out); this needs to be replicated by the phantom. The soft-

tissue equivalents in the phantom (tongue and cheek muscles) are made from agar gel commonly used in phantom construction [163]. The anatomy of the mandible includes cortical (compact) and cancellous (spongy) bone; this should also be reflected by the phantom. The assembly of the components should produce a cavity of dimensions like those of the human oral cavity. Non-destructive disassembly of the phantom must also be possible, for example, to facilitate replacement of agar gel inside the cavities. Finally, it must be possible to attach the phantom securely inside the scanner and head coils, whilst being able to activate and maintain various motions of the components such as opening and closing of the mouth during scanning.

6.3 Phantom Construction

The construction of the phantom is depicted in Fig.6.1. The acrylic frame of the phantom comprises of a front and back plate joined by an upper palate plate and two lower struts. Nylon fasteners, rather than glue, are used to join the acrylic plates and struts to enable easy disassembly and storage.

All structural elements of the phantom are confined to a compact cylindrical volume so that it may be used in a 30cm horizontal magnet bore but also easily adapted for use in the head coils of larger scanners. In the setup, a 3D printed bracket enables it to be clamped securely to a rear slot in the head coil (Fig.6.2).

The tongue has two cavities for filling with agar gel, mounted and sealed by clamping its flanged base between two acrylic plates (having two separate compartments of the tongue mimics the tongue's anatomy and a common post-surgical situation following partial resection and reconstruction of the

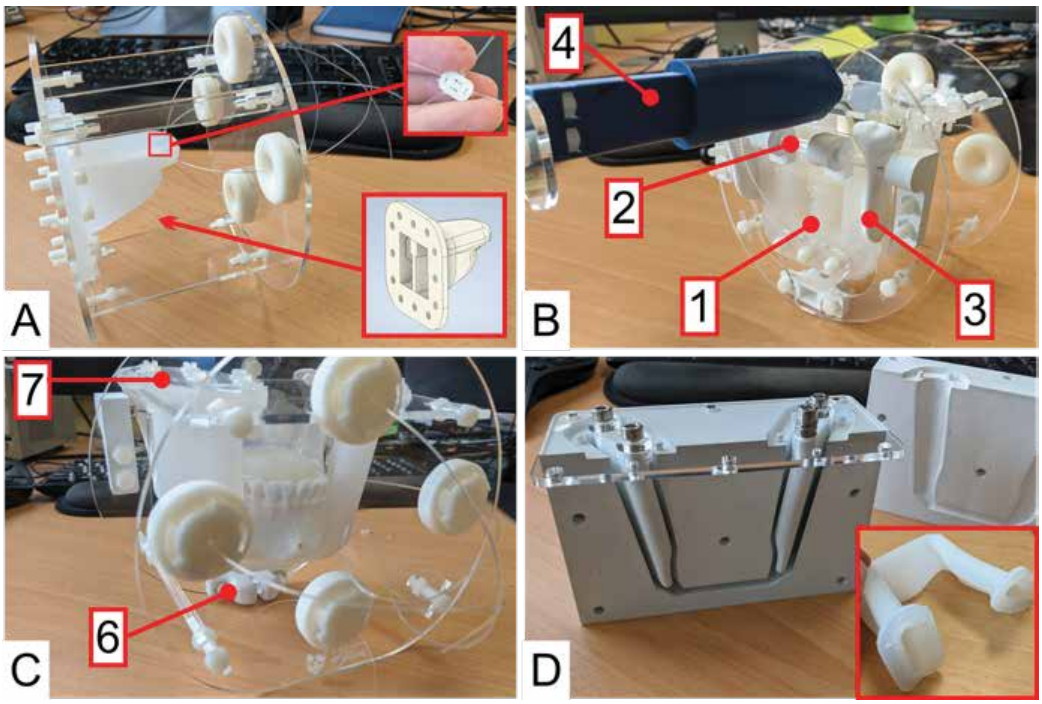

Figure 6.1: Making of the components of the phantom. A: actuation method, shown on early prototype with fixed-base tongue only. Insets show the embedded steering tip and tongue geometry. B: backplate view of full phantom assembly with mandible and cheeks. The tongue is now on a separate backplate (1), hinged from an acrylic rod (2) along with the mandible (3). Clamping bracket (4) secures the phantom in the head coil. C: front view of full assembly. Mandible is actuated by the lower control cable that passes round a pulley on the backplate (5). Cheeks are suspended from the palate plate (6) and they join underneath the mandible to form the floor of the mouth. D: multipart mould for silicone cheeks casting; inset shows resulting silicone.

tongue). Nylon cables tied to a plastic steering point are embedded in the tongue tip during the liquid-silicone casting process and passed through tapered 3D printed bushings mounted on the front plate. Puppet-like pulling of these cables thereby enables simple lateral movement in two axes, and the tongue can be stuck out by pulling multiple cables simultaneously. This allows for more random motion than could be achieved with MR compatible actuators that would always deliver similar movements. The cheeks each

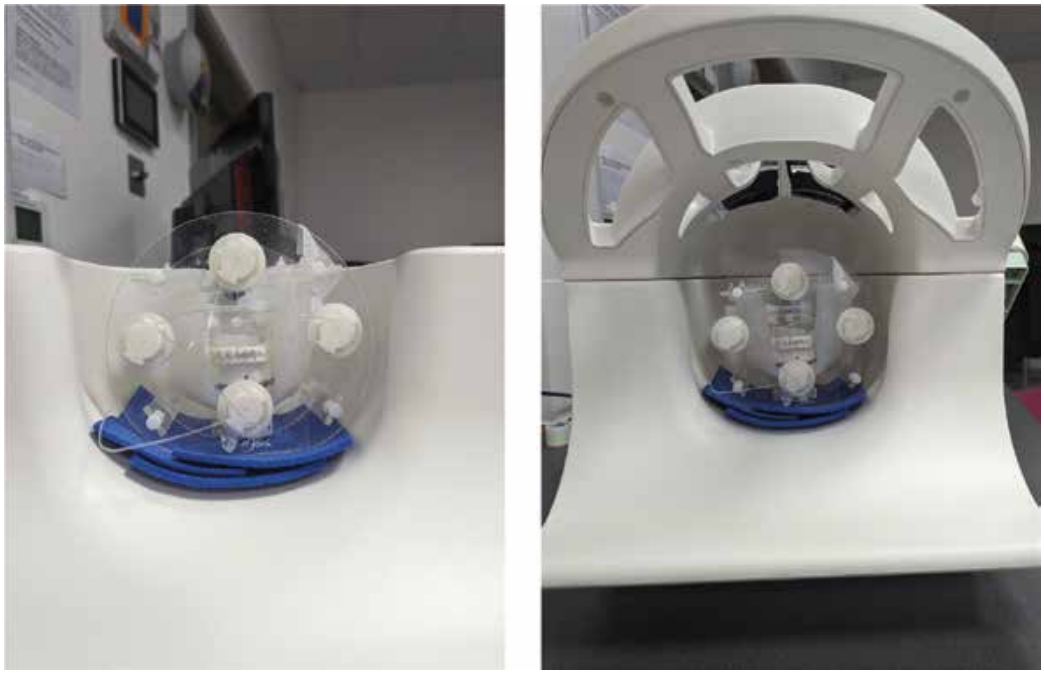

Figure 6.2: Phantom mounted in a head/neck coil array (64 coils) with (right) and without (left) the top section of the head coil attached

have a cavity for filling with agar gel, flanges like the tongue, and pass up and through holes in the palate plate to be secured and sealed by sandwiching the flanges between acrylic clamping plates and the topside of the palate. Clamping the flanges between acrylic plates prevents leakage from the agar gel-filled phantom cavities.

To incorporate mandibular motion, the tongue backplate and the mandible are suspended from an acrylic rod on the main backplate, allowing both parts to swing back around its axis. The lower control cable is attached to the chin and exits through the front plate via a pulley on the backplate, directing its pulling force along the correct line of action for opening the mouth. An opposite force is required to return it to the closed position, which is provided by the floor of the mouth upon which the mandible rests. This is integrated

with the cheeks in a single silicone casting. The cheeks stretch when the mandible pivots downwards and provide an elastic restoring force to pull the chin back up again.

The silicone parts are cast in 3D printed moulds with laser cut lids with holes for air to escape as they fill. Cavities for filling with agar gel are created by attaching 3D printed inserts to the lid, which project into the casting volume and hence leave behind voids when they are removed. Liquid silicone is injected upwards into a hole in the mould base to avoid trapping air bubbles, which is then plugged while the silicone cures. For the cast silicone to be removable, it must neither enclose nor be enclosed by plastic in the direction of removal. For this reason, the moulds have an open-ended design, and consist of multiple segments clamped together with bolts, such that the mould can be disassembled to release the casting.

6.4 Methods

The tongue, bilateral floor of the mouth and cheeks were constructed from moulded silicone 'skins' (Smooth-On Ecoflex00 − 20 FAST) and filled with agar hydrocolloid (Biozoon, Germany; concentration of 2g per 100ml of water). The mandible was derived from a 3D scanned STL mesh model of a human mandible (donated, from high-resolution CT scans), processed with Autodesk Meshmixer to form a printable hollow solid, and 3D printed on a Stratasys F170 using Stratasys acrylonitrile styrene acrylate (ASA) plastic to represent the cortical bone. Hollow spaces inside the mandibular structure were filled with plaster (West Design Products, UK) to represent cancellous bone in the mandible. The phantom frame was constructed using laser cut

3mm acrylic sheet (Hindleys, UK). M5 and M3 nylon fasteners were used to attach the different parts of the phantom to the frame. Nylon strings were attached to the tongue and jaw to provide a mechanism for moving them. The associated hinge and pivot parts were created from 6mm solid acrylic rod and 3D printed ASA plastic.

Single-slice rtMRI data is acquired using the sequence developed in Chapter 4, both sagittal and axial videos are acquired. The imaging parameters described in Section 4.3 are used and the data is binned to 95 spokes/frame. A sliding window with a stride of five is used to increase the apparent temporal resolution from 243ms to 17ms. During the acquisition, the wires controlling the tongue are pulled forward and upwards (simulating the action of sticking the tongue out). Image reconstruction is performed on the scanner using the gridding reconstruction method (Section 4.4).

6.5 MRI Use of the Oral-Cavity Phantom

Frames from a single-slice rtMRI video are shown in Fig.6.3 (Video 6.1). In the sagittal orientation, the tongue and chin can be clearly seen. The tip of the tongue displays a dark area where the plastic steering point has been embedded. The axial/transverse view shows the two cheeks of the phantom and highlights the two compartments of the tongue. These two compartments could be filled with slightly different agar (or other) hydrocolloids, which, due to differences in relaxation properties, would result in slightly differing contrast across the two compartments and, thus, could mimic the local situation after surgical tongue reconstruction.

The SNR of these reconstructed frames appears lower than in the equiv-

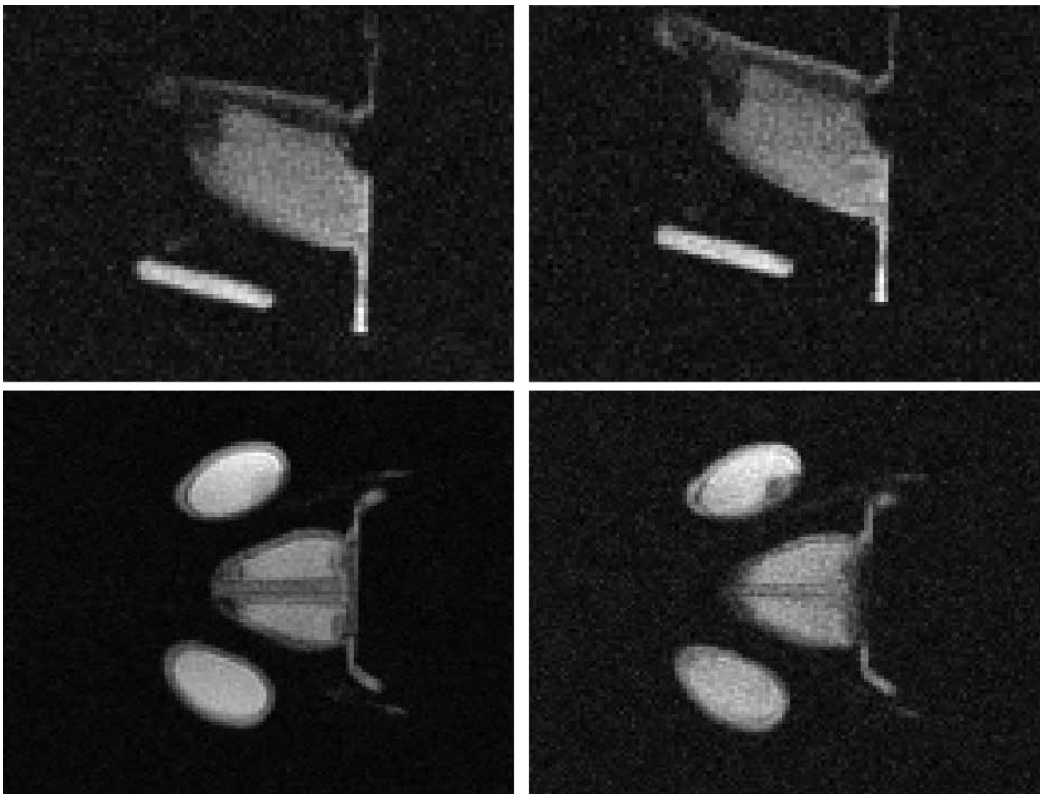

Figure 6.3: Two frames each taken from rtMRI videos of the phantom where the tongue is being moved up and stretched forwards. Top: sagittal orientation. Bottom: axial orientation.

alent imaging conducted on the oral cavity of a human. This is due to the lower proton density present in the phantom. The only MRI-active parts of the phantom are the agar gel-filled pockets of the tongue and cheeks, whereas the human oral cavity contains many more MRI-visible types of different soft tissues. This lower proton density also makes automated shimming challenging. Despite this, contrast in the phantom-based rtMRI videos is sufficient to resolve the dynamics of important small features of the phantom such as the tip of the tongue.

The phantom is also a useful tool to observe the effects of surgical reconstruction plates on image quality. Reconstruction plates are routinely used in oral and maxillofacial surgery, thus, understanding artefacts caused by them is important if imaging post-surgery is required while the reconstruction plates remain in situ. Artefacts induced by susceptibility effects vary between different pulse sequences (and between parameters in these sequences), as well as for products and materials from different manufacturers. In the phantom, reconstruction plates are attached by screwing them onto the mandible, similar to typical clinical use (Fig.6.4). As the mandible is filled with plaster (to emulate cancellous bone), the screws can thread into this material and securely attach the plate to the phantom.

With a selection of small to medium sized reconstruction plates (Medartis, Switzerland) in place, imaging experiments previously carried out in the absence of reconstruction plates were repeated. Images obtained with and without reconstruction plates in two planes are shown in Fig.6.5 and Video 6.2. Approximately 4.5 cm from the plates, no distortion of the tongue and cheek region is visible in images of the phantom. For relatively small plates

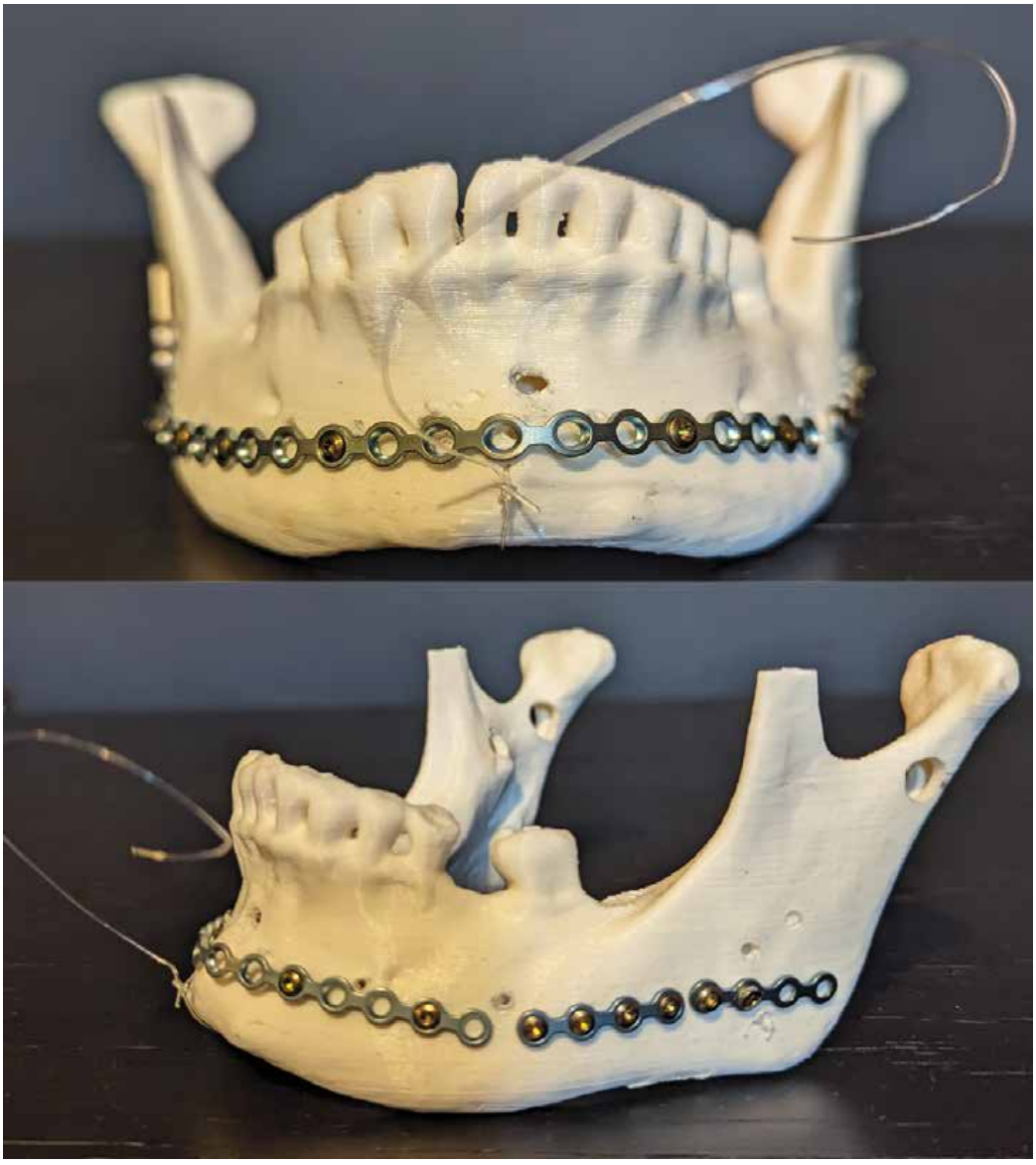

Figure 6.4: Pictures of surgical reconstruction plates attached to the phantom mandible; front view (top) and side view (bottom). The plates are Medartis 20-hole straight plate, 6-hole straight plate, and 4-hole straight plate, respectively.

and screws (7mm) made from non-magnetic materials cpTi (plates) and Ti alloy (screws), the distance from the mandible to the tongue and cheek positions is sufficient to provide undistorted images of these areas. The high receiver bandwidth (1447Hz/pixel) used will also reduce susceptibility artefacts. Increased distortion can be seen when larger plates, designed to replace the entire mandible, are imaged (Fig.6.5, bottom row). These findings are relevant for clinical practice as post-operative MRI (and rtMRI) diagnostics play an important role, for example, in monitoring for the recurrence of malignant tumours of the oral cavity.

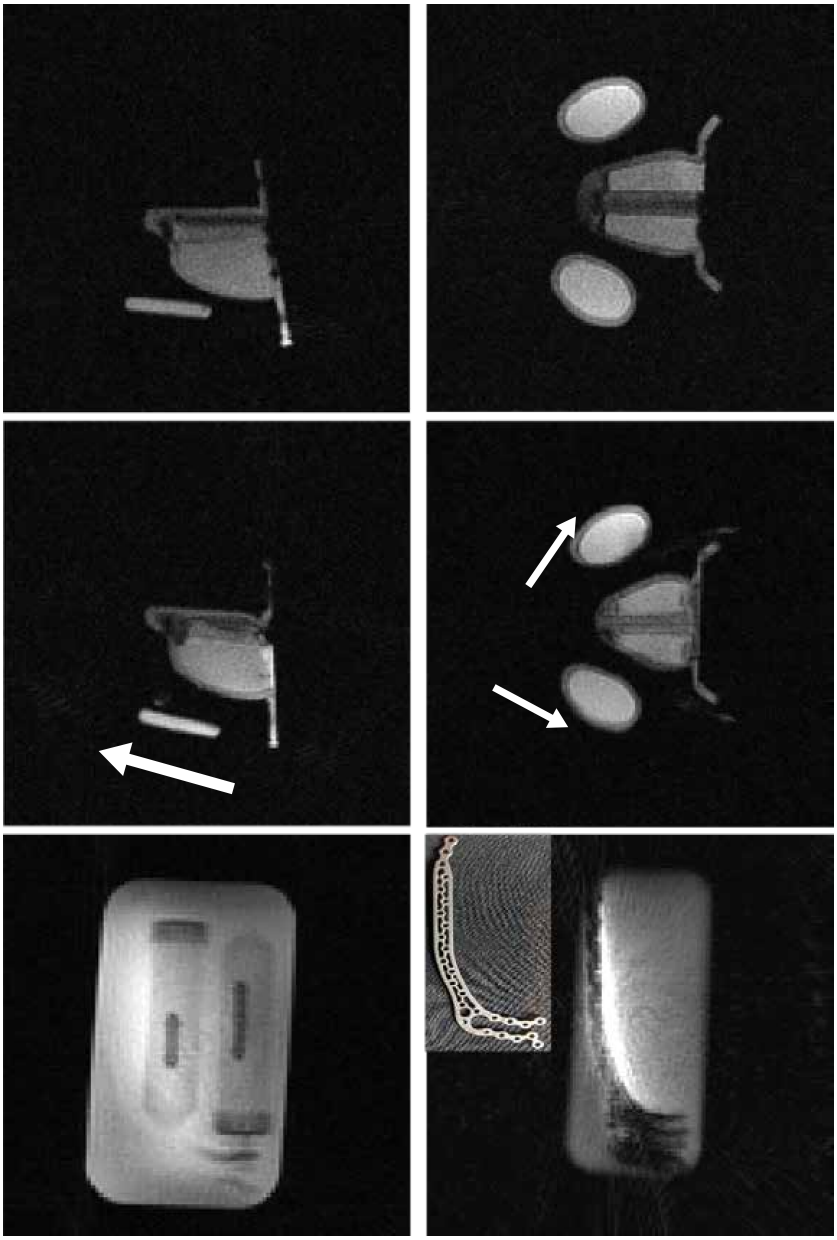

Figure 6.5: Effects of reconstruction plates on image quality. Top: frames of rtMRI videos without reconstruction plates attached, sagittal (left) and axial (right) planes shown. Middle: identical rtMRI frames obtained with mini-plates and a medium-sized plate screwed onto the mandible (see Fig.6.4). The white arrows indicate the approximate position of the mandible and metal plates. There is no image distortion from the presence of the reconstruction plates in the tongue and cheek region. Bottom: static MRI images of mini-plates (left) and large mandibular replacement plate (right) directly immersed into agar gel, demonstrating the limited short-range image distortion effects of this type of reconstruction plates.

6.6 Summary

The current design of the phantom is a useful platform to test dynamic MRI sequences and to evaluate susceptibility artefacts due to the presence of surgical reconstruction plates. There are two main aspects of the phantom which require further development, the first is improving the SNR (which is low due to the reduced proton density), this could be achieved by increasing the size of the tongue and cheeks so that they can store more agar. The second aspect which could be further developed is the movement mechanism of the tongue, which currently only produces small-range movements. A possible alteration could be moving the anchor point deeper into the tongue structure or adding additional semi-flexible structures to distribute the pulling force more evenly across the tongue. Due to the limitations of the phantom it was decided that scanning using the SMS rtMRI sequences would be done on volunteers rather than using the phantom.

7 Applications of Compressed Sensing Real-time MRI

7.1 Introduction

The objective of this chapter is the exploration of future applications of the developed rtMRI sequence and to give a broad context of how this sequence may be a useful addition to current clinical imaging methods.

The first section discusses head/neck imaging. This can be considered as a subset of musculoskeletal imaging (MSK). However, imaging of the head/neck poses unique challenges (compared to other areas of anatomy) due to its wide range of functions which involve multiple anatomical structures. In addition to this, there are a large number of air/tissue and tissue/tissue interfaces. The second section explores more general MSK applications such as knee and wrist imaging.

7.2 Head/Neck Imaging

The use of MRI in head/neck imaging is now well established. For example, MR angiography is routinely used for the investigation of blood vessels when planning surgery [164]. In addition to these standard sequences, more ad-

vanced sequences such as diffusion weighted MRI are finding their place in clinical imaging [165]. Current imaging techniques provide static information and do not capture the extensive and important dynamics of the oral cavity. Imaging methodologies to image the dynamics of the oral cavity include ultrasound and video fluoroscopy [166, 167]. These techniques suffer from poor image quality (in the case of ultrasound) or require the use of ionizing radiation (video fluoroscopy). rtMRI enables the recording of function at both high spatial ($2.2mm^2$) and temporal resolutions (up to 37.5ms) without the need for ionizing radiation. This section demonstrates a variety of potential applications of both single-slice rtMRI and SMS rtMRI in the context of imaging the dynamics of the oral cavity.

7.2.1 Speech

Real-time MRI is emerging as a useful technique to study the dynamics of speech. For example, Niebergall et al. (2013) demonstrated the use of rtMRI to study vowel formation in German speakers [156]. Chen et al. (2019) used rtMRI, at a temporal resolution of 28ms, to study the deformation of the tongue during speech [168]. Works by Wiltshire at al. (2021) and Lu et al. (2022) used rtMRI (at a temporal resolution of 33ms) to study the dynamics of speech in people who stutter [169, 170]. These works show the potential linguistic and clinical applications of rtMRI in the context of speech imaging.

For a demonstration of speech imaging using the rtMRI sequence developed in this thesis, the imaging of vowel pronunciation is performed (in English). During rtMRI acquisition, the healthy volunteer pronounces each vowel. This experiment is performed at two different spatial resolutions, the

first uses a spatial resolution of 2.2mm^2 (Video 7.1) and the second experiment uses a resolution of 1.1mm^2 (Video 7.2). To enable this higher spatial resolution, the TR is increased from 2.5ms to 2.9ms. For the 20 spokes/frame reconstruction shown in Fig.7.1 this increase in TR results in a reduction of temporal resolution from 50ms to 58ms.

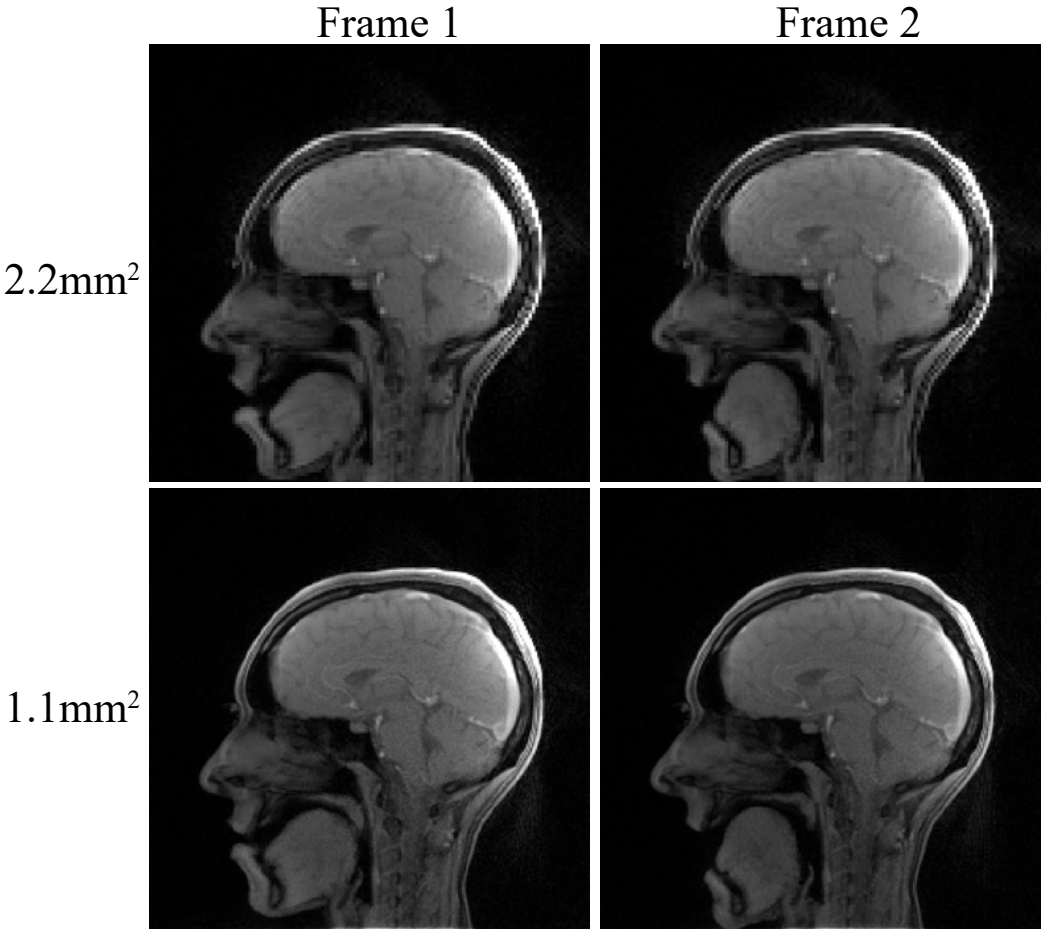

Figure 7.1: Comparison of frames from rtMRI videos reconstructed at spatial resolutions of 2.2mm^2 (top) and 1.1mm^2 (bottom).

The benefit of a higher spatial resolution is shown in Fig.7.2, the higher spatial resolution frame (right) shows improved delimination between anatomical structures such as the tongue-air boundary and the lips. Fig.7.3 shows

examples of x-t and y-t plots extracted from the high-resolution rtMRI speech data. These plots allow important aspects of speech such as the change in airway size and the raising of the tongue to be visualised.

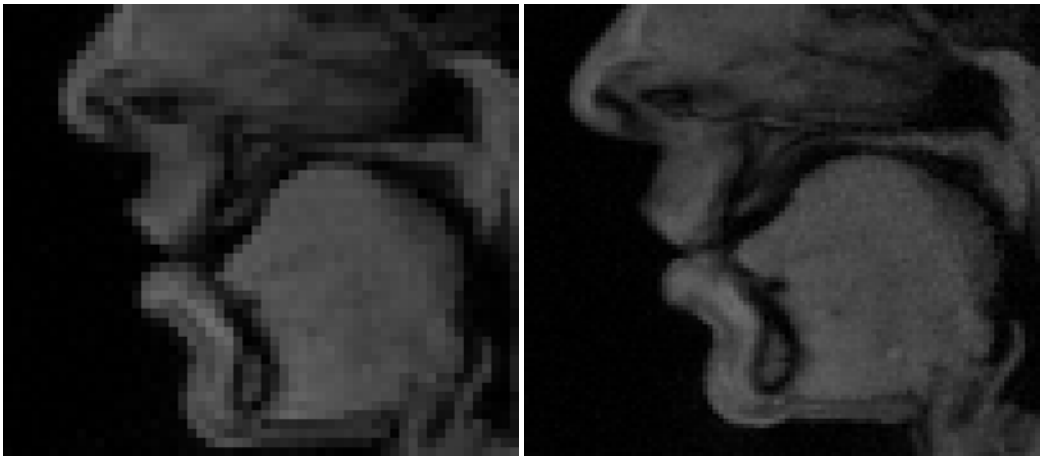

Figure 7.2: Comparison of a low resolution (2.2mm^2, left) and a high resolution (1.1mm^2, right) rtMRI frame. In both cases the mouth is zoomed into to highlight improved delimitation of features such as the tongue-air boundary and tips of lips.

The majority of rtMRI speech studies (including the works cited above) use a single slice (typically mid-sagittal) acquisition approach. An exception to this is a 3D spiral sequence developed by Zhao et al. (2021) [171]. In this work, the authors show that their sequence can be used to acquire 12 slices with a temporal resolution of 61ms. However, their method requires careful manual shimming and off-resonance correction to minimise distortions introduced through spiral sampling. In addition to this, a custom coil designed for speech imaging is used. The SMS rtMRI sequence developed in this thesis presents an alternative method to acquire speech data from multiple locations without the need for these shimming and correction strategies. SMS rtMRI data of vowel formation is acquired using the developed sequence

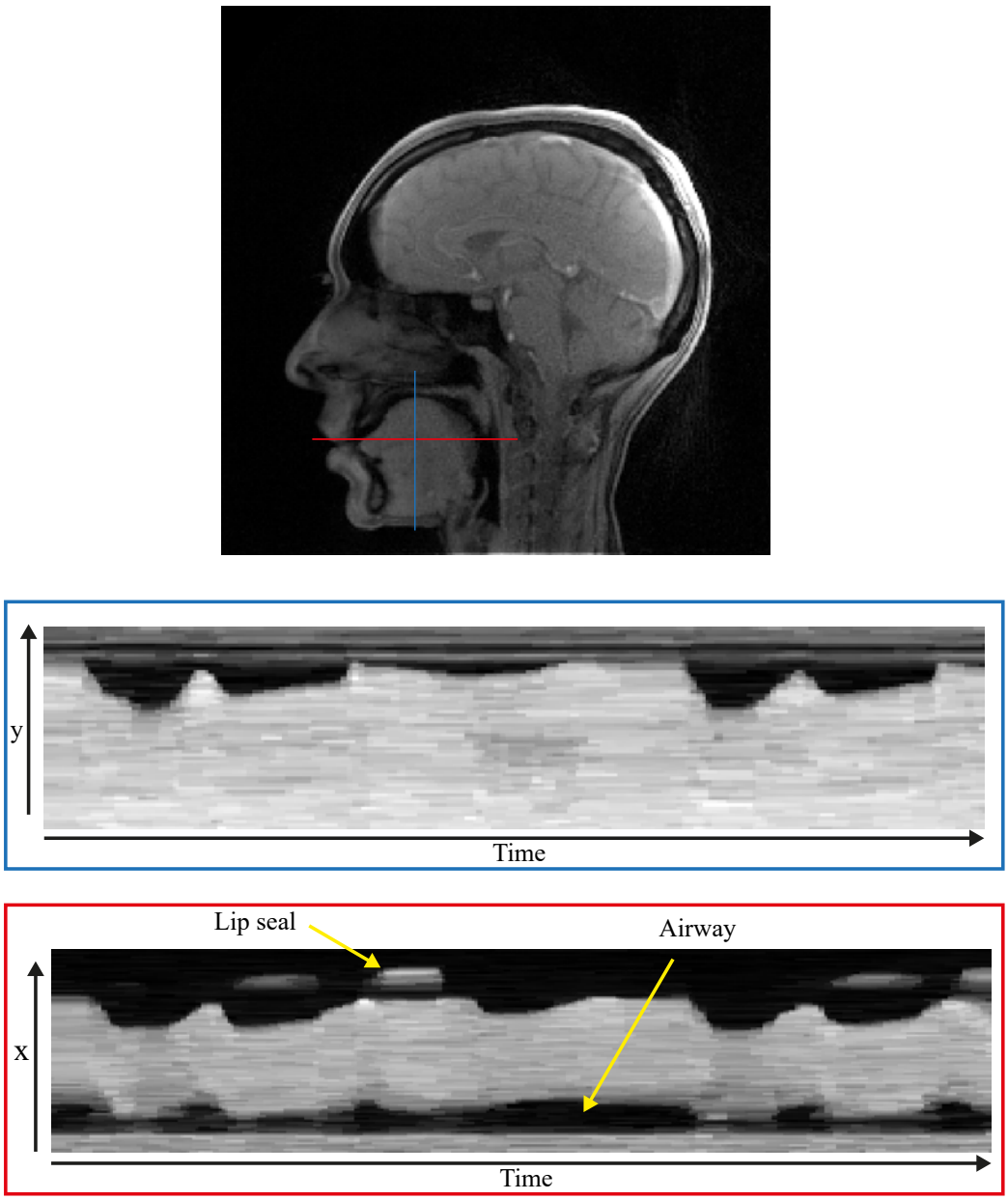

Figure 7.3: Top: a frame from a single-slice rtMRI video of speech. The blue line is used to form a y-t plot (middle) and the red line is used to form a x-t plot (bottom).

(three slices 12mm apart are acquired (Video 7.3)). Fig.7.4 shows two frames (25 spokes/frame) from the rtMRI, important structures (in the context of

speech imaging) are identifiable such as the tip of the tongue and the lips. Acquiring multiple slices is advantageous as it allows the imaging of movement, which is not solely confined to the center of the head. An example of this is the pronunciation of some consonants, which results in lateral stretching of the tongue and airway [171]. It may also be important when imaging patients with a structural asymmetry, such as a partial glossectomy (in which a section of the tongue is resected), as function may only be impacted on a specific side of the tongue [172].

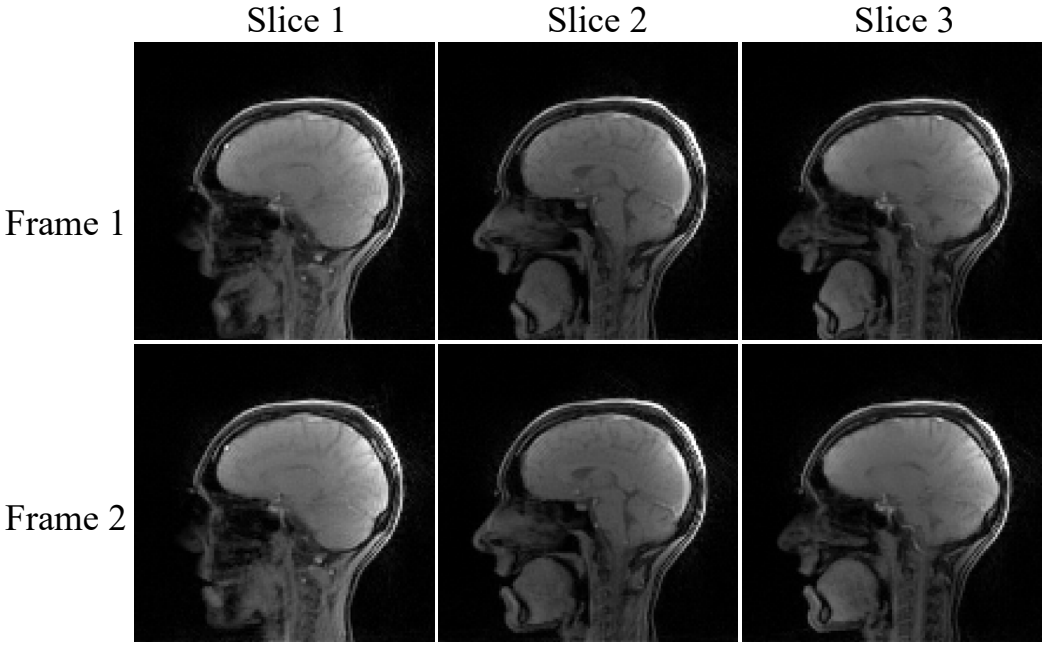

Figure 7.4: Two frames from an SMS rtMRI video of vowel formation. Each frame consists of three slices (12mm) slice distance.

7.2.2 Swallowing

The action of swallowing is a complex movement involving a variety of anatomical structures. Disease and surgical interventions can result in patients having difficulty swallowing, this is referred to as dysphagia [173]. The current standard technique to investigate dysphagia is video fluroscopy, which requires the use of ionizing radiation [167]. rtMRI provides an alternative method to monitor the dynamics of swallowing without the need to use radiation. An example of this is demonstrated by Zhang et al. (2012), in this work single slice rtMRI is used to image the swallowing of pineapple juice (which due to the presence of paramagnetic manganese ions is a natural contrast agent [174]) in healthy volunteers [154]. In terms of clinical applications, a pilot study of using rtMRI to image swallowing of yogurt in post-treatment tongue cancer patients was performed by Zu et al. (2013) [175]. The authors showed that the transit time of the bolus (i.e. the time it takes for the yogurt to move from the front to the back of the mouth) in cancer patients is longer than in healthy volunteers.

Both of the previously cited studies used a single slice radial rtMRI sequence. A multislice sequence is demonstrated by Voskuilen et al. (2020) [159]. In the work by Voskuilen et al. (2020) a 3D radial sequence (7 slices, 6mm slice thickness) is used to monitor the swallowing of pineapple juice in healthy volunteers at a temporal resolution of 83ms. However, as stated by the authors, this 3D radial technique suffers from significant blurring artefacts due to the large amount of undersampling required to achieve the high temporal resolution.

Video 7.4 and Fig.7.5 show an example of imaging the process of swallow-

ing using the proposed SMS rtMRI sequence. During the SMS rtMRI acquisition (25 spokes/frame, temporal resolution: 62.5ms) the volunteer performed a dry swallow (i.e. swallowing saliva rather than a bolus of food/liquid). In both the x-t plot and the video, the transportation of the bolus is visible. Although the central slice shows the most information, in terms of viewing the transportation of the bolus, the additional slices help to demonstrate the large scale movement of the tongue required to transport the bolus from the front of the mouth to the back.

The dry swallow task performed is not optimal as it does not fully replicate the physiological processes of a loaded swallow. However, it provides a demonstration that the proposed SMS rtMRI sequence can be used for this imaging application.

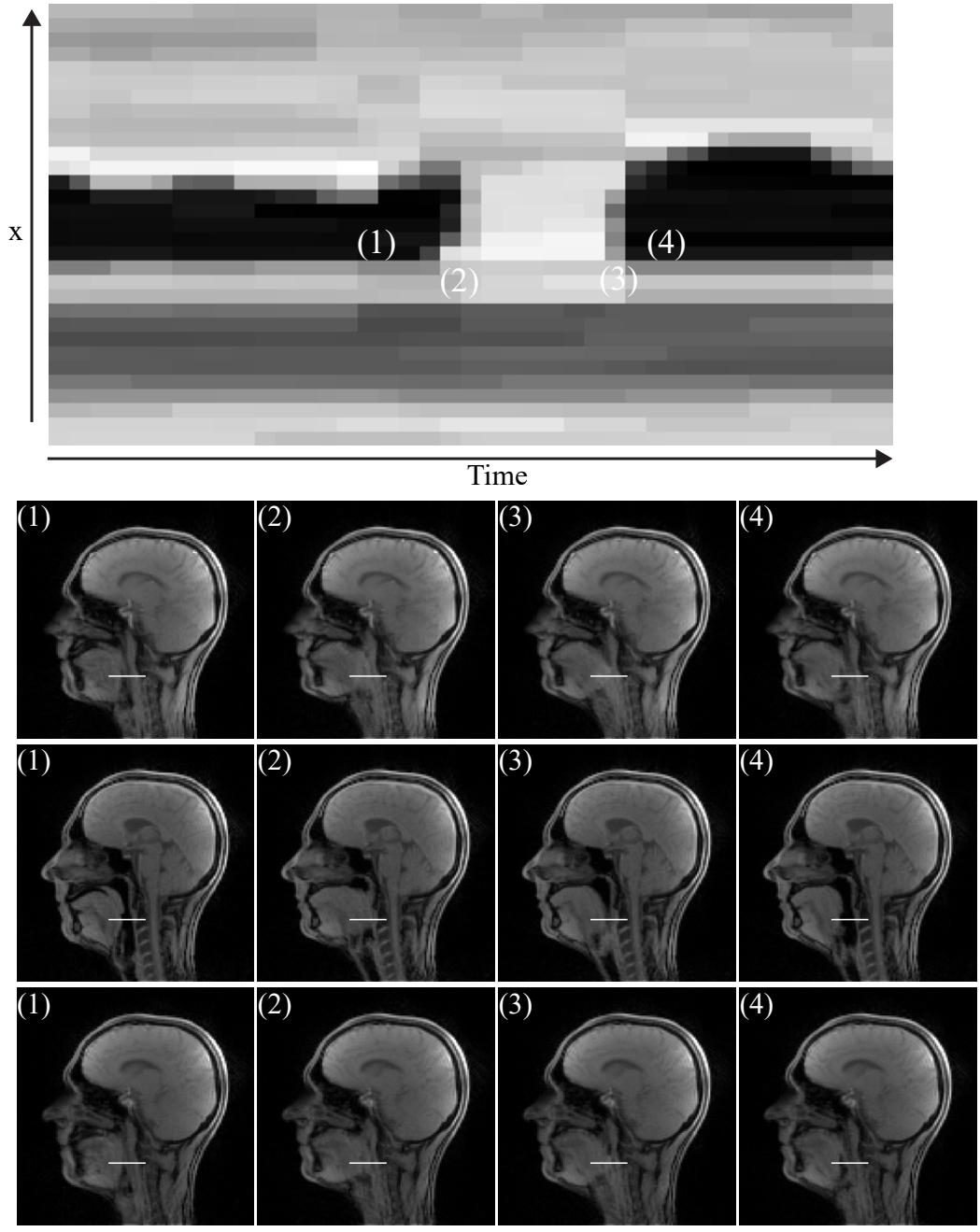

Figure 7.5: Top: x-t plot (from central slice) of a dry swallow, the transportation of the bolus between (1) and (4) is visible. Bottom: three slices from a three-slice rtMRI acquisition. The white lines across the images indicate the position of the x-t plot.

7.3 Dynamic Musculoskeletal Imaging

The imaging of joint kinematics is an emerging application of rtMRI [4]. Early attempts to use MRI to study joint movement recorded static images of the joint at different positions rather than recording a time series of images. In contrast, rtMRI allows continuous motion to be recorded [4]. The advantage of this is that it allows for the full range of motion to be recorded rather than a few positions.

7.3.1 Example Applications

To demonstrate an example of dynamic MSK imaging, the proposed SMS rtMRI sequence is used to record the knee movement of a healthy volunteer. The imaging parameters described in Section 4.3 are used with 3 slices acquired simultaneously. Video 7.5 and Fig.7.6 show the results from this acquisition binned to 15 spokes/frame (37.5ms temporal resolution). These results show the large bulk motion which occurs in knee movement can be recorded using rtMRI. However, due to the use of a small volume coil only a small portion of the knee's anatomy is visible. This issue could be resolved through the use of flexible contour coils which can be wrapped around the anatomy of interest.

Imaging the dynamics of the knee offers insight into joint kinematics that standard static scans cannot achieve. The dynamic information can be used to inform biomechanical models of the joints and muscles. For example, Draper et al. (2008) showed that (single-slice) rtMRI can be used to model the tilt of the patella as the knee is flexed [176]. The authors stated that a limitation of the single-slice rtMRI approach is the inability to model

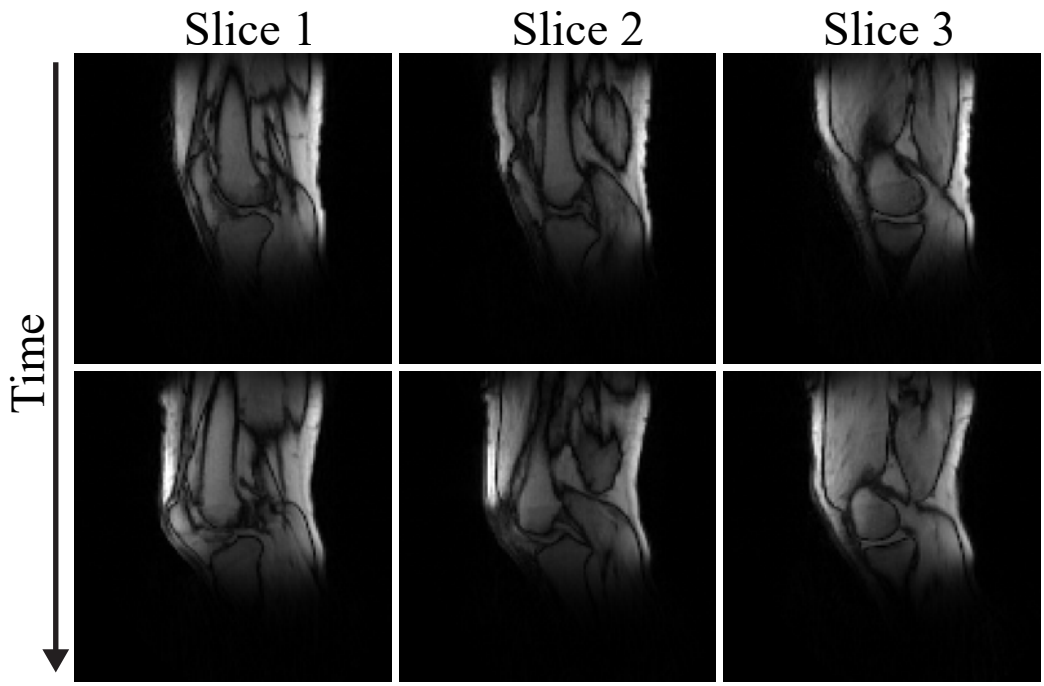

Figure 7.6: Two frames from a SMS rtMRI video, each frame consists of 3 slices. The knee begins at rest (top) and is then bent (bottom).

through-plane motion. SMS rtMRI may allow these values to be calculated for multiple locations simultaneously enabling a more 3D view of knee kinematics rather than a single slice.

The imaging of foot/ankle movement was also explored using the developed rtMRI sequence (Fig.7.7). During rtMRI acquisition (15 spokes/frame, Video 7.6) a healthy volunteer moved their foot from a tilted upwards position (dorsi flexion) to a tilted downwards position (plantar flexion).

rtMRI data of foot/ankle movement could be used to calculate bio-mechanical properties of muscles/joints. For example, muscle moment arms which provide a measure of a muscle's ability to produce torque [177]. This information is useful when determining how disease/rehabilitation affects the performance of a muscle [178, 179]. The calculation of muscle moment arms in the ankle

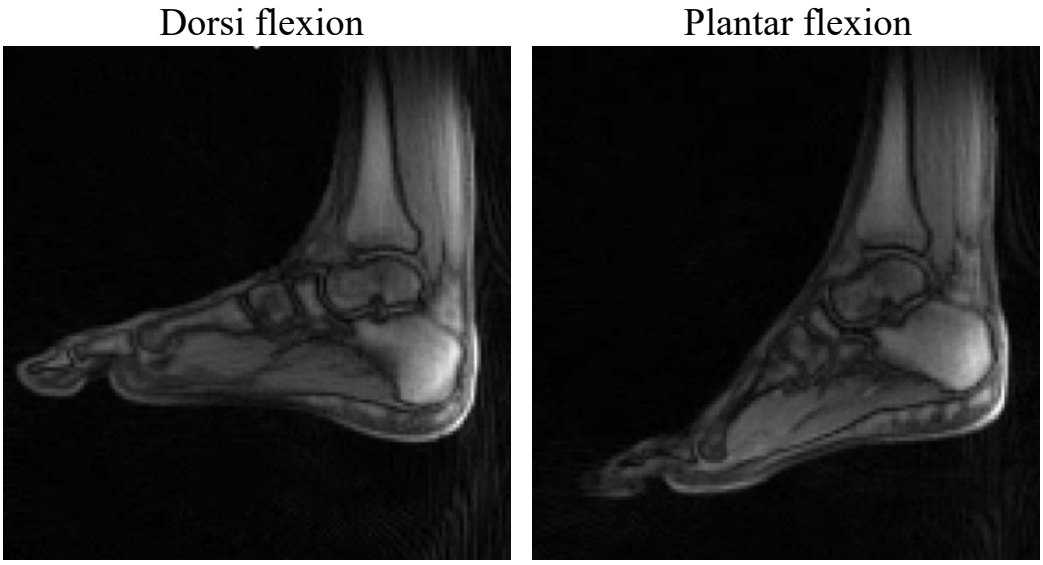

Figure 7.7: Two frames from a single-slice rtMRI (15 spokes/frame) video of foot/ankle movement showing the foot in the dorsi flexion (left) and plantar flexion (right) positions.

(using MRI) has been demonstrated by Clarke et al. (2015), the authors used a Cartesian sampling scheme to image the movement of the ankle and the images were then used to calculate the moment arms [180]. In the work by Clarke et al. (2015) the ankle was moved very slowly (to avoid motion artefacts) resulting in a 2 minute acquisition time. The proposed rtMRI scheme is more robust to fast motion and using SMS rtMRI will allow for improved anatomical coverage. Using rtMRI in this context would require the development of automated segmentation algorithms to extract the required joint/muscle positions for each frame.

Finally, imaging of wrist motion, in which the hand is moved horizontally from side to side, is attempted using the single-slice rtMRI sequence. From the results (Fig.7.8, Video 7.7) it is possible to extract individual frames where the structures in the wrist can be identified; however, during move-

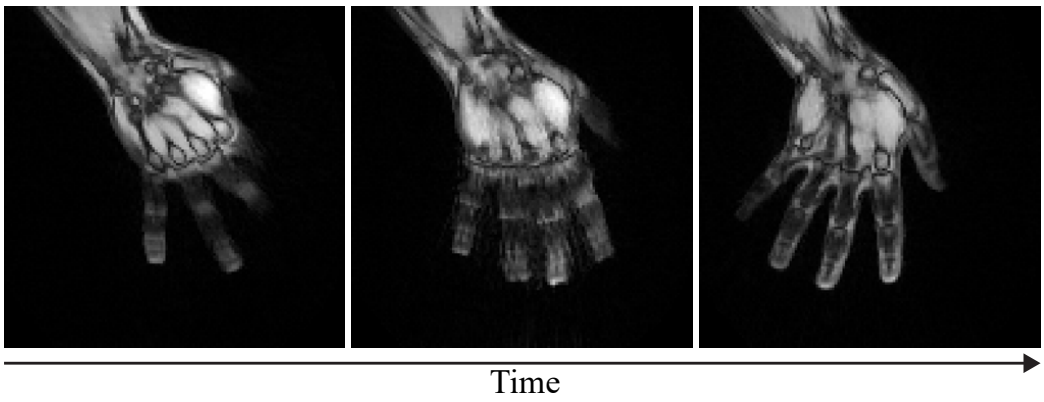

Figure 7.8: Three frames from a single-slice rtMRI video of wrist movement. In the central frame blurring is visible.

ment, signal dropout and blurring occurs. This could be due to through-plane motion as there is nothing to prevent the subject's wrist from vertical movements rather than solely horizontal ones (which are in-plane). An improved experimental setup which confines wrist mobility to the desired imaging plane may help reduce this problem.

The sequence parameters and regularization parameters used in these examples are optimized for the head/neck imaging task described in Chapter 5. Significant improvements in image quality are likely achievable through optimizing the acquisition and reconstruction parameters such as field-of-view, slice thickness, in-plane resolution and regularization level. For example, in wrist imaging it has been shown that a 6mm slice thickness (compared to the 8mm used in this thesis) enables improved visualisation of wrist structures [181]. An additional technique which may improve image quality is the use of multiple coil sensitivity profiles binned into different motion states. This could reduce the blurring seen in some applications, particularly the wrist motion application, which contains both through and in-plane motion.

7.3.2 Limitations

In MSK imaging it is desirable to have good contrast between water, fat and muscle. The current GRE sequence lacks this contrast. There are two main approaches to overcome this issue. The first is the use of a multi-echo GRE sequence [182, 183]. A demonstration of this is shown in a work by Tan et al. (2019) in which a rtMRI sequence is adapted to acquire 3 echoes per TR [184]. The authors use the multiple echos to obtain water and fat separated rtMRI videos of the knee at a temporal resolution of 70ms.

The second approach is to use bSSFP sequences (discussed briefly in Chapter 4) which have higher SNR and improved contrast compared to GRE sequences [4, 185]. For example, in a work by Mazzoli et al. (2017) a bSSFP rtMRI sequence, with water-fat separation, is used to image the movement of the knee and wrist, however, the temporal resolution is low (250ms for knee imaging and 100ms for wrist imaging [142]).

7.4 Summary

This chapter has demonstrated the potential applications of the developed rtMRI sequence in head/neck imaging and more general MSK applications. Application specific parameter optimization and improved experimental set-up is needed to further improve image quality.

8 Conclusion and Future Work

8.1 Conclusion

This thesis had three principle objectives. These were introduced in Chapter 1 and are repeated below:

- The development of real-time MRI imaging methodologies capable of recording movement at a temporal resolution of up to 37.5ms and spatial resolution of $2mm^2$ in multiple (1-7) locations simultaneously.
- The development of an image reconstruction pipeline capable of reconstructing both single-slice and simultaneous multislice real-time MRI data, with improved image reconstruction quality compared to standard reconstruction approaches.
- The exploration of fast imaging sequences in a variety of clinical and sports science applications.

Addressing objectives one and two, Chapter 4 and Chapter 5 described the development and testing of an rtMRI sequence capable of both single-slice and, using SMS acceleration, multi-slice data acquisition. In addition, a CS reconstruction pipeline capable of handling the acquired rtMRI data was developed. Specifically, it has been shown that three-slice SMS rtMRI

images can be obtained with adequate image quality (in terms of contrast, edge sharpness and noise level) at a 2.2mm^2 in-plane resolution and 37.5ms temporal resolution. However, further improvements in the reconstruction pipeline to improve image quality at higher levels (five to seven) of SMS acceleration are required. Currently, at higher SMS acceleration, the temporal resolution must be sacrificed to achieve a comparable image quality to three-slice acceleration, which may not be acceptable in some applications.

The third objective of the thesis aimed to explore potential applications of rtMRI (both single-slice and SMS rtMRI). This thesis demonstrated the use of SMS rtMRI to image functions such as speech and (dry) swallowing. The simultaneous acquisition of multiple slices helps to demonstrate that the movement of anatomical structures underlying these functions is not confined to a single-slice. Currently, these are the main applications for the rtMRI sequence developed in this thesis, as high (37.5ms) temporal resolutions can be achieved with good contrast, edge sharpness and low noise levels. Applications in MSK imaging were also explored. However, more sequence development/optimization is required to overcome current limitations with contrast and through-plane motion artefacts.

In summary, this thesis has shown the development of both the sequence and reconstruction pipeline to enable SMS rtMRI at temporal resolutions of up to 37.5ms (higher can be achieved if image quality is sacrificed). The output and future directions of this work is two-folded. The first is further technical developments in acquisition and reconstruction. The second is deeper exploration of how the sequence can be used in clinical/research applications. This will require close collaboration with clinicians to iden-

tify more applications, help design the rtMRI imaging protocols required for these applications and integrate rtMRI images with high-resolution static structural scans for improved data visualisation [136].

8.2 Future Work

The current capabilities of the sequence and reconstruction pipeline developed in this thesis open up new avenues for future work (in addition to further clinical exploration of rtMRI) both on the methodological side and on supporting other MRI applications (such as neuroimaging and X-nuclei imaging).

8.2.1 Sequence Development

This thesis has shown that rtMRI can be used to record joint movement at temporal resolutions of up to 37.5ms. This may enable the calculation of dynamic moment arms in the knee and ankle [179, 180]. However, in the context of MSK imaging, the current sequence is not optimal due to poor contrast between different tissue types. As discussed in Section 7.3.2, the use of a bSSFP pulse sequence may provide the solution to this problem; bSSFP with SMS acceleration has been demonstrated in cardiac imaging (using Cartesian sampling) [131]. Implementing a rtMRI bSSFP sequence would also benefit cardiac imaging applications due to improved blood/muscle contrast of bSSFP over GRE sequences [186].

The radial trajectories used in this thesis enable the high level of undersampling required to achieve high temporal resolutions. Exploration of

alternative trajectories and how they compare to the radial trajectories, is another area of future work. In particular, the development of a spiral SMS sequence may enable higher temporal resolutions due to the more efficient k-space sampling compared to radial sampling [187].

8.2.2 Low-Rank Reconstruction

The compressed sensing reconstruction models used throughout this thesis have exploited the sparsity present in real-time MRI data, particularly in the temporal dimension. An additional element that can be exploited is the spatiotemporal correlations present in the rtMRI data. A method called low-rank (LR) reconstruction is increasingly being used to achieve this [188]. In the context of dynamic MRI, LR reconstruction aims to recover a time series of images from undersampled k-space measurements by exploiting underlying temporal correlations. LR techniques typically involve generating a Casorati matrix, $\mathbf{X}$. The structure of $\mathbf{X}$ is defined in eq.(8.1) where $x(r_i, t_j)$ is the value of pixel $i = [1, \ldots, M]$ at time point $t = [1, \ldots, Nt]$.

$$\mathbf{X} = \begin{bmatrix} x(r_1, t_1) & x(r_1, t_2) & \ldots & x(r_1, t_{Nt}) \\ x(r_2, t_1) & x(r_2, t_2) & \ldots & x(r_2, t_{Nt}) \\ \vdots & \ddots & x(r_i, t_j) & \vdots \\ x(r_N, t_1) & x(r_M, t_2) & \ldots & x(r_N, t_{Nt}) \end{bmatrix} \tag{8.1}$$

The singular values, $\sigma = \text{diag}(\mathbf{\Sigma})$, of $\mathbf{X}$ can be found using SVD (eq.(8.2)). From Fig.8.1 it can be seen that the magnitude of the singular values decays rapidly; this means that the majority of useful information is stored in relatively few singular values. This in turn indicates that there are strong

spatiotemporal correlations present in the image time series. Mathematically, this implies that the matrix is low-rank, meaning that few columns of matrix $\mathbf{X}$ are linearly independent [189].

$$\mathbf{X} = \mathbf{U}\boldsymbol{\Sigma}\mathbf{V}^{\mathbf{H}} \tag{8.2}$$

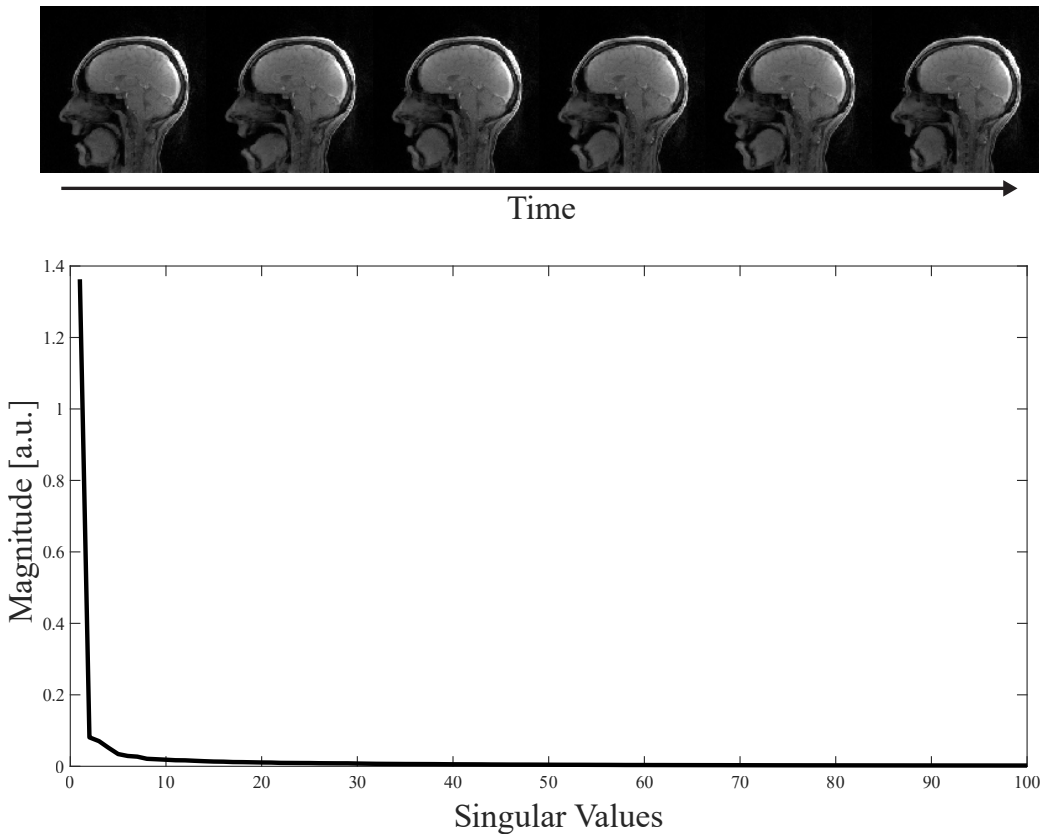

Figure 8.1: Top: 10 frames extracted from a single-slice rtMRI video consisting of 100 frames to show the changes in the image domain over time. Bottom: the plot of singular values from this rtMRI video, the rapid decay of the magnitude of singular values can be seen.

The LR reconstruction model is based on the optimization problem shown in eq.(8.3), where $\mathbf{A}(\mathbf{x})$ transforms the Casorati matrix to k-t space and $\mathbf{y}$ is the measured k-space for each time point. This optimization problem

attempts to promote a solution which fufills the low-rank assumption. The regularization term, $\|\mathbf{X}\|_*$, is known as nuclear norm regularization and is defined in eq.(8.4) where $\sigma_r(\mathbf{X})$ is the rth singular value of the Casorati matrix. As with CS reconstruction, the λ parameter controls the level of regularization.

$$\hat{\mathbf{X}} = \arg\min_{\mathbf{X}} \frac{1}{2} \|\mathbf{A}(\mathbf{X}) - \mathbf{y}\|_2^2 + \lambda \|\mathbf{X}\|_* \tag{8.3}$$

$$\|\mathbf{X}\|_* = \sum_{r=1}^{\min(M,Nt)} \sigma_r(\mathbf{X}) \tag{8.4}$$

A variation of low-rank reconstruction is locally low-rank reconstruction (LLR). In LLR, the image is divided into blocks and a Casorati matrix is formed for each block. This moves away from the assumption made in LR reconstruction that all pixels are globally correlated and instead restricts the correlation to small local image patches of a defined size. While LLR reconstruction can result in less temporal blurring than LR reconstruction, if global correlations are present then LLR will ignore them [188]. The LLR reconstruction model is shown in eq.(8.5), the key difference with LR reconstruction is the introduction of the operator $P_i(\mathbf{X})$, forming the local Casorati matrix from the ith patch of pixels.

$$\hat{\mathbf{X}} = \arg\min_{\mathbf{X}} \frac{1}{2} \|\mathbf{A}(\mathbf{X}) - \mathbf{y}\|_2^2 + \lambda \sum_{i=1}^{N_{Patches}} \|P_i(\mathbf{X})\|_* \tag{8.5}$$

Low-rank techniques can also be used in conjunction with sparsity regularization. This combination has been shown to improve image quality (over implementing a single technique) [190]. However, the cost of applying both

regularization methods is increased reconstruction time needed to perform the required matrix decompositions. Combining SMS accelerated rtMRI with low-rank/locally low-rank reconstruction is an area of future work aimed at further improving image quality at high level of undersampling.

8.2.3 Machine Learning

Machine learning (ML) techniques are now being developed for many areas of MRI. Example applications include identification of disease from MR images [191], denoising of images [192], motion correction [193], automated segmentation of tissues [194, 195], developing novel trajectories [196] and reconstruction of images from recorded k-space data [197]. This last application is most relevant for this thesis [198, 197].

Applying ML to dynamic imaging problems, especially non-regular movements (e.g. speech), introduces additional challenges [197]. The lack of a ground truth prevents the use of supervised learning approaches, where the image reconstructed from undersampled k-space data is compared to a fully sampled ground truth image. This has motivated the use of unsupervised learning ML methods which do not require a ground truth [199]. A review of recent developments in unsupervised MRI reconstruction can be found in Zeng et al. (2021) [197].

Blumenthal et al. (2024) demonstrated the use of an unsupervised ML reconstruction, using a training scheme called self-supervised data undersampling, for radial rtMRI reconstruction [200]. The authors showed that the ML reconstruction method outperformed parallel imaging based reconstruction in terms of apparent SNR and temporal fidelity. However, it is worth noting

that a comparison to compressed sensing reconstruction was not made. In addition, the authors used the ML algorithm to estimate the coil sensitivity profiles for each time frame. The advantage of this joint estimation approach is that it removes the assumption that coil sensitivity profiles are invariant over time.

Combining the SMS rtMRI with unsupervised ML image reconstruction offers the opportunity for improved image quality at high levels of undersampling. However, careful verification of the reconstructed images is required to ensure the trained network is robust at the desired temporal resolution, level of SMS acceleration and slice distances. It is also be important to verify that the trained network is not biased towards healthy tissue. This problem was demonstrated by Nataraj et al. (2020) who showed that some ML networks trained using a dataset containing healthy tissue and common brain tumours failed to reconstruct images that instead contained rare brain tumours [201]. Alongside this bias problem are the ethical and regulatory issues with ML based reconstruction (such as patient data privacy in training data) [202].

8.2.4 Alternative Applications

This thesis has focused on dynamic imaging applications using the developed rtMRI sequence. In this final section, potential applications other than dynamic imaging are briefly explored.

Neuroimaging

Functional Magnetic Resonance Imaging (fMRI) provides noninvasive brain physiology information at relatively high spatiotemporal resolution ($\approx$ 1mm

and 1s respectively) [203]. These signals are indirect, pseudo measures of neuronal activity (NA) with interpretation hindered by complex neurophysiology and associated vascular weightings.

A recently proposed technique called direct imaging of neuronal activity (DIANA) was demonstrated (in rodents) using a fast (TR=5ms) 2D-line scanning GRE sequence at high field (9.4T) [204]. A diagram of the 2D-line scanning sequence is shown in Fig.8.2. Using this sequence, with stimulation of the whisker pad, Toi et al. (2022) observed a spike $\approx$ 30ms after stimulation in the somatosensory cortex. Toi et al. (2022) hypothesised that this represents direct imaging of neuronal spiking activity. Replicating these findings in humans and understanding the signal source has proven difficult, raising concerns about this method [205, 206, 207].

By adding an additional loop to repeatedly acquire a line of k-space, I converted the rtMRI sequence (with Cartesian sampling) to replicate the Toi et al. (2022) 2D-line scanning sequence. A small study was performed to test whether the DIANA signal could be observed in the human brain at 3T. Results[1] from the attempt to replicate the work, by using electrical stimulation across the ring finger and thumb, are shown in Fig.8.3. A signal spike $\approx$ 15ms after the stimulation was observed in the somatosensory cortex, similar to that seen by Toi et al. (2022). This time is inline with nerve conduction times from the hand to the brain [208]. However, principle component analysis of individual coil images reveals that banding artefacts are present in $\approx$ 52% of coil images (Fig.8.4). Removing the coil images, which showed these artefacts, resulted in the suppression of the signal spike. This indicates that electrical noise from the stimulation equipment may have been

[1]These initial results were presented at the 2024 ISMRM meeting.

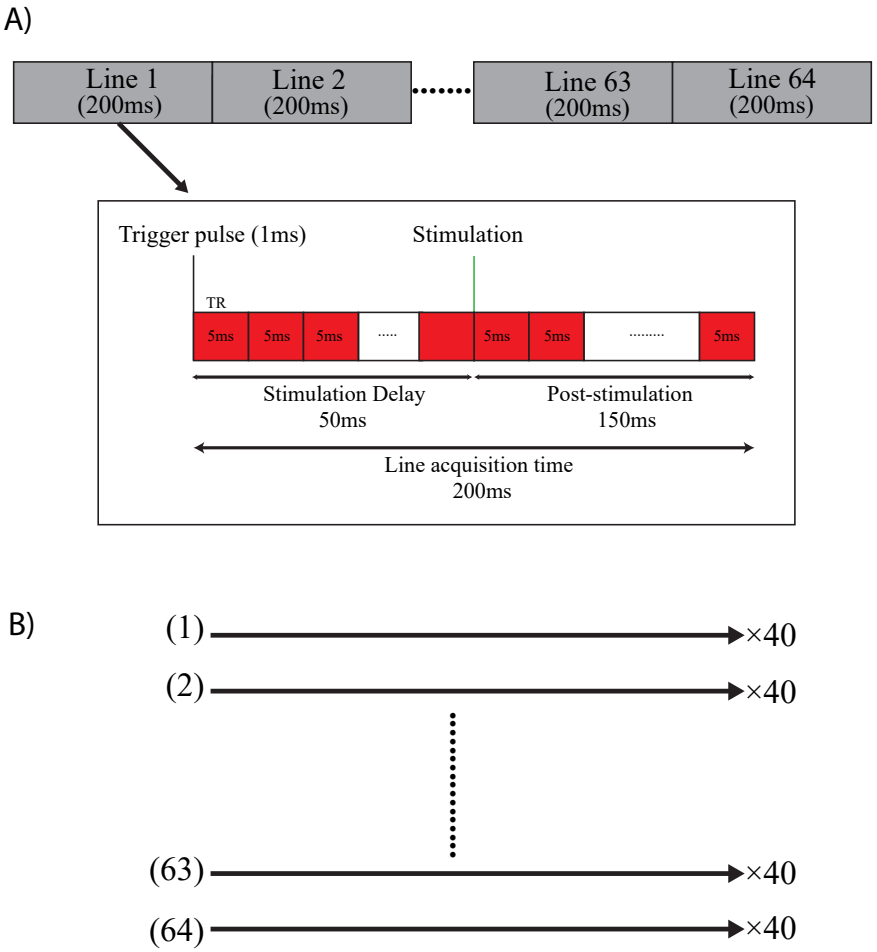

Figure 8.2: Illustration of the 2D-line scanning sequence used in DIANA fMRI. Each gray imaging block (A) represents the repeated acquisition of a line of k-space (B). Each line of k-space is acquired 40 times during the block, yielding a per line acquisition time of 200ms. At the start of an imaging block a trigger pulse is used to synchronise the acquisition to the stimulation equipment. The first ten line repeats are acquired before the electrical stimulation is applied, 30 line repeats are acquired post-stimulation. In total 64 lines of k-space are acquired resulting in a total acquisition time of 12.8s per image.

the cause of the spike rather than a physiological response to the stimulation.

An additional potential confound is neuronal inhibition (i.e. the response

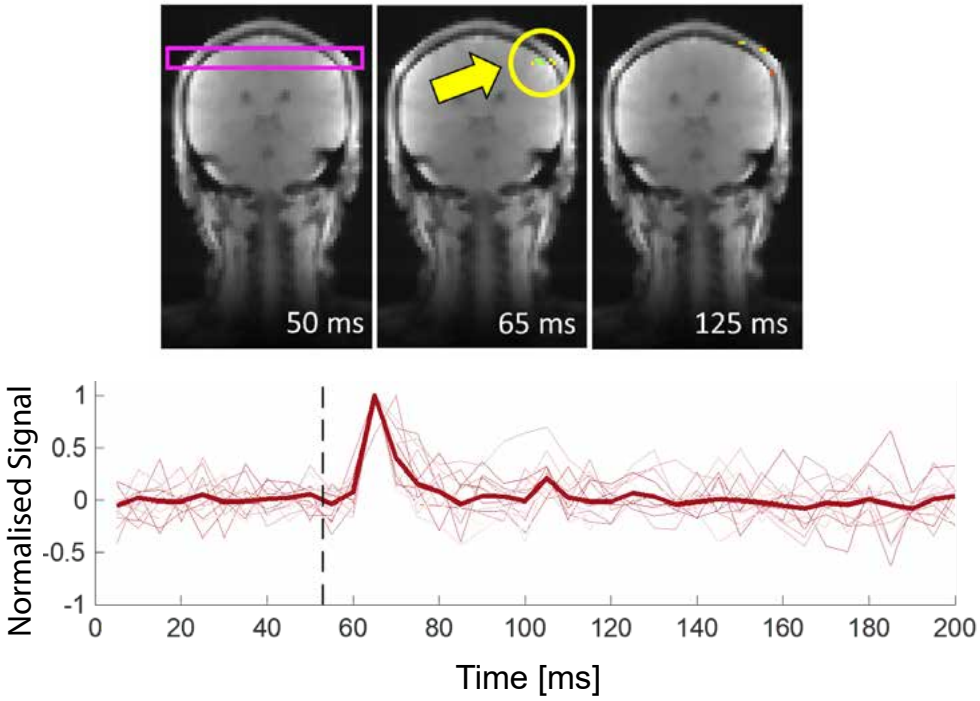

Figure 8.3: Top: example of a response seen after electrical stimulation, the yellow circle highlights the region of interest. Bottom: the solid line is the result from averaging the signal from 6 volunteers (the results from each subject are shown in the thinner lines), a signal spike $\approx$ 15ms after stimulation (dotted vertical line at 50ms) can be seen.

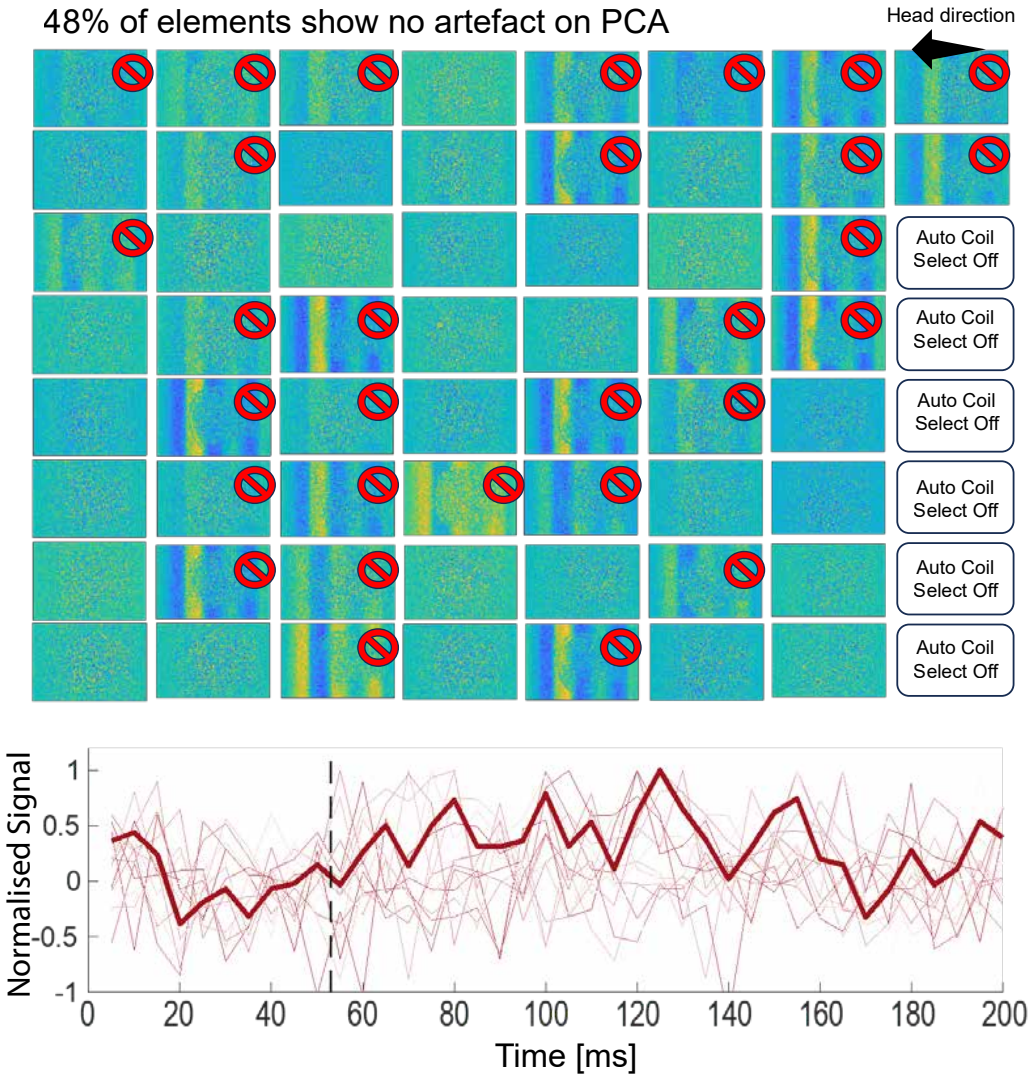

Figure 8.4: Top: visualisation of principle components for each coil image. Red marks on the top right corners identify coil images with banding artefacts. Removing these coil images from the reconstruction process eliminates the spike response after stimulation from the signal (bottom).

to the stimulation reduces over time) due to the constant stimulation used in DIANA experiments. This is particularly problematic when using Cartesian 2D-line scanning as the majority of time will be spent sampling higher frequency components and a large amount of habituation may have occurred before the center of k-space is reached. Adapting the DIANA sequence to use radial sampling, which can be achieved using the sequence developed in this thesis, could help overcome this issue as the center of k-space is acquired throughout the acquisition. Future work will explore the use of radial sampling for DIANA fMRI and will use a visual stimulation paradigm instead of electrical stimulation. This will enable further exploration of the DIANA signal source and help determine the validity of this method in neuroscience research.

Sodium Imaging

Sodium ions play an important role in cellular regulation, neuronal signalling and muscle action [209]. Imaging the roles of this element directly is, therefore, an attractive goal. The isotope ^{23}Na (natural abundance = 100%) can be used for MRI but its signal-to-noise is much inferior to ^{1}H imaging (3000-20000 times lower) due to low concentration and reduced sensitivity (due to the lower Larmor frequency of 33.78MHz) [210]. ^{23}Na is a quadrupolar nucleus ($S = \frac{3}{2}$), in biological tissue this results in fast relaxation. For example, typical T_1 and T_2 values in muscle tissue are 12ms and 2ms respectively [210]. To circumvent low SNR and prevent the need for large amounts of signal averaging that impacts on acquisition time, accelerated signal acquisition techniques are therefore critical. One way to achieve this is through the

use of radial sampling [209].

Provisional in-vivo results (acquired using a $^{1}H/^{23}Na$ dual-tuned surface coil) from a human calf are shown in Fig.8.5. The left part of this figure shows a standard T_2-weighted ^{1}H image of a calf as a reference. The middle and right images are ^{23}Na images acquired with Cartesian and radial sampling (using the radial sequence developed in this thesis) respectively. The ^{23}Na image acquired using Cartesian sampling (64 lines) consists of 150 averages and the image acquired using radial sampling (64 spokes) consists of 100 averages. Using a TR = 2.5ms, radial sampling reduces the acquisition time from 24s to 16s. Importantly, the image quality between both trajectories is comparable, thus, demonstrating how radial acquisition can be used to accelerate ^{23}Na imaging. The radial data was reconstructed using gridding with density compensation. Combining sodium imaging with CS reconstruction will enable further improvements in image quality [211]. Additionally, the development of center out trajectories would be beneficial for ^{23}Na imaging as it would allow for shorter echo times to be achieved [212, 213]. This is critical due to the fast relaxation time of ^{23}Na, which results in a rapid signal decay [214]. Additionally, the use of ML networks to denoise images may improve image quality in ^{23}Na imaging [215, 216].

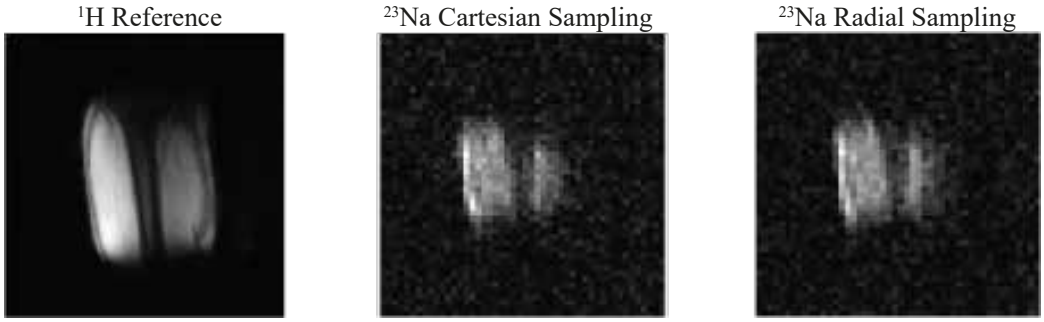

Figure 8.5: Left: ^{1}H image of the right calf. The middle panel is a ^{23}Na image of the same calf acquired using Cartesian sampling (150 averages). The right panel is a ^{23}Na image of the calf acquired using radial sampling (100 averages), resulting in a reduction of acquisition time from 24s to 16s.

8.2.5 Closing Summary

rtMRI is a unique imaging methodology that enables the dynamics of the human body to be recorded. This thesis has shown that the combination of a radial rtMRI GRE sequence with SMS acceleration and CS reconstruction enables both a high temporal resolution (up to 37.5ms) and multiple slices (1-7) to be imaged. However, the use of SMS acceleration introduces intensity variations in the images, which increase as the levels of SMS acceleration and undersampling increases. To enable further improvements in image quality (at high temporal resolutions), the LLR and ML reconstruction techniques described in Section 8.2 should be investigated.

Appendices

A

Video Descriptions

This appendix details the rtMRI videos referenced throughout this thesis.

Video 5.1 Compares rtMRI data, at increasing levels of undersampling, reconstructed using the proposed CS algorithm, CG-SENSE and gridding.

Video 5.2 Compares rtMRI videos (25 spokes/frame) reconstructed at increasing levels of coil compression.

Video 5.3 Compares three slice SMS rtMRI videos acquired using SMS GA sampling, at increasing levels of undersampling, reconstructed using the proposed CS algorithm and CG-SENSE.

Video 5.4 Compares three slice SMS rtMRI videos acquired using GA sampling, at increasing levels of undersampling, reconstructed using the proposed CS algorithm and CG-SENSE.

Video 5.5 Compares the central slices from SMS rtMRI videos (originally containing three slices) acquired using SMS GA sampling (left) and GA sampling (right) at increasing levels of undersampling.

Video 5.6 Comparison of SMS rtMRI videos (three slices) acquired using SMS GA sampling (top) and GA sampling (bottom) at decreasing slice

distances.

Video 5.7 Comparison of five slice SMS rtMRI videos at increasing levels of undersampling acquired using SMS GA sampling (top) and GA sampling (bottom). All videos are reconstructed using the proposed CS reconstruction pipeline.

Video 5.8 Comparison of five slice SMS rtMRI videos (25 spokes/frame) at increasing levels of regularization acquired using SMS GA sampling (top) and GA sampling (bottom).

Video 5.9 Comparison of seven slice SMS rtMRI videos at increasing levels of undersampling acquired using SMS GA sampling (top) and GA sampling (bottom). All videos are reconstructed using the proposed CS reconstruction pipeline.

Video 5.10 Compares SMS rtMRI videos (25 spokes/frame, three slices) reconstructed at increasing levels of coil compression.

Video 5.11 Compares single-slice rtMRI videos (15 spokes/frame) with different median filter widths applied after reconstruction (using the proposed CS reconstruction pipeline).

Video 5.12 Compares SMS rtMRI videos (15 spokes/frame, three slices) with different median filter widths applied after reconstruction (using the proposed CS reconstruction pipeline).

Video 6.1 Single-slice rtMRI videos of the dynamic phantom being stretched forward to emulate the action of sticking the tongue out. A rtMRI video

in the sagittal orientation is shown followed by an rtMRI video in the axial orientation.

Video 6.2 Single-slice rtMRI videos of the dynamic phantom, with metal plates attached to the jaw, being stretched forward to emulate the action of sticking the tongue out. A rtMRI video in the sagittal orientation is shown followed by an rtMRI video in the axial orientation.

Video 7.1 Single-slice rtMRI video (20 spokes/frame, temporal resolution: 50ms) of speech (pronunciation of vowels) at a spatial resolution of 2.2mm^2.

Video 7.2 Single-slice rtMRI video (20 spokes/frame, temporal resolution: 58ms) of speech (pronunciation of vowels) at a spatial resolution of 1.1mm^2.

Video 7.3 SMS rtMRI video (three slices, 25 spokes/frame, temporal resolution: 62.5ms) of speech (pronunciation of vowels) at a spatial resolution of 2.2mm^2.

Video 7.4 SMS rtMRI video (three slices, 25 spokes/frame, temporal resolution: 62.5ms) of a dry swallow at a spatial resolution of 2.2mm^2.

Video 7.5 SMS rtMRI video (three slices, 15 spokes/frame, temporal resolution 37.5ms) of knee movement.

Video 7.6 Single-slice rtMRI video of foot/ankle movement (15 spokes/frame, temporal resolution 37.5ms).

Video 7.7 Single-slice rtMRI video of wrist movement (15 spokes/frame, temporal resolution 37.5ms).

References

[1] Donald W McRobbie et al. *MRI from Picture to Proton*. Cambridge University Press, Sept. 2006.

[2] Michael Jacobs. "Handbook of MRI pulse sequences". en. In: *J. Magn. Reson. Imaging* 24.1 (July 2006), pp. 256–256.

[3] E Mark Haacke et al. *Magnetic Resonance Imaging: Physical Principles and Sequence Design*. Wiley & Sons, Limited, John, 2014.

[4] Krishna S Nayak et al. "Real-Time Magnetic Resonance Imaging". en. In: *J. Magn. Reson. Imaging* 55.1 (Jan. 2022), pp. 81–99.

[5] Shuo Zhang, Kai Tobias Block, and Jens Frahm. "Magnetic resonance imaging in real time: advances using radial FLASH". en. In: *J. Magn. Reson. Imaging* 31.1 (Jan. 2010), pp. 101–109.

[6] Martin Uecker et al. "Real-time MRI at a resolution of 20 ms". en. In: *NMR Biomed.* 23.8 (Oct. 2010), pp. 986–994.

[7] Sajan Goud Lingala et al. "Recommendations for real-time speech MRI". en. In: *J. Magn. Reson. Imaging* 43.1 (Jan. 2016), pp. 28–44.

[8] Shuo Zhang et al. "Real-time magnetic resonance imaging of cardiac function and flow-recent progress". en. In: *Quant. Imaging Med. Surg.* 4.5 (Oct. 2014), pp. 313–329.

[9] L M Shapiro and G E Gold. "MRI of weight bearing and movement". In: *Osteoarthritis Cartilage* 20.2 (Feb. 2012), pp. 69–78.

[10] Sebastian Krohn et al. "Multi-slice real-time MRI of temporomandibular joint dynamics". en. In: *Dentomaxillofac. Radiol.* 48.1 (Jan. 2019), p. 20180162.

[11] D J Larkman et al. "Use of multicoil arrays for separation of signal from multiple slices simultaneously excited". en. In: *J. Magn. Reson. Imaging* 13.2 (Feb. 2001), pp. 313–317.

[12] Malcolm H Levitt. *Spin Dynamics: Basics of Nuclear Magnetic Resonance*. en. John Wiley & Sons, May 2013.

[13] Robin A de Graaf. *In vivo NMR spectroscopy: Principles and techniques*. en. 3rd ed. Nashville, TN: John Wiley & Sons, Mar. 2019.

[14] Jorge Zavala Bojorquez et al. "What are normal relaxation times of tissues at 3 T?" en. In: *Magn. Reson. Imaging* 35 (Jan. 2017), pp. 69–80.

[15] Thomas A Gallagher, Alexander J Nemeth, and Lotfi Hacein-Bey. "An introduction to the Fourier transform: relationship to MRI". en. In: *AJR Am. J. Roentgenol.* 190.5 (May 2008), pp. 1396–1405.

[16] "K-space in the clinic". en. In: *J. Magn. Reson. Imaging* 19.2 (Feb. 2004), pp. 145–159.

[17] D B Twieg. "The k-trajectory formulation of the NMR imaging process with applications in analysis and synthesis of imaging methods". en. In: *Med. Phys.* 10.5 (1983), pp. 610–621.

[18] F H Epstein, J P Mugler 3rd, and J R Brookeman. "Spoiling of transverse magnetization in gradient-echo (GRE) imaging during the approach to steady state". en. In: *Magn. Reson. Med.* 35.2 (Feb. 1996), pp. 237–245.

[19] Michael Markl and Jochen Leupold. "Gradient echo imaging". en. In: *J. Magn. Reson. Imaging* 35.6 (June 2012), pp. 1274–1289.

[20] *MAGNETOM Vida*. en. `https://www.siemens-healthineers.com/en-uk/magnetic-resonance-imaging/3t-mri-scanner/magnetom-vida`. Accessed: 2024-4-2.

[21] Jason Sanders and Edward Kandrot. *CUDA by Example: An Introduction to General-purpose GPU Programming*. en. Addison-Wesley, 2011.

[22] Jeffrey Tsao and Sebastian Kozerke. "MRI temporal acceleration techniques". en. In: *J. Magn. Reson. Imaging* 36.3 (Sept. 2012), pp. 543–560.

[23] Jesse Hamilton, Dominique Franson, and Nicole Seiberlich. "Recent advances in parallel imaging for MRI". en. In: *Prog. Nucl. Magn. Reson. Spectrosc.* 101 (Aug. 2017), pp. 71–95.

[24] Benjamin M Kozak et al. "MRI Techniques to Decrease Imaging Times in Children". en. In: *Radiographics* 40.2 (Feb. 2020), pp. 485–502.

[25] Hiroyuki Kabasawa. "MR Imaging in the 21st Century: Technical Innovation over the First Two Decades". en. In: *Magn. Reson. Med. Sci.* 21.1 (Mar. 2022), pp. 71–82.

[26] Juergen Hennig. "An evolution of low-field strength MRI". en. In: *MAGMA* 36.3 (July 2023), pp. 335–346.

[27] Sairam Geethanath et al. "Compressed sensing MRI: a review". en. In: *Crit. Rev. Biomed. Eng.* 41.3 (2013), pp. 183–204.

[28] Anagha Deshmane et al. "Parallel MR imaging". en. In: *J. Magn. Reson. Imaging* 36.1 (July 2012), pp. 55–72.

[29] Wingchi E Kwok. "Basic Principles of and Practical Guide to Clinical MRI Radiofrequency Coils". In: *Radiographics* 42.3 (May 2022), pp. 898–918.

[30] Erik G Larsson et al. "SNR-optimality of sum-of-squares reconstruction for phased-array magnetic resonance imaging". en. In: *J. Magn. Reson.* 163.1 (July 2003), pp. 121–123.

[31] David J Larkman. "The g-Factor and Coil Design". In: *Parallel Imaging in Clinical MR Applications*. Ed. by Stefan O Schoenberg, Olaf Dietrich, and Maximilian F Reiser. Berlin, Heidelberg: Springer Berlin Heidelberg, 2007, pp. 37–48.

[32] Olaf Dietrich et al. "Measurement of signal-to-noise ratios in MR images: influence of multichannel coils, parallel imaging, and reconstruction filters". en. In: *J. Magn. Reson. Imaging* 26.2 (Aug. 2007), pp. 375–385.

[33] Michael A Ohliger and Daniel K Sodickson. "An introduction to coil array design for parallel MRI". en. In: *NMR Biomed.* 19.3 (May 2006), pp. 300–315.

[34] Mark A Griswold et al. "Autocalibrated coil sensitivity estimation for parallel imaging". en. In: *NMR Biomed.* 19.3 (May 2006), pp. 316–324.

[35] Martin Uecker. *Parallel Magnetic Resonance Imaging*. 2015.

[36] Olaf Dietrich. "MRI from k-Space to Parallel Imaging". In: *Parallel Imaging in Clinical MR Applications*. Ed. by Stefan O Schoenberg, Olaf Dietrich, and Maximilian F Reiser. Berlin, Heidelberg: Springer Berlin Heidelberg, 2007, pp. 3–17.

[37] K P Pruessmann et al. "SENSE: sensitivity encoding for fast MRI". en. In: *Magn. Reson. Med.* 42.5 (Nov. 1999), pp. 952–962.

[38] D K Sodickson and W J Manning. "Simultaneous acquisition of spatial harmonics (SMASH): fast imaging with radiofrequency coil arrays". en. In: *Magn. Reson. Med.* 38.4 (Oct. 1997), pp. 591–603.

[39] P M Jakob et al. "AUTO-SMASH: a self-calibrating technique for SMASH imaging. SiMultaneous Acquisition of Spatial Harmonics". en. In: *MAGMA* 7.1 (Nov. 1998), pp. 42–54.

[40] Martin Blaimer et al. "SMASH, SENSE, PILS, GRAPPA: how to choose the optimal method". en. In: *Top. Magn. Reson. Imaging* 15.4 (Aug. 2004), pp. 223–236.

[41] K P Pruessmann et al. "Advances in sensitivity encoding with arbitrary k-space trajectories". en. In: *Magn. Reson. Med.* 46.4 (Oct. 2001), pp. 638–651.

[42] Joseph Suresh Paul, Raji Susan Mathew, and M S Renjith. "Theory of Parallel MRI and Cartesian SENSE Reconstruction: Highlight". In: *Medical Imaging in Clinical Applications: Algorithmic and Computer-Based Approaches*. Ed. by Nilanjan Dey, Vikrant Bhateja, and Aboul Ella Hassanien. Cham: Springer International Publishing, 2016, pp. 311–328.

[43] Oliver Maier et al. "CG-SENSE revisited: Results from the first ISMRM reproducibility challenge". en. In: *Magn. Reson. Med.* 85.4 (Apr. 2021), pp. 1821–1839.

[44] Jiaming Liu et al. "Chapter 3 - Optimization Algorithms for MR Reconstruction". In: *Advances in Magnetic Resonance Technology and Applications*. Ed. by Mehmet Akçakaya, Mariya Doneva, and Claudia Prieto. Vol. 7. Academic Press, Jan. 2022, pp. 59–72.

[45] Martin Hanke. *A Taste of Inverse Problems*. Other Titles in Applied Mathematics. Society for Industrial and Applied Mathematics, Aug. 2017.

[46] Fa-Hsuan Lin et al. "Parallel imaging reconstruction using automatic regularization". In: *Magnetic Resonance in Medicine* 51.3 (2004), pp. 559–567. DOI: https://doi.org/10.1002/mrm.10718. eprint: https://onlinelibrary.wiley.com/doi/pdf/10.1002/mrm.10718. URL: https://onlinelibrary.wiley.com/doi/abs/10.1002/mrm.10718.

[47] Katherine L Wright et al. "Non-Cartesian parallel imaging reconstruction". en. In: *J. Magn. Reson. Imaging* 40.5 (Nov. 2014), pp. 1022–1040.

[48] Jonathan R Shewchuk. *An Introduction to the Conjugate Gradient Method Without the Agonizing Pain*. Tech. rep. USA, Feb. 1994.

[49] Mathias Nittka. "Measurement of Coil Sensitivity Profiles". In: *Parallel Imaging in Clinical MR Applications*. Ed. by Stefan O Schoenberg, Olaf Dietrich, and Maximilian F Reiser. Berlin, Heidelberg: Springer Berlin Heidelberg, 2007, pp. 107–112.

[50] Evan Cummings, Jacob A Macdonald, and Nicole Seiberlich. "Chapter 6 - Parallel Imaging". In: *Advances in Magnetic Resonance Technology and Applications*. Ed. by Mehmet Akçakaya, Mariya Doneva, and Claudia Prieto. Vol. 7. Academic Press, Jan. 2022, pp. 129–157.

[51] Olaf Dietrich. "Limitations of Parallel Imaging". In: *Parallel Imaging in Clinical MR Applications*. Ed. by Stefan O Schoenberg, Olaf Dietrich, and Maximilian F Reiser. Berlin, Heidelberg: Springer Berlin Heidelberg, 2007, pp. 177–179.

[52] P Mansfield. "Multi-planar image formation using NMR spin echoes". In: *J. Phys. C: Solid State Phys.* 10 (Feb. 1977).

[53] W Scott Hoge et al. "Efficient single-shot Z-shim EPI via spatial and temporal encoding". In: *2011 IEEE International Symposium on Biomedical Imaging: From Nano to Macro*. IEEE, Mar. 2011, pp. 1565–1568.

[54] Melissa W Haskell, Jon-Fredrik Nielsen, and Douglas C Noll. "Off-resonance artifact correction for MRI: A review". en. In: *NMR Biomed.* 36.5 (May 2023), e4867.

[55] Benjamin Zahneisen et al. "Extended hybrid-space SENSE for EPI: Off-resonance and eddy current corrected joint interleaved blip-up/down reconstruction". en. In: *Neuroimage* 153 (June 2017), pp. 97–108.

[56] Robbert J H van Gorkum et al. "Analysis and correction of off-resonance artifacts in echo-planar cardiac diffusion tensor imaging". en. In: *Magn. Reson. Med.* 84.5 (Nov. 2020), pp. 2561–2576.

[57] Said Boujraf et al. "Ultrafast bold fMRI using single-shot spin-echo echo planar imaging". en. In: *J. Med. Phys.* 34.1 (Jan. 2009), pp. 37–42.

[58] P A Bandettini et al. "Spin-echo and gradient-echo EPI of human brain activation using BOLD contrast: a comparative study at 1.5 T". en. In: *NMR Biomed.* 7.1-2 (Mar. 1994), pp. 12–20.

[59] Saskia Bollmann and Markus Barth. "New acquisition techniques and their prospects for the achievable resolution of fMRI". en. In: *Prog. Neurobiol.* 207 (Dec. 2021), p. 101936.

[60] Wenchuan Wu and Karla L Miller. "Image formation in diffusion MRI: A review of recent technical developments". en. In: *J. Magn. Reson. Imaging* 46.3 (Sept. 2017), pp. 646–662.

[61] Julian Maclaren et al. "Prospective motion correction in brain imaging: a review". en. In: *Magn. Reson. Med.* 69.3 (Mar. 2013), pp. 621–636.

[62] F Godenschweger et al. "Motion correction in MRI of the brain". en. In: *Phys. Med. Biol.* 61.5 (Mar. 2016), R32–56.

[63] Bénédicte M A Delattre et al. "Spiral demystified". en. In: *Magn. Reson. Imaging* 28.6 (July 2010), pp. 862–881.

[64] James G Pipe and Nicholas R Zwart. "Spiral trajectory design: a flexible numerical algorithm and base analytical equations". en. In: *Magn. Reson. Med.* 71.1 (Jan. 2014), pp. 278–285.

[65] Valentin Fauveau et al. "Performance of spiral UTE-MRI of the lung in post-COVID patients". en. In: *Magn. Reson. Imaging* 96 (Feb. 2023), pp. 135–143.

[66] Jiang Du et al. "Two-dimensional ultrashort echo time imaging using a spiral trajectory". en. In: *Magn. Reson. Imaging* 26.3 (Apr. 2008), pp. 304–312.

[67] Ya-Jun Ma et al. "Volumetric imaging of myelin in vivo using 3D inversion recovery-prepared ultrashort echo time cones magnetic resonance imaging". en. In: *NMR Biomed.* 33.10 (Oct. 2020), e4326.

[68] Zhixing Wang et al. "Dynamic cardiac MRI with high spatiotemporal resolution using accelerated spiral-out and spiral-in/out bSSFP pulse sequences at 1.5 T". In: *Magn. Reson. Mater. Phys. Biol. Med.* 36.6 (Dec. 2023), pp. 857–867.

[69] Bhushan Borotikar et al. "Dynamic MRI to quantify musculoskeletal motion: A systematic review of concurrent validity and reliability, and perspectives for evaluation of musculoskeletal disorders". en. In: *PLoS One* 12.12 (Dec. 2017), e0189587.

[70] Xue Feng, Zhixing Wang, and Craig H Meyer. "Real-time dynamic vocal tract imaging using an accelerated spiral GRE sequence and low rank plus sparse reconstruction". In: *Magn. Reson. Imaging* 80 (July 2021), pp. 106–112.

[71] Yongwan Lim et al. "Dynamic off-resonance correction for spiral real-time MRI of speech". en. In: *Magn. Reson. Med.* 81.1 (Jan. 2019), pp. 234–246.

[72] Bertram J Wilm et al. "Diffusion MRI with concurrent magnetic field monitoring". en. In: *Magn. Reson. Med.* 74.4 (Oct. 2015), pp. 925–933.

[73] Mustafa Çavuşoğlu. "Arterial spin labeling MRI using spiral acquisitions and concurrent field monitoring". In: *J. Magn. Reson.* 356 (Nov. 2023), p. 107572.

[74] Nadine N Graedel et al. "Feasibility of spiral fMRI based on an LTI gradient model". en. In: *Neuroimage* 245 (Dec. 2021), p. 118674.

[75] P C Lauterbur. "Image Formation by Induced Local Interactions: Examples Employing Nuclear Magnetic Resonance". en. In: *Nature* 242.5394 (Mar. 1973), pp. 190–191.

[76] Li Feng. "Golden-Angle Radial MRI: Basics, Advances, and Applications". en. In: *J. Magn. Reson. Imaging* 56.1 (July 2022), pp. 45–62.

[77] Li Feng et al. "Golden-angle radial sparse parallel MRI: combination of compressed sensing, parallel imaging, and golden-angle radial sampling for fast and flexible dynamic volumetric MRI". en. In: *Magn. Reson. Med.* 72.3 (Sept. 2014), pp. 707–717.

[78] Li Feng et al. "GRASP-Pro: imProving GRASP DCE-MRI through self-calibrating subspace-modeling and contrast phase automation". en. In: *Magn. Reson. Med.* 83.1 (Jan. 2020), pp. 94–108.

[79] Wenwen Jiang, Peder E Z Larson, and Michael Lustig. "Simultaneous auto-calibration and gradient delays estimation (SAGE) in non-Cartesian parallel MRI using low-rank constraints". en. In: *Magn. Reson. Med.* 80.5 (Nov. 2018), pp. 2006–2016.

[80] Amir Moussavi et al. "Correction of gradient-induced phase errors in radial MRI". en. In: *Magn. Reson. Med.* 71.1 (Jan. 2014), pp. 308–312.

[81] Sebastian Rosenzweig, H Christian M Holme, and Martin Uecker. "Simple auto-calibrated gradient delay estimation from few spokes using Radial Intersections (RING)". en. In: *Magn. Reson. Med.* 81.3 (Mar. 2019), pp. 1898–1906.

[82] Leslie Greengard and June-Yub Lee. "Accelerating the Nonuniform Fast Fourier Transform". In: *SIAM Rev.* 46.3 (Jan. 2004), pp. 443–454.

[83] J A Fessler and B P Sutton. "Nonuniform fast Fourier transforms using min-max interpolation". In: *IEEE Trans. Signal Process.* 51.2 (Feb. 2003), pp. 560–574.

[84] R D Hoge, R K Kwan, and G B Pike. "Density compensation functions for spiral MRI". en. In: *Magn. Reson. Med.* 38.1 (July 1997), pp. 117–128.

[85] J G Pipe and P Menon. "Sampling density compensation in MRI: rationale and an iterative numerical solution". en. In: *Magn. Reson. Med.* 41.1 (Jan. 1999), pp. 179–186.

[86] Philip J Beatty, Dwight G Nishimura, and John M Pauly. "Rapid gridding reconstruction with a minimal oversampling ratio". en. In: *IEEE Trans. Med. Imaging* 24.6 (June 2005), pp. 799–808.

[87] J I Jackson et al. "Selection of a convolution function for Fourier inversion using gridding (computerised tomography application)". In: *IEEE Trans. Med. Imaging* 10.3 (Sept. 1991), pp. 473–478.

[88] William H Press et al. *Numerical Recipes 3rd Edition: The Art of Scientific Computing*. 3rd ed. USA: Cambridge University Press, Aug. 2007.

[89] Üstün Aydıngöz, Adalet Elçin Yıldız, and F Bilge Ergen. "Zero Echo Time Musculoskeletal MRI: Technique, Optimization, Applications, and Pitfalls". en. In: *Radiographics* 42.5 (July 2022), pp. 1398–1414.

[90] Philipp Lurz et al. "Feasibility and reproducibility of biventricular volumetric assessment of cardiac function during exercise using real-time radial k-t SENSE magnetic resonance imaging". en. In: *J. Magn. Reson. Imaging* 29.5 (May 2009), pp. 1062–1070.

[91] Christoph Kolbitsch et al. "Highly efficient whole-heart imaging using radial phase encoding-phase ordering with automatic window selection". en. In: *Magn. Reson. Med.* 66.4 (Oct. 2011), pp. 1008–1018.

[92] Frank Ong, Martin Uecker, and Michael Lustig. "Accelerating Non-Cartesian MRI Reconstruction Convergence Using k-Space Preconditioning". en. In: *IEEE Trans. Med. Imaging* 39.5 (May 2020), pp. 1646–1654.

[93] Sonali Bagchi and Sanjit K Mitra. *The Nonuniform Discrete Fourier Transform and Its Applications in Signal Processing*. Springer US.

[94] Emmanuel J Candès, Justin K Romberg, and Terence Tao. "Stable signal recovery from incomplete and inaccurate measurements". en. In: *Commun. Pure Appl. Math.* 59.8 (Aug. 2006), pp. 1207–1223.

[95] Emmanuel J Candes and Michael B Wakin. "An Introduction To Compressive Sampling". In: *IEEE Signal Process. Mag.* 25.2 (Mar. 2008), pp. 21–30.

[96] Simon Foucart and Holger Rauhut. *A Mathematical Introduction to Compressive Sensing*. Springer New York, Aug. 2013.

[97] Michael Lustig, David Donoho, and John M Pauly. "Sparse MRI: The application of compressed sensing for rapid MR imaging". en. In: *Magn. Reson. Med.* 58.6 (Dec. 2007), pp. 1182–1195.

[98] A Graps. "An introduction to wavelets". In: *IEEE Computational Science and Engineering* 2.2 (1995), pp. 50–61.

[99] Jong Chul Ye. "Compressed sensing MRI: a review from signal processing perspective". en. In: *BMC Biomed Eng* 1 (Mar. 2019), p. 8.

[100] E J Candes, J Romberg, and T Tao. "Robust uncertainty principles: exact signal reconstruction from highly incomplete frequency information". In: *IEEE Trans. Inf. Theory* 52.2 (Feb. 2006), pp. 489–509.

[101] Ss Vasanawala et al. "PRACTICAL PARALLEL IMAGING COMPRESSED SENSING MRI: SUMMARY OF TWO YEARS OF EXPERIENCE IN ACCELERATING BODY MRI OF PEDIATRIC PATIENTS". en. In: *Proc. IEEE Int. Symp. Biomed. Imaging* 2011 (Dec. 2011), pp. 1039–1043.

[102] Li Feng. "Chapter 8 - Sparse Reconstruction". In: *Magnetic Resonance Image Reconstruction*. Ed. by Mehmet Akçakaya, Mariya Doneva, and Claudia Prieto. Vol. 7. Advances in Magnetic Resonance Technology and Applications. Academic Press, 2022, pp. 189–221. DOI: https://doi.org/10.1016/B978-0-12-822726-8.00018-X.

[103] Christian G Graff and Emil Y Sidky. "Compressive sensing in medical imaging". en. In: *Appl. Opt.* 54.8 (Mar. 2015), pp. C23–44.

[104] Oren N Jaspan, Roman Fleysher, and Michael L Lipton. "Compressed sensing MRI: a review of the clinical literature". en. In: *Br. J. Radiol.* 88.1056 (Sept. 2015), p. 20150487.

[105] Dong Liang et al. "Accelerating SENSE using compressed sensing". en. In: *Magn. Reson. Med.* 62.6 (Dec. 2009), pp. 1574–1584.

[106] Ricardo Otazo et al. "Combination of compressed sensing and parallel imaging for highly accelerated first-pass cardiac perfusion MRI". en. In: *Magn. Reson. Med.* 64.3 (Sept. 2010), pp. 767–776.

[107] Christopher M Sandino et al. "Compressed Sensing: From Research to Clinical Practice with Deep Neural Networks". en. In: *IEEE Signal Process. Mag.* 37.1 (Jan. 2020), p. 111.

[108] Haifeng Wang et al. "A survey of GPU-based acceleration techniques in MRI reconstructions". en. In: *Quant. Imaging Med. Surg.* 8.2 (Mar. 2018), pp. 196–208.

[109] Ching-Hua Chang and Jim Ji. "Compressed sensing MRI with multichannel data using multicore processors". en. In: *Magn. Reson. Med.* 64.4 (Oct. 2010), pp. 1135–1139.

[110] Sebastian Schaetz et al. "Accelerated Computing in Magnetic Resonance Imaging: Real-Time Imaging Using Nonlinear Inverse Reconstruction". en. In: *Comput. Math. Methods Med.* 2017 (Dec. 2017).

[111] Seunghoon Nam et al. "Compressed sensing reconstruction for whole-heart imaging with 3D radial trajectories: a graphics processing unit implementation". en. In: *Magn. Reson. Med.* 69.1 (Jan. 2013), pp. 91–102.

[112] Ashish A Tamhane et al. "Iterative image reconstruction for PROPELLER-MRI using the nonuniform fast fourier transform". en. In: *J. Magn. Reson. Imaging* 32.1 (July 2010), pp. 211–217.

[113] Yu-Hsuan Shih et al. *cuFINUFFT: a load-balanced GPU library for general-purpose nonuniform FFTs*. 2021.

[114] Alex H Barnett, Jeremy F Magland, and Ludvig af Klinteberg. *A parallel non-uniform fast Fourier transform library based on an "exponential of semicircle" kernel*. 2019.

[115] A H Barnett. *Aliasing error of the $exp(\beta\sqrt{1-z^2})$ kernel in the nonuniform fast Fourier transform*. 2020.

[116] Jeffrey A Fessler. *Optimization methods for MR image reconstruction (long version)*. 2019.

[117] Markus Barth et al. "Simultaneous multislice (SMS) imaging techniques". en. In: *Magn. Reson. Med.* 75.1 (Jan. 2016), pp. 63–81.

[118] Andreia S Gaspar, Ana R Fouto, and Rita G Nunes. "Chapter 3 - Simultaneous multi-slice MRI". In: *Advances in Magnetic Resonance Technology and Applications*. Ed. by In-Young Choi and Peter Jezzard. Vol. 4. Academic Press, Jan. 2021, pp. 37–52.

[119] Samy Abo Seada et al. "Multiband RF pulse design for realistic gradient performance". en. In: *Magn. Reson. Med.* 81.1 (Jan. 2019), pp. 362–376.

[120] Hong Shang et al. "Multiband RF pulses with improved performance via convex optimization". In: *J. Magn. Reson.* 262 (Jan. 2016), pp. 81–90.

[121] Christoph Stefan Aigner et al. "Efficient high-resolution RF pulse design applied to simultaneous multi-slice excitation". en. In: *J. Magn. Reson.* 263 (Feb. 2016), pp. 33–44.

[122] David G Norris et al. "Power Independent of Number of Slices (PINS) radiofrequency pulses for low-power simultaneous multislice excitation". en. In: *Magn. Reson. Med.* 66.5 (Nov. 2011), pp. 1234–1240.

[123] Stephen R Yutzy et al. "Improvements in multislice parallel imaging using radial CAIPIRINHA". en. In: *Magn. Reson. Med.* 65.6 (June 2011), pp. 1630–1637.

[124] Yiteng Zhang et al. "Clinical Applications and Recent Updates of Simultaneous Multi-slice Technique in Accelerated MRI". In: *Acad. Radiol.* (Jan. 2024).

[125] Benjamin B Risk, Mary C Kociuba, and Daniel B Rowe. "Impacts of simultaneous multislice acquisition on sensitivity and specificity in fMRI". en. In: *Neuroimage* 172 (May 2018), pp. 538–553.

[126] Hesamoddin Jahanian et al. "Advantages of short repetition time resting-state functional MRI enabled by simultaneous multi-slice imaging". en. In: *J. Neurosci. Methods* 311 (Jan. 2019), pp. 122–132.

[127] Stanislas Rapacchi et al. "Simultaneous multi-slice cardiac cine with Fourier-encoded self-calibration at 7 Tesla". en. In: *Magn. Reson. Med.* 81.4 (Apr. 2019), pp. 2576–2587.

[128] Omer Burak Demirel et al. "Improved simultaneous multislice cardiac MRI using readout concatenated k-space SPIRiT (ROCK-SPIRiT)". en. In: *Magn. Reson. Med.* 85.6 (June 2021), pp. 3036–3048.

[129] Johnathan Le et al. "Deep learning for radial SMS myocardial perfusion reconstruction using the 3D residual booster U-net". In: *Magn. Reson. Imaging* 83 (Nov. 2021), pp. 178–188.

[130] Jamal S Rana et al. "Changes in Mortality in Top 10 Causes of Death from 2011 to 2018". en. In: *J. Gen. Intern. Med.* 36.8 (Aug. 2021), pp. 2517–2518.

[131] Muhummad Sohaib Nazir et al. "Simultaneous multi slice (SMS) balanced steady state free precession first-pass myocardial perfusion cardiovascular magnetic resonance with iterative reconstruction at 1.5 T". en. In: *J. Cardiovasc. Magn. Reson.* 20.1 (Dec. 2018), p. 84.

[132] Changyu Sun et al. “Non-Cartesian slice-GRAPPA and slice-SPIRiT reconstruction methods for multiband spiral cardiac MRI”. en. In: *Magn. Reson. Med.* 83.4 (Apr. 2020), pp. 1235–1249.

[133] Haonan Wang et al. “Radial simultaneous multi-slice CAIPI for ungated myocardial perfusion”. In: *Magn. Reson. Imaging* 34.9 (Nov. 2016), pp. 1329–1336.

[134] Ziyue Wu et al. “Evaluation of upper airway collapsibility using real-time MRI”. In: *Journal of Magnetic Resonance Imaging* 44.1 (2016), pp. 158–167. DOI: https://doi.org/10.1002/jmri.25133.

[135] Weiyi Chen et al. “Real-time multislice MRI during continuous positive airway pressure reveals upper airway response to pressure change”. en. In: *J. Magn. Reson. Imaging* 46.5 (Nov. 2017), pp. 1400–1408.

[136] Aneurin J Kennerley et al. “Real-time magnetic resonance imaging: mechanics of oral and facial function”. en. In: *Br. J. Oral Maxillofac. Surg.* 60.5 (June 2022), pp. 596–603.

[137] S J Riederer et al. “MR fluoroscopy: technical feasibility”. en. In: *Magn. Reson. Med.* 8.1 (Sept. 1988), pp. 1–15.

[138] F Farzaneh et al. “MR fluoroscopy: initial clinical studies”. en. In: *Radiology* 171.2 (May 1989), pp. 545–549.

[139] Jennifer A Steeden et al. “Real-time assessment of right and left ventricular volumes and function in children using high spatiotemporal resolution spiral bSSFP with compressed sensing”. en. In: *J. Cardiovasc. Magn. Reson.* 20.1 (Dec. 2018), p. 79.

[140] Oliver Bieri and Klaus Scheffler. “Fundamentals of balanced steady state free precession MRI”. en. In: *J. Magn. Reson. Imaging* 38.1 (July 2013), pp. 2–11.

[141] Xue Feng et al. “Non-Cartesian balanced steady-state free precession pulse sequences for real-time cardiac MRI”. en. In: *Magn. Reson. Med.* 75.4 (Apr. 2016), pp. 1546–1555.

[142] Valentina Mazzoli et al. “Water and fat separation in real-time MRI of joint movement with phase-sensitive bSSFP”. en. In: *Magn. Reson. Med.* 78.1 (July 2017), pp. 58–68.

[143] O. Bieri, M. Markl, and K. Scheffler. "Analysis and compensation of eddy currents in balanced SSFP". In: *Magnetic Resonance in Medicine* 54.1 (2005), pp. 129–137. DOI: https://doi.org/10.1002/mrm.20527. eprint: https://onlinelibrary.wiley.com/doi/pdf/10.1002/mrm.20527. URL: https://onlinelibrary.wiley.com/doi/abs/10.1002/mrm.20527.

[144] Stefanie Winkelmann et al. "An optimal radial profile order based on the Golden Ratio for time-resolved MRI". en. In: *IEEE Trans. Med. Imaging* 26.1 (Jan. 2007), pp. 68–76.

[145] Stefan Wundrak et al. "A Small Surrogate for the Golden Angle in Time-Resolved Radial MRI Based on Generalized Fibonacci Sequences". In: *IEEE Transactions on Medical Imaging* 34.6 (2015), pp. 1262–1269. DOI: 10.1109/TMI.2014.2382572.

[146] R R Ernst and W A Anderson. "Application of Fourier Transform Spectroscopy to Magnetic Resonance". In: *Rev. Sci. Instrum.* 37 (Jan. 1966), pp. 93–102.

[147] Stephen Boyd et al. "Distributed Optimization and Statistical Learning via the Alternating Direction Method of Multipliers". In: *Foundations and Trends® in Machine Learning* 3.1 (2011), pp. 1–122.

[148] Sathish Ramani and Jeffrey A Fessler. "Regularized parallel mri reconstruction using an alternating direction method of multipliers". In: *2011 IEEE International Symposium on Biomedical Imaging: From Nano to Macro*. IEEE, Mar. 2011, pp. 385–388.

[149] Brendt Wohlberg. *ADMM Penalty Parameter Selection by Residual Balancing*. 2017.

[150] Tobias C Wood. *Algorithms for Least-Squares Noncartesian MR Image Reconstruction*. 2022.

[151] Martin Buehrer et al. "Array compression for MRI with large coil arrays". en. In: *Magn. Reson. Med.* 57.6 (June 2007), pp. 1131–1139.

[152] M Uecker et al. "ESPIRiT—an eigenvalue approach to autocalibrating parallel MRI: where SENSE meets GRAPPA". In: *Magnetic resonance* (2014).

[153] Rizwan Ahmad et al. "Plug-and-Play Methods for Magnetic Resonance Imaging: Using Denoisers for Image Recovery". In: *IEEE Signal Processing Magazine* 37.1 (2020), pp. 105–116. DOI: 10.1109/MSP.2019.2949470.

[154] Shuo Zhang, Arno Olthoff, and Jens Frahm. "Real-time magnetic resonance imaging of normal swallowing". en. In: *J. Magn. Reson. Imaging* 35.6 (June 2012), pp. 1372–1379.

[155] Mai Le and Jeffrey A Fessler. "Efficient, Convergent SENSE MRI Reconstruction for Nonperiodic Boundary Conditions via Tridiagonal Solvers". en. In: *IEEE Trans Comput Imaging* 3.1 (Mar. 2017), pp. 11–21.

[156] Aaron Niebergall et al. "Real-time MRI of speaking at a resolution of 33 ms: undersampled radial FLASH with nonlinear inverse reconstruction". en. In: *Magn. Reson. Med.* 69.2 (Feb. 2013), pp. 477–485.

[157] Daeun Kim et al. "Region-optimized virtual (ROVir) coils: Localization and/or suppression of spatial regions using sensor-domain beamforming". en. In: *Magn. Reson. Med.* 86.1 (July 2021), pp. 197–212.

[158] Daeun Kim et al. "Single breath-hold CINE imaging with combined simultaneous multislice and region-optimized virtual coils". en. In: *Magn. Reson. Med.* 90.1 (July 2023), pp. 222–230.

[159] Luuk Voskuilen et al. "A 12-channel flexible receiver coil for accelerated tongue imaging". en. In: *MAGMA* 33.4 (Aug. 2020), pp. 581–590.

[160] Gabriel Prieto Renieblas et al. "Structural similarity index family for image quality assessment in radiological images". en. In: *J Med Imaging (Bellingham)* 4.3 (July 2017), p. 035501.

[161] Segrey Kastryulin et al. "Image quality assessment for Magnetic Resonance Imaging". In: *IEEE Access* 11 (Mar. 2022), pp. 14154–14168.

[162] Kathryn E Keenan et al. "Quantitative magnetic resonance imaging phantoms: A review and the need for a system phantom". en. In: *Magn. Reson. Med.* 79.1 (Jan. 2018), pp. 48–61.

[163] Hirokazu Kato et al. "Composition of MRI phantom equivalent to human tissues". en. In: *Med. Phys.* 32.10 (Oct. 2005), pp. 3199–3208.

[164] Anton Hasso. *Diagnostic Imaging of the Head and Neck: MRI with CT & PET Correlations*. en. Lippincott Williams & Wilkins, Nov. 2011.

[165] Y L Dai and A D King. "State of the art MRI in head and neck cancer". In: *Clin. Radiol.* 73.1 (Jan. 2018), pp. 45–59.

[166] Terrence D. Case. "ULTRASOUND PHYSICS AND INSTRUMENTATION". In: *Surgical Clinics of North America* 78.2 (1998), pp. 197–217. ISSN: 0039-6109. DOI: https://doi.org/10.1016/S0039-6109(05)70309-1. URL: https://www.sciencedirect.com/science/article/pii/S0039610905703091.

[167] Christina A. Rappazzo and Catherine L. Turk. "The Videofluoroscopic Swallow Study: Introduction, Limitations, and Challenges". In: *Pediatric Dysphagia: Challenges and Controversies*. Ed. by Julina Ongkasuwan and Eric H. Chiou. Cham: Springer International Publishing, 2018, pp. 67–86. ISBN: 978-3-319-97025-7. DOI: 10.1007/978-3-319-97025-7_5. URL: https://doi.org/10.1007/978-3-319-97025-7_5.

[168] Weiyi Chen et al. "Intermittently tagged real-time MRI reveals internal tongue motion during speech production". en. In: *Magn. Reson. Med.* 82.2 (Aug. 2019), pp. 600–613.

[169] Charlotte E E Wiltshire et al. "Speech Movement Variability in People Who Stutter: A Vocal Tract Magnetic Resonance Imaging Study". en. In: *J. Speech Lang. Hear. Res.* 64.7 (July 2021), pp. 2438–2452.

[170] Yijing Lu et al. "Characteristics of articulatory gestures in stuttered speech: A case study using real-time magnetic resonance imaging". In: *J. Commun. Disord.* 97 (May 2022), p. 106213.

[171] Ziwei Zhao et al. "Improved 3D real-time MRI of speech production". en. In: *Magn. Reson. Med.* 85.6 (June 2021), pp. 3182–3195.

[172] Christina Hagedorn et al. "Characterizing post-glossectomy speech using real-time MRI". In: *International Seminar on Speech Production, Cologne, Germany*. 2014, pp. 170–173.

[173] Pere Clavé and Reza Shaker. "Dysphagia: current reality and scope of the problem". en. In: *Nat. Rev. Gastroenterol. Hepatol.* 12.5 (May 2015), pp. 259–270.

[174] Domenico Rizzo et al. "Origin of the MRI Contrast in Natural and Hydrogel Formulation of Pineapple Juice". en. In: *Bioinorg. Chem. Appl.* 2021 (Jan. 2021), p. 6666018.

[175] Yihe Zu et al. "Evaluation of Swallow Function After Tongue Cancer Treatment Using Real-Time Magnetic Resonance Imaging: A Pilot Study". In: *JAMA Otolaryngol. Head Neck Surg.* 139.12 (Dec. 2013), pp. 1312–1319.

[176] Christine E Draper et al. “Feasibility of using real-time MRI to measure joint kinematics in 1.5T and open-bore 0.5T systems”. en. In: *J. Magn. Reson. Imaging* 28.1 (July 2008), pp. 158–166.

[177] Michael A Sherman, Ajay Seth, and Scott L Delp. “What is a moment arm? Calculating muscle effectiveness in biomechanical models using generalized coordinates”. en. In: *Proc. ASME Des. Eng. Tech. Conf.* 2013 (Aug. 2013).

[178] Corinne R Adams et al. “Effects of rotator cuff tears on muscle moment arms: a computational study”. en. In: *J. Biomech.* 40.15 (June 2007), pp. 3373–3380.

[179] Freya Hik and David C Ackland. “The moment arms of the muscles spanning the glenohumeral joint: a systematic review”. en. In: *J. Anat.* 234.1 (Jan. 2019), pp. 1–15.

[180] E C Clarke et al. “A non-invasive, 3D, dynamic MRI method for measuring muscle moment arms in vivo: Demonstration in the human ankle joint and Achilles tendon”. In: *Med. Eng. Phys.* 37.1 (Jan. 2015), pp. 93–99.

[181] Abhijit J Chaudhari et al. “Real-time MRI of the moving wrist at 0.55 tesla”. en. In: *Br. J. Radiol.* 96.1151 (Nov. 2023), p. 20230298.

[182] Joanna Yuen et al. “Multi-echo GRE imaging of knee cartilage”. en. In: *J. Magn. Reson. Imaging* 45.5 (May 2017), pp. 1502–1513.

[183] Scott B Reeder et al. “Water-fat separation with IDEAL gradient-echo imaging”. en. In: *J. Magn. Reson. Imaging* 25.3 (Mar. 2007), pp. 644–652.

[184] Zhengguo Tan et al. “Dynamic water/fat separation and B 0 inhomogeneity mapping-joint estimation using undersampled triple-echo multi-spoke radial FLASH”. en. In: *Magn. Reson. Med.* 82.3 (Sept. 2019), pp. 1000–1011.

[185] Harald H Quick et al. “Real-time MRI of joint movement with true-FISP”. en. In: *J. Magn. Reson. Imaging* 15.6 (June 2002), pp. 710–715.

[186] Klaus Scheffler and Stefan Lehnhardt. “Principles and applications of balanced SSFP techniques”. en. In: *Eur. Radiol.* 13.11 (Nov. 2003), pp. 2409–2418.

[187] Dinghui Wang et al. "High SNR rapid T1-weighted MPRAGE using spiral imaging with long readouts and improved deblurring". In: *Magnetic Resonance in Medicine* 89.3 (2023), pp. 951–963. DOI: https://doi.org/10.1002/mrm.29492. eprint: https://onlinelibrary.wiley.com/doi/pdf/10.1002/mrm.29492. URL: https://onlinelibrary.wiley.com/doi/abs/10.1002/mrm.29492.

[188] Anthony G Christodoulou. "Chapter 9 - Low-Rank Matrix and Tensor–Based Reconstruction". In: *Advances in Magnetic Resonance Technology and Applications*. Ed. by Mehmet Akçakaya, Mariya Doneva, and Claudia Prieto. Vol. 7. Academic Press, Jan. 2022, pp. 223–247.

[189] Zhanxuan Hu et al. "Low Rank Regularization: A review". In: *Neural Netw.* 136 (Apr. 2021), pp. 218–232.

[190] Junbo Chen, Shouyin Liu, and Min Huang. "Low-Rank and Sparse Decomposition Model for Accelerating Dynamic MRI Reconstruction". en. In: *J. Healthc. Eng.* 2017 (Aug. 2017).

[191] Yogesh Kumar et al. "Artificial intelligence in disease diagnosis: a systematic literature review, synthesizing framework and future research agenda". en. In: *J. Ambient Intell. Humaniz. Comput.* 14.7 (2023), pp. 8459–8486.

[192] Jose V Manjon and Pierrick Coupe. *MRI denoising using Deep Learning and Non-local averaging*. 2019.

[193] Veronika Spieker et al. "Deep Learning for Retrospective Motion Correction in MRI: A Comprehensive Review". en. In: *IEEE Trans. Med. Imaging* 43.2 (Feb. 2024), pp. 846–859.

[194] Ali Işın, Cem Direkoğlu, and Melike Şah. "Review of MRI-based Brain Tumor Image Segmentation Using Deep Learning Methods". In: *Procedia Comput. Sci.* 102 (Jan. 2016), pp. 317–324.

[195] Tommaso Ciceri et al. "Review on deep learning fetal brain segmentation from Magnetic Resonance images". In: *Artif. Intell. Med.* 143 (Sept. 2023), p. 102608.

[196] Tomer Weiss et al. *PILOT: Physics-Informed Learned Optimized Trajectories for Accelerated MRI*. 2021.

[197] Gushan Zeng et al. "A review on deep learning MRI reconstruction without fully sampled k-space". en. In: *BMC Med. Imaging* 21.1 (Dec. 2021), p. 195.

[198] Shanshan Wang et al. "Deep learning for fast MR imaging: A review for learning reconstruction from incomplete k-space data". In: *Biomed. Signal Process. Control* 68 (July 2021), p. 102579.

[199] Zoubin Ghahramani. "Unsupervised Learning". In: *Advanced Lectures on Machine Learning: ML Summer Schools 2003, Canberra, Australia, February 2 - 14, 2003, Tübingen, Germany, August 4 - 16, 2003, Revised Lectures*. Ed. by Olivier Bousquet, Ulrike von Luxburg, and Gunnar Rätsch. Berlin, Heidelberg: Springer Berlin Heidelberg, 2004, pp. 72–112.

[200] Moritz Blumenthal et al. "Self-supervised learning for improved calibrationless radial MRI with NLINV-Net". In: *arXiv [cs.CV]* (Feb. 2024).

[201] G Nataraj and R Otazo. "Investigating robustness to unseen pathologies in model-free deep multicoil reconstruction". In: *Proc. ISMRM Workshop on Data Sampling & Image* (2020).

[202] Filippo Pesapane et al. "Artificial intelligence as a medical device in radiology: ethical and regulatory issues in Europe and the United States". en. In: *Insights Imaging* 9.5 (Oct. 2018), pp. 745–753.

[203] Gary H Glover. "Overview of functional magnetic resonance imaging". en. In: *Neurosurg. Clin. N. Am.* 22.2 (Apr. 2011), pp. 133–9, vii.

[204] Phan Tan Toi et al. "In vivo direct imaging of neuronal activity at high temporospatial resolution". In: *Science* 378.6616 (2022), pp. 160–168.

[205] Shota Hodono et al. *Initial experiences with Direct Imaging of Neuronal Activity (DIANA) in humans*. 2023.

[206] Valerie Doan Phi Van, Sajal Sen, and Alan Jasanoff. "A different interpretation of the DIANA fMRI signal". en. In: *Sci Adv* 10.13 (Mar. 2024), eadl2034.

[207] Sang-Han Choi et al. "No Replication of Direct Neuronal Activity-related (DIANA) fMRI in Anesthetized Mice". en. In: *bioRxiv* (May 2023).

[208] Sunil Chouhan. "Normal Motor and Sensory Nerve Conduction Velocity of Radial Nerve in Young Adult Medical Students". en. In: *J. Clin. Diagn. Res.* 10.1 (Jan. 2016), pp. CC01–3.

[209] Olgica Zaric et al. "Frontiers of Sodium MRI Revisited: From Cartilage to Brain Imaging". In: *Journal of Magnetic Resonance Imaging* 54.1 (2021), pp. 58–75. DOI: https://doi.org/10.1002/jmri.27326.

[210] Guillaume Madelin et al. "Sodium MRI: methods and applications". en. In: *Prog. Nucl. Magn. Reson. Spectrosc.* 79 (May 2014), pp. 14–47.

[211] Qingping Chen, N. Jon Shah, and Wieland A. Worthoff. "Compressed Sensing in Sodium Magnetic Resonance Imaging: Techniques, Applications, and Future Prospects". In: *Journal of Magnetic Resonance Imaging* 55.5 (2022), pp. 1340–1356. DOI: https://doi.org/10.1002/jmri.28029.

[212] Armin M Nagel et al. "Sodium MRI using a density-adapted 3D radial acquisition technique". en. In: *Magn. Reson. Med.* 62.6 (Dec. 2009), pp. 1565–1573.

[213] Frank Riemer et al. "Sodium ((23)Na) ultra-short echo time imaging in the human brain using a 3D-Cones trajectory". en. In: *MAGMA* 27.1 (Feb. 2014), pp. 35–46.

[214] Deborah Burstein and Charles S Springer Jr. "Sodium MRI revisited". en. In: *Magn. Reson. Med.* 82.2 (Aug. 2019), pp. 521–524.

[215] Simon Koppers et al. "Sodium Image Denoising Based on a Convolutional Denoising Autoencoder". In: *Bildverarbeitung für die Medizin 2019*. Springer Fachmedien Wiesbaden, 2019, pp. 98–103.

[216] Rebecca R Baker et al. "Rapid 2D 23Na MRI of the calf using a denoising convolutional neural network". en. In: *Magn. Reson. Imaging* 110 (July 2024), pp. 184–194.